Second harmonic generation in III-nitride waveguides

Maksym Gromovyi

UNIVERSITÉ CÔTE D'AZUR

ÉCOLE DOCTORALE
SCIENCES FONDAMENTALES ET APPLIQUÉES

THÈSE DE DOCTORAT

Génération de seconde harmonique dans des guides d'ondes à base de nitrure d'éléments III

Maksym GROMOVYI

CNRS-CRHEA

Présentée en vue de l'obtention du grade de docteur en Physique **d'**Université Côte d'Azur
Dirigée par : Jean-Yves Duboz, Marc de Micheli
Soutenue le : 30 mars 2018

Devant le jury, composé de :
Giuseppe Leo, Professeur, Paris-Diderot
Jacqueline Bloch, DR, C2N Marcoussis
Jean-Yves Duboz, DR, CNRS-CRHEA
Katia Gallo, Professeur, KTH
Marc De Micheli, DR, INPHYNI
Nicolas Grandjean, Professeur, EPFL
Vincent Berger, Professeur, CEA
Yannick Dumeige, Maître de conf., FOTON

ANR GaNeX

Génération de seconde harmonique dans des guides d'ondes à base de nitrure d'éléments III

Second harmonic generation in III-nitride waveguides

Jury :

Rapporteurs

Giuseppe Leo, Professeur, Université Paris-Diderot
Nicolas Grandjean, Professeur, EPFL

Examinateurs

Jacqueline Bloch, Directrice de recherche, C2N Marcoussis
Jean-Yves Duboz, Directeur de recherche, CNRS-CRHEA
Katia Gallo, Professeur, KTH
Marc De Micheli, Directeur de recherche, INPHYNI
Yannick Dumeige, Maître de conférences, FOTON

Invités
Vincent Berger, Professeur, Directeur DRF, CEA, Paris

Génération de seconde harmonique dans des guides d'ondes à base de nitrure d'éléments III

Résumé: Ce travail est consacré à l'étude de la génération de deuxième harmonique (SHG) dans des guides d'ondes de Nitrure d'éléments III.

Un des buts principaux de ce travail, était d'identifier les origines des pertes à la propagation dans les guides d'ondes GaN et de fortement les réduire dans des guides présentant des possibilités d'accord de phase, pour améliorer l'efficacité de la SHG. Nous avons fait un progrès très important dans cette direction et avons fabriqué des guides d'ondes plans de GaN épitaxiés sur des substrats de saphir avec des pertes à la propagation inférieures à 1dB/cm dans le visible. Dans ces guides d'ondes à faibles pertes, il a été possible d'obtenir un processus de SHG efficace en utilisant l'accord de phase modal. Nous avons obtenu 2% de conversion entre une pompe dans le proche infrarouge et un harmonique dans le visible, ce qui correspond à une efficacité de conversion normalisée de 0,15%$W^{-1}cm^{-2}$. Les pertes à la propagation et l'efficacité de conversion obtenues sont les meilleurs résultats rapportés jusqu'ici pour des guides d'ondes plan en GaN.

De plus, nous avons étudié des guides d'ondes de Nitrure d'éléments III épitaxiés sur des substrats de Si, dont la fabrication demande de relever plusieurs défis, mais qui ouvrent des possibilités intéressantes.

La première est la possibilité de graver sélectivement les nitrures ou le Si, ce que nous avons utilisé pour développer une plate-forme permettant la fabrication d'objets suspendus comme des micro-disques, des guides d'ondes et des micro-disques couplés à un guide d'ondes. Cette plate-forme a permis la première démonstration de SHG doublement résonante en utilisant un accord de phase modal entre des modes de galerie du micro-disque. Bien que toutes les expériences que nous avons exécutées aient été faites dans une région spectrale limitée, l'étude numérique présentée dans ce manuscrit démontre la grande adaptabilité de cette plate-forme basée sur la possibilité de faire varier la composition des guides d'ondes AlGaN de GaN pur à AlN pur.

La deuxième possibilité liée à l'épitaxie de nitrures d'éléments III sur Si, est qu'en la combinant avec des techniques de report, on peut jouer avec des guides nitrures d'éléments III sur SiO_2. Nos résultats numériques révèlent le potentiel complet des guides d'ondes d'AlGaN en démontrant qu'en utilisant différentes combinaisons de mode et en jouant sur la composition et la géométrie des guides d'ondes, il est possible d'obtenir un signal de deuxième harmonique dans l'ultra-violet, le visible ou le proche-infrarouges. Ces résultats montrent aussi, que pour améliorer encore l'efficacité de la SHG, on doit fabriquer des guides d'ondes canaux présentant un isolement optique parfait du substrat de Si et une inversion de polarité précisément placée dans le cœur du guide d'ondes. Dans une telle structure on pourrait profiter simultanément du confinement de la puissance, de l'accord de phase modal et d'un recouvrement optimisé des modes en interaction. Dans ce cas, nos calculs montrent que l'efficacité de conversion pourrait atteindre 100%$W^{-1}cm^{-2}$.

Au cours de ce travail nous avons pu tester des guides canaux et des guides présentant une inversion de polarité dans le cœur. La qualité des flancs des guides canaux s'est avérée être tout à fait encourageante, mais leur performance non linéaire sont restées très limitées, principalement à cause de fortes pertes à la propagation dues au couplage avec le substrat absorbant et à la forte rugosité de surface des couches inversées. Les structures utilisant les techniques de report, n'ont pu être testées car elles ont cassé en cour de fabrication. L'obtention de guides optimisés exige de progresser encore pour réaliser des couches de confinement optique plus épaisses et/ou d'adapter la technique de report à ces matériaux.

Mots-clés: optique non linéaire intégrée, génération de deuxième harmonique, guides d'ondes en Nitrure d'éléments III, accord de phase modale, inversion de polarité.

Second harmonic generation in III-nitride waveguides

Abstract: This work is dedicated to the study of the second harmonic generation (SHG) in III-Nitride waveguides.
One of the main goals of this work, was to identify the origins of the propagation losses in GaN waveguides, and to strongly reduce them in waveguides presenting some phase matching possibilities, in order to improve the SHG efficiency. We have made a very important progress in this direction, and fabricated by hetero-epitaxy GaN planar waveguides on sapphire substrates with propagation losses below 1dB/cm in the visible spectral region. These low-loss waveguides were used for the demonstration of an efficient second harmonic generation process using modal phase matching. We obtained 2% of power conversion from the near-infrared to the visible spectral regions with a normalized efficiency of $0.15\%W^{-1}cm^{-2}$. The obtained propagation losses and conversion efficiency are the best-reported results so far for GaN planar waveguides.
In addition, we have studied epitaxial III-nitride waveguides on Si substrates, which are very challenging to fabricate, but opens new interesting opportunities.
The first one is the possibility to etch selectively the nitrides or the Si. The selective chemical etching was used to develop a platform allowing the fabrication of suspended objects such as micro-disks, waveguides and micro-disks coupled to a waveguide. This platform has allowed the first demonstration of doubly resonant SHG using phase matching between the whispering gallery modes of a micro-disk. Although all the experiments we performed were done in a limited spectral region, the numerical study presented in this manuscript demonstrates the large adaptability of this platform based on the possibility of varying the composition of AlGaN waveguides from pure GaN to pure AlN.
The second opportunity of epitaxial III-nitrides layers on Si is the possibility to combine them with report technologies to obtain III-nitride waveguides on SiO_2. Our numerical results reveal the full potential of AlGaN waveguides by demonstrating that using different mode combinations and playing with waveguides composition and geometry, it is possible to obtain a second harmonic signal in the ultraviolet, the visible or the near-infrared spectral regions. These results also demonstrate, that to further improve the SHG efficiency, one has to fabricate ridge waveguides presenting a perfect optical isolation from the Si substrate and a polarity inversion precisely positioned in the core of the waveguide. In these structures one could benefit simultaneously from the power confinement, the modal phase matching and an optimized overlap of the interacting modes. In this case, we calculate that the conversion efficiencies could be as high as $100\%W^{-1}cm^{-2}$.
Both ridge waveguides and polarity inversion were tested in this work. The quality of the ridges was quite encouraging, but their nonlinear performance remained limited mainly because of the high propagation losses due to the coupling with the absorbing substrate and to the roughness of the surface of the epitaxial inverted layers. The structures fabricated using the report technique, haven't been tested, as they were broken during their fabrication. Getting fully optimized waveguides requires further progresses in realizing thicker optical buffer layers and/or adapting the report technique to these materials.
Keywords: integrated nonlinear optics, second harmonic generation, III-nitride waveguides, modal phase matching, polarity inversion.

Remerciements

C'est avec plaisir et reconnaissance que je profite de ces quelques lignes pour remercier les nombreuses personnes qui ont contribué, de différentes manières, à la réalisation de cette thèse.

Tout d'abord, je tiens à remercier mes directeurs de thèse, Jean-Yves Duboz et Marc De Micheli. Merci pour la confiance que vous m'avez toujours accordée, pour votre soutien et vos conseils tout au long de ces années.

I would like to thank my reading committee members, Giuseppe Leo and Nicolas Grandjean, and the members of my oral defense, Jacqueline Bloch, Katia Gallo, Yannick Dumeige and Vincent Berger for your time, involvement and helpful comments. It is a great honor for me to have you in my thesis committee.

This thesis has benefited from the financial support and fruitful collaboration within the GANEX project. It has been a great pleasure to participate in the project. Special thanks go to all the members of the quantum dot & photonic nanostructures research group in C2N laboratory.

Je profite de l'occasion qui m'est donnée pour remercier chaleureusement Julien Brault, Fabrice Semond, Stéphanie Rennesson, Aimeric Courville, Eric Frayssinet Guy Feuillet et Pascal Baldi pour leur coopération et les discussions scientifiques enrichissantes que nous avons toujours eues.

Je remercie ma professeur de français, Maryse De Micheli, pour ses cours géniaux.

Особливе спасибі мамі і брату за вашу люблячу підтримку, яка допомогла мені завершити цю роботу.

Дякую Каті за незліченні пригоди, про які я навіть не мріяв.

Contents

Chapter 1

Introduction

The first demonstration of the second harmonic generation by Franken in 1961 followed the invention of the ruby laser by Maiman just a year earlier. Second harmonic generation is an example of the second order nonlinear process which can occur in non-centrosymmetric materials which have a non-zero second order nonlinear susceptibility $\chi^{(2)}$. The $\chi^{(2)}$ susceptibility gives the nonlinear part of the polarization proportional to the square of the applied electric field $P_{\mathrm{NL}} = \chi^{(2)} E^2$. The nonlinear response of the material dipoles is very small, therefore one needs to use high electric fields E to observe the phenomenon, which can be obtained within an intense laser beam. Moreover, it is essential to obtain a constructive interference of the nonlinear responses from all the dipoles in the material, or in widely accepted terminology, to fulfil the phase matching condition. Typically the phase matching condition can be reached only for a particular wavelength within a few nanometres spectral range. It explains, why experimental nonlinear optics have got an active development only after the invention of the laser and benefit from all the progress done in the field of optical material elaboration and structuration. Indeed, it turns out, that one needs to get not only high spatial power density, which can be obtained by the focalization of the beam emitted by any bright source, but in addition, all this power has to be concentrated within a small spectral range, which can be efficiently done only with a laser.

Lasers have enabled a realization of different nonlinear processes in optics. Surprisingly enough, a few decades later these nonlinear processes have allowed to fill the gaps in the emission spectrum that were present before. It is well known, that the emission spectrum of a laser is limited by the gain range of the underlying active material, therefore lasers emit either at fixed wavelengths or are tunable within a limited spectral range, determined by the gain range. On the other hand, nonlinear optics allow to start from bright sources at fixed wavelength and cover a large spectral range by using processes such as optical parametric oscillation, sum- and difference- frequency generation; in thee cases the covered spectral range is fundamentally limited only by the transparency of the used nonlinear materials. In addition, nonlinear processes such as spontaneous parametric down conversion and spontaneous four wave mixing are actively used in quantum optics for generating heralded single photons and entangled photon pairs. The non centro-symmetry is also responsible for the electro-optical modulation, which in combination with optical fiber gave us high speed internet connections. It is truly remarkable, how nonlinear effects that is often associated with something complicated and negligible small, became so versatile in many domains ranging from everyday life to the applied and fundamental

research.

1.1 Nonlinear polarization and phase matching

Here we give a rough description how nonlinear effects can occur and what is needed for them to be efficient. In linear optics one assumes that the applied electric field E induces a polarization which is proportional to this field:

$$P(t) = \varepsilon_0 \chi^{(1)} E(t), \tag{1.1}$$

where P is the polarization, $\chi^{(1)}$ is the electric susceptibility and ε_0 is the electric permittivity of free space. For the general arguments in this section we neglect the effects of dispersion and losses, so we can use directly the relations between the time functions for the polarization and the electric field and not their spectral components.

When the amplitude of the applied field reaches even a fraction of a percent of the internal atomic field E_{at} nonlinear corrections should be added to the formula (1.1). The characteristic atomic field is defined in the following way:

$$E_{at} = \frac{e}{4\pi\varepsilon_0 a_B^2} \approx 5 \cdot 10^{11} \mathrm{V/m} \tag{1.2}$$

where e is the charge of the electron and a_B is the Bohr radius. Figure 1.1 schematically shows what happens in this situation. For a particular case of non-centrosymmetric material, which is a subject of the study in this work, the sinusoidal electric field with sufficiently high amplitude E_0 will induce the oscillation of the dipole moment $p(t)$ which is no longer a pure sinusoid. Indeed, for high deviations from the equilibrium state the dipole displacements will be different in opposite directions due to the absence of the symmetry. In this case, we still have periodic function for the dipole that can be decomposed in the Fourier series, which will contain the constant term and the terms oscillating at the frequencies ω, 2ω and so on, see Fig. 1.1. The constant term is responsible for the so-called optical rectification and the term with 2ω frequency is responsible for the second harmonic generation.

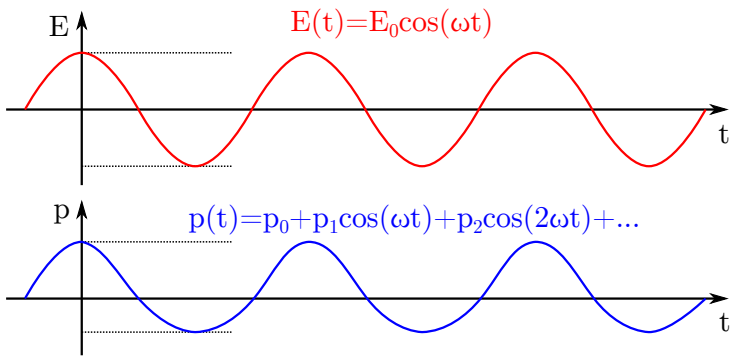

Figure 1.1 – Sinusoidal electric field with sufficiently large amplitude E_0 induces periodic oscillation of the dipole moment $p(t)$, which contains terms with higher frequencies ω, 2ω, 3ω and so on.

The nonlinear correction to the formula (1.1) has the form:

$$P = \varepsilon_0 \left(\chi^{(1)} E + \chi^{(2)} EE + \chi^{(3)} EEE + ... \right), \tag{1.3}$$

where $\chi^{(2)}$ is the second-order nonlinear susceptibility and $\chi^{(3)}$ is the third-order nonlinear susceptibility. It should be noted that the second-order nonlinear susceptibility and all even-order susceptibilities are non-zero only in non-centrosymmetric crystals, while odd-order susceptibilities are present in all materials. The second-order susceptibility is responsible for the second harmonic generation, which is the main subject of the study in this manuscript.

The first and the second terms in formula (1.3) are comparable, when the electric field reaches the value E_{at}. This gives an estimation for the second-order susceptibility:

$$\chi^{(2)} \sim \frac{\chi^{(1)}}{E_{at}} \sim \frac{1}{E_{at}} \approx 2\,\mathrm{pm/V}, \tag{1.4}$$

which represents the right order of magnitude for the $\chi^{(2)}$.

In practice one never reaches the values of the atomic electric fields E_{at}. In order to get an important nonlinear signal one uses constructive interference from many dipoles induced within the nonlinear material. In real situation it is difficult to rich the desired constructive interference and the Fig. 1.2 shows why this is the case. Figure 1.2

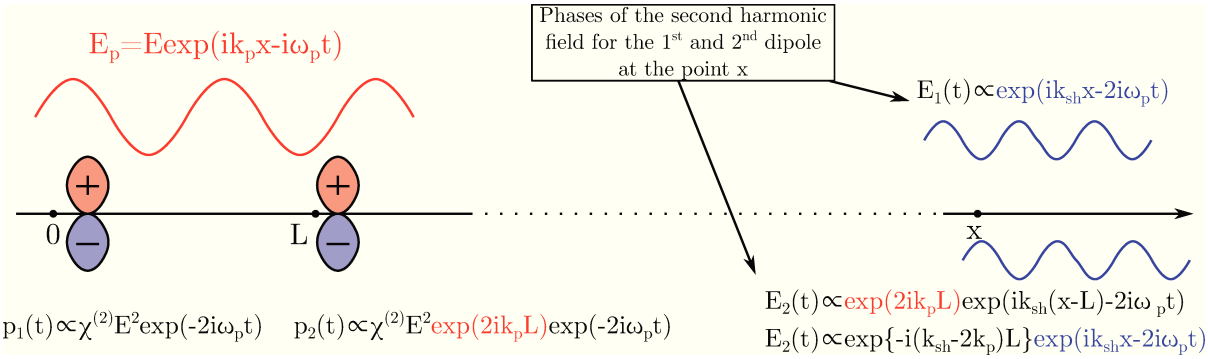

Figure 1.2 – The pump field E_p induces nonlinear polarization responses $p_1(t)$ and $p_2(t)$ in two dipoles located at the distance L from each other. The light emitted by these dipoles have different phase at the point x.

displays two dipoles induced by the electric field within monochromatic plane wave for the pump with the frequency ω_p and the wave vector k_p. For these dipoles we consider only second-order nonlinear responses $p_1(t)$ and $p_2(t)$, which are responsible for the second harmonic generation. Since this dipoles are displaced from each other by distance L in the pump field, the second dipole has an additional phase factor $\exp(2ik_\mathrm{p}L)$. Both dipoles are oscillating at the frequency $2\omega_\mathrm{p}$, so they will emit light at this frequency with the wave vector k_sh. The phases of the emitted light at the point x will be different for two dipoles. The field emitted by the second dipole will have an additional phase factor $\exp\{-i(k_\mathrm{sh}-2k_\mathrm{p})L\}$, due to the initial phase factor $\exp(2ik_\mathrm{p}L)$ and to the fact that this dipole is located closer to the point x. The fields emitted by the two dipoles enter in destructive interference when the following conditions is satisfied:

$$(k_\mathrm{sh}-2k_\mathrm{p})L_c = \pi \quad \longrightarrow \quad L_c = \frac{\lambda_\mathrm{p}}{4|n(\lambda_\mathrm{sh})-n(\lambda_\mathrm{p})|} \tag{1.5}$$

where n is the refractive index, λ_p is the wavelength of the pump, $\lambda_\mathrm{sh} = \lambda_\mathrm{p}/2$ is the wavelenght of the second harmonic and L_c is the so-called coherence length. Typically

the value of the coherence length L_c is several micrometers and after this distance the harmonic signal is reduced due to destructive interferences.

Therefore, in order to get constructive interference for all the dipoles in the sample one needs to satisfy the condition $k_{\mathrm{sh}} = 2k_{\mathrm{p}}$. In Fig. 1.2 it is assumed that dipoles are oscillating at the frequency $2\omega_p$, but in more general case one considers ω_{sh} frequency for the dipoles. More general condition for the constructive interference for the second harmonic generation have the form:

$$\omega_{\mathrm{sh}} = 2\omega_{\mathrm{p}}, \quad k_{\mathrm{sh}} = 2k_{\mathrm{p}}, \tag{1.6}$$

these are called phase matching conditions and often interpreted as energy and momentum conservation governing the conversion of two photons at the pump frequency into one photon of at the second harmonic frequency.

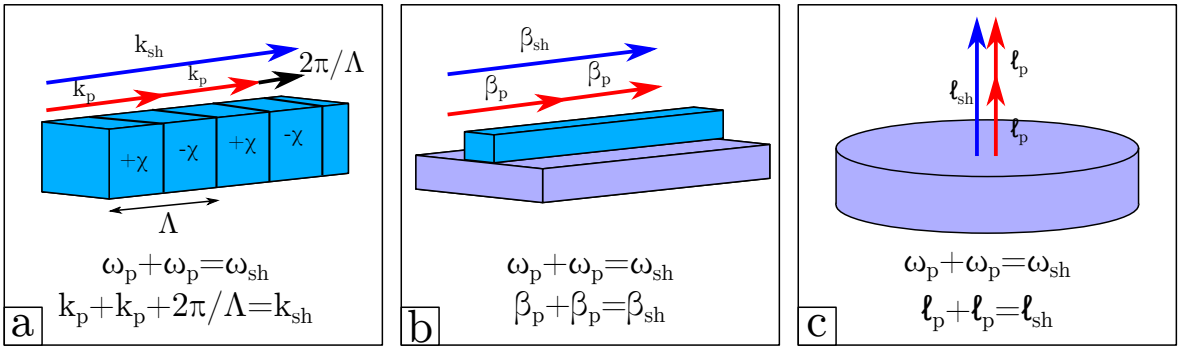

Figure 1.3 – (a) A scheme the quasi-phasematching. (b) and (c) Schemes of the modal phase matching in ridge waveguides and micro-disks respectively.

The equations (1.6) can be satisfied if $n(\lambda_{\mathrm{sh}}) = n(\lambda_{\mathrm{p}})$, which does not hold due to the chromatic dispersion. That is why one needs to apply some ingenuity in order to satisfy the conditions (1.6). One of the most common techniques in bulk optics is birefringent phase matching. It is based on the fact that waves with different polarizations can have different refractive indices for the same direction of propagation in birefringent crystals. One can get $n_o(\lambda_{\mathrm{sh}}) = n_e(\theta, \lambda_{\mathrm{p}})$ for a particular angle of propagation θ, where n_o and n_e are ordinary and extraordinary refractive indices. In this work, we want to study second harmonic generation in waveguides in order to benefit from the higher energy confinement. Therefore, the propagation direction is imposed by the construction of the waveguide and we cannot play with it to achieve the phase matching conditions.

Another approach, which works for waveguides, is based on a similar idea and is called the modal phase matching. Waveguides may support multiple modes for a given direction of propagation. These modes have different effective refractive indices, and one can satisfy (1.6) by using different modes for the pump and the second harmonic. For example, $n_{\mathrm{TM20}}(\lambda_{\mathrm{sh}}) = n_{\mathrm{TM00}}(\lambda_{\mathrm{p}})$, where n_{TM00} and n_{TM20} are the effective refractive indices of the TM00 and TM20 modes respectively.

A more general technique that works for both bulk and integrated optics is quasi-phasematching. As it was schematically explained in Fig. 1.2, the signals from two dipoles displaced by the distance L_c interfere destructively with each other. Since the induced nonlinear polarization is proportional not only to the square of the pump field but also

to the second-order susceptibility $\chi^{(2)}$, one can additionally control the phase of emitted radiation by periodically changing the sign of the the $\chi^{(2)}$ coefficient. By inverting the sign of the $\chi^{(2)}$ coefficient after each L_c distance one can change the destructive interference into constructive one.

Figure 1.3 shows the schemes of the quasi-phasematching (QPM) in part (a) and the modal phase matching (MPM) in the case of ridge waveguides in part (b) and micro-disks in part (c). In the case of the QPM the periodic modulation of the $\chi^{(2)}$ coefficient with the period $\Lambda = 2L_c$ is equivalent to the introduction of additional wave vector $K = 2\pi/\Lambda$ which allows to balance the existing difference for the wave vectors of the pump $k_{\mathrm{p}} = \dfrac{2\pi}{\lambda_{\mathrm{p}}} n(\lambda_{\mathrm{p}})$ and the second harmonic $k_{\mathrm{sh}} = \dfrac{2\pi}{\lambda_{\mathrm{sh}}} n(\lambda_{\mathrm{sh}})$. MPM in ridge waveguides requires momentum conservation for the effective wave vectors $\beta = \dfrac{2\pi}{\lambda} n_{\mathrm{eff}}$, where n_{eff} is the effective refractive index of the respective mode. MPM in micro-disks also has a peculiarity, it turns out that in this case the condition of the momentum conservation is naturally changed into angular momentum conservation $\ell_{\mathrm{sh}} = 2\ell_{\mathrm{p}}$, where ℓ is an integer which gives the orbital angular momentum in $\hbar$ units for the light confined in a micro-disk.

1.2 Integrated nonlinear optics

This section underlines the advantages of the integrated nonlinear optics which uses waveguides or micro-disks for second harmonic generation.

Once the phase matching conditions are satisfied the second harmonic signal from all dipoles in the sample adds up, and the second harmonic field E_{sh} becomes proportional to the number of dipoles and therefore to the propagation distance L. E_{sh} is also proportional to the amplitude of the dipole oscillations and therefore to the square of the pump field E_{p}, so we have $E_{\mathrm{sh}} \sim E_{\mathrm{p}}^2 L$. As a consequence, for the powers of the pump and the second harmonic we have the following relation:

$$P_{\mathrm{sh}} \sim P^2 \frac{L^2}{S_{\mathrm{eff}}}, \tag{1.7}$$

where P is the power of the pump, P_{sh} is the power of the generated second harmonic, L is the interaction distance and S_{eff} is the effective area of the beam.

Formula (1.7) shows that in order to get stronger second harmonic signal one needs to reduce the effective area S_{eff} of the beam and maintain this area over a propagation distance L as long as possible. In the case of bulk optics the small effective area can be reached with the beam focalization. But the more one focalizes the beam the quicker it tends to diverge. Indeed, the Rayleigh length z_R is proportional to the focalization waist area $z_R = \pi w^2/\lambda$, see Fig. 1.4(a). It this case S_{eff} and L are not independent from each other, and we get $S_{\mathrm{eff}} \sim L\lambda$ and for the second harmonic power:

$$P_{\mathrm{sh}} \sim P^2 \frac{L}{\lambda}, \tag{1.8}$$

where λ is the wavelength of the pump.

On the other hand, once the light is focalized and injected in a waveguide it remains confined over a distance limited only by the propagation losses. In this case, the effective area S_{eff} is determined by the cross-section of the waveguide and does not depend on the

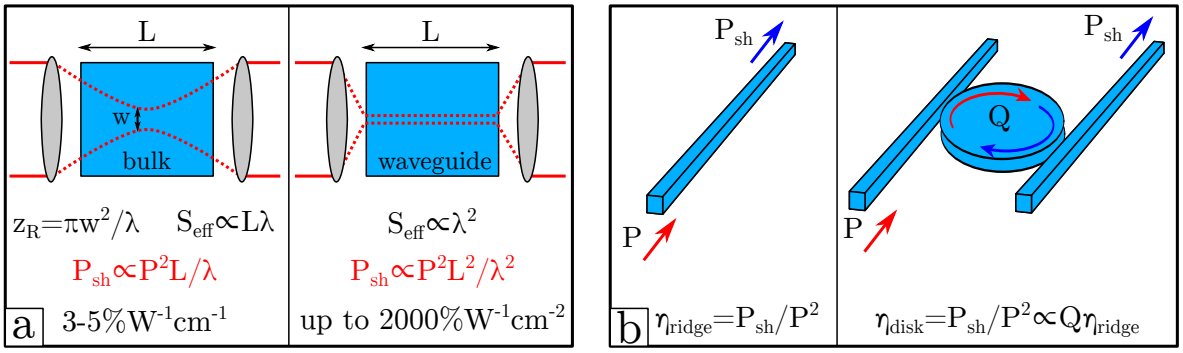

Figure 1.4 – (a) Scheme shows advantage of waveguides over bulk crystals for the second harmonic generation. (b) Scheme shows advantage of resonant cavities over ridge waveguides for the second harmonic generation. The propagation losses in the ridge waveguide and micro-disk are supposed to be the same for the correct comparison.

propagation distance L. In most cases, the cross-section of the waveguide is about the size of the pump wavelength, so for the second harmonic power in the case of a waveguide we have:

$$P_{\text{sh}} \sim P^2 \frac{L^2}{\lambda^2}, \tag{1.9}$$

where L is the propagation distance and λ is the pump wavelength. The additional factor L/λ in the formula (1.9) in comparison to the formula (1.8) demonstrates the clear advantage of integrated nonlinear optics in terms of the conversion efficiency.

The SHG efficiency can be further improved by using resonant fields enhancement in cavities. An example of a micro-disk cavity is show in Fig. 1.4(b). The resonant field enhancement is proportional to the quality factor of the micro-disk $P_{\text{circ}} \sim QP_{\text{external}}$, where P_{circ} is the power circulating in the micro-disk and P_{external} is the external power coupled or decoupled from the micro-disk. It is true that the pump power critically coupled to the micro-disk will be enhanced and therefore will produce stronger second harmonic signal inside the micro-disk. But only a small $\sim 1/Q$ fraction of this second harmonic signal can be decoupled from the micro-disk. If the second harmonic power inside the micro-disk were linearly proportional to the pump power, there would be no advantage in using micro-disk cavity. But since the second harmonic power generated inside the micro-disk is proportional to the square of the pump power, the cavity allows to improve the conversion efficiency by a factor proportional to Q, see Fig. 1.4. Of course, such improvement can only occur when the pump and the second harmonic are both resonant and critically coupled to the external waveguides, which is very difficult to realize experimentally.

1.3 State of the art for III-nitride waveguides

In recent years, a considerable amount of research has been focused on GaN as a novel material for nonlinear optics and photonics. GaN is a large band gap semiconductor which is well known for its outstanding optoelectronic properties and numerous applications in domains of light emitting devices, high power and high frequency electronics. It is mainly grown in a form of thin films by metalorganic vapour phase epitaxy (MOVPE) or by

molecular beam epitaxy (MBE) on sapphire or silicon substrates. During an epitaxial growth, GaN crystalizes in a wurtzite phase which has inherent second order nonlinear properties due to its noncentro-symmetric crystalline structure.

A unique combination of a direct band gap, a large transparency window and a high second order nonlinearity [1, 2] makes GaN an interesting candidate for nonlinear optics. In addition, GaN films can further be structured to fabricate waveguides, microrings[3], microdiscs [4] and photonic crystals[5, 6, 7]. These photonic structures can improve second harmonic generation (SHG), since they provide higher power densities, longer propagation distances and cavity field enhancements. In order to realize an efficient SHG process one also needs to satisfy phase matching conditions and at the same time preserve low propagation losses, which can be a challenging task.

One of the most well known techniques, that allows to satisfy phase matching conditions in waveguides, is quasi-phasematching (QPM) [8, 9]. Several groups, including our group, have been trying to grow periodically oriented GaN and AlN structures (PO-GaN and PO-AlN) which allow quasi-phasematching [10, 11, 12, 13]. However, this approach leads to very high propagation losses, which suppress all the advantages of the achieved phase matching. So far, there were only few reports on second harmonic generation in PO-GaN and power conversions for these structure remain very low $<0.1\%$ with an efficiency of $1.2 \cdot 10^{-4}\%{\cdot}\mathrm{W}^{-1}\mathrm{cm}^{-2}$ [13].

An alternative technique to QPM is modal phase matching (MPM), which was already reported for GaN and AlN based planar waveguides [14, 15], micro-disks [16] and mirorings [17]. The best power conversion of $1.8 \cdot 10^{-3}\%$ was achieved in GaN microrings with an efficiency of $1.5 \cdot 10^{-2}\%{\cdot}\mathrm{W}^{-1}$ [17]. In this case both poor modal overlaps and relatively high propagation losses have contributed to the low conversion efficiency. In the meantime a very high power conversion of 12% was recently reported for AlN microrings [18]. Although AlN has a 10 times smaller non-linear coefficient $\chi^{(2)}_{\mathrm{AlN}} = 1\,\mathrm{pm}\,/\,\mathrm{V}$ [18, 2] compared to GaN $\chi^{(2)}_{\mathrm{GaN}} = 10\,\mathrm{pm}\,/\,\mathrm{V}$ [2], ultra low propagation losses have largely compensated for the small non-linearity [18]. This shows that propagation losses are a key factor and that they limit the performance of AlGaN based structures. There have been few studies addressing this issue, however the origins of the propagation losses are still unclear and despite the fact that epitaxial GaN layers have a better crystalline quality than sputtered AlN layers, the propagation losses remain quite high, around 1dB/cm in the near-infrared [19] and 10dB/cm in the visible spectral region [20].

There has been some partial progress on the problems of phase matching and propagation losses, however low-loss AlGaN based structures optimized for efficient nonlinear interactions have not been demonstrated so far. The large band gap is the main fundamental advantage of AlGaN over other materials widely used for integrated nonlinear optics such as $LiNbO_3$, AlGaAs, Si, InP, SiN. The large band gap allows to realize nonlinear interaction in the visible and the ultraviolet spectral regions which are not accessible for other materials. It also eliminates the problem of two-photon absorption in the near-infrared region, which poses fundamental limits on the performance of other small band gap materials.

1.4 Organization of the manuscript

The main efforts of this work were concentrated on the development of the low-loss GaN waveguides designed for the second harmonic generation based on the modal phase matching. This manuscript presents the efforts and the obtained results in the following order. Chapter 2 gives a broad theoretical overview of all the structures that were experimentally studied during this PhD project. This chapter presents the modelling results for the phase matching and the SHG efficiency together with the impact of the propagation losses on the different platforms based on waveguides and microdisks. It shows the wide tunability of these platforms and discusses the viable methods which may allow improving the SHG efficiency. The next Chapter 3 describes the main epitaxy techniques that were used for the waveguides fabrication. Chapter 4 gives an overview of the linear and nonlinear optical characterization techniques. Chapter 5 present the experimental result for the waveguides that were grown on sapphire substrates. We present how we identify the main sources of the propagation losses and show how these losses can be drastically reduced. Here we describe waveguides with propagation losses going below 1dB/cm at 633nm which allow efficient second harmonic generation with power conversion reaching 2%. Chapter 6 describes the experimental results for the waveguides fabricated on Si substrates. Here we also present the first demonstration of the doubly-resonant second harmonic generation in GaN micro-disks. After the conclusions the last chapter of this manuscript presents the details on the models and calculations that were used throughout this work.

From the manuscript it may be not clear what work was done by myself and what by my colleagues. Therefore, I would like to mention that during this PhD project I was working predominantly on the modelling and optical characterization in INPHYNI laboratory. All the fabrication was done by my colleagues in CRHEA laboratory. The modelling includes simulations of the phase matching conditions, calculations of the SHG efficiency and estimations of the propagation losses in planar waveguides, ridge waveguides and micro-disks. For this purpose I have developed numerous analytical models in Mathematica and used finite-element software (COMSOL) for more complicated problems. Another large part of my work was dedicated to the linear and nonlinear characterization of the fabricated waveguides. I was also doing the measurements of the surface roughness by the AFM technique. Therefore, all the results of the design, modelling and characterizations can be used for the evaluation of my contribution, with one exception of micro-disks. The micro-disks were both fabricated and characterized in C2N laboratory, while I have done only the simulations.

Chapter 2

Modelling results

This chapters will give a large overview of different platforms such as planar and ridge waveguides or micro-disks, which have been used for the second harmonic generation experiments described later in the manuscript. The goal here is to explain different approaches for the phase matching that can be used for these structures and estimate the conversion efficiencies one can expect for different configurations in the ideal case. The influence of the propagation losses on the conversion efficiencies is also estimated here. In the conclusion to this the chapter, we will discuss the advantages and disadvantages of the waveguide and micro-disk platforms for second harmonic generation.

2.1 Planar and ridge waveguides

This section starts with the description of the GaN/AlGaN platform for planar and ridge waveguides, for which GaN serves as the guiding layer and AlGaN the optical cladding. This platform is well adapted for the power conversion from the near infrared to the visible spectral regions. The results of the simulations show that this platform presents a wide tunability range obtained by varying the GaN layer thickness and the AlGaN content. The description continues with the AlN waveguides both on sapphire and SiO_2 substrates, which can be used for the power conversion from the visible to the ultraviolet spectral regions. The parameters necessary for the SHG generation in the ultraviolet together with the tunability range of the AlN-based platforms are described in details in Section 2.1.2. The conversion efficiencies of the second harmonic generator based on modal phase matching are presented both for GaN- and AlN-based waveguides. The improvements due to the planar polarity inversion and the negative impact of the propagation losses are also calculated. In this section all the calculations were done in Mathematica using a standard analytical model for a three layer waveguides. The final formulas and other details of the simulations are presented in Chapter 8.

2.1.1 GaN/AlGaN platform

The GaN/AlGaN platform both for planar and ridge waveguides was predominantly used for second harmonic generation experiments during this PhD project. The advantage of this platform is that it provides both an optical cladding and a relatively high refractive index contrast (2.1 for AlN against 2.34 GaN at 1μm wavelength). The AlGaN optical cladding isolates the guided modes from the substrate and the initial low-quality epitaxial

layers. This helps to reduce the propagation losses and to improve the SHG efficiency. The high refractive index contrast between AlN and GaN allows to use the interaction between different order modes in multi-mode waveguides and satisfy the phase matching conditions by the modal phase matching technique. As it will be shown below this platform is highly broad-band and its application range is limited only by the transparency window of GaN.

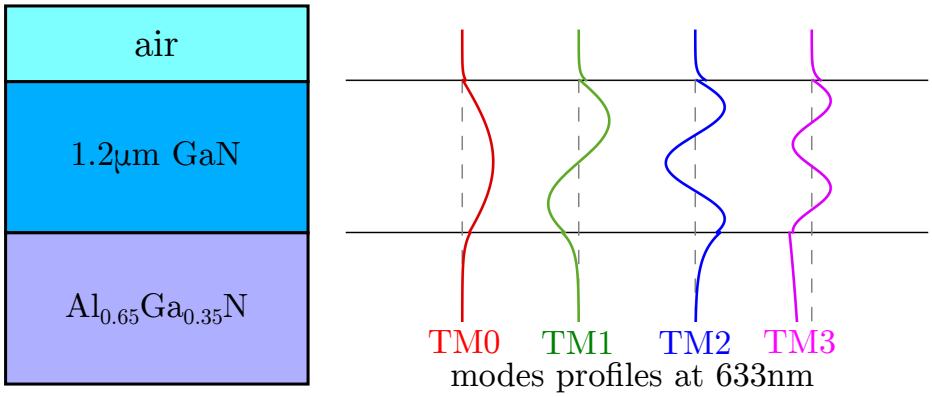

Figure 2.1 – A scheme of GaN-based waveguide together with the TM-mode profiles at 633nm wavelength.

A scheme of a typical waveguide used for the SHG experiments is shown in Fig. 2.1. This figure also displays the TM-mode profiles at 633nm wavelength. The biggest advantage of the AlGaN optical cladding is based on the fact that the modes used for the nonlinear interactions are highly confined in the GaN layer. This is the case for the TM0, TM1 and TM2 modes in Fig. 2.1, while a significant part of the modal power of the TM3 mode is confined in the AlGaN substrate. The evolution of the effective indices and the mode confinement for different TE- and TM-modes at 633nm with respect to the GaN layer thickness is presented in Fig. 2.2. The horizontal axes in all the plots displayed in Fig. 2.2 highlight the cut-off thickness for different modes. The behaviour of the TE- and TM-modes is very similar. At the cut-off thickness of the TM(j+1) mode, more than 90% of the power of the TM(j) mode is already confined in GaN layer. Therefore if one wants to use TM2 mode for the second harmonic generation it would be beneficial to choose the GaN thickness which corresponds to the cut-off thickness of the TM3 mode. In this situation the waveguide would be supporting only the modes used in the nonlinear interactions and the confinement of these modes would be larger that 90%. For example, this is the case for the waveguide displayed in Fig. 2.1, since it will be shown below that this waveguide is designed for the second harmonic generation from the TM0 mode at 1250nm to the TM2 mode at 625nm.

The structure of the $\chi^{(2)}$ tensor of AlGaN allows interaction both between TE-and TM-modes, but the interaction between the TM pump and the TM second harmonic is governed by the highest nonlinear coefficient $\chi^{(2)}_{zzz}$. In this section the calculation results are presented for the modes highly confined in the guiding layer. For this case there is no significant difference for the TE and TM modes except the fact that the interaction between TM modes gives higher conversion efficiencies due to the larger nonlinear coefficient. Therefore, only the results for the nonlinear interactions between the TM-modes

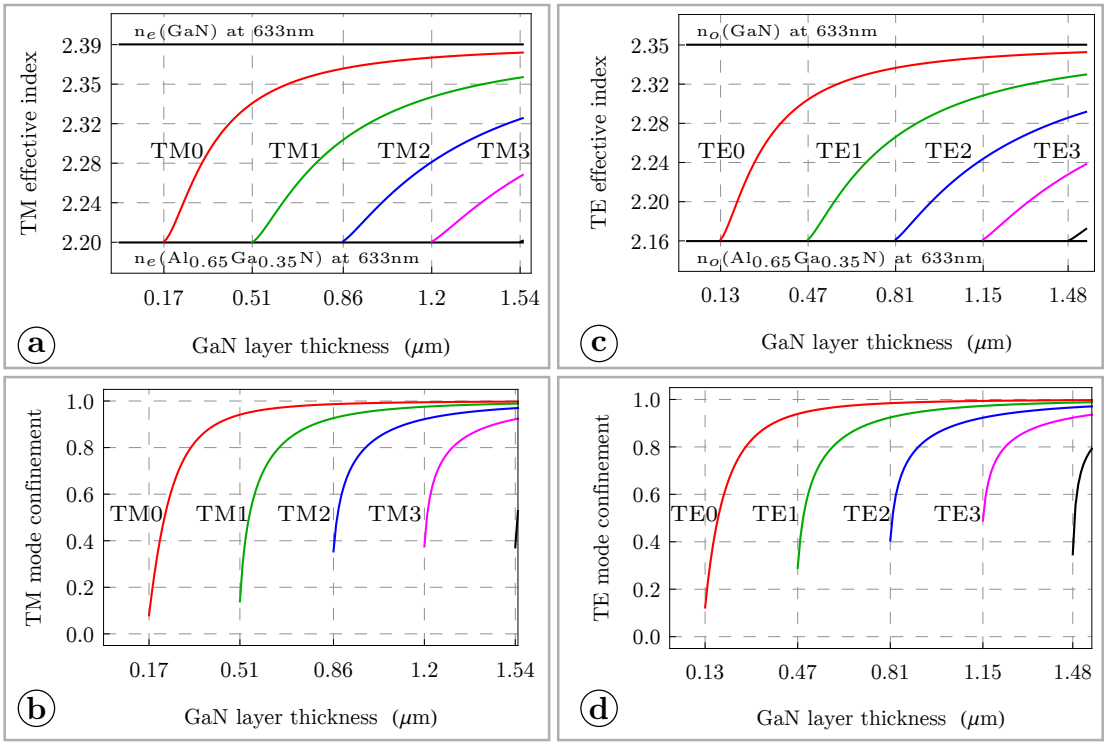

Figure 2.2 – (a) Effective refractive index for the TM-modes as a function of the GaN layer thickness for the waveguide in Fig. 2.1 at 633nm wavelength. (c) The same evolution of the effective refractive index for the TE-modes. (b),(d) Confinement of the modal power in the GaN layer as a function of the thickness of this layer for the TM- and TE-modes respectively.

are presented here. The results for the TE-modes would double the length of this section without adding any significantly new information.

The calculations take into consideration ordinary and extraordinary dispersions for both GaN [21] and AlGaN [22] materials, and the variation of the $\chi^{(2)}$ nonlinear coefficient with the Al content for AlGaN alloys[2]. It was assumed that $\chi^{(2)}_{zzz}(\mathrm{GaN}) = 10\,\mathrm{pm/V}$, $\chi^{(2)}_{zzz}(\mathrm{AlN}) = 1\,\mathrm{pm/V}$, and for AlGaN alloys a linear approximation was used $\chi^{(2)}_{zzz}(\mathrm{Al}_y\mathrm{Ga}_{1-y}\mathrm{N}) = y \cdot \chi^{(2)}_{zzz}(\mathrm{AlN}) + (1-y) \cdot \chi^{(2)}_{zzz}(\mathrm{GaN})$, which fits well the data provided in [2]. The details of the calculations are presented in Chapter 8.

Here we present the phase matching conditions and the efficiencies for the second harmonic generation for different configurations of the nonlinear interactions between the first three modes TM0, TM1 and TM2. As an example, the dispersion for these modes in the waveguide from the Fig. 2.1 is presented in Fig. 2.3(a). Since $n_{\mathrm{TM0}}(\lambda) < n_{\mathrm{TM0}}(\lambda/2)$ the frequency doubling between the TM0 pump and the TM0 second harmonic can be reached only in the presence of a periodic modulation of the $\chi^{(2)}$ nonlinear coefficient allowing the quasi-phasematching (QPM) described in Section 1.1. The quasi-phasemathing will not be considered here in details, but will be used as a reference solution with the highest SHG efficiency. Alternatively the conditions $n_{\mathrm{TM0}}(\lambda) = n_{\mathrm{TM1}}(\lambda/2)$ and $n_{\mathrm{TM0}}(\lambda) = n_{\mathrm{TM2}}(\lambda/2)$ can be satisfied for the 1.25μm and 1.95μm wavelengths respectively, as it is shown in Fig. 2.3(b). The phase matching based on the interaction between modes of different orders is commonly called modal phase matching (MPM). This technique was also mentioned in Section 1.1 and it will be considered here in details, since it was the main technique used

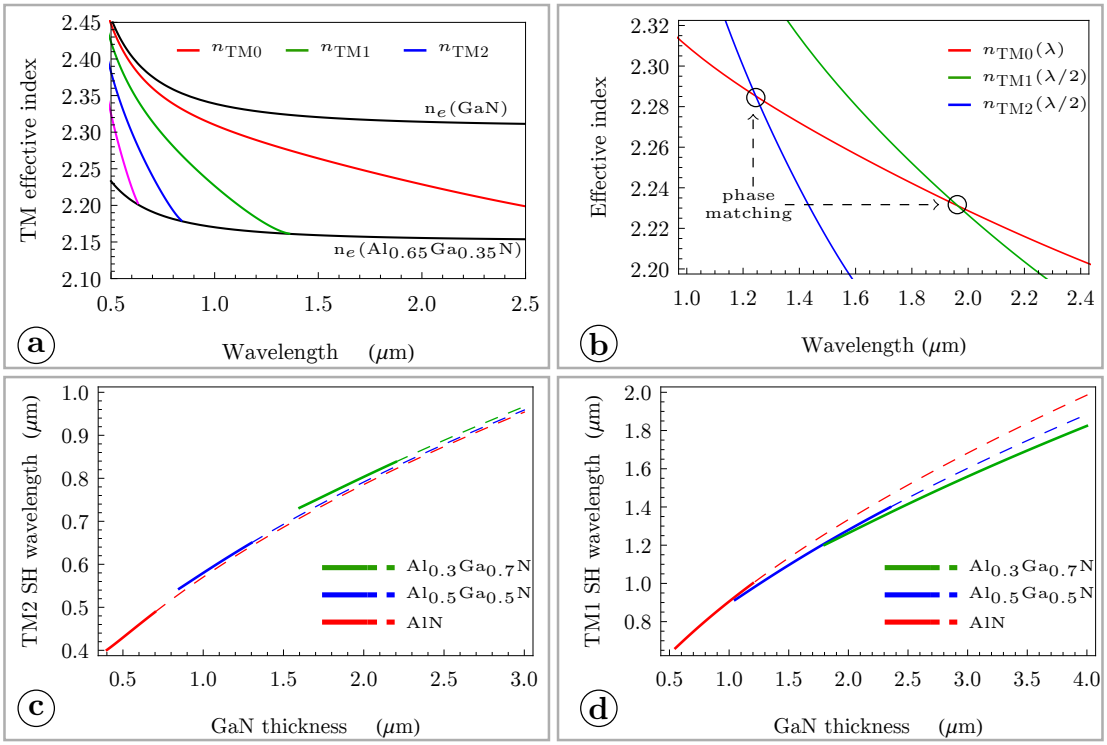

Figure 2.3 – (a), (b) Dispersion curves for the effective refractive indices of three guided modes; a modal phase matching (MPM) is reached between TM0 and TM2 modes at 1250nm, and between TM0 and TM1 modes at 1950nm. (c) TM2 second harmonic wavelength as a function of GaN guiding layer thickness for the different AlGaN substrates. (d) TM1 second harmonic wavelength as a function of GaN guiding layer thickness for different AlGaN substrates; the dashed segments of the curves on in Figs. 1(c) and 1(d) indicate a multi-mode nature of waveguides at the wavelength of the pump.

during this PhD project.

Figures 2.3(a) and (b) present the MPM results for the special case of the waveguide shown in Fig. 2.1. In more general cases the phase matching wavelengths depend on the thickness of the GaN guiding layer as well as on the Al content in the AlGaN alloy, as shown in the Figs. 2.3(c) and 2.3(d). It should be noted that the phase matching wavelength strongly depend on the GaN thickness, and is less sensitive to the Al content in the AlGaN alloy. The Al content determines the index contrast and therefore the spectral range in which MPM is possible, and whether for a given GaN thickness the waveguide is mono-mode or multi-mode at the pump wavelength. The GaN/AlN configuration allows covering the broadest spectral range. To summarize the results presented in the Fig. 2.3(c) and 2.3(d) we can conclude that the TM0/TM2 configuration is well suitable for the near-infrared to visible conversion, while the TM0/TM1 case is more adapted for the mid-infrared to near-infrared conversion. Therefore, by using only these two mode combinations one can obtain nonlinear interactions over the whole transparency window of GaN.

The main drawback of MPM is that the interaction between a fundamental mode and

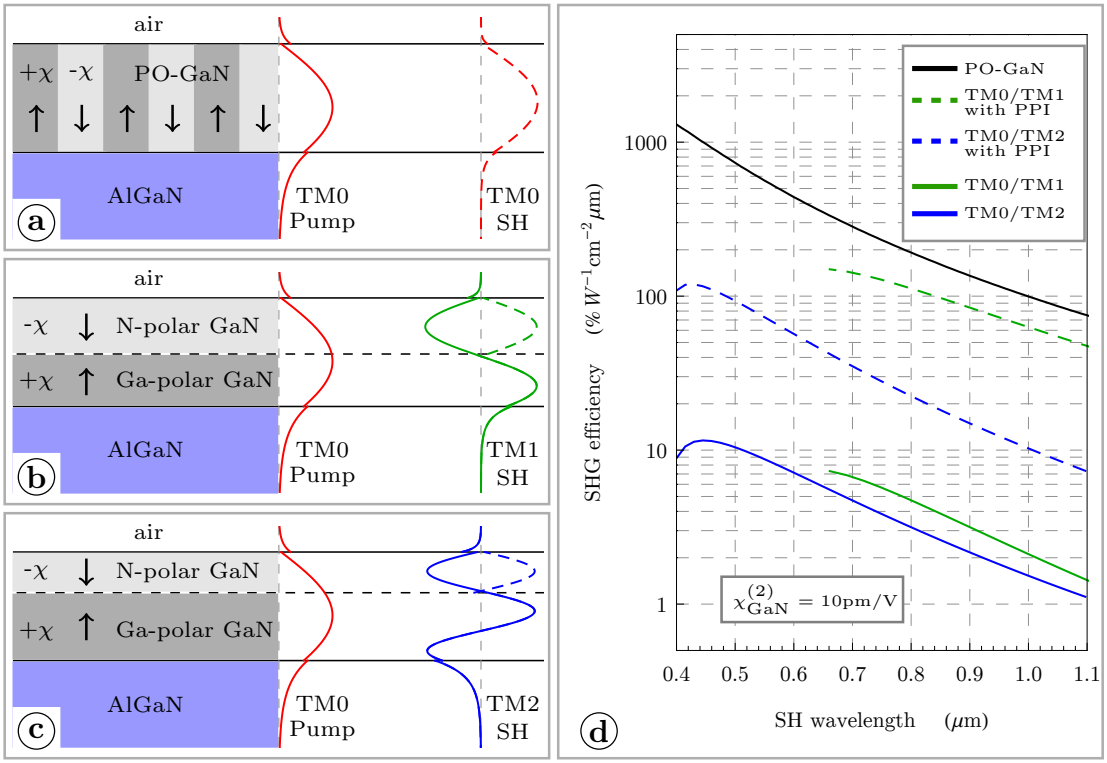

Figure 2.4 – (a) PO-GaN waveguide allows a power conversion between fundamental modes due to the quasi-phasematching (QPM). In (b) and (c) we show a standard modal phase matching (MPM) technique with an additional improvement of modal overlaps due to the planar polarity inversion (PPI). The plot (d) presents the conversion efficiencies as a function of the harmonic wavelength for the cases of MPM, MPM with an improved overlap and QPM. Efficiencies are given in $\%{\cdot}\mathrm{W}^{-1}\mathrm{cm}^{-2}\cdot\mu\mathrm{m}$ units and all the calculations are done within the assumption of nondepletion of the pump. In the plot (d) solid black curve represents a reference solution for the case of QPM between TM0-modes in PO-GaN; the green curves corresponds to MPM between TM0 and TM1 modes, while the blue curves corresponds to MPM between TM0 and TM2 modes. In the plot (d) both the blue and green dashed lines give the conversion efficiencies with improved overlaps due to the planar polarity inversion (PPI), while the solid blue and green lines represent a standard MPM with poor modal overlaps.

a higher order mode leads to a poor fields overlap:

$$\text{overlap} = \left(\int_{-\infty}^{+\infty} \chi_{zzz}(z) \mathcal{E}_P^2(z) \mathcal{E}_{SH}(z)\, dz \right)^2 , \tag{2.1}$$

where $\mathcal{E}_P$ and $\mathcal{E}_{SH}$ are the modal field profiles for the pump and the second harmonic respectively, χ_{zzz} is a nonlinear coefficient profile (the z-axis corresponds to the direction of the crystal growth). Indeed, $\mathcal{E}_P^2$ always stays positive, while $\mathcal{E}_{SH}$ changes sign for TM1 and TM2 modes leading to a small value of the integral (2.1). The overlap (2.1) depends not only on field profiles, but also on the distribution of the χ_{zzz} nonlinear coefficient along the z axis. As a consequence, there exists a neat solution allowing to improve the modal overlap by using a planar polarity inversion, as schematically shown in the Figs.

2.4(b) and 2.4(c). The inversion of the χ_{zzz} sign at the point where the TM1 field goes to zero conterbalances the sign change of $\mathcal{E}_{SH}$ and drastically increase the value of the integral (2.1), see Fig. 2.4(b). The same approach partially works for the TM2 mode, see Fig. 2.4(c). This approach is particularly interesting as χ_{zzz} sign is determined by the polarity of GaN and its inversion can be experimentally realized for GaN waveguides. One approach consists in reversing the GaN polarity directly during the MBE growth by Mg doping [23]. This method was already used for the fabrication of PO-GaN structures[10]. Another approach consists in bonding two Ga-polar GaN layers face to face. It should be noted that wafer bonding has already been used for the fabrication of GaN photonic circuits on SiO_2 substrates [17].

Figure 2.4(d) summarizes the theoretical efficiencies that can be reached in planar waveguides for the cases of simple modal phase matching, MPM with an improved overlap due to the planar polarity inversion and quasi-phasematching for PO-GaN. All the results are obtained within the assumption of non depletion of the pump. Since the calculations are done for planar waveguides, we give the efficiencies in $\%\cdot W^{-1}cm^{-2}\cdot\mu m$ units. It means that, for example, to estimate the efficiencies in standard $\%\cdot W^{-1}cm^{-2}$ units for $2\mu m$ wide ridge waveguide one needs to divide by 2 all the values given in Fig. 2.4(d). In theory the highest conversion efficiencies can be reached in PO-GaN waveguides, but so far the performance of these structures was largely compromised by the optical losses due to the macroscopic surface roughness induced by different growth rates for N- and Ga- polarities. From the Fig. 2.4(d) we can conclude that MPM with the planar polarity inversion can provide an interesting compromise between pure MPM and quasi-phasematching in PO-GaN, since it can provide conversion efficiencies reaching $100\%\cdot W^{-1}cm^{-2}$ in ridge waveguides and at the same time it can eliminate the problem of the high surface roughness present in PO-GaN.

2.1.2 AlN/sapphire and AlN/SiO_2 platforms

In the previous section it was shown that the GaN/AlGaN platform is widely tunable within the whole GaN transparency window ($0.36\mu m$-$7\mu m$). There are other platforms based on $LiNbO_3$ or AlGaAs well suited for the integrated nonlinear optics in this spectral region. GaN has several advantages discussed in Section 1.3, but it would be particularly interesting to realize the frequency conversion from the visible to the ultraviolet spectral region, which is fundamentally inaccessible with other materials. For this purpose one needs to use AlN waveguides. Sapphire and SiO_2 are two main substrates which are also transparent in the ultraviolet and are commonly used for the fabrication of the AlN waveguides. Therefore, in this section we discuss the application of two platforms, namely AlN/sapphire and AlN/SiO_2, for the frequency doubling from the visible to the ultraviolet spectral regions. Although sapphire has a slightly higher refractive index than SiO_2 (1.77 against 1.46 at 500nm), the simulation results are very close for both substrates. Some details for the AlN/sapphire platform are presented below, while for the AlN/SiO_2 platform only the conversion efficiencies are summarized in the end of this section.

An example of AlN waveguide that can be used for the frequency doubling from the visible to the ultraviolet spectral regions is shown in Fig. 2.5. This frequency doubling can be realized with modal phase matching between a TM0 pump at 600nm and a TM2 second harmonic at 300nm wavelength. The plots in Figs. 2.6 present the confinement and highlight the cut-off thickness for the different modes at 300nm. According to these plots

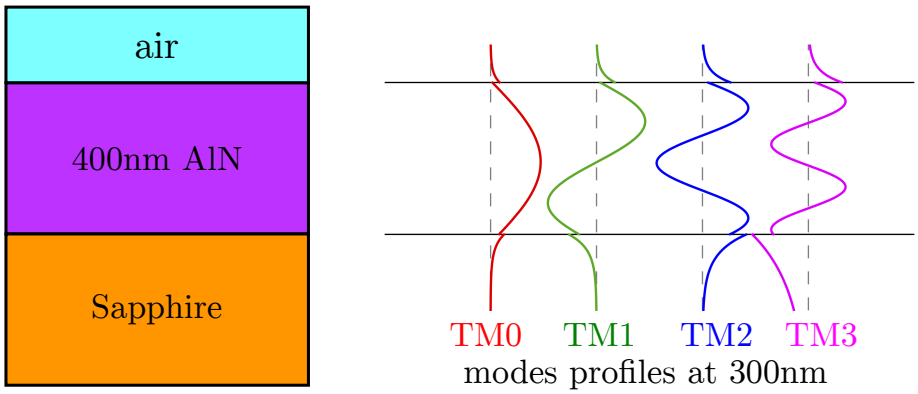

Figure 2.5 – A scheme of AlN-based waveguide together with the TM-mode profiles at 300nm wavelength

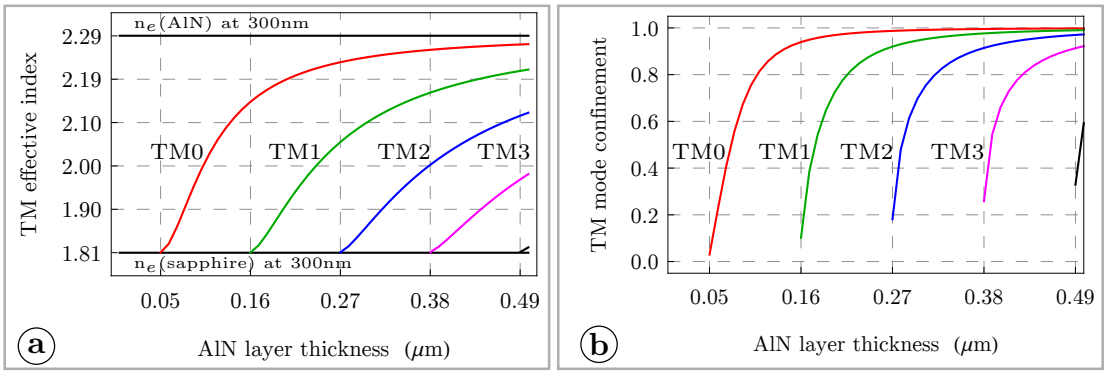

Figure 2.6 – (a) Effective refractive index for the TM-modes as a function of the AlN layer thickness for the waveguide in Fig. 2.5 at 300nm wavelength. (b) Confinement of the TM-modes in the AlN layer as a function of the thickness of this layer.

the 380nm thickness of the AlN layer corresponds to the cut-off for the TM3 mode and >90% confinement of the TM2 mode. High confinement can increase the SHG efficiency, since it leads to lower propagation losses and improves the overlap with the nonlinear material.

The dispersion curves for the TM-modes showing the possibility to reach the described phase matching conditions are displayed in Figs. 2.7(a) and (b). These plots also confirm that the TM0/TM1 mode combination can be used in this particular case to transfer the power from a TM0 pump mode at 940nm to a second harmonic TM1 mode at 470nm wavelength. By changing the AlN layer thickness one can tune the second harmonic (SH) wavelength over a broad spectral range as it is confirmed by the plots in Figs. 2.6(c) and (d). These plots show that the TM0/TM2 mode combination can be used to achieve the second harmonic generation in the ultraviolet, while the TM0/TM1 mode combination can only be used to convert power from the near-infrared to the visible spectral regions. Therefore, the TM0/TM1 mode combination is less interesting for the case of AlN waveguides since the same spectral range can be covered using GaN waveguides with a much larger nonlinear coefficient. The summary of the conversion efficiencies for different mode combinations is given in Fig. 2.9. Analogously to the previous section this

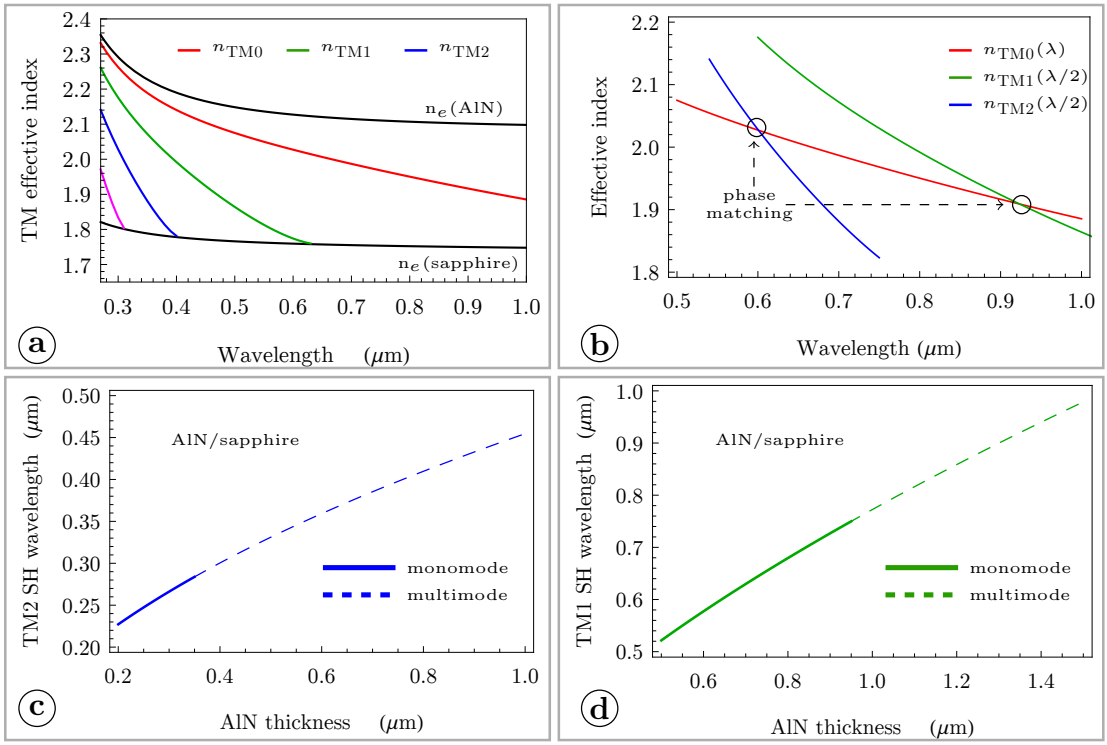

Figure 2.7 – (a), (b) Dispersion curves for the effective refractive indices of three TM modes; the modal phase matching (MPM) is reached between TM0 and TM2 modes at 600nm, and between TM0 and TM1 modes at 940nm. (c) TM2 second harmonic wavelength as a function of AlN guiding layer thickness on sapphire substrate. (d) TM1 second harmonic wavelength as a function of AlN guiding layer thickness on sapphire substrate. The dashed segments of the curves on in Figs. 1(c) and 1(d) indicate a multimode nature of the waveguides at the wavelength of the pump.

figure also shows the improvements of the SHG efficiency that can be achieved both with the planar and periodic polarity inversions. The results giving the wavelength tunability and the SHG efficiency in the case of AlN waveguides on SiO_2 substrates are summarized in Figs. 2.8 and 2.10.

In this chapter $\chi^{(2)}_{zzz} = 1$pm/V value was used for the calculation of the SHG efficiency in AlN waveguides. It should be noted, that there is a large variation of the value of the AlN nonlinear coefficient in the literature. A value as high as 7pm/V was reported recently [24]. In this chapter, all the calculation are done with $\chi^{(2)}$ =1pm/V, but it is easy to scale the results of Fig. 2.9 and 2.10 if the recent value up to the $\chi^{(2)}$ value which is more accurate for the good quality layers that are grown now. In order to do this scaling it is sufficient to multiply the values given by the plots in Figs. 2.9 and 2.10 by the square of the numerical value of the new $\chi^{(2)}$ coefficient given in pm/V units.

The results of the simulations show that the second harmonic generation in the ultraviolet is possible for both cases of AlN waveguides on sapphire and SiO_2 substrates. Depending on the real value of the AlN nonlinear coefficient, the conversion efficiency can vary from a fraction of a percent up to several tens of percent for the case of the simple modal phase matching. Using the planar polarity inversion to increase the overlap integral can increase the SHG efficiency by one order of magnitude, while the interaction between the fundamental modes in PO-AlN structures can give a two orders of magnitude

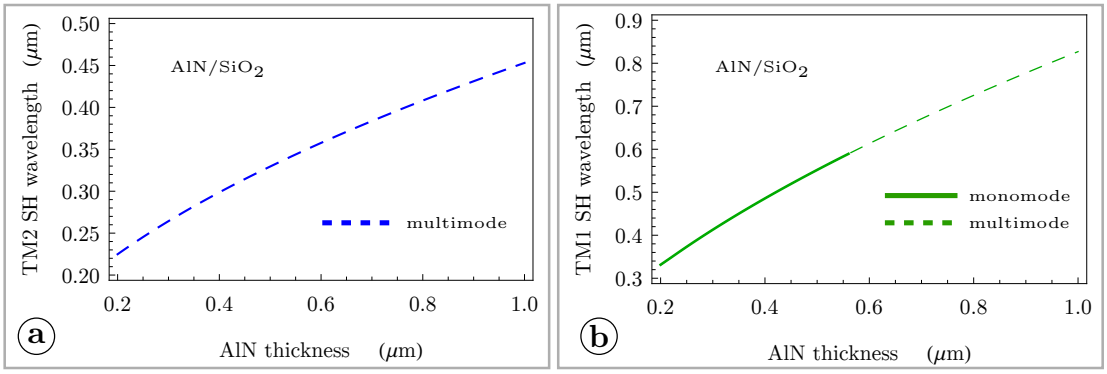

Figure 2.8 – (a) TM2 second harmonic wavelength as a function of AlN guiding layer thickness on SiO_2 substrate. (b) TM1 second harmonic wavelength as a function of AlN guiding layer thickness on SiO_2 substrate. The dashed segments of the curves on in Figs. 1(a) and 1(b) indicate a multi-mode nature of the waveguides at the wavelength of the pump.

improvement of this efficiency.

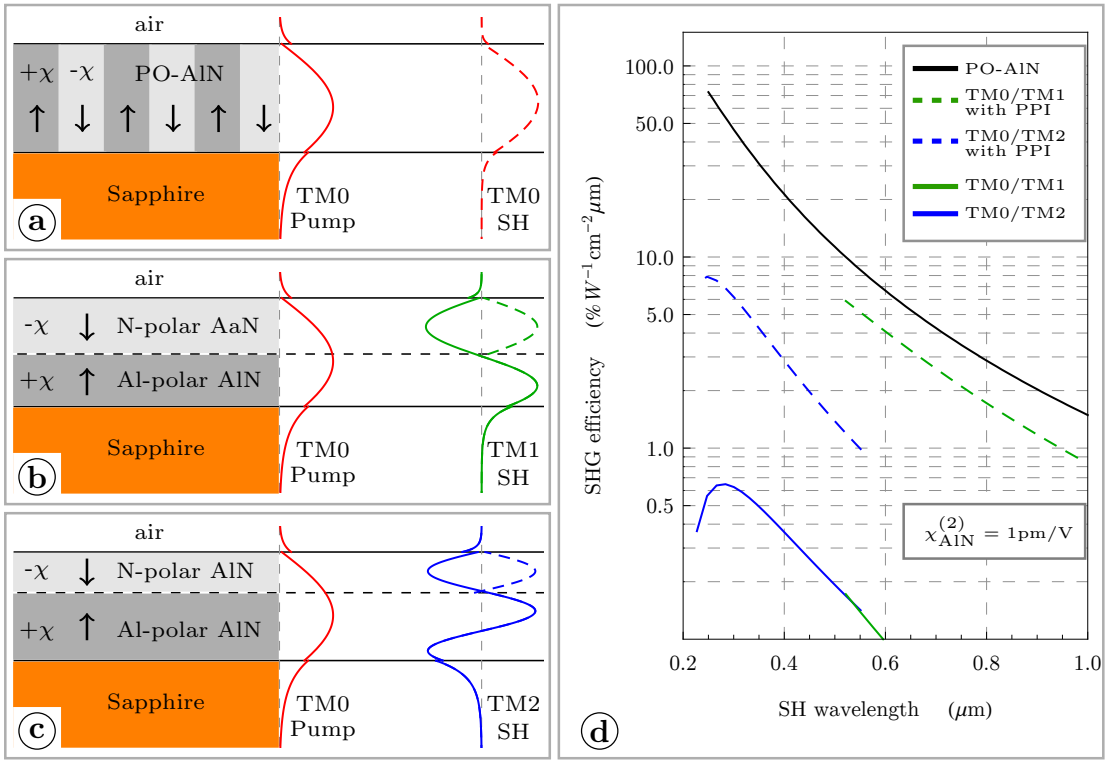

Figure 2.9 – (a) PO-AlN waveguide yields a power conversion between fundamental modes due to the quasi-phasematching (QPM). In (b) and (c) we show a standard modal phase matching (MPM) technique with an additional improvement of modal overlaps due to the planar polarity inversion (PPI). The plot (d) presents the conversion efficiencies as a function of the harmonic wavelength for the cases of MPM, MPM with an improved overlap and QPM. Efficiencies are given in $\%{\cdot}\mathrm{W}^{-1}\mathrm{cm}^{-2}\cdot\mu\mathrm{m}$ units and all the calculations are done within the assumption of nondepletion of the pump. In the plot (d) solid black curve represents a reference solution for the case of QPM between TM0-modes in PO-AlN; the green curves corresponds to MPM between TM0 and TM1 modes, while the blue curves corresponds to MPM between TM0 and TM2 modes. In the plot (d) both the blue and green dashed lines give the conversion efficiencies with improved overlaps due to the planar polarity inversion (PPI), while the solid blue and green lines represent a standard MPM with poor modal overlaps.

2.1.3 Influence of the propagation losses

In the previous sections 2.1.1 and 2.1.2 the simulation results for the SHG efficiencies were obtained under the assumption of ideal lossless waveguides. In the real world, semiconductor waveguides show relatively high propagation losses reaching several dB/cm in the near-infrared and the visible spectral regions. The conversion efficiency $\eta^{(\mathrm{SHG})}$ in the prsence of propagation losses is related to the ideal conversion efficiency $\eta_0^{(\mathrm{SHG})}$ by a simple formula:

$$\eta^{(\mathrm{SHG})} = \eta_0^{(\mathrm{SHG})} \exp\left[-(\alpha_\omega + \alpha_{2\omega}/2)L\right] \frac{\sinh^2\left[(\alpha_\omega - \alpha_{2\omega}/2)L/2\right]}{\left[(\alpha_\omega - \alpha_{2\omega}/2)L/2\right]^2}, \tag{2.2}$$

where α_ω and $\alpha_{2\omega}$ are the extinction coefficients for the pump and the second harmonic respectively and L is the propagation distance. Common units for the extinction coefficient α are cm^{-1}, and they are related to the losses typically given in dB/cm by the

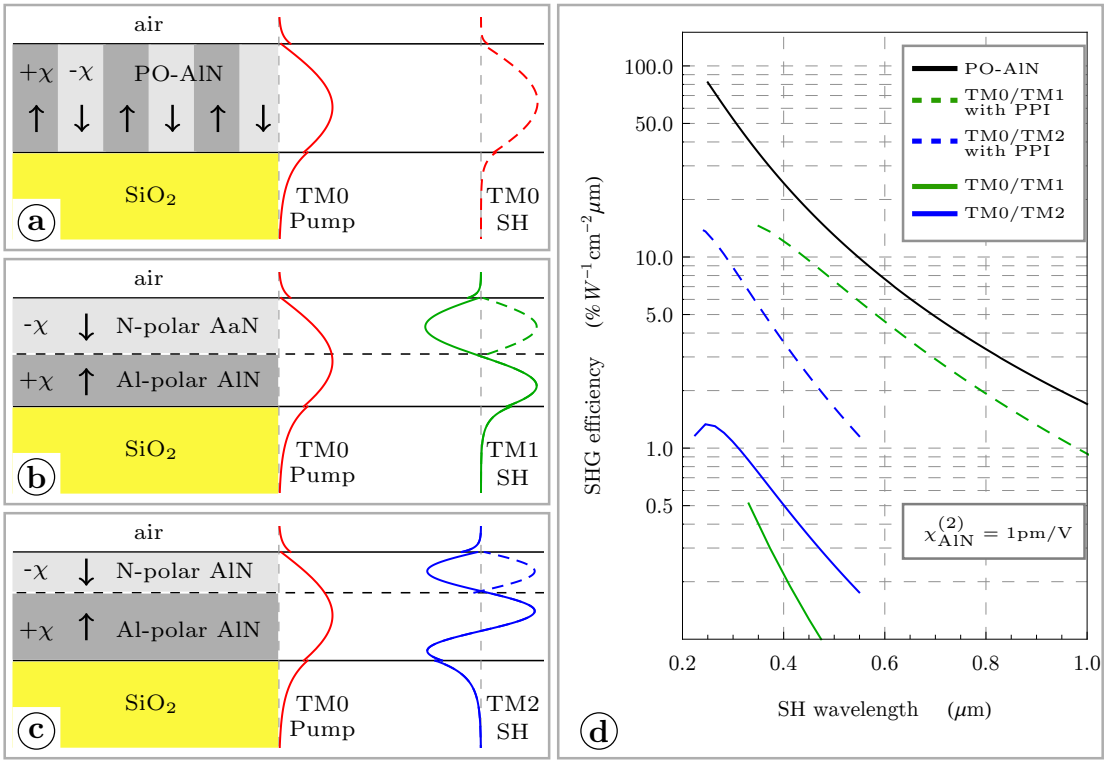

Figure 2.10 – (a) PO-AlN waveguide yields a power conversion between fundamental modes due to the quasi-phasematching (QPM). In (b) and (c) we show a standard modal phase matching (MPM) technique with an additional improvement of modal overlaps due to the planar polarity inversion (PPI). The plot (d) presents the conversion efficiencies as a function of the harmonic wavelength for the cases of MPM, MPM with an improved overlap and QPM. Efficiencies are given in $\%{\cdot}\mathrm{W}^{-1}\mathrm{cm}^{-2}\cdot\mu\mathrm{m}$ units and all the calculations are done within the assumption of nondepletion of the pump. In the plot (d) solid black curve represents a reference solution for the case of QPM between TM0-modes in PO-AlN; the green curves corresponds to MPM between TM0 and TM1 modes, while the blue curves corresponds to MPM between TM0 and TM2 modes. In the plot (d) both the blue and green dashed lines give the conversion efficiencies with improved overlaps due to the planar polarity inversion (PPI), while the solid blue and green lines represent a standard MPM with poor modal overlaps.

formula:

$$\text{Loss (dB/cm)} \approx 4.34\,\alpha\,(\mathrm{cm}^{-1}). \tag{2.3}$$

As one can see from the formula (2.2), if $\alpha_{2\omega} = 2\alpha_{\omega}$ the factor with the cardinal hyperbolic sine function has the value 1. It should be noted, that for both GaN and AlN waveguides the reported losses for the second harmonic were approximately twice as high as the losses for the pump [18, 25]. Therefore for the simplicity we will assume that $\alpha_{2\omega} \approx 2\alpha_{\omega}$. In the following part of this chapter, we call "value of the propagation losses in the waveguides", the value of the propagation losses of the pump and assume that the losses for the second harmonic are twice as high. Anyway, if there is 0-10dB/cm deviation from this relation, the $\sinh^2$ correction factor for the SHG varies between 1.0 and 1.5 and this variation is insignificant in comparison with the overall impact of >10dB/cm propagation losses.

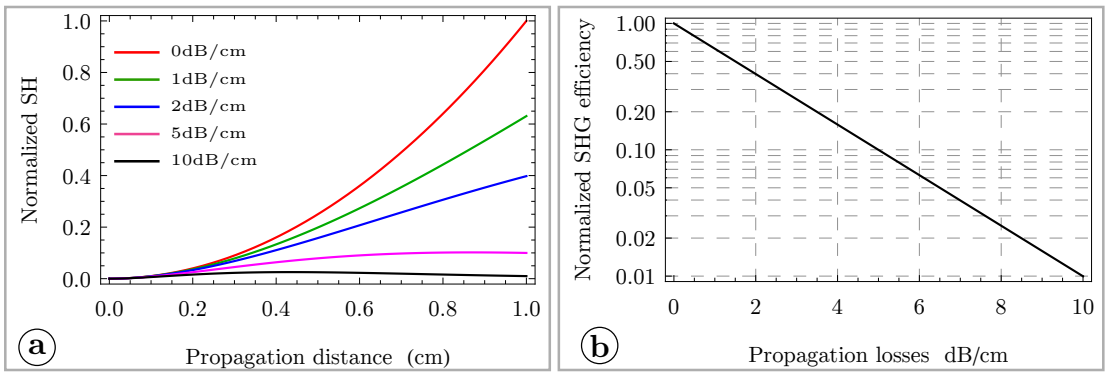

Figure 2.11 – (a) Normalized second harmonic (SH) signal as a function of the propagation distance in waveguides with different values of the propagation losses. (b) A log-linear plot of the SHG efficiency as a function of the propagation losses.

The evolution of the second harmonic (SH) signal with the propagation distance in the waveguides with different values of the propagation losses is shown in Fig. 2.11(a). Without losses there is an expected quadratic growth of the SH signal represented by the red curve, while the black curve which barely comes off the horizontal axis corresponds to propagation losses as high as 10dB/cm. The exponential decrease of the SHG efficiency with the value of the propagation losses is shown in the log-linear plot of Fig. 2.11(b). This plot clearly underlines the necessity to reduce the losses below 1dB/cm to achieve a high conversion efficiency. This explains why the reduction of the propagation losses was one of the main goals of this PhD project.

2.2 SHG with the whispering gallery modes in micro-disks

This chapter continues with the description of the second harmonic generation in micro-disks. First, the peculiarities of modal phase matching between whispering gallery modes of a micro-disks are explained. Then a detailed description of two particular cases of mode combination is given. At the end, the optimal solutions for different modes combinations in micro-disks with the expected conversion efficiencies are summarized.

2.2.1 General description of phase matching and effective index method

This section presents some general ideas explaining how the phase matching conditions can be reached and calculated in the case of micro-disks. The detailed description of the simulations is presented in Chapter 8.

The devices composed of a micro-disk coupled to a waveguide were fabricated by using a selective chemical etchant which preserves AlGaN epitaxial layers and attacks Si substrate. An SEM image of a typical micro-disk device is shown in Fig. 2.12(a), and the details of the fabrication procedure will be given in Chapter 6. It should be noted, that the direct growth of GaN on Si substrate is limited due to the thermal expansion coefficient mismatch, which causes crack formation. Therefore an intermediate AlN layer

should always be used in order to put some additional compressive strain on the GaN layer. For this reason, all the calculation for micro-disks were done under the assumption that the guiding layer contains both GaN and AlN parts, see Fig. 2.12(b).

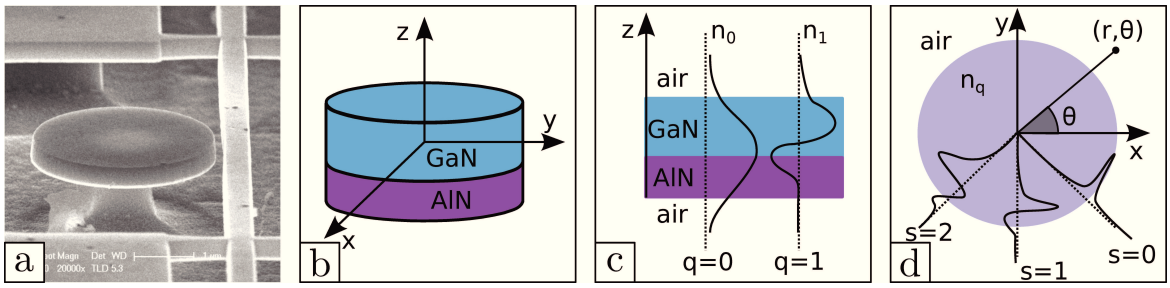

Figure 2.12 – (a) An SEM image of a micro-disk coupled to a waveguide. (b) A scheme of AlGaN microdisk. (c) A scheme of the vertical fields distributions in a planar waveguide. (d) A scheme of radial fields distribution in a micro-disk.

In order to calculate the whispering gallery modes in a micro-disk the effective index method was used. First, an analytical solution for the four layered air/GaN/AlN/air planar waveguide was found. This solution would give the field distribution in the vertical z-direction and the effective refractive indices for the modes in the planar waveguide, see Fig. 2.12(c). Then, the obtained effective indices were used as new refractive indices in the 2D problem with the cylindrical symmetry, see Fig. 2.12(d). The 2D problem would give the radial and angular field distributions and resonance frequencies for the whispering gallery modes. For the proper calculation of the whispering gallery modes, this procedure has to be iterated, since all the parameters in the system depend on the wavelength and the modes are defined only for resonant wavelengths, which are initially unknown. The details of the calculations are presented in Chapter 8.

Within the effective index approximation the complex field amplitude for a given mode can be represented as a product of the functions of vertical z, radial r and angular θ coordinates:

$$E(z, r, \theta, t) = \mathcal{A}\eta_q(z)\psi_s(r)\exp\left(i\omega t - i\ell\theta\right), \tag{2.4}$$

where $\eta_q(z)$ defines the vertical field distribution, $\psi_s(r)$ gives the radial field distribution and the exponential factor defines the phase of the field rotating in the micro-disk. The indices q and s run through the integer values, with $q\,, s = 0$ corresponding to the fundamental mode with one lobe, $q\,, s = 1$ corresponding to the first order mode with two lobes in the vertical and radial directions respectively, and so on, see Fig. 2.12(c) and (d).

The new property that separates the whispering gallery modes from the modes in a ridge waveguide is the fact that ℓ is also restricted to integer values. Indeed, due to the cylindrical symmetry after a complete round trip $\theta = 2\pi$ the field must turn back to its initial value at $\theta = 0$, which is possible only if ℓ is an integer. The physical meaning of the parameter ℓ becomes clear after one calculates the angular momentum of the electromagnetic field for a given mode in a micro-disk:

$$\mathbf{J} = \varepsilon_0 \int \mathbf{r} \times (\mathbf{E} \times \mathbf{B})\, d^3\mathbf{r} = \hat{\mathbf{e}}_z \frac{\ell}{\omega}\varepsilon_0 \int \mathcal{E}^2(r, z)\, d^3\mathbf{r} = \hat{\mathbf{e}}_z \hbar\ell \frac{\text{Energy}}{\hbar\omega} = \hat{\mathbf{e}}_z \hbar\ell \text{N}_{\text{photons}}, \tag{2.5}$$

where $\hat{\mathbf{e}}_z$ is the unit vector in the z-direction. The formula (2.5) clearly shows that ℓ can be interpreted as an orbital angular momentum of one photon measured in the units of

$\hbar$. No surprise, that the values of the angular momentum for the electromagnetic field is quantized, since in this situation the equation for the guided modes is analogous to the Schrödinger equation with some minor modifications. An example of the field distributions for the angular momentum $\ell = 5$ and different radial order $s = 0, 1, 2$ is show in Figs. 2.13(a)-(c) In practice, the fields with are used for the nonlinear interactions have a much higher angular momentum, but the images for these fields would be much less informative due to the large number of angular lobes and high concentration of the field power near the edge of the mico-disk.

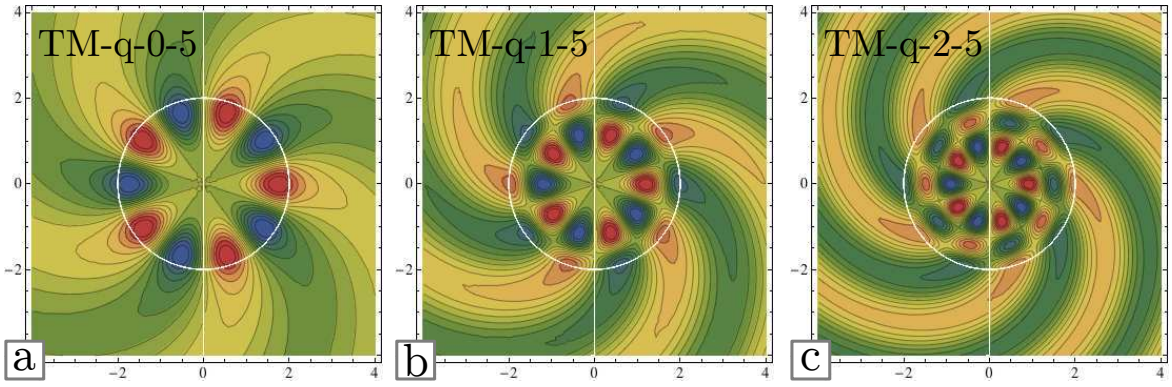

Figure 2.13 – (a)-(c) Examples of the field distributions for the whispering gallery modes.

The phase matching conditions for the second harmonic generation with the whispering gallery modes have the form:

$$\begin{aligned} 2\omega_{\mathrm{P}} &= \omega_{\mathrm{SH}} \\ 2\ell_{\mathrm{P}} &= \ell_{\mathrm{SH}}, \end{aligned} \tag{2.6}$$

where ω_{P}, ℓ_{P} and ω_{SH}, ℓ_{SH} are the frequency and angular momentum of the pump and the second harmonic respectively. These conditions obviously correspond to energy and angular momentum conservation for the conversion of two pump photons into one second harmonic photon.

Although the conditions (2.6) have a clear physical meaning, form the practical point of view it may not be obvious what one should do in order to satisfy these phase matching conditions. In order to understand the practical side of this problem, we introduce an intuitive representation for the angular momentum ℓ:

$$\ell = \beta R_{\mathrm{eff}} = \frac{2\pi}{\lambda} n_{\mathrm{eff}} R_{\mathrm{eff}}, \tag{2.7}$$

where β is the effective wave vector of a given mode in the planar waveguide, n_{eff} is the effective index of this mode, R_{eff} is the effective radius of a given whispering gallery mode. It should be noted that the effective wave vector β is commonly used in the literature and is determined by a simple formula $\beta = \frac{2\pi}{\lambda} n_{\mathrm{eff}}$. On the contrary, the effective radius of a mode R_{eff} is much less common, and the only proper way to define this radius is through the formula $R_{\mathrm{eff}} = \ell/\beta$. Nevertheless, this notion is very useful for interpreting the conservation laws.

By using the interpretation (2.7) the phase matching conditions can be rewritten in the form:

$$\ell_{\mathrm{P}} = \frac{2\pi}{\lambda_{\mathrm{P}}} n_{\mathrm{eff}}^{\mathrm{P}} R_{\mathrm{eff}}^{\mathrm{P}} - \text{integer}, \tag{2.8}$$

$$n_{\mathrm{eff}}^{\mathrm{SH}} R_{\mathrm{eff}}^{\mathrm{SH}} = n_{\mathrm{eff}}^{\mathrm{P}} R_{\mathrm{eff}}^{\mathrm{P}}, \tag{2.9}$$

where $n_{\mathrm{eff}}^{\mathrm{P}}$, $R_{\mathrm{eff}}^{\mathrm{P}}$ and $n_{\mathrm{eff}}^{\mathrm{SH}}$, $R_{\mathrm{eff}}^{\mathrm{SH}}$ are the effective refractive index and the effective radius for the pump and the second harmonic respectively, and by definition $\lambda_{\mathrm{P}} = 2\lambda_{\mathrm{SH}}$. The condition that ℓ_{SH} must be an integer is automatically satisfied because of the relation (2.9).

First of all it should be noted that the similar condition in the case of a simple waveguide is $n_{\mathrm{eff}}^{\mathrm{SH}} = n_{\mathrm{eff}}^{\mathrm{P}}$, which means that the phase matching conditions for the micro-disk are more complicated. The additional constraint given by (2.8) significantly reduces the number of possible solutions for phase matching. In Section 2.1 it was demonstrated on multiple occasions that the wavelength of the second harmonic is a continuous function of the waveguide thickness, it is also the case for the waveguide width. In the case of the micro-disk the single condition (2.9) by itself would give the behaviour identical to the case of the waveguides, namely, the phase-matched wavelength of the pump would be a continuous function of the disk diameter or the disk thickness. The additional constraint of resonance (2.8) in the case of the micro-disks selects only discrete points on this curves, for which this constraint is satisfied. In the real situation these points are spread over small segments defined by the spectral width of the pump and the second harmonic. From the practical point of view it means that doubly resonant second harmonic generation in micro-disks can be achieved only within a discrete set of the disk geometries, which obviously complicates its experimental realization.

There are several simple facts, which help to search possible modes combinations which may allow satisfying the phase matching conditions (2.8) and (2.9). For example, for a fixed wavelength and a fixed number of vertical lobes the mode with 3 radial lobes has a smaller effective radius than the mode with 1 radial lobe. Similarly, between two modes with the same number of radial and vertical lobes, the mode at a lager wavelength will have a smaller effective radius. By combining these simple rules with the evolution of the effective refractive indices in planar waveguides, one can select the right mode combination. The next two sections give more detailed description for two particular examples of mode combinations.

2.2.2 Phase matching between TM-0-0-ℓ_{P} pump and TM-0-2-ℓ_{SH} second harmonic

This section presents a particular case of phase matching between the TM-0-0-ℓ_{P} pump and the TM-0-2-ℓ_{SH} second harmonic. This mode combination was used for the experimental demonstration of the doubly-resonant second harmonic generation in GaN/AlN micro-disks, see Fig. 2.14(a). Due to the necessity to fine tune the pump to achieve the phase-matching condition, we realize the experiment using a tunable laser source emitting in the telecom C-band at 1.55μm obtain the SH in the visible region. The experimental results for this case will be presented in Chapter 6.

The same TM polarization was chosen for both modes in order to exploit the highest $\chi_{zzz}^{(2)}$ nonlinear coefficient. In this mode combination both the pump and the second

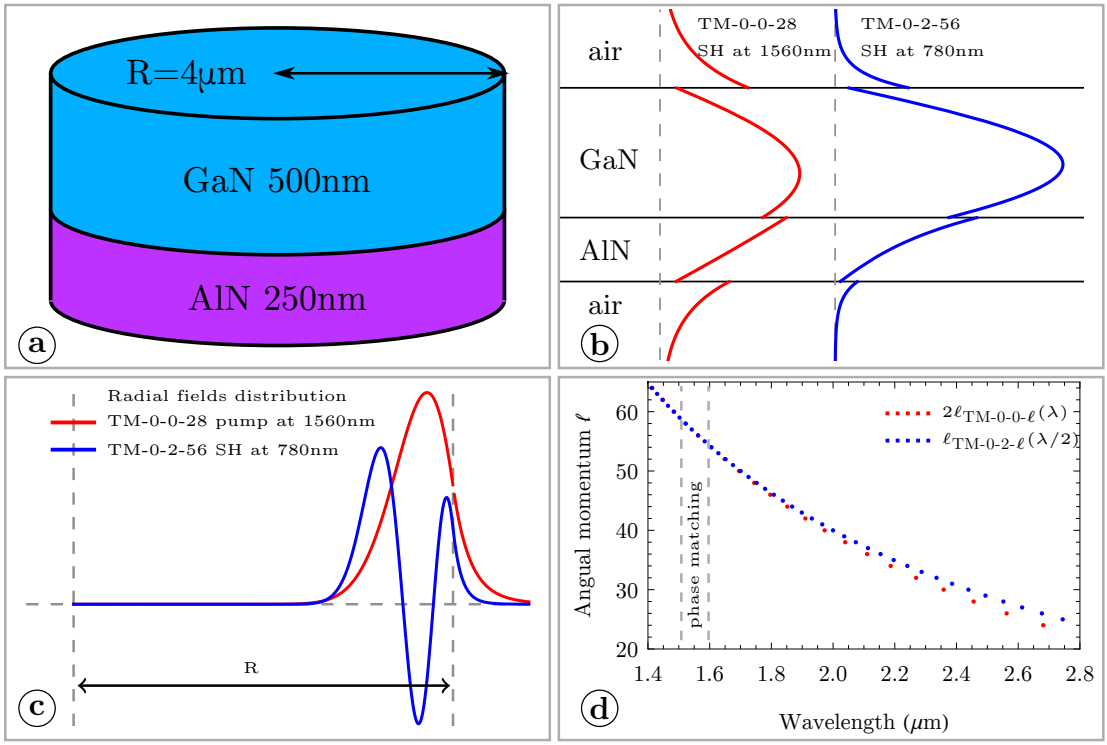

Figure 2.14 – (a) A scheme of the micro-disk that was used for the SHG experiments with the TM-0-0-ℓ_{P}/ TM-0-2-ℓ_{SH} mode configuration. (b) Vertical field profiles for the pump and the second harmonic in this micro-disk. (c) Radial field profiles for the pump and the second harmonic in this micro-disk. (d) Angular momentum for the pump and the second harmonic as a function of the resonant wavelengths.

harmonic have one vertical lobe, see Fig. 2.14(b). Therefore, for the effective refractive indices we have the following inequality $n_{\text{eff}}^{\text{SH}} > n_{\text{eff}}^{\text{P}}$. In order to compensate for this inequality and satisfy condition (2.9), the mode with a smaller effective radius must be used for the second harmonic $R_{\text{eff}}^{\text{SH}} < R_{\text{eff}}^{\text{P}}$. For this purpose the TM-0-2-ℓ_{SH} mode with 3 radial lobes was used for the second harmonic, see Fig. 2.14(c). As it will be demonstrated in Section 2.2.4 a mode with 2 radial lobes could also be used, but this case would require disks with much larger thicknesses and smaller diameters, which increase the fabrication challenges.

Once the number of vertical and radial lobes is fixed the mode can still carry different angular momentum ℓ. The solutions with different angular momentum ℓ exist at fixed resonant wavelenghts. The plot in Fig. 2.14(d) shows the angular momentum for the pump and the second harmonic as a function of the wavelength. The red and blue dots in this plot come closer to each other in the 1.5-1.6μm region, showing the possibility to reach the phase matching conditions $2\ell_{\text{P}} = \ell_{\text{SH}}$ and $\lambda_{\text{P}} = 2\lambda_{\text{SH}}$ for the angular momentum value around 55 for the second harmonic. Indeed, by following more precisely the TM-0-0-27 and TM-0-2-54 mode combination one can see that the resonant wavelengths of these two modes evolve with the disk radius and reach $\lambda_{\text{P}} = 2\lambda_{\text{SH}}$ condition around 3.965μm radius, see Fig. 2.15(a). The same behaviour can be observed for two other mode combinations in Figs. 2.15(b) and (c). As a result, there exist 3 doubly resonant solutions with a pump in the 1.5-1.6μm spectral region shown in Fig. 2.15(d).

The solutions with the TM-0-0-28 pump were chosen for the experimental realization,

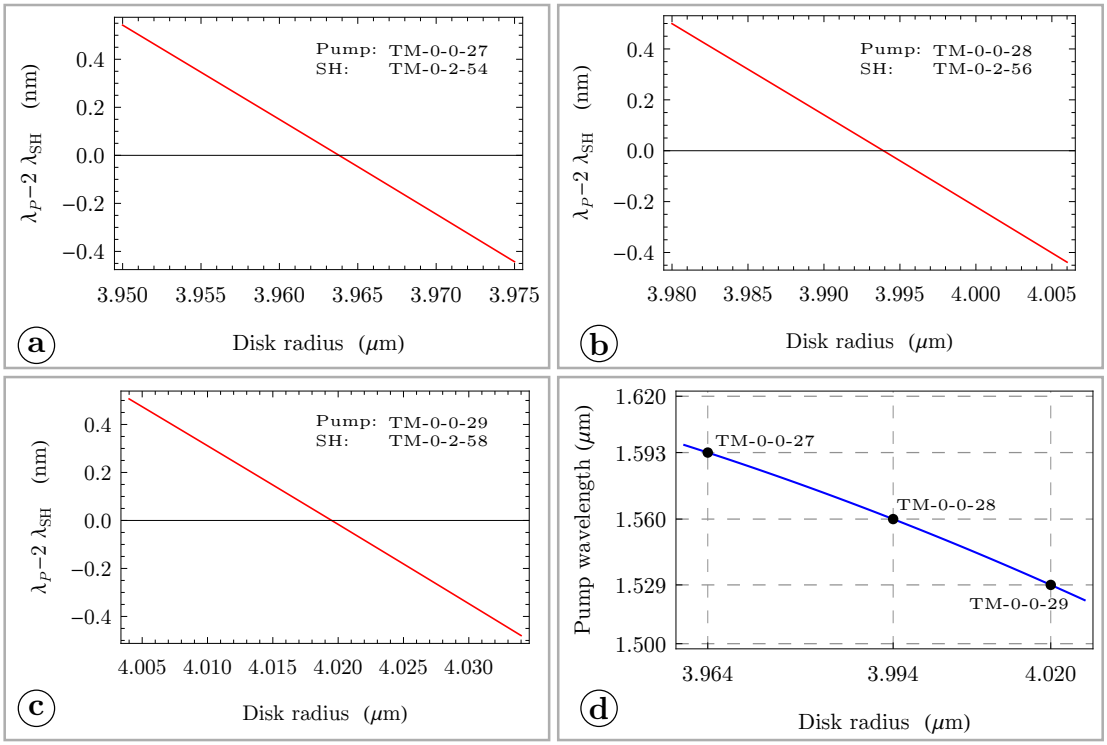

Figure 2.15 – (a)-(c) Evolution of the $\lambda_P - 2\lambda_{SH}$ difference for three particular mode combinations with the disk radius. (d) Solutions for the doubly resonant phase matching for the TM-0-0-ℓ_P/TM-0-2-ℓ_{SH} mode configuration.

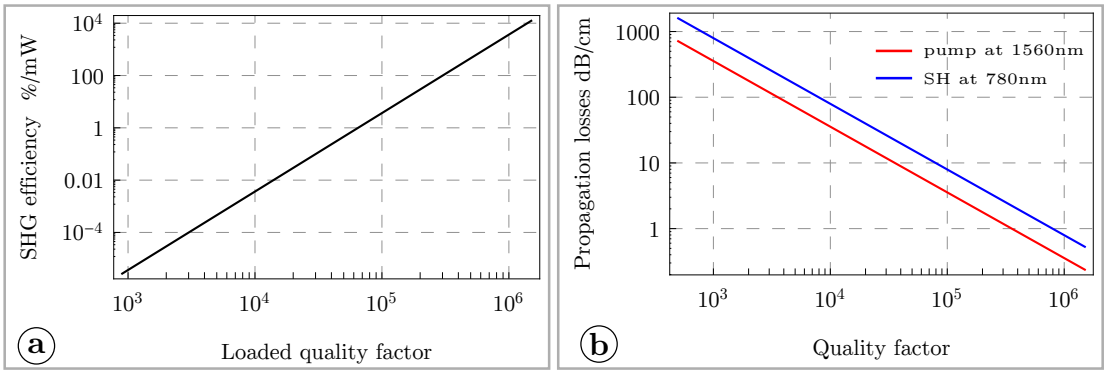

Figure 2.16 – (a) The SHG conversion efficiency as a function of the loaded quality factor for the TM-0-0-ℓ_P/TM-0-2-ℓ_{SH} mode configuration. (b) Relation between the propagation losses and the quality factors for the pump and the second harmonic.

which will be described later in the manuscript. Although, in Fig. 2.15(d) the solutions are presented by 3 dots, in real situation these solutions should exist over small segments defined mainly by the spectral with of the pump mode. Taking into account the typical 10^4 quality factors observed on the fabricated micro-disks, the spectral width of the pump mode is about 0.15nm. Depending on the quality factors determined both by the propagation and the coupling losses, one can expect different conversion efficiencies. The highest SHG efficiency is expected under critical coupling, when $Q_{\text{loaded}} = \frac{1}{2}Q_{\text{int}} = \frac{1}{2}Q_{\text{coup}}$, where Q_{loaded} is the total quality factor, Q_{int} is the intrinsic quality factor determined by the propagation losses and Q_{coup} is the quality factor determined by the coupling losses. The

theoretical conversion efficiencies under critical coupling both for the pump and the second harmonic are presented in Fig. 2.16(a). The Fig. 2.16(b) gives the relation between the quality factors and the propagation losses in dB/cm.

2.2.3 Phase matching between TE-0-0-ℓ_P pump and TM-0-0-ℓ_{SH} second harmonic

At this point, the main peculiarities of the phase matching in micro-disk were explained using both general reasoning and particular example. Here we want to address another particular example, since it is somewhat different from other solutions, which will be presented later.

This case is special, because it allows reaching phase matching between fundamental modes for both the pump and the second harmonic. In order to understand, why this solution is possible, one needs to compare the dispersion curves of modes confined in two planar waveguides with significantly different thickness. Figure 2.17(a) shows the dispersion curves for the fundamental and the first order modes of a planar waveguide which corresponds to the micro-disk studied in the previous section. In this plot both for the red and green curves the effective index at 800nm wavelength is larger than the effective index at 1600nm wavelength. The fact that the refractive index is larger at the shorter wavelength for a given mode is explained by the material dispersion and a better mode confinement at a shorter wavelength. This is almost always the case, and this index contrast needs to be compensated by using modes with different radial orders in order to benefit from the modal dispersion. But it turns out that in a very particular situation of sufficiently thin layers the effective index of the TM0 mode at 800nm can be smaller than the effective refractive index of the TE0 mode at 1600nm, as it is shown in Fig. 2.17(b). This situation occurs due to the fact that the TM modes tend to have a poor confinement in sufficiently thin layers due to the field discontinuities.

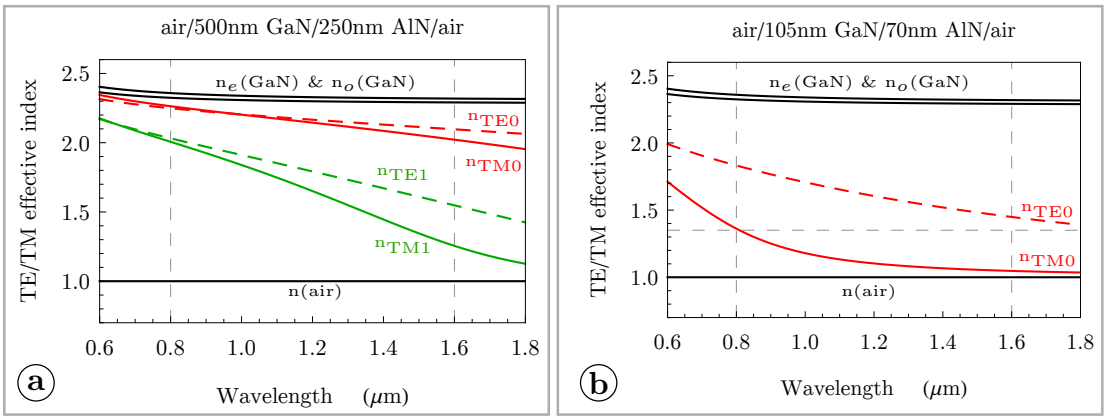

Figure 2.17 – (a)-(b) Dispersion curves for the effective refractive indices for TE and TM modes in two planar waveguides with different thickness.

It is important to underline that the special condition $n_{\text{eff}}^{\text{SH}} < n_{\text{eff}}^{\text{P}}$ can only be reached at the price of poor mode confinement, when only about 50% of the mode power is confined in the guiding layer. Nevertheless, even in this situation the interaction between the fundamental modes can give higher conversion efficiencies in comparison to the previously considered case. This arises because the poor mode confinement in the z direction is

compensated for by the good radial overlap. Although the effective refractive index of the TM second harmonic is smaller than the effective index of the TE pump, this difference is rather small. Therefore, a significantly large radius is needed, so that the relation $R_{\text{eff}}^{\text{SH}} > R_{\text{eff}}^{\text{P}}$ for the modes with one radial lobe does not dominate in the phase matching condition (2.9).

An example of the micro-disk that can be used for the SHG based on the phase matching between the TE-0-0-ℓ_{P} pump and the TM-0-0-ℓ_{SH} second harmonic is shown in Fig. 2.18(a). The plots in Figs. 2.18(b) and (c) represent the vertical and the radial field distributions for these modes. The discrete set of solutions for the doubly-resonant SHG for the pump around 1.55μm wavelength is given in Fig. 2.18(d). The conversion efficiency as a function of the loaded quality factor in the case of critical coupling is presented in Fig. 2.19.

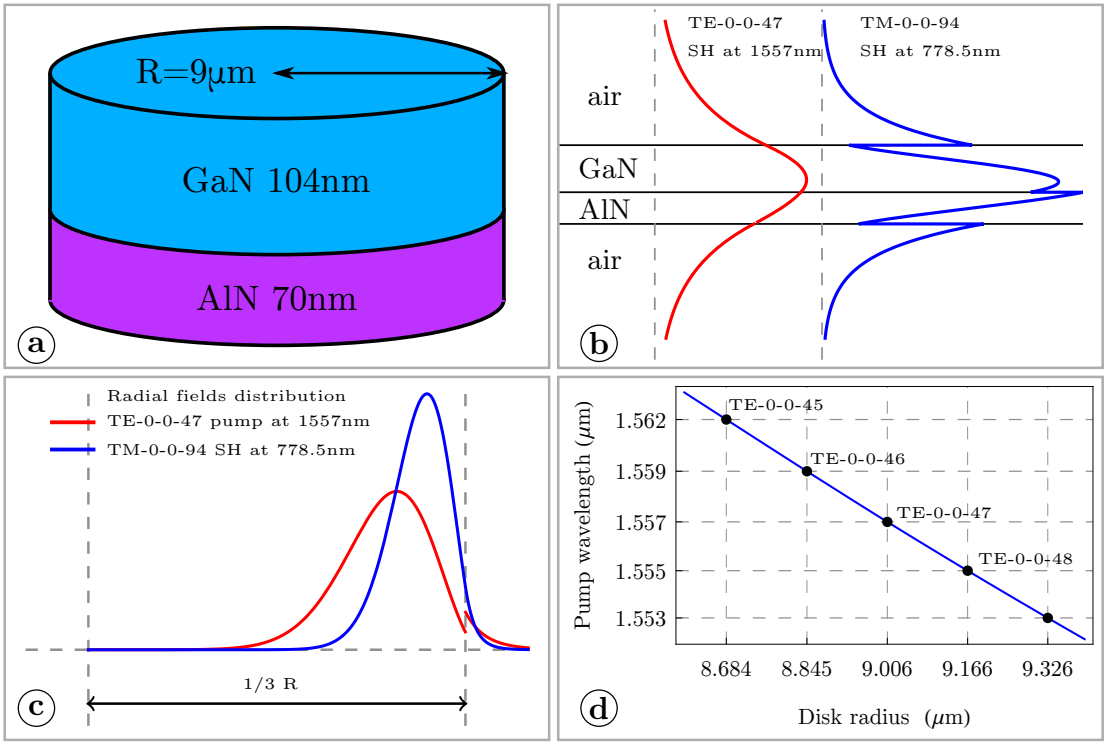

Figure 2.18 – (a) A scheme of the micro-disk that can be used for the SHG with the TE-0-0-ℓ_{P}/TM-0-0-ℓ_{SH} mode configuration. . (b) Vertical field profiles for the pump and the second harmonic in this micro-disk. (c) Radial field profiles for the pump and the second harmonic in this micro-disk. (d) Solutions for the doubly resonant phase matching for the TE-0-0-ℓ_{P}/TM-0-0-ℓ_{SH} mode configuration.

2.2.4 Summary for different mode combinations

After two particular examples which were described in details, this section gives a summary of the SHG conversion efficiencies that can be reached with other mode combinations. Moreover, in the previous sections we did not discuss whether the proposed solutions were unique, or whether they were optimal for a given mode combination. Therefore, here we will present the optimisation procedure that was used in order to define the thickness

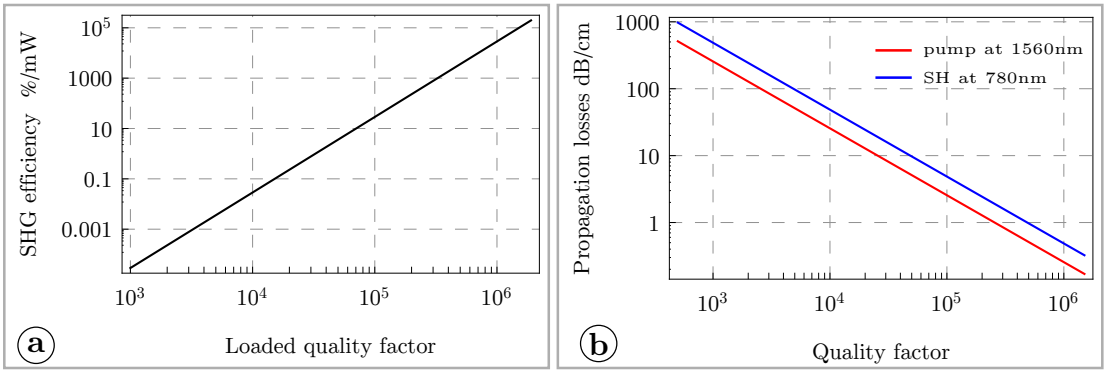

Figure 2.19 – (a) The SHG conversion efficiency as a function of the loaded quality factor for the TE-0-0-ℓ_{P}/TM-0-0-ℓ_{SH} mode configuration. (b) Relation between the propagation losses and the quality factors for the pump and the second harmonic.

for the guiding layers, the disk diameter and the ratio between GaN and AlN, for a particular choice of the mode combination.

First of all, we would like to recall that the choice of the pump wavelength in the telecom C-band is explained simply by the availability of the finely tunable TUNICS laser source for this spectral region. For the targeted wavelengths, the phase matching condition can be satisfied for different combination of the disk thickness and diameter. This is the case due to the two main tendencies: 1) in the thicker planar layer, the modal dispersion is weaker for the TE0 an TM0 modes and therefore the difference $n_{\mathrm{eff}}^{\mathrm{SH}} - n_{\mathrm{eff}}^{\mathrm{P}}$ is smaller; 2) for the larger values of the disk diameter, there is a smaller difference in the values of the effective mode radii $R_{\mathrm{eff}}^{\mathrm{SH}} - R_{\mathrm{eff}}^{\mathrm{P}}$ for a given mode combination. Therefore, once the phase matching is reached for a given mode combination and a given pump wavelength, this phase matching can be maintained by simultaneously increasing the disk thickness and diameter; the same phase matching can also be maintained by simultaneously reducing the disk thickness and diameter.

In order to understand in which direction (either larger or smaller micro-disks) one should go, it is necessary to recall how the power coupled to a given cavity depends on the free spectral range of this cavity. It is commonly known, that the intra-cavity power is enhanced by a value equal to the quality factor with respect to the external power. This enhancement is also a function of the free spectral range:

$$P_{\mathrm{circ}} = \frac{\delta\omega_{\mathrm{FSR}}}{2\pi\omega} \frac{4Q_{\mathrm{coup}}}{\left(1 + \frac{Q_{\mathrm{coup}}}{Q_{\mathrm{intr}}}\right)^2} P_{\mathrm{in}} \tag{2.10}$$

where P_{circ} is the power circulating inside the micro-disk, P_{in} is the external power either coupled to or decoupled from the micro-disk, Q_{coup} is the coupling quality factor, Q_{intr} is the intrinsic quality factor and $\delta\omega_{\mathrm{FSR}}$ is the free spectral range. The free spectral range $\delta\omega_{\mathrm{FSR}}$ determines the spectral distance between two resonant solutions for a given mode with an adjacent values ℓ and $\ell + 1$ of the angular momentum that it can carry.

The formula (2.10) shows that the internal power is proportional to the free spectral range and it reaches its maximal value for the case of critical coupling $Q_{\mathrm{intr}} = Q_{\mathrm{coup}}$. For a given mode and a wavelength the free spectral range is larger in smaller micro-disks. For this reason it would be beneficial to use smaller micro-disks under the condition that the phase matching for a given mode combination can still be maintained. It is

obvious though, that one cannot infinitely decrease the size of a micro-disk, since at some point the radiation losses start to dominate the intrinsic quality factor. Therefore, in the search for the optimal solution an additional constraint $Q_{\text{radiation}} > 10^6$ was used for all the simulations, where $Q_{\text{radiation}}$ is radiation quality factor due to the intrinsic radiation nature of the whispering gallery modes. In this case the intrinsic quality factor is dominated by the losses due to the waveguide imperfections, as in practice one never reaches the 10^6 quality factors for the real AlGaN micro-disks.

Finally, the ratio between GaN and AlN layers in micro-disk is determined by an empirical relation between the thickness of these layers, which is necessary for the compensation of the tensile strain during the growth. Table 2.1 gives the thickness of AlN layers, which is necessary for the growth of a given GaN layer.

GaN layer thickness (nm)	300nm	400-500	600-700	>800
AlN layer thickness (nm)	100-150	150-300	200-350	>350

Table 2.1 – The relation between GaN and AlN layer necessary to compensate the tensile strain and avoid crack during the fabrication.

All the constraints and the tendencies mentioned above were used in order to optimize the SHG efficiency for a given mode combination. The summary of the results obtained for the different mode combinations is given in Table 2.2. This table gives the optimal values of the micro-disk radius and of the thickness of the GaN and AlN layer, together with the corresponding conversion efficiency η in the ideal case of critical coupling. The conversion efficiencies are calculated assuming that the loaded quality factor is equal to 10^5. It should be noted, that loaded quality factors reaching the values of $0.8 \cdot 10^5$ for GaN micro-disks and $2.3 \cdot 10^5$ for AlN micro-rings have already been reported in the literature [18, 26].

	Pump: TM-0-0-ℓ_P	Pump: TE-0-0-ℓ_P
SH: TM-0-0-ℓ_{SH}	—— ——	GaN 105nm AlN 70nm R=9μm η =4%/mW
SH: TM-0-1-ℓ_{SH}	GaN 850nm AlN 350nm R=2.4μm η=10%/mW	—— ——
SH: TM-0-2-ℓ_{SH}	GaN 400nm AlN 250nm R=3μm η=1%/mW	GaN 300nm AlN 150nm R=3.2μm η=0.03%/mW

Table 2.2 – Summary and the micro-disk parameters and the conversion efficiencies for different modes combinations.

The empty squares in the Table 2.2 indicate that there is no solution for this mode combination with a radiation quality factor exceeding 10^6. According to this table the highest conversion efficiency could be expected for the TM-0-0-ℓ_P and TM-0-1-ℓ_{SH} mode combination. In practice the TM-0-0-$2\ell_{SH}$/TM-0-0-ℓ_{SH} mode combination was chosen for the first demonstration of the doubly resonant second harmonic generation because this solution gives a good compromise between the expected conversion efficiency and the fabrication and characterization challenges. This choice will be described in details in Chapter 6.

2.3 Conclusions

In this chapter, I discussed in details the potential of modal phase matching in SHG experiments both in waveguides and in micro-disks. The conversion efficiencies are calculated for different mode combinations and the impact of the propagation losses is estimated here. It is shown, that GaN and AlN waveguides can be used for second harmonic generation within the whole transparency window of these materials. The conversion efficiencies can reach $10\%W^{-1}cm^{-2}$ for ideal lossless waveguides in the case of a simple modal phase matching. Further improvements using the polarity inversion to improve the overlap integral, can lead to conversion efficiencies as high as $1000\%W^{-1}cm^{-2}$. It was also demonstrated, that the whispering gallery modes can be used for the doubly resonant second harmonic generation in the micro-disks. In this case much larger conversion efficiencies reaching 10%/mW can be obtained due to the cavity field enhancement. This improvement comes at the price of fabrication and characterization difficulties. It should also be noted that the high conversion efficiencies in micro-disks can only be reached in the case of critical coupling for both the pump and the second harmonic, situation which is not easy to obtained experimentally. The coupling is a separate and rather complicated problem, which we don't address here in details.

Chapter 3

Epitaxy

Epitaxy is at the heart of CRHEA's activity. Although epitaxy and growth are terms often used without any distinction, it is important to recall the difference between the two. Crystalline growth is the process of a crystal increasing in size by atomic deposition and ordering on its surface. It may describe many different processes. Epitaxy is restricted to the specific case when a substrate is used, and the crystal grows on the substrate surface. In this work, all growth processes are epitaxial. Two different substrates have been used: sapphire and silicon.

There are two main types of epitaxy.

Molecular Beam Epitaxy (MBE) is performed in vacuum, with a pressure before the epitaxy in the range of 10^{-10} Torr and during the epitaxy in the range of 10^{-5} Torr. Atomic species are evaporated form solid sources (Ga, Al) and deposited on the surface. This pressure is low enough so that there is no chemical reaction before atoms arrive on the surface. In the specific case of nitrides, the N cannot be provided from a solid source. It comes either from a gas source, ammonia (NH3) which decomposes on the surface, or from a plasma source which provides N radical (in addition to ions and molecules) on the surface. Again, the pressure remains low enough so that the atomic beams remain ballistic. Another specificity of MBE is that the low pressure allows using electron beams to study the surface. The Reflection High Energy Electron Diffraction (RHEED) is used to measure the lattice parameter of the material on the surface and to measure the roughness at the atomic scale. This gives a precious information on the growth mode and the strain and/or composition on the surface.

Vapor Phase Epitaxy (VPE) is the second type of epitaxy, based on gaseous chemical precursors sent to the surface, which decompose and leave the desired atoms on the surface. In this work, precursors were Metal Organic (MO) molecules. This epitaxy technique, thus called MOVPE, is the most commonly used in the industry for growing nitrides. The pressure ranges from 0.1 to 1 atm, and parasitic reactions occur in the reactor, although some tricks are used in the gas injection geometry in order to minimize these effects.

3.1 Molecular Beam Epitaxy

Two reactors were used in this work, a RIBER 32P and a RIBER-Compact-21. Due to mainly historical reasons, the R-32 was used for growing samples on sapphire, while the C-21 was used for growing on silicon. Both reactors take 2-inch wafers.

3.1.1 Epitaxy on sapphire

The samples were grown on c-plane (0001) sapphire substrates using ammonia (NH_3) as nitrogen precursor, and solid sources for the III-elements, i.e. a double-filament effusion cell and a cold lip effusion cell for Ga and Al, respectively. At first, the sapphire substrates were nitridated by exposing the surface to an ammonia flow 5 SCCM (Standard Cubic Centimer per Minute) at a temperature of 850-900°C [27]. The modification of the surface can be followed by RHEED: it has been shown that the surface in-plane lattice constant changes when the sapphire surface is exposed to NH_3 due to the conversion of the sapphire surface into AlN. Then, a low temperature GaN layer (typical thickness 50 nm) was grown at a temperature of 450°C to ensure the metal polarity of the nitride heterostructures [28], followed by a 100-nm AlN buffer layer at 900-950°C and the growth of the thick $Al_xGa_{1-x}N$ cladding layers at a temperature between 800-900°C (defined as a function of the Al concentration i.e. the growth temperature is typically equals to $(800 + 100 \cdot x)$°C).

Although the substrate is rotated during growth, the layer thickness varies and decreases from the center to the edge of the 2-inch wafers: typically, the variation of a GaN layer thickness on the whole 2-inch wafer is within 4%, and within 10% for an $Al_xGa_{1-x}N$ layer between the center and the half-radius of the wafer and 20% between the center and the edge.

The Al content of the $Al_xGa_{1-x}N$ layers was determined in-situ by RHEED oscillations, and confirmed by energy dispersive X-ray spectroscopy in a scanning electron microscope (SEM). The maximum Al variation across a 2-inch wafer is 10% of the nominal composition, and is typically within 5%. The AlN layer is used to exert a compressive strain on the above $Al_xGa_{1-x}N$ layer and hence avoids the formation of cracks [29]. The growth rate of the layers were monitored by laser reflectivity in real-time, by recording the reflected intensity variation of a 532 nm green laser diode during the growth [30]. The growth rates for the low temperature GaN layer was 0.3 μm/h, for the AlN buffer layer 0.1 μm/h, and for the $Al_xGa_{1-x}N$ layer around 0.5 μm/h. Finally, the growth of the GaN waveguide was done at 800°C with a growth rate of 1 μm/h. X-ray diffraction (XRD) measurements, using a four-circle diffractometer, were performed to study the crystalline quality of the $Al_xGa_{1-x}N$ layers by doing ω-scans of the (0002) symmetric reflection and the (30-32) skew symmetric reflection: typical values of 0.35° and 0.8° for the full width at half maximum (FWHM) of the peak reflections are found for (0002) and (30-32), respectively. The dislocation density in these layers is typically between $2 \cdot 10^{10}\text{cm}^{-2}$ and $4 \cdot 10^{10}\text{cm}^{-2}$, as confirmed by transmission electron microscopy (TEM) measurements [31]. In the case of GaN, typical values for the FWHM of the (0002) reflection peak is $0.08° - 0.1°$ [32] and the dislocation density is in the high 10^9cm^{-2} range (typically $5 \cdot 10^9\text{cm}^{-2}$ for thick layers) [33]. As will be discussed later, highly dislocated regions $> 10^{10}\text{cm}^{-2}$ exhibit optical losses.

3.1.2 Epitaxy on Silicon

The samples were grown on Si (111) substrates using ammonia as nitrogen precursor, and solid sources for the III-elements. Si(111) surface is used because of its hexagonal symmetry. The more conventional Si(100) with its square symmetry leads to the formation of domains rotated by 90° relative to each other unless special surface preparations (off-axis surface, removal of all single steps) are used. As Si is very reactive to ammonia, a very precise process has been developed and must be strictly followed in order to avoid

creating a thick amorphous SiN layer on the Si surface. Details on this process can be found in [34].

The silicon substrates are prepared before epitaxy by chemical treatment in order to remove the residual silicon oxide and stabilize the surface by hydrogen (HF last treatment). Alternatively, one can also remove the oxide in the reactor by heating the substrate at very high temperature (1200°C).

An AlN buffer layers is grown first. Its thickness can vary from 40 to 300 nm, and the growth temperature from 900 to 1200°C. The impact of these parameters is explained in [34]. One additional challenge when growing nitrides on Si is the difference of thermal expansion coefficients between Si and nitrides: its relative value reaches -38% between Si and AlN. The negative value expresses the fact that Si lattice varies less with temperature than the AlN one. During the growth at (800-1000°C), the nitride layer is about strain free. When cooling down to room temperature, the nitride lattice constant reduces more than the Si one, and the nitride film becomes in tensile stress. Above a certain stress value and thickness, the elastic energy exceeds the critical value corresponding to the creation of free surfaces within the layer and cracks appear. This problem severely limits the thickness of non-cracked nitride layers on Si. A solution has been found, which allows fabricating thicker layers. If the AlN buffer is grown thick enough, it completely relaxes and reaches its own lattice constant at the growth temperature. Then, the trick consist in growing GaN in conditions (2D mode) where the GaN does not relax and remains in large compressive strain. During the cooling down, the thermal expansion coefficient difference with Si comes into play and brings the GaN layer to a state close to zero strain. Efficiency of this process is improved when an additional AlN/GaN pair is inserted in between the AlN buffer and the GaN top layer. However, in this structure, when the AlN interlayer relaxes during the growth, it may crack. At this moment, some GaN from the underlying layer is transported towards the AlN layer along the cracks and fills up the cracks, so that, at the end, the sample appears un-cracked. However, this mass transport creates some voids in the GaN interlayer which induce light scattering and optical losses. A solution consists in replacing the GaN interlayer by an AlGaN interlayer, which reduces the tensile strain in the subsequent AlN layer and avoid the crack formation. As can be deduced from the previous discussion, strain issues are critical during the growth of nitrides on Si, and following in real time the strain is an essential issue. This is performed by curvature measurements with a Laytec system : a laser beam is separated in two spots on the surface, and the two reflected beams are measured: the separation between them increases with the wafer curvature. The Laytec system also measures the growth rate by laser reflectometry at 405 nm and 950 nm : the interferences are measured as a function of the increasing thickness. The RHEED is also used to monitor the growth mode. The thickness uniformity is a few % across the radius (the substrate is rotating).

Let us finally mention the growth on SOI (Silicon on insulator). The surface being Si, the chemical aspects are similar as on Si substrates. The main difference is the temperature on the surface. Due to the SiO_2 layer, the surface temperature is lower than with regular Si under the same heating conditions. This can easily be adjusted by increasing the heating power. The actual problem is the temperature control. The SiO_2 layer creates optical interference in the infrared emission that is used by the pyrometer to monitor the temperature. After a few runs with the same SOI substrates, the temperature can be calibrated. When SOI with very thin SiO_2 are used ($<$100 nm), delamination sometimes occurs at high temperature.

3.2 Metal Organic Vapor Phase Epitaxy

In this study, a home made MOVPE reactor was used, with a vertical geometry (gases are directed towards the surface at normal incidence). It has been used for growing structures on sapphire only. The growth was performed at 1080°C and 800 mbar. The precursors were trimethyl gallium (TMGa) and aluminum (TMAl), and ammonia. The standard flows for growing GaN are 3 L/min for nitrogen (carrier gas), 5 L/min for hydrogen (carrier gas), 7 cm^3/min for TMGa et 3,5 L/min for ammoniac. We immediately observe the very large V/III ratio, which is typical for GaN epitaxy, and largely due to the small decomposition rate of ammonia at this temperature.

The reactor is equipped with a Laytec system which monitors the curvature and the thickness (laser at 633 nm). This laser reflectivity also allows monitoring the surface roughness by measuring the absolute value of the reflectivity.

3.3 Surface roughness

The surface roughness turns out to be an important parameter for optical waveguides. It depends on the growth mode. In a first case, ad-atoms (atoms on the surface) diffuse on the surface and get incorporated on existing steps. Hence, steps move along the surface which remains smooth. This is favored at high temperature and for atoms for a low sticking coefficient, leading to a large diffusion length. This is typical for GaN surfaces grown by MOVPE. On the contrary, at lower temperature, ad-atoms diffuse on a short distance and are incorporated in islands. This regime of kinetic roughness gives rise to a rougher surface with a shorter correlation distance. This is typical for GaN surfaces grown by MBE. Details on the roughness parameters will be given later, together with the assessment of the associated optical losses.

We detail here a short MOVPE run which has been used many times in order to smoothen the surface of samples grown by MBE. Indeed, as explained in the previous section, MBE surface tend to be rougher than MOVPE ones, more precisely they have a shorter roughness correlation parameter. Hence, we have used MOVPE to smooth the surface of MBE samples, which had otherwise interesting properties (polarity, heterostructure composition) which justified to grow them by MBE.

The goal was to grow 60 nm of GaN. Pressure was set to 300 mbar. Gas fluxes were set to 5 L/min for hydrogen, 3 L/ min for nitrogen and 3.5 L/min for ammonia. Then, the temperature was increased to 1080°C with a ramp of 80°C/ min. When the temperature has reached 1080°, we introduce 7 sccm of TMGa during 1 minute, corresponding to about 60 nm of GaN (growth rate of 3.6mum/h). Then the temperature is decreased to room temperature under NH_3, H_2 and N_2 flows. The ammonia is stopped before room temperature, at about 500°C.

3.4 Polarity inversion

As will be explained elsewhere, inverting the polarity of the material is of interest. This can be done during the epitaxy. This has been demonstrated at CRHEA by introducing a high Mg doping in Ga-polar GaN layer during the MBE process [35]. The Mg content should be larger than $10^{20}cm^{-3}$. Locally, pyramidal defects and stacking faults were observed. The

high Mg content can even lead to the formation of Mg_3N_2 which is cubic. The total layer thickness where the inversion occurs is 10 nm. Note that a similar inversion was obtained by MOVPE by the group of UCSB [36]. At CRHEA, pyramidal defects associated with Mg have been frequently observed in highly doped GaN grown by MOVPE, which could lead to polarity inversion. However, the inversion was developed in MBE only at CRHEA, and this is the technique which has been used in this work.

To finish, we would like to indicate that there is an alternative way to epitaxy to fabricate structures with polarity inversion. Two layers can be grown with the usual metal polarity. Then by bonding them face to face, we obtain the desired structure. However, this requires to remove the substrate at least on one side of the structure. The position of the inversion plane in the final structure is simply determined by the thickness of the initial layers. This approach has been used at the end of the study with AlN layers, where the inversion during epitaxy is not yet developed, and may even be impossible.

Chapter 4

Experimental set-ups for linear and nonlinear characterisation

This chapter describes main optical characterization techniques that were used in the cases of planar and ridge waveguides. Although planar waveguides are rarely used in the integrated optics, a large part of this manuscript is dedicated to the study of planar waveguides. This can be explained by an obvious fact, that in order to fabricate good ridge waveguides one has to start from high quality planar guiding layers with low propagation losses. Our detailed study of planar waveguides has allowed us to reveal the main sources of propagation losses and how to reduce these losses. The obtained high quality planar layers were used for the further fabrication of ridge waveguides, the characterization technique of which will also be presented in this chapter.

The Section 4.1 presents a prism coupling technique that was used both for linear and nonlinear characterization of the planar waveguides. This technique allows for a selective coupling of light into a given mode in a planar waveguide and measurements of the effective refractive indices and the propagation losses of this guided mode. As it will be explained below, the results of these measurements are important for the further study of the nonlinear processes. The Section 4.2 describes the set-ups that were used for the second harmonic generation experiments in planar and ridge waveguides. Although the main goal of this PhD project was the realization of an efficient nonlinear process, namely the efficient second harmonic generation, this could not be achieved without the detailed preliminary study of linear processes in the waveguides.

4.1 Linear characterization of planar waveguides

By the linear characterization of planar waveguides in our case we mean the measurements of the effective refractive indices and propagation losses of the different guided modes. This characterization was done predominantly in the visible spectral region. A He-Ne laser emitting about 2mW of continuous power at the 633nm wavelength was used as a light source. The photos presented below were taken by two cameras. The first camera, eScope DP-M07 is a pen digital microscope camera that can be connected directly to a PC though a USB port. This camera was used for taking images that were used mainly for illustration purpose. The second camera is a cooled high resolution sCMOS camera for visible spectrum (350nm to 1100nm) from Photonic Science company. The images taken by this camera were used for precise measurements of the intensity distribution and

the estimation of the propagation losses, as it will be explained below.

It should be noted that the linear characterization is always a very important step before the study of the nonlinear processes. First of all, in order to calculate the phase matching conditions for the nonlinear processes one needs to know precisely the refractive indices of the materials of the waveguides. The prism coupling technique described below allows measuring the effective refractive indices of the guided modes and deducing the refractive index profile of the guiding layers. This method was used for the determination of the refractive indices of AlGaN alloys in previous studies [21]. Moreover, the drastic impact of the propagation losses on the SHG efficiency was shown in the previous Chapter 2. Therefore, the study of the propagation losses is also very important and it represents a significant part of this work.

4.1.1 Prism coupling technique

Prism coupling is a very useful technique that allows for a selective coupling of light in a given mode in a planar waveguide [37]. It is also based on a phase matching, as it is shown in Fig. 4.1(a). In this figure the light after entering in the TiO_2 prism is reflected by total internal reflection on the TiO_2/air interface and forms the evanescent field in the air gap between the prism and the waveguide. The radiation mode in the prism couples to the mode confined in the waveguide through this evanescent field. The power transfer through this coupling becomes efficient when the phase matching condition is reached:

$$\beta = k_{||}, \tag{4.1}$$

where β is the effective wave vector of the guided mode and $k_{||}$ is the component of the wave vector in the prism parallel to the direction of propagation in the waveguide.

By using the refraction law and some geometrical considerations, it can be shown that the condition (4.1) can be reached by choosing the proper coupling angle θ:

$$\theta = \arcsin\left[n_{\text{eff}}\cos\alpha - \sin\alpha\sqrt{n_{\text{p}}^2 - n_{\text{eff}}^2}\right], \tag{4.2}$$

where n_{eff} is the effective refractive index of the guided mode, n_{p} is the refractive index for the prism for a given light wavelength and polarization and α is the angle of the prism shown in Fig. 4.1(a). Formula (4.2) gives the relation between the coupling angle θ and the effective index of the guided mode n_{eff}. Since different guided modes have different effective indices, they will also have different coupling angles and therefore the selective light coupling to a given mode is possible.

Once the light is coupled to a given guided mode, it can also be decoupled after a certain distance of propagation in the waveguide by a second prism, see Fig. 4.1(b). Now the decoupling angle is determined by the material and the angle α of the second prism by the formula (4.2). By measuring the decoupling angles for different modes with a goniometer one can determine their effective indices n_{eff} by the formula

$$n_{\text{eff}} = \sin\alpha\sqrt{n_{\text{p}}^2 - \sin^2\theta} + \cos\alpha\sin\theta. \tag{4.3}$$

Often, one calculates n_{eff} starting from the waveguide structure and materials. But it is also possible to solve an inverse problem and determine the waveguide structure and the material refractive indices from the effective indices n_{eff} experimentally measured.

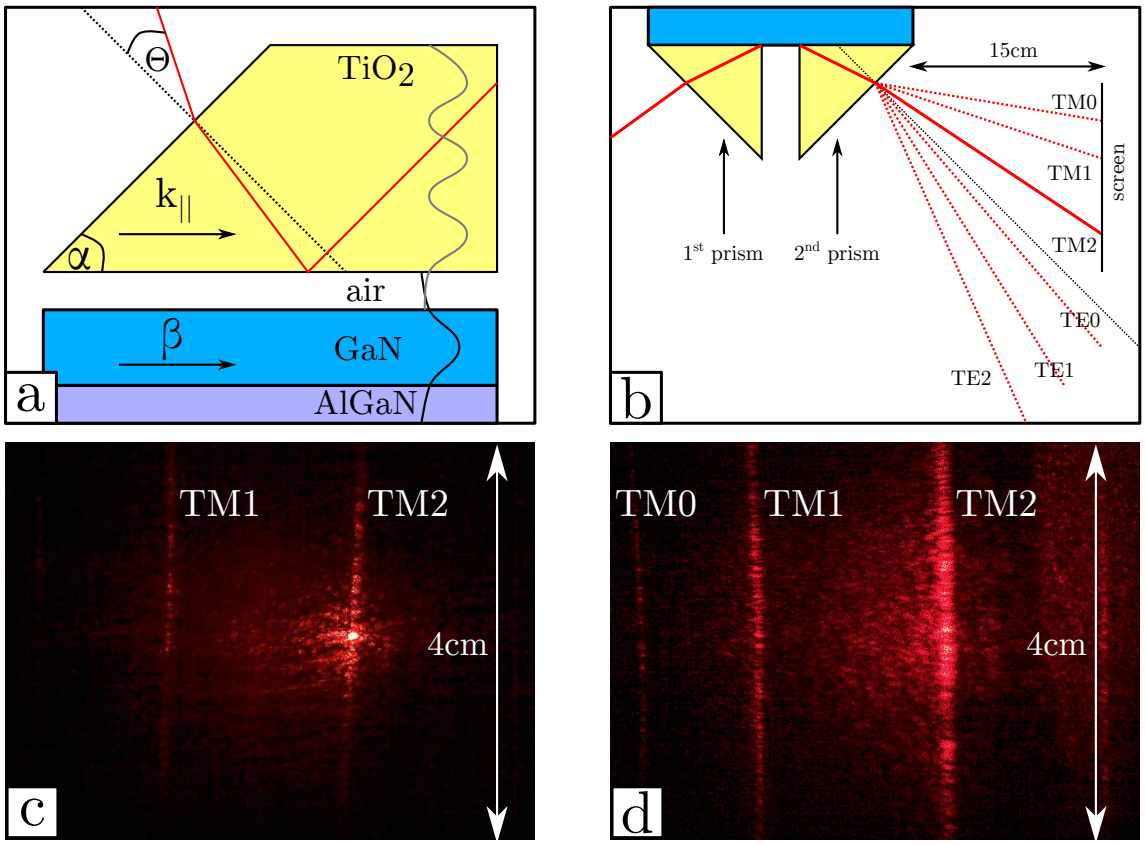

Figure 4.1 – (a) Scheme of the prism coupling technique. (b) Scheme of the m-lines experiment. (c) Example of m-lines with a relatively small inter-modal coupling and small diffusion in the plane in the waveguide. (d) Example of m-lines with a relatively strong inter-modal coupling and large light diffusion in the plane of the waveguide.

The prism coupling technique is useful not only for the measurement of the refractive indices. Simply, by observing the light decoupled from the waveguide and projected on the screen one can observe the so called m-lines and get some information about the waveguide quality, see Figs. 4.1(c) and (d). These figures shows the photos of m-lines projected on a screen located 15cm from the second prism for two different waveguides. In both cases the light was injected in the TM2 mode, but the images differ significantly. In the first case in Fig. 4.1(c) one can observe much less coupling between modes and much less diffusion in the plane of the waveguide in comparison with the Fig. 4.1(d). Therefore one can conclude that in the first case the waveguide has a better quality.

In the previous Chapter 2 is was shown that the second harmonic generation requires interaction between different modes at different wavelengths. Therefore for the realization of the SHG experiment in planar waveguides it would be useful to know how the coupling angles for different modes evolve with the wavelength. Figs. 4.2(a) and (b) give this evolution for the TE- and TM-modes in a 1μm GaN waveguide on AlN substrate. The angles for two polarizations have different signs, since the modes are decoupled to different sides with the respect to the normal to the prism input facet in Fig. 4.1(b). According to the generally accepted convention, the positive sign for the angle is chosen for the

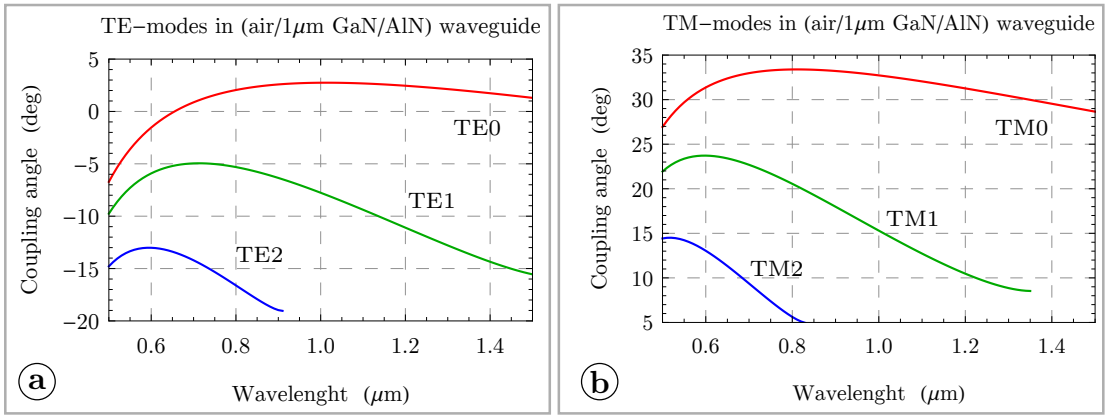

Figure 4.2 – (a) Coupling angles for the TE-modes in 1μm GaN waveguide on AlN substrate. (b) Coupling angles for the TM-modes for the same waveguide.

deviation towards the sample .

The last thing we would like to underline in this section is the fact, that an efficient coupling with the first prism is a challenging task, while >90% decoupling with the second prism can be easily achieved in the experiment. Indeed, on the contact region between the waveguide and the first prism there are two processes of coupling and decoupling witch are competing against each other. Therefore, very particular conditions on the contact zone, beam diameter and position must be reached in order to have an efficient coupling. In particular, the prism must be correctly pressed on the waveguide by the screw in order to minimize the air gap thickness. In contrast, the decoupling with the second prism is very simple and one just needs to create a sufficiently large contact zone for all the light to escape from the waveguide. Figs. 4.3(a) and (b) show that when a sufficiently large contact zone is created, the light is completely decoupled by the second prism. This detail is very important, because it demonstrates that the power decoupled by the second prism represents the power confined in the waveguide within the reflection correction on TiO_2/air interface. And therefore the decoupled power can be used for the estimation of the SHG efficiency in the planar waveguides.

4.1.2 Measurement of propagation losses

The prism coupling technique can also be used for the measurement of the propagation losses. For this purpose it is sufficient to couple the light with the first prism and observe the light scattering by the surface roughness along the propagation line, as it is shown on the scheme in Fig. 4.4(a). The photos taken by the eScope camera show actual light scattering for the TE1 and TM1 modes in Figs. 4.4(b) and (c) respectively. One observes a smaller intensity for the light scattered towards the camera in the case of TM modes due to the fact that the direction of the dipole oscillations for the TM modes is almost perpendicular to the plane of the waveguide, while for the TE modes the direction of these oscillations is parallel to the plane of the waveguide.

The photos taken by the eScope camera will be used for the illustrations of the mode propagation and m-lines throughout the manuscript. These photos will often be saturated but in our opinion they better represent the actual visual experience of an experimentalist. For the actual quantitative measurements we will use the photos taken with the sCMOS

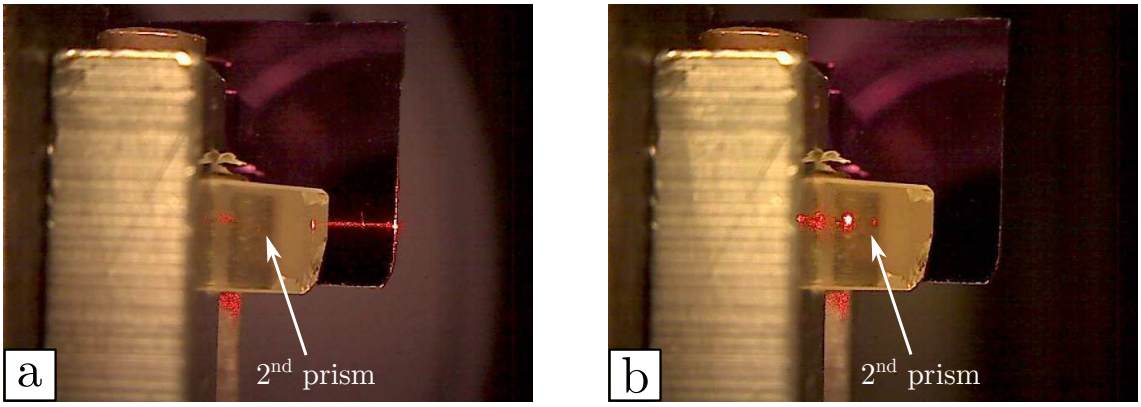

Figure 4.3 – (a) There is no contact between the waveguide and the second prism, so the light freely propagates in the waveguide by passing the prism. (b) The waveguide is pressed towards the prism by a screw, the contact is made good enough and the light is decoupled from the waveguide.

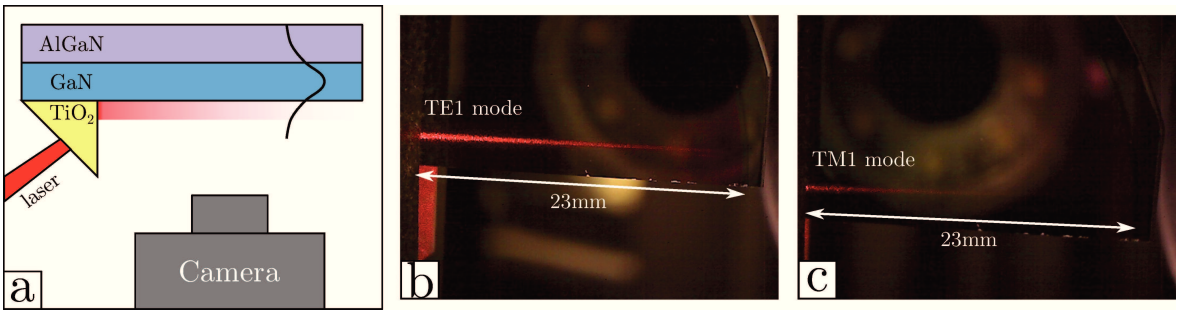

Figure 4.4 – (a) Scheme of the propagation losses measurement. (b) and (c) Uniform light scattering along the propagation lines for TE1 and TM1 modes.

Photonic Science camera. An example of such photo taken by the sCMOS camera is given in Fig. 4.5(a). It shows the light scattered along the 11mm propagation distance for the TE0 mode in the sample form Figs. 4.4(b) and (c).

From Fig. 4.5(a) one can see that the light scattering is mostly uniform with several local perturbations by point defects. Our loss estimation is based on the assumption that for the uniform scattering the intensity of the scattered light at a given point along the propagation line is proportional to the power confined inside the waveguide at this point. Therefore by measuring the rate at which the intensity of the scattered light decreases along the propagation line we can estimated the actual propagation losses in the waveguide.

In order to estimate the propagation losses the photos taken by the sCMOS camera were analysed in a Matlab program. Each photo represents 1824x1080 matrix of pixels with values between 0 and 70000. With the help of the program the propagation beam can be located as it is shown in Fig. 4.5(b). Then the part with a uniform scattering can be selected, by eliminating the segments with the point defects in the beginning and the end of the propagation line, see Fig. 4.5(c). For the loss estimation in the extracted beam the pixel values in the direction perpendicular to the propagation line were summed and

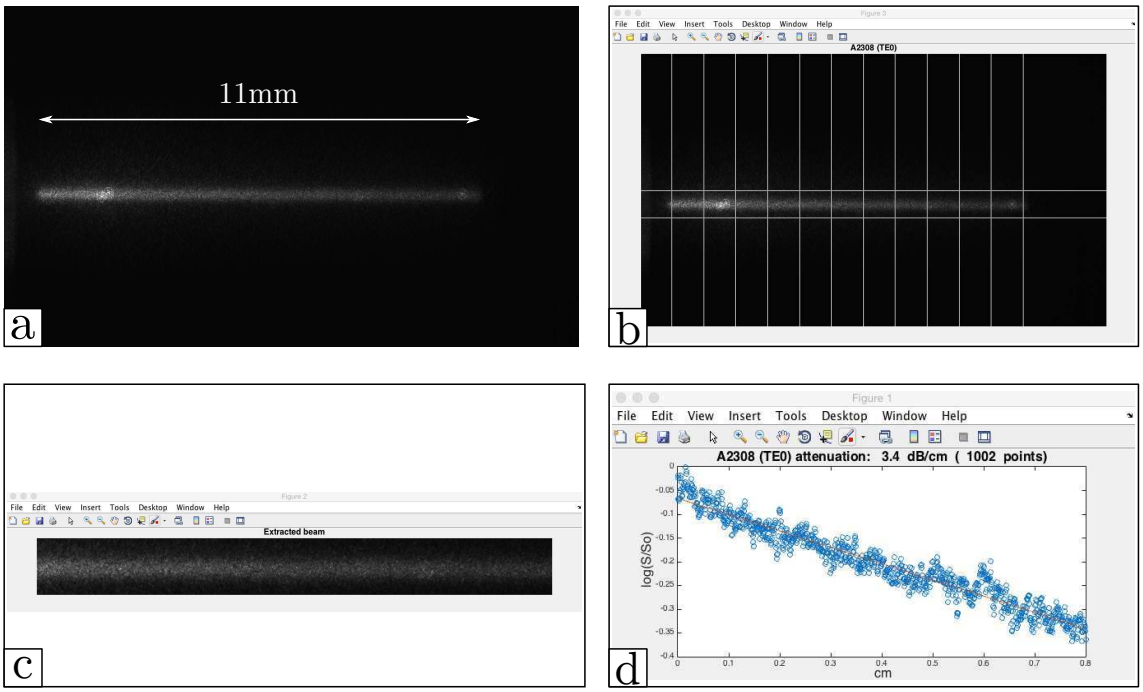

Figure 4.5 – (a) Image of the propagation line taken by the sCMOS camera. (b) Localization of the propagation line in the Matlab program. (c) Extracted beam. (d) Log-linear plot of the intensity attenuation with the propagation distance.

the obtained values were traced as a function of the propagation distance in the log-linear plot in Fig. 4.5(d). The obtained data follow very well an exponential decay and the slope of the fit line in Fig. 4.5(d) gives the estimate for the propagation losses. In order to get a statistical variation the losses were typically measured in different places on a sample.

4.2 Nonlinear characterization of waveguides

The main nonlinear process that was studied in this work was the second harmonic generation (SHG). In all the SHG experiments the power conversion was performed between the near-infrared and the visible spectral regions. We have used an NT242 OPO source from EKSPLA company as the pump source in the near-infrared. In the 1100-1400nm spectral region this tunable laser was emitting pulses with around 50μJ energy, 4ns pulse duration and 1000Hz repetition rate, although only a small fraction of the maximal pulse energy was used for the nonlinear experiments. For the average power measurements OP-2 VIS and OP-2 IR high-sensitivity semiconductor sensors were used. For the measurements of the pulse energy in the pulse by pulse regime J-10SI-HE and J-10GE-HE quantum EnergyMax sensors were used. Both the sensors (for the average power and the pulse energy) were from Coherent company. The mode images were done with the help of sCMOS and SWIR cameras from Photonic Science company.

4.2.1 Second harmonic generation in planar waveguides

The scheme of the experimental set-up used for the second harmonic generation in planar waveguides is shown in Fig. 4.6(a). Planar waveguides don't have any lateral confinement, therefore the pump is focused before the injection, in order to benefit from a higher power density. The pump is injected in the planar waveguide by using the standard prism-coupling technique described above. The injection by this technique in the infrared region is challenging, but fortunately we were using a tunable laser source for our experiments. In this case the simplest way to reach the injection of the infrared light is to start from the injection of the visible light and then tune the wavelength together with the injection parameters to slowly change the spectral range.

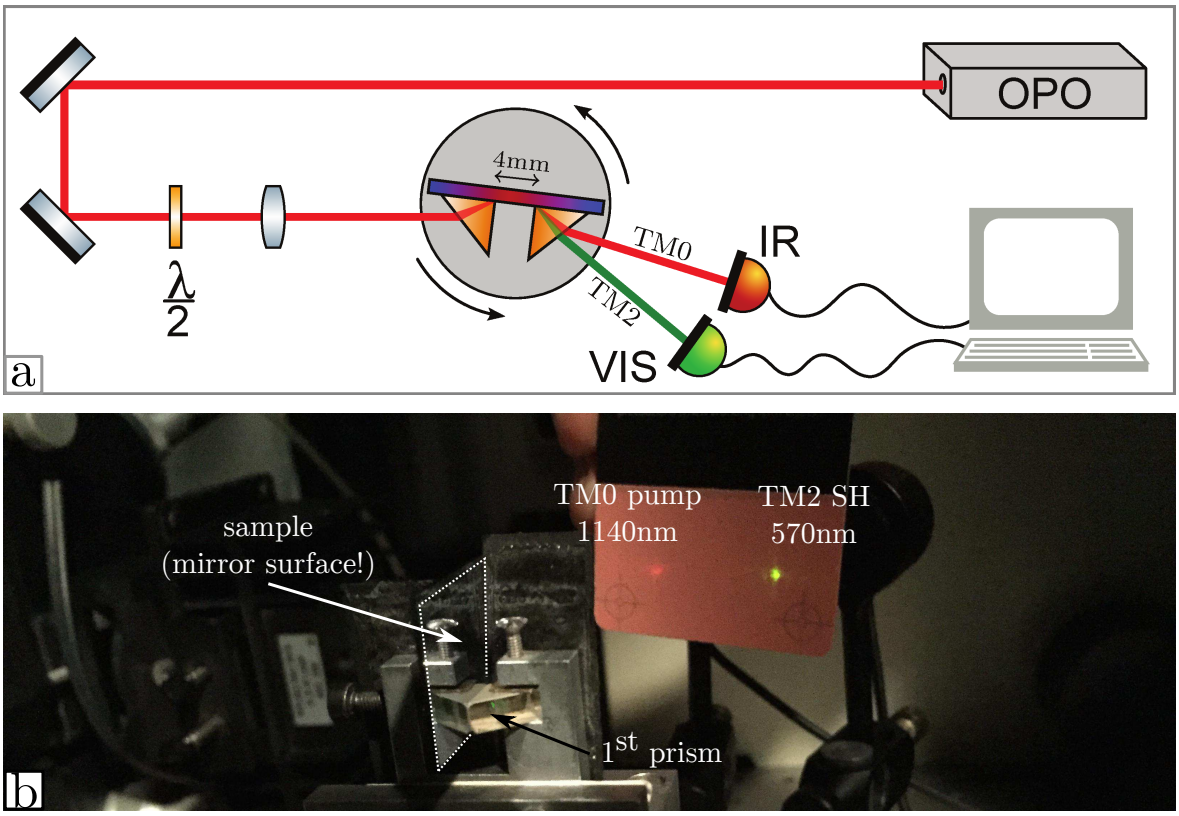

Figure 4.6 – (a) Scheme of the SHG experiment for the planar waveguides. (b) Photo of the pump and the second harmonic decoupled from the waveguide.

Once injected, the pump propagates along distance of several millimetres. If the phase matching condition are reached the second harmonic generation occurs. In our experiments we were typically using the modal phase matching between the TM0 pump and the TM2 second harmonic. The pump and the second harmonic are decoupled by the second prism at different angles. Although the effective refractive indices for the pump and the second harmonic are the same due to the phase matching conditions, the decoupling angles are actually different. This happens due to the fact that the refractive index of the prism in the formula (4.2) is different for two different wavelengths in this case. An example of an image from a real experiment is shown in Fig. 4.6(b). After the decoupling the signals are sent to the respective detectors for further measurements. For the SHG experiments we were typically doing two main measurements. We were

measuring acceptance curves which give the second harmonic signal as a function of the pump wavelength. In addition, the energy of the second harmonic pulses were measured as a function of the energy of the pump pulses in order to estimate the SHG efficiency. The specific plots and result of these measurements will be presented in the next chapters.

4.2.2 Second harmonic generation in ridge waveguides

The scheme of the experimental set-up used for the second harmonic generation in ridge waveguides is shown in Fig. 4.7(a). Before the injection the diameter of the pump beam is reduced to match the opening of the objective. The light is coupled to the ridge waveguide by a Mitutoyo objective (M Plan Apo NIR x50) with a 17mm working distance. Typically the second harmonic generation was based on modal phase matching between the TM00 pump and the TM20 harmonic. An image of the second harmonic signal that was generated after 4mm propagation distance is shown in Fig.4.7(c). The pump and the second harmonic are collected by the second Mitutoyo objective (M Plan Apo NIR x100) with a 12mm working distance. Both the light coupling and collection are controlled by the XYZ alignment stages shown in Fig. 4.7(b). The pump and the second harmonic are separated and sent by a system of mirrors to either cameras or detectors. The cameras were used for the modes imaging, see Figs. 4.7(d) and (e). The detectors were used either for the acceptance curve measurements or for the efficiency estimations. Particular examples of these measurements will be presented later in the manuscript.

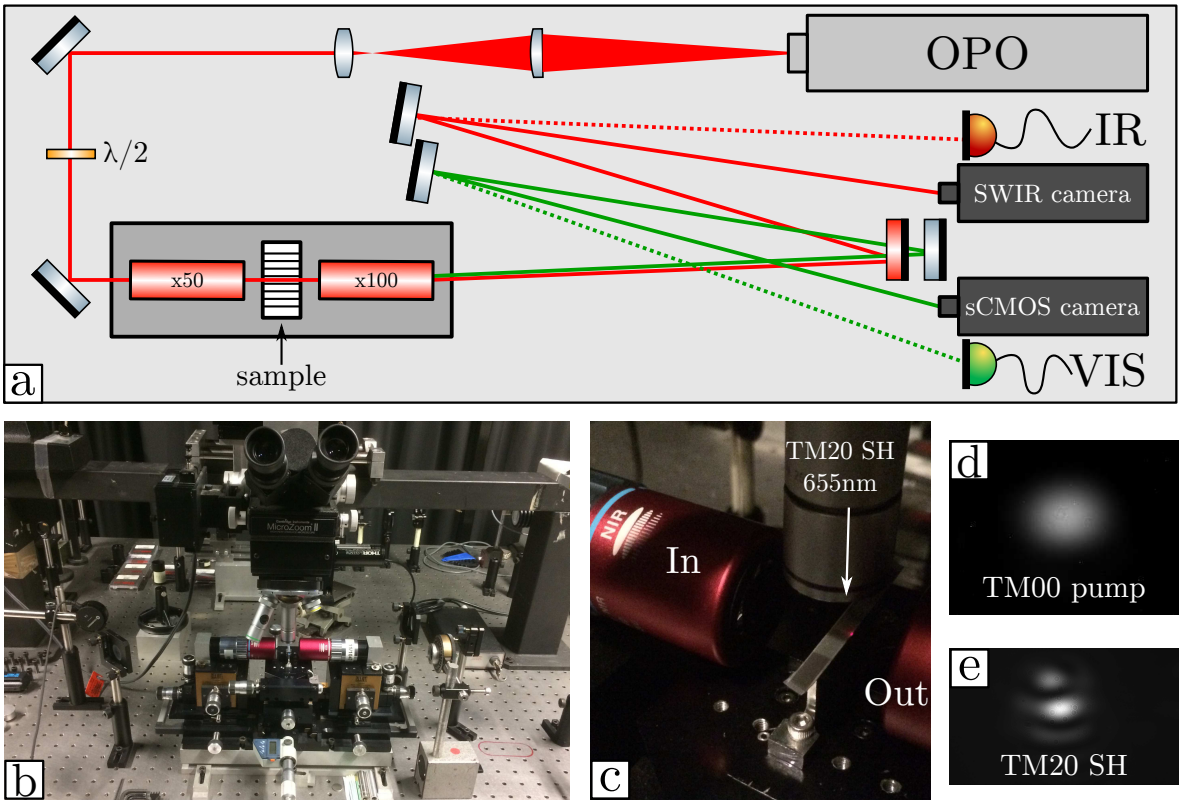

Figure 4.7 – (a) Scheme of the SHG experiment for the ridge waveguide. (b) Photo of the injection platform (c) Second harmonic signal at 655nm wavelength. (e) and (d) Examples of images for the TM00 pump and the TM20 second harmonic.

Chapter 5

Waveguides on sapphire substrates

III-V nitrides are mainly grown in the form of thin films by metalorganic vapour phase epitaxy (MOVPE) or by molecular beam epitaxy (MBE) on sapphire or silicon substrates. Sapphire substrates seem to be a more natural choice for the fabrication of AlGaN based waveguides for integrated nonlinear optics, since sapphire has a large transparency window spanning from 200nm up 5μm, a high damage threshold and a refractive index that is lower than that of AlGaN semiconductors. The large transparency window of sapphire almost matches that of AlGaN which allows revealing all the potential of III-V semiconductors and realizing nonlinear interactions anywhere from the ultraviolet up to mid-infrared spectral regions depending on a particular application. The high damage threshold is very important since one often requires high power densities to realize efficient nonlinear processes. The fact that sapphire has lower refractive index than AlGaN (1.75 against 2.34 at 1μm wavelength) is crucial for the fabrication of waveguides based on total internal reflection, moreover the high index contrast of 0.6 allows to exploit a high modal dispersion and perform modal phase matching by using interactions between different modes in multi-modes waveguides.

Nevertheless, sapphire has also several disadvantages. The high index contrast between GaN and sapphire leads to relatively thin ($<$1μm) guiding layers and the growth of thin high quality layers is a challenging task due to the lattice mismatch between GaN and sapphire. In addition sapphire is a very hard material and it turns out to be fairly difficult to etch, slice and polish sapphire substrates. Slicing, polishing, wafer bonding and even substrate removal are often an important part of waveguide fabrication procedures and therefore one can encounter some additional technological challenges due to the hardness of sapphire substrates.

This chapter describes an evolution in chronological order of AlGaN based waveguides on sapphire substrates. The ultimate goal was to fabricate AlGaN waveguides adapted to second harmonic generation with as low propagation losses as possible. The section 5.1 naturally presents the simplest version of GaN waveguides directly grown on sapphire substrates. High propagation losses and possible origins of theses losses are discussed here in details. The section 5.2 demonstrates the evolution of the optical buffer layer from a simple AlN cladding to a more complicated AlN/AlGaN cladding. These buffer layers have allowed to reduce the propagation losses by isolating the modes guided in GaN layer form the highly perturbed nucleation layers near the substrate and the sapphire substrate itself. The sections 5.3 and 5.4 combine both theoretical and experimental results, showing that the surface roughness has a significant impact on the propagation

losses. Here it is demonstrated that by reducing the surface roughness and by using AlGaN optical cladding layer one can fabricate GaN waveguides with propagation losses below 1dB/cm in the visible spectral region. These planar waveguides were used to perform efficient second harmonic generation experiments from the near-infrared to the visible spectral regions with a power conversion reaching 2%; the summary of these experiments are given in the section 5.5. The sections 5.6 and 5.7 describe the first tests and challenges linked to ridge waveguides fabrication and planar polarity inversion, the goal of which is to increase the efficiency of the second harmonic generation. At the end of this chapter conclusions and future perspectives are discussed.

5.1 GaN/sapphire planar waveguides

This section presents the simplest case of GaN waveguides directly grown on sapphire substrates. As it is shown below, in this case it is possible to fabricate waveguides adapted for the second harmonic generation based on the modal phase matching, but these waveguides show rather high propagation losses going above 10dB/cm in the visible spectral region. These high propagation losses have a drastically negative impact on the nonlinear conversion efficiency and prevent from performing measurements of the second harmonic generation with the experimental set-up sensibility accessible in this study. Nevertheless this section summarizes the linear characterization results for two GaN waveguides grown by MBE and MOVPE techniques. The comparison of the results for these waveguides allows to underline an important difference between the layers grown by MBE and MOVPE techniques; this comparison also gives a first indication of the possible sources of propagation losses such as the surface roughness of the waveguides and the low quality nucleation layers at the interface between GaN and sapphire.

The two waveguides presented below are both grown on sapphire substrates and have 1μm thick guiding layer. For the simplicity we use the reference numbers that were attributed to these samples according to our laboratory classification, namely N2121 for the waveguide grown by MBE technique and G3289 for the waveguide grown by MOVPE technique. N2121 sample was grown in the MBE reactor, where first a 30nm GaN nucleation layer was deposited at 450 °C followed by 970nm layer grown at 800 °C. G3289 sample was grown in a MOPVE reactor at 1080 °C.

The 1μm thick GaN guiding layer for N2121 and G3289 waveguides was chosen to allow for modal phase matching between the TM0 pump in the near-infrared and a higher order mode (TM1, TM2, TM3 or TM4) in the visible. The overall waveguide structure and the TM-modes profiles at 633nm wavelength are shown in the Fig. 5.1. The modal phase matching occurs at a different wavelength for each different mode combination. The summary of possible solutions for the second harmonic generation in a 1μm planar GaN waveguide on a sapphire substrate is presented in Table 5.1.

The realization of an efficient SHG requires low propagation losses for the high order TM-mode in the visible spectral region. Therefore, in order to estimate the propagation losses, a linear characterization of the N2121 and G3289 waveguides was performed using the experimental setup using an He-Ne laser at 633nm and described earlier in Section 4.1.2. According to the modelling a 1μm GaN waveguide on a sapphire substrate supports 5 TE and 5 TM modes. In practice it was possible to get a visual confirmation of the light injection only in the first and the second order TE and TM modes. The rest of the

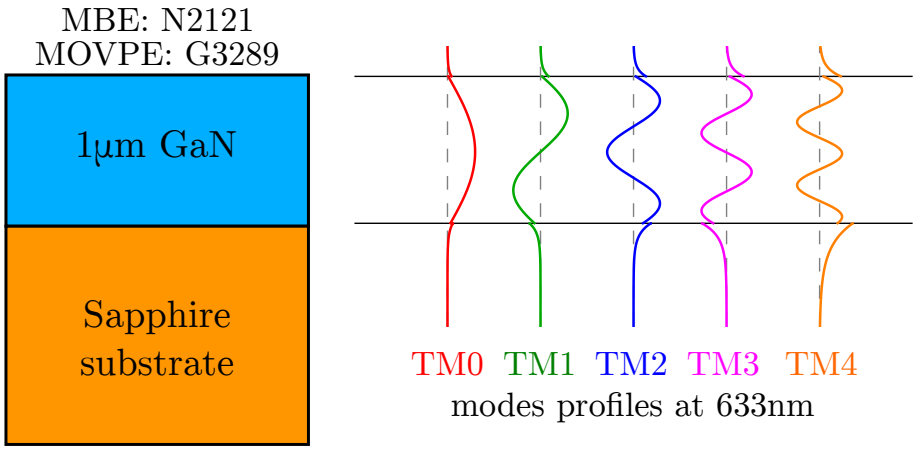

Figure 5.1 – A scheme of two planar waveguides that are presented in this section together with the TM-modes profiles at 633nm wavelength. Both waveguides have 1μm GaN guiding layer thickness. N2121 waveguide was grown by MBE technique. G3289 waveguide was grown by MOVPE technique.

Modes combination	TM0 pump TM1 SH	TM0 pump TM2 SH	TM0 pump TM3 SH	TM0 pump TM4 SH
SH wavelength	985nm	566nm	470nm	423nm

Table 5.1 – The second harmonic (SH) wavelengths that can be generated by using modal phase matching in 1μm GaN waveguide on a sapphire substrate. When the pump is injected in the fundamental TM0 mode, the second harmonic can be generated in the higher order TM1, TM2, TM3 and TM4 modes.

modes could not be observed due to over increasing propagation losses. As one can see from the Table 5.2 the losses were already high for the fundamental TE0 and TM0 modes, reaching 20 dB/cm for the MBE grown sample. Moreover, it was impossible to make a reliable estimation of even larger propagation losses for the higher order modes due to the setup limitations.

Sample	MBE: N2121		MOVPE: G3289	
Mode	TE0	TM0	TE0	TM0
Losses (dB/cm)	20±4	17±4	11±2	11±2

Table 5.2 – Propagation losses measured in dB/cm for the fundamental TE0 and TM0 modes for N2121 and G3289 waveguides. The errors estimation includes losses variation depending on the position on a given sample and ±1mm uncertainty in the propagation distance measurement.

Figures 5.2(a)-(c) show saturated images of the light diffused along the propagation lines. Two important facts should be underlined here. First, the propagation losses of the MBE grown sample were higher than those of an equivalent sample grown by MOVPE technique. And second, there was a rapid increase of the propagation losses with the mode order for both samples. A comparison of the Figs. 5.2(b) and 5.2(c) clearly shows this rapid increase: as the TE0 mode propagates almost 12mm with 10dB/cm loss, the

TE1 mode in the same sample propagates only a few millimetres with over 20dB/cm loss.

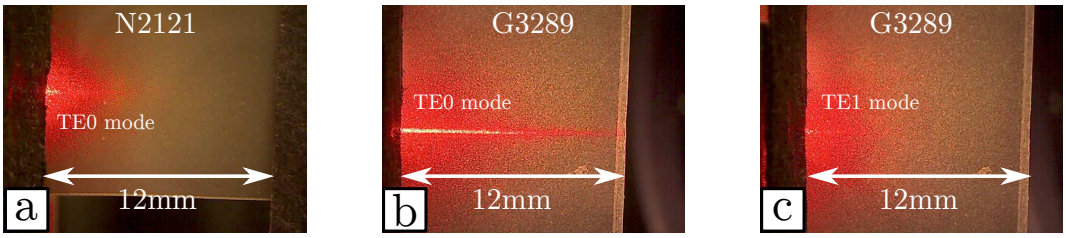

Figure 5.2 – (a) A saturated image of the light diffused along the propagation line for the TE0 mode in the N2121 sample. (b),(c) The same images for the TE0 and TE1 modes in the G3289 sample.

It is commonly known that with the high order modes are less confined in the guiding layer. In our case the higher order modes have a larger power percentage guided near the interfaces, in the air and in the sapphire substrate, see Fig. 5.1. Since the propagation losses also increase with the mode order it would be logical to assume that the GaN/air and GaN/sapphire interfaces could be the main sources of these losses. The GaN/sapphire interface contains many defects due to the lattice mismatch. As it was noted by many authors, these defects definitely contribute to the propagation losses although a theoretical model which provides a good quantitative description of this effect has not been proposed yet. The situation is opposite for the case of the surface roughness. The surface roughness can be easily measured by atomic force microscopy (AFM) and there are numerous theoretical models which allow calculating the impact of the surface roughness on the propagation losses. Despite these facts, there are only a few studies of the propagation losses in AlGaN waveguides and the impact of the typical surface roughness of MBE and MOVPE grown AlGaN waveguides has not been fully revealed yet..

Figures 5.3(a) and 5.3(b) show AFM scans of the surfaces for N2121 and G3289 waveguides. These images clearly show the different typical surface roughnesses observed for MBE and MOVPE grown waveguides respectively. An exponential fit $\sigma^2 \exp(-r/\Lambda)$ of the radial autocorrelation functions for these surfaces is used in order to characterize both the root mean squared amplitude (rms, σ) and the lateral scale Λ of the roughness. The numerical values for these parameters are given in the table attached to the Fig. 5.3. As one can see from this table, the σ amplitudes for the two samples are almost the same, while there is a big difference in the characteristic lateral scale values of Λ for the MBE and MOVPE surfaces. The surface roughness of GaN layers is closely related to the Ga atom mobility during the growth. The amplitude σ of this roughness increases with the thickness of the grown layer and the characteristic lateral scale Λ of this roughness is determined by the Ga diffusion length and thus by the growth temperature [38]. The difference in the temperature of growth, which is 800 °C for MBE and 1080 °C for MOVPE, explains the difference in the characteristic lateral scale Λ for the two surfaces.

Later in the section 5.3 it will be shown that for MBE grown samples, the small lateral scale Λ and thus high spatial frequencies of the surface roughness is responsible for the coupling between the guided and the radiated modes. This coupling makes a major contribution to the propagation losses. On the other hand, the lower spatial frequencies of the surface roughness in MOVPE grown samples is responsible for the coupling between

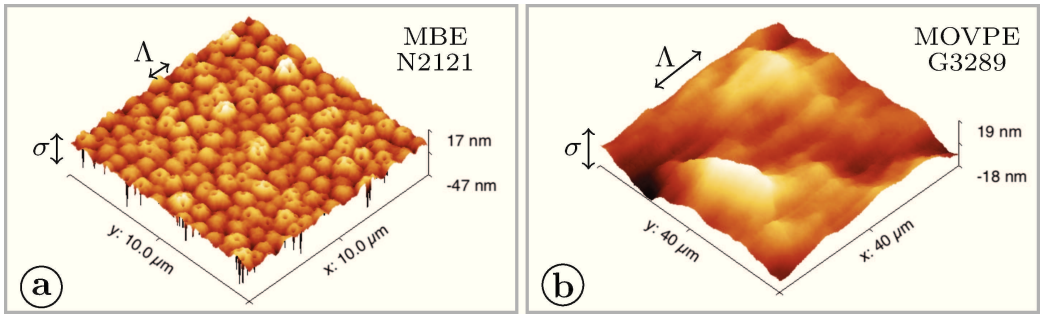

sample	epitaxy	rms, σ	Λ
N2121	MBE	4.1nm	0.17μm
G3289	MOVPE	5.2nm	6μm

Figure 5.3 – (a) An AFM image of 10μm by 10μm surface area for N2121 sample grown by MBE technique. (b) A similar 40μm by 40μm AFM scan for G3289 sample grown by MOVPE. The roughness amplitude σ and the characteristic lateral scale Λ are determined from an exponential fit $\sigma^2 \exp(-r/\Lambda)$ of the autocorrelation function for the surfaces. The table attached to this figure summarizes the numerical values of σ and Λ for these two samples.

guided modes propagating in slightly different directions; this effect creates a mode diffusion in the plane of the planar waveguide. It should be noted that the roughness difference for N2121 and G3289 samples cannot explain the whole 9dB/cm and 6dB/cm losses difference in the propagation losses for the TE0 and TM0 modes respectively. The coupling between the guided and the radiation modes induced by the N2121 surface roughness can contribute only up to 2dB/cm to the propagation losses for the fundamental modes. The rest of the difference can probably be explained by the overall lower than average material quality of N2121 sample, which can clearly be seen from the higher than usual density of nanometre scale holes in the Fig. 5.3(a). Although 2dB/cm seams to be a reasonable value for the propagation losses, this value grows persistently with the mode order quickly overcoming 10dB/cm for the higher order modes. The same principle applies for the mode diffusion induced by the MOVPE surface roughness. This diffusion is almost negligible for the fundamental modes, but it becomes non-negligible for the higher order modes. Since the modal phase matching requires low propagation losses for the higher order modes, the losses induced by the surface roughness will clearly limit the SHG efficiency.

In conclusion, this section presents the characterization results for two GaN waveguides grown directly on the sapphire substrate by MBE and MOVPE techniques. This characterization allowed to identify two main sources of propagation losses, namely the low quality of the GaN layer near the GaN/Sapphire interface and the typical surface roughness for the MBE and MOVPE techniques. The sections below will address theses issues and will present several solutions allowing to reduce the propagation losses.

5.2 AlGaN optical cladding

In the previous section the low quality GaN layer near the GaN/Sapphire interface was identified as one of the main sources of the propagation losses. The current section describes one possible solution which allows reducing the influence of this layer on the modes guided in GaN. This solution consist in growing an optical cladding layer with a refractive index lower than that of GaN. Naturally AlGaN turns out to be a perfect material for the optical cladding in this case. AlN has a lower refractive index than GaN (2.1 against 2.34 at 1μm wavelength) and the refractive index of $Al_xGa_{1-x}N$ continuously varies with the Al content x between GaN and AlN indices. Moreover, a 0.24 refractive index contrast is still enough to to fulfill the phase matching condition for second harmonic generation using the modal dispersion of GaN/AlGaN waveguides where GaN serves as a guiding layer and AlGaN serves as a cladding. In this configuration a mode guided in GaN has only a small overlap with the sapphire interface through the mode evanescent tale; this drastically reduces the impact of the low quality layers on the propagation losses.

In theory, the simplest solution would be to use an AlN layer as an optical cladding. In practice, the samples were grown by the MBE technique and a direct growth of AlN on sapphire substrates was not optimized in our laboratory at the time when this work was performed. The growth had to be initiated with a low temperature GaN layer, followed by the growth of a relatively thick AlN optical cladding in which appear numerous cracks due to the tensile stress caused by the fact that AlN has a smaller lattice parameter than GaN. Obviously, numerous cracks are not compatible with the goal to fabricate a low-loss waveguide where modes could propagate on a several centimetres distance. Fortunately, a relatively simple solution to this problem was found. It turns out that, under proper conditions, a subsequent growth of AlGaN layer on top of the AlN layer can cover up the cracks and block their propagation to the next epitaxial layers. Indeed, AlGaN is grown in this case, under compressive strain, since it has a larger lattice parameter than AlN and thus grows without cracking. Furthermore, some lateral growth within the cracks tends to fill them up, so that cracks are barely visible at the end of the process. By using a relatively thick $\sim 1\mu$m AlGaN layer it was possible to obtain crack-free optical cladding for further GaN guiding layers. Therefore this approach with combined AlN/AlGaN optical cladding was used during this work.

5.2.1 Monomode GaN/AlGaN waveguide

In the beginning, we fabricate a monomode GaN waveguide at 633nm in order to test the AlN/AlGaN optical cladding. The meaning of the slightly misused *monomode* term will be explained below. The scheme of this waveguide, named N2239 accordingly to the laboratory classification, is shown in Fig. 5.4. The optical cladding consisted of a 125nm AlN layer which had some internal cracks and a 1μm $Al_{0.65}Ga_{0.35}N$ layer which was crack-free. The thickness and the Al percentage for the AlGaN layer were chosen in order to get the necessary optical isolation and to have a big enough index contrast compared to GaN, to allow satisfying the phase matching condition using the modal dispersion. The 500nm thickness of the GaN layer was chosen in order to support only one guided TM-mode (and one TE-mode) highly confined in this layer. Indeed, as it is shown in Fig. 5.4 only the TM0 mode is highly confined (more than 93% of modal power at 633nm) in the GaN layer, while the higher order modes TM1, TM2, TM3 are mainly confined in the AlGaN optical

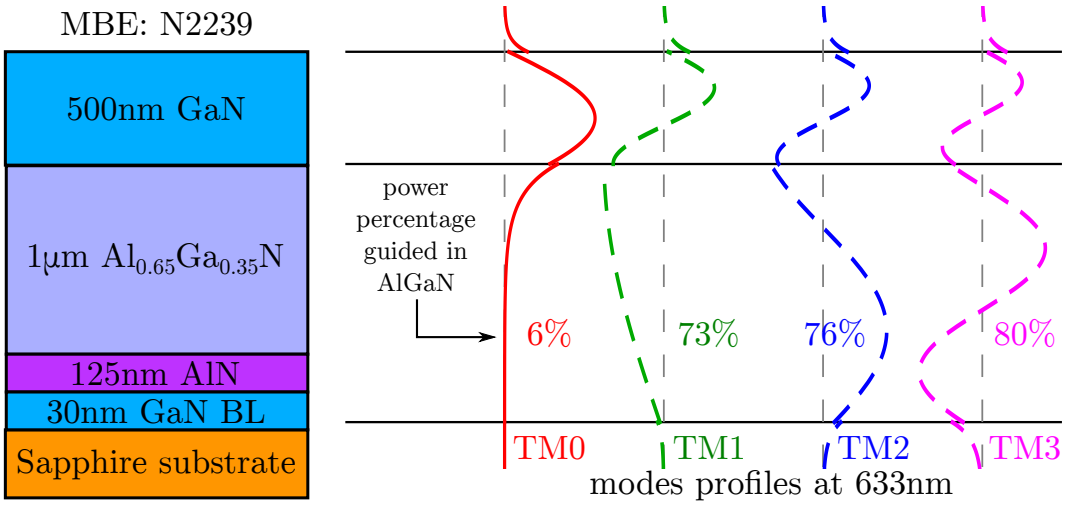

Figure 5.4 – A scheme of the N2239 planar waveguide grown by the MBE technique together with four TM-modes profiles at the 633nm wavelength. The 125nm AlN layer contains numerous cracks, which are covered by the 1μm AlGaN layer. This relatively thick AlGaN layer isolates the TM0-mode from the negative impact of the cracks and from the low-quality layers near the sapphire interface. This isolation works only for the TM0-mode, since 93% of the fundamental mode is guided in the GaN layer, while almost all power of the higher modes is concentrated in the AlGaN layer.

cladding. It should be noted that a 510nm GaN thickness corresponds to the TM1-mode cut-off in a three layer air/GaN/$Al_{0.65}Ga_{0.35}N$ waveguide at 633nm. Although it is true that the whole structure grown on a sapphire substrate supports multiple guided modes, we use the term *monomode* considering only the GaN guiding layer and addressing AlGaN as a new substrate.

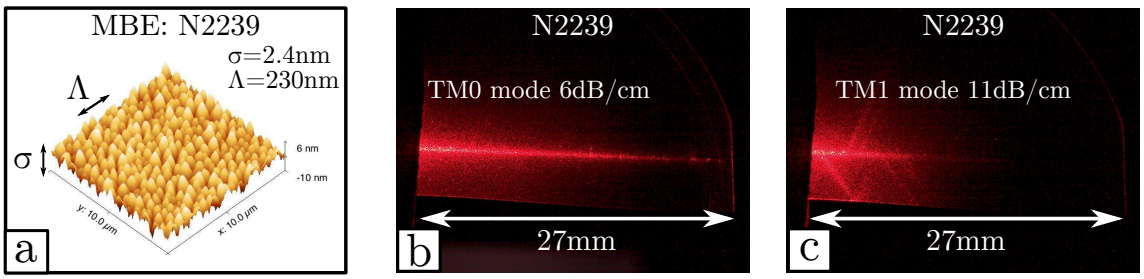

Figure 5.5 – (a) An AFM image of 10μm by 10μm surface area of the N2239 sample grown by MBE. The surface morphology is typical for the MBE growth. The roughness amplitude is 2.4nm and the characteristic lateral scale is around 230nm. (b) and (c) Saturated images of the light diffused along the propagation lines for the TM0 and TM1 modes. The TM0 mode is mainly localized in the GaN layer and not impacted by the buried cracks and the low quality sapphire interface. It contrast, about 70% of the TM1 modal power is guided in AlGaN layer, so the propagation of this mode is strongly impacted by the above mentioned defects. As a consequence, the TM1 mode has two times larger propagation losses than the TM0 mode and a clear patten of the light scattering on the cracks is visible in the Fig. (b).

The AFM scan in Fig. 5.5(a) shows that the nanometre hole defects were eliminated in the N2239 sample. In addition, in comparison with the N2121 sample presented in the previous section, this sample shows a surface roughness presenting more or less the same lateral scale Λ but a smaller amplitude σ. The smaller amplitude σ was expected since N2239 sample has a thinner GaN layer than the N2121 sample and it is known that the amplitude of the surface roughness develops mainly during the growth of GaN layer and increases with its thickness.

Both the reduced surface roughness and the optical cladding layer had a positive impact on the propagation losses as it is shown in Fig. 5.5(b). For the TM0-mode highly confined in GaN layer 6dB/cm propagation losses were measured at 633nm wavelength. The comparison with the results obtained with N2121 sample in Fig. 5.2(a) showed that using a cladding layer, can drastically improve the propagation losses. In should be noted that the 6dB/cm propagation losses in the visible spectral region were already at the state of the art for AlGaN semiconductors. It is important to underline that the situation was completely different for the case of the TM1-mode mainly confined in AlGaN layer. This mode was exposed to the cracks buried in the AlN layer and as a result a significant scattering and higher propagation losses were observed for this mode, see Fig. 5.5(c)

N2239 sample has shown the viability of this new approach based on the use of an AlN/AlGaN optical cladding layer. It was expected that by switching from the 500nm thick GaN layer to a 1200nm thick layer supporting three TM-modes highly confined in GaN, it would be possible to reach 6dB/cm losses for the TM2 mode and even smaller losses for the TM0 and TM1 modes at 633nm. In order to test this hypothesis two multimode GaN/AlGaN waveguides were fabricated. The results of their characterization are presented in the next section.

5.2.2 Multimode GaN/AlGaN waveguides

This section presents the characterization results for two multimode GaN/AlGaN waveguides. These waveguides were fabricated by two different approaches. The first waveguide N2291 was grown from bottom to top by the MBE technique, with the same structure as the N2239 sample, except the thickness of the GaN layer, which was thicker (1200nm). see Fig. 5.6. The second waveguide G3416 was identical to N2239, on top of which we added a 600nm thick GaN layer obtained by regrowth in a MOVPE reactor. The total thickness of the GaN layer in G3416 sample was 1100nm, see Fig. 5.7. The 1200nm GaN layer thickness corresponds to the TM3-mode cut-off for the air/GaN/$Al_{0.65}Ga_{0.35}N$ waveguide.

Due to resource limitations, we limited the number of epitaxial samples and tried to re-use them when possible. In this context, we re-use some samples after optical characterization and performed a second epitaxy on top of them. In addition to the reduction of epitaxy time, it also allows assessing the influence of the additional layer grown on top a known structure. The price to pay is the contamination at the regrowth interface, possibly including macroscopic defects. This was the case for the G3416/N2239 sample. Some additional defects were introduced at the regrowth interface, since it was very difficult to properly clean the samples after the optical characterization. It is interesting that two different fabrication approaches led to different characterization results. In this section we will gain some further insight on the origins of the propagation losses by comparing the results for N2291 and G3416 samples.

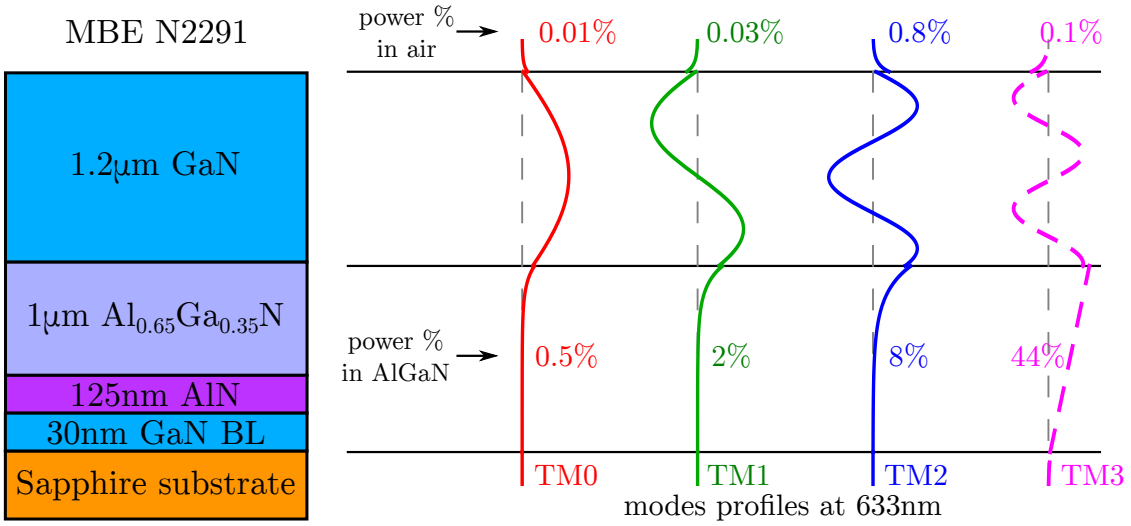

Figure 5.6 – A scheme of the N2291 planar waveguide together with four TM-modes profiles at the 633nm wavelength. This waveguides was grown by MBE technique. In this waveguide three guided modes (TM0, TM1 and TM2) are mainly confined in the GaN layer and thus isolated from the buried cracks and the low quality sapphire interface. The percentages indicate the parts of the modal power guided in the air and AlGaN layers for different modes. These percentages are used in the text to support the explanation concerning possible origins of the propagation losses

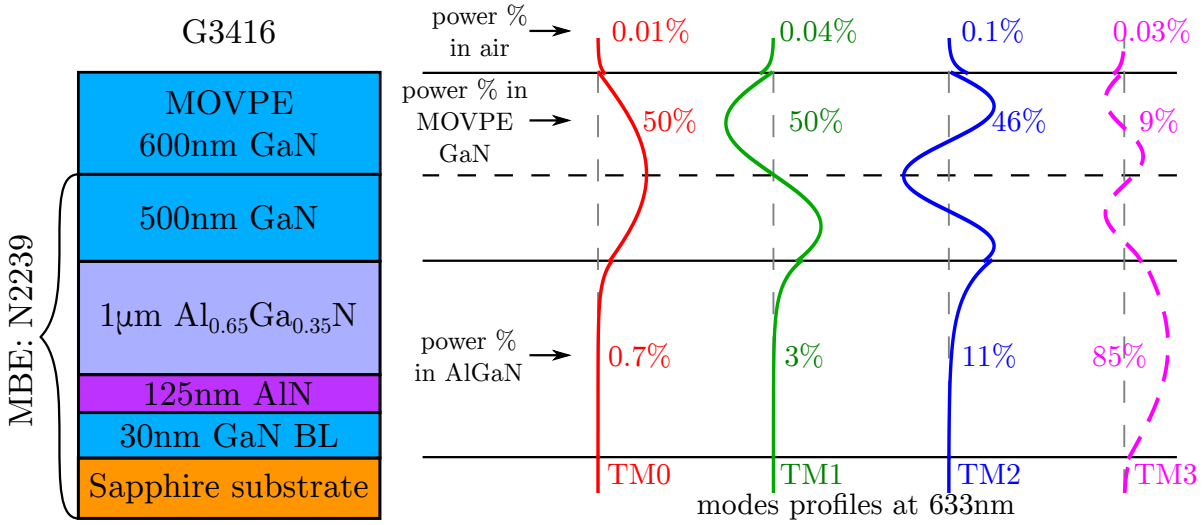

Figure 5.7 – A scheme of the G3416 planar waveguide together with four TM-modes profiles at the 633nm wavelength. This waveguide was grown starting from the N2239 waveguide by depositing 600nm GaN layer by MOVPE. In this waveguide already three guided modes (TM0, TM1 and TM2) are mainly confined in the GaN layer and thus isolated from the buried cracks and the low quality sapphire interface. The percentages indicate the parts of the modal power guided in the corresponding layer (air, MOVPE GaN and AlGaN) for different modes.

As it is shown in Fig. 5.6 the sample N2291 supports three TM-modes highly confined in the GaN layer. Moreover, the confinement of the TM2 mode in N2291 sample is close

Sample	MBE: N2291					
Mode	TM0	TM1	TM2	TE0	TE1	TE2
Losses (dB/cm)	7±1	13±3	16±3	10±1	19±3	-

Table 5.3 – Propagation losses in dB/cm for the TM- and TE-modes in N2291 waveguide. The errors estimation includes losses variation depending on the position on the sample and ±1mm uncertainty in the propagation distance measurement.

to the confinement of the fundamental TM0 in N2239 sample from the previous section. Therefore one would expect observing the same propagation losses for these two modes. But according to the measurements summarized in Table 5.3 this is not the case. The sample N2291 shows higher than expected propagation losses. For the fundamental TM0 mode we still got 7dB/cm and losses increase further up to 16 dB/cm for the higher order modes. One possible reason for this result is an increased amplitude of the surface roughness for N2291 sample, see Fig. 5.8. Indeed, as the thickness of the GaN layer increased from 500nm to 1200nm the amplitude of the surface roughness also increased from 2.3nm to 5.5nm. So we gained in the confinement of the fundamental mode but lost in the roughness amplitude and the losses for the fundamental mode remained at the same level. The fact that the losses increase for the higher order modes supports the idea that the main source of these losses comes from the interfaces. And the air/GaN interface should give a major interfaces. And the air/GaN interface should give a major contribution in this case because of its well known kinetic surface roughness and high refractive index contrast.

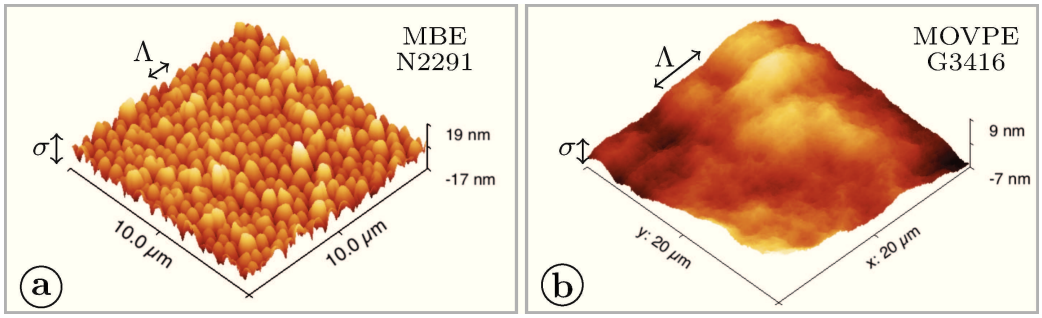

sample	epitaxy	rms, σ	Λ
N2291	MBE	5.5nm	0.15μm
G3416	MOVPE	2.3nm	3.5μm

Figure 5.8 – (a) An AFM image of 10μm by 10μm surface area of the N2291 sample grown by MBE technique. (b) A similar 20μm by 20μm AFM scan of the G3416 sample grown by MOVPE. The roughness amplitude σ and the characteristic lateral scale Λ are determined from the exponential fit $\sigma^2 \exp(-r/\Lambda)$ of the autocorrelation function for the surfaces. The table attached to this figure summarizes the numerical values of the σ and Λ parameters for two samples.

The main difference between N2291 and G3416 samples is the surface roughness. As it can be seen in Fig. 5.8 the MOVPE surface has a much larger lateral scale Λ in comparison with the MBE surface. The amplitudes σ remain comparable in both samples. It was impossible to make a reliable estimation of the propagation losses for G3416 sample due

to the large number of point defects which were revealed during the MOVPE regrowth. These defects were affecting the monotonous light diffusion along the propagation line based on which one could estimate the propagation losses. Nevertheless, by comparing the images of the mode propagation in Fig. 5.9 one could speculate that the propagation losses should be comparable in both samples for the fundamental TM0 mode, while for the higher order TM1, TM2, TM3 modes the sample G3416 should have lower propagation losses than the sample N2291.

At this point it is important to underline the differences observed for N2291 and G3416 waveguides during the optical characterization and relate them to the difference in the surface morphology for these samples. First, let us analyse the photos of the modes propagation in Fig. 5.9. For N2291 sample one can clearly see that the propagation distance rapidly decreases with the mode order: while the fundamental TM0 mode propagates over 12mm, the TM3 mode can hardly go further than a few millimetres, see Fig. 5.9(a)-(d). In contrast, there is no such big difference in terms of propagation distance for G3416 sample, see Fig. 5.9(e)-(h). More precise numerical analysis in the next section 5.3 will show that the small lateral scale $\Lambda \approx$150nm of the surface roughness for N2291 sample is responsible for the coupling between guided and the radiated modes, which is the main cause of propagation losses. Moreover, as it is shown in Fig. 5.6 the part of the modal power near the air/GaN interface gradually increases from 0.01% for the TM0 mode up to 0.1% for the TM3 mode. This means that the higher order modes are more exposed to the impact of the surface roughness and should present higher propagation losses, which is confirmed by the experiment.

In contrast, the much larger lateral scale $\Lambda \approx 3.5\mu$m of the surface roughness for G3416 sample cannot be responsible for the coupling between the guided and the radiation modes. That is why the propagation distance for all the modes in Fig. 5.2(e)-(h) remains more or less the same. Nevertheless, MOVPE-type surface roughness is responsible for another effect that can be observed in Fig. 5.10. This figure presents the photos of the light decoupled from the waveguides using a prism and projected on a screen placed around 15cm away from the sample. As we can observe for N2291 sample the light stays concentrated in one point for all modes. The brightness of this point naturally decreases as losses become bigger and less light is decoupled from the waveguide. In contrast, for the G3416 waveguide the change in the brightness of the decoupled light is less significant for different modes and in addition one can observe a significant diffusion of the light along the direction which corresponds to the plane of the waveguide, see Fig. 5.10(e)-(h). Indeed, as the TM0 mode stays concentrated almost in one point the light for the TM2 is spread over 4cm on the screen. The next section 5.3 will show that the roughness with a lateral scale of a few micrometres is responsible for the in-plane diffusion of the guided modes towards slightly different directions, but keeping the same mode order, as observed during the experiments. As shown in Fig. 5.7, the part of modal power near the air/GaN interface increases from 0.01% for the TM0 mode up to 0.1% for the TM2 mode. As a result the TM2 mode is more exposed to the surface roughness and shows more diffusion. A very peculiar thing happens with the TM3 mode. From Fig. 5.7 we see that this mode is mainly confined in the AlGaN layer and its power percentage guided near the air/GaN interface drops to 0.03%. As a result the TM3 mode becomes less exposed to the surface roughness than TM2 mode, so it should show less light diffusion, which is confirmed by part (h) in Fig. 5.10.

In addition we would like to discuss some alternative explanation about possible

sources of the observed light diffusion. One can argue that this light diffusion may be induced by some particular properties of the whole 600nm MOVPE layer, or defects on MBE/MOVPE interface which appeared during the regrowth. This cannot explain the monotonous increase of the light diffusion for the TM0-TM2 modes, since the part of the modal power guided in the MOVPE layer is almost the same for all three modes, and the part near the MBE/MOVPE interface is almost the same for the TM0 and TM2 modes and nearly equal zero for the TM1 mode, see Fig. 5.7. To conclude we would like to note that although the light diffusion seems to be less harmful than propagation losses, it starts to play its negative role in the second harmonic generation experiments based on modal phase matching. Typically one would like to use TM0-TM2 mode conversion in these experiments, but it turns out that the spread angle of the light diffusion is large enough to violate the phase matching condition for the diffused light, which obviously would reduce the SHG efficiency.

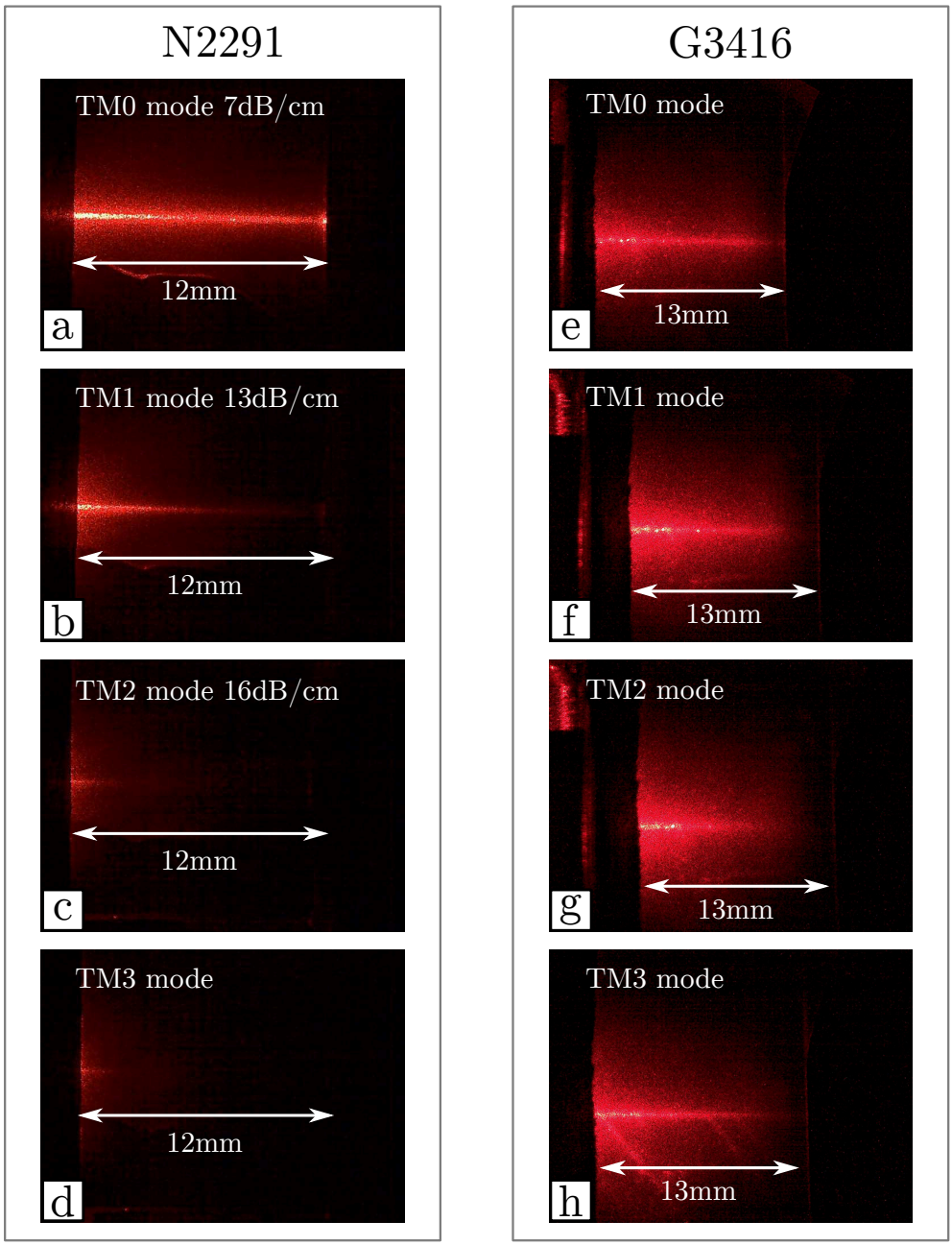

Figure 5.9 – (a)-(d) Saturated images of the light diffused along the propagation lines of TM0-TM3 modes in the N2291 sample. (e)-(h) The same images for the G3416 sample. In comparison with G3416 sample, the N2291 sample shows both more intense light scattering towards the camera and more drastic increase in the propagation losses for the higher order modes. It was impossible to estimate propagation losses for the G3416 sample due to the numerous point defects which appeared after MOVPE regrowth and which intensively scatter the light and perturb the measurement. Nevertheless, these images clearly show longer propagation distances for the corresponding modes in the G3416 sample in comparison with N2291 sample.

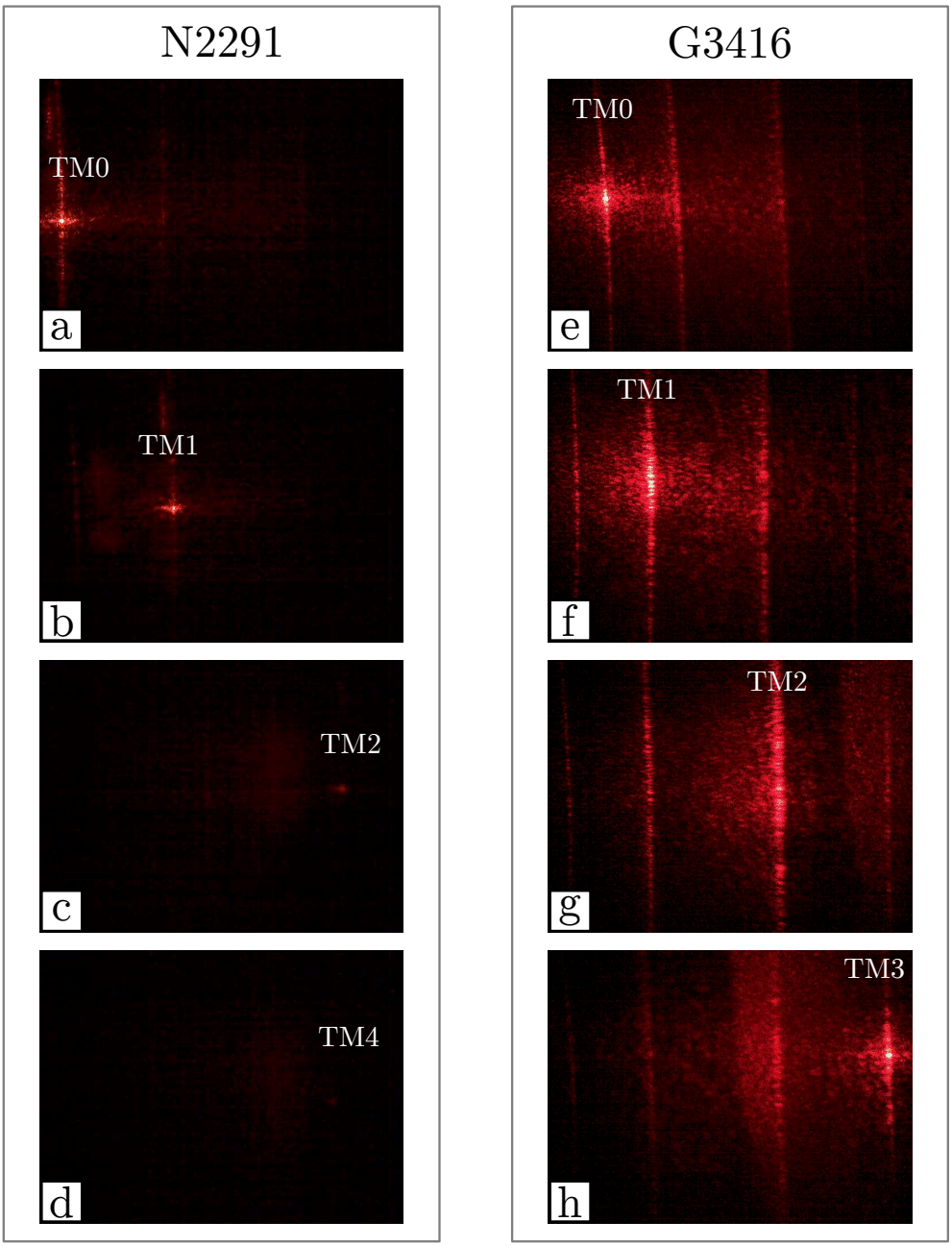

Figure 5.10 – (a)-(d) Saturated images of the m-lines for the N2291 sample with the light injection in the modes TM0 in part (a), TM1 in part (b), TM2 in part (c) and TM3 in part (d) respectively. (e)-(h) The similar images for the G3416 sample. Some residual inter-modal coupling is visible on all the images. For the N2291 sample, as one goes from the fundamental mode TM0 to the higher order modes, the light intensity of the m-lines decreases. In contrast, for the G3416 sample the m-lines becomes more diffused for the higher order modes, except the TM3 mode in part (h). This difference can be explained by the difference in the surface morphology for the two samples.

5.3 Impact of the surface roughness

This section gives a more detailed description of the surface roughness influence on the modes propagation in waveguides. Some numerical estimations of the losses and the diffusion described in the previous section 5.2 are presented here. The goal of this chapter was not to develop a rigorous theoretical analysis of these effects, but to give some rough numerical estimations showing a qualitative agreement between the theory and the experiment.

5.3.1 MBE surface

First we would like to estimate the impact of an MBE-type surface roughness on the propagation losses. As an example we will consider the N2291 sample which was presented in the previous section 5.2. As a basic numerical model we will take the analytical model for the losses induced by the coupling between the guided and the radiated modes due to the sinusoidal perturbation of the waveguide surface developed by Marcuse [39]. The rather cumbersome formulas for this model were developed only for the case of TE modes coupling to the substrate radiation modes. Therefore here we present the estimations only for this case in order to show only the order of magnitude for the propagation losses which can be induced by the typical MBE surface.

In order to use Marcuse model several surface profiles were extracted from the AFM scan for N2291 sample. A typical example of such a profile is shown in Fig. 8.4(a) by the blue dotted curve. Further an approximation of this profile by Fourier series was

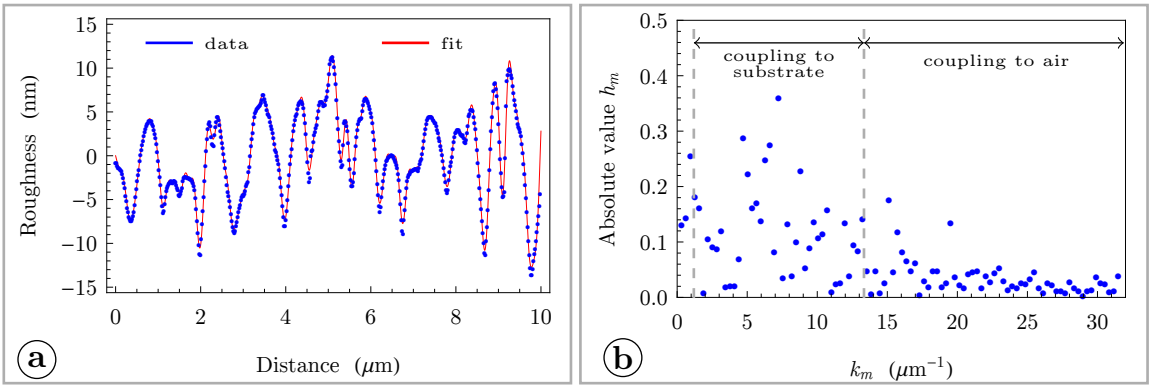

Mode	TE0	TE1	TE2
Loss to substrate	2±0.5 dB/cm	10±2 dB/cm	23±6 dB/cm

Figure 5.11 – (a) A typical surface profile for N2291 sample; the blue dotted curve shows the experimental data and the red solid curve shows the approximation with the Fourier series. (b) Absolute values of the decomposition coefficients h_m as a function of spatial frequencies k_m. The table attached to this figure summarizes the numerical values of the propagation losses induced by the coupling between the guided modes and the substrate radiation modes.

developed in the following form:

$$\text{fit} = \sigma \sum_{m=1}^{\infty} h_m \sin\left(\frac{\pi m x}{L}\right) = \sigma \sum_{m=1}^{\infty} h_m \sin\left(k_m x\right), \tag{5.1}$$

where L is the length of the AFM scan, σ is the *rms* roughness and h_m are decomposition coefficients normalized by the condition $\sum_{m=1}^{\infty} |h_m|^2 = 1$.

The fit function traced by the red solid curve in Fig. 8.4(a) represents the Fourier series with the first 100 decomposition terms. As the result of this decomposition the surface roughness was approximated by the sum of sinusoidal perturbations with different spatial frequencies k_m. For the estimation of the propagation losses it was assumed that each spatial frequency k_m gives an independent contribution to the propagation losses with the normalized weight h_m. The absolute value for the weights h_m as a function of the spatial frequencies k_m is presented in Fig. 8.4(b).

In order to couple a guided mode with a wave vector β to a substrate radiation mode with a wave vector $\beta_{\text{substrate}}$ the phase matching condition $\beta - \beta_{\text{substrate}} = k_m$ should be satisfied. This condition basically expresses the momentum conservation for the photons involved in the scattering. Different spatial frequencies k_m can couple the light to different radiation modes, that is why the plot in Fig. 8.4(b) is divided into two parts, which represent scattering to the substrate and to the air. As it was mentioned earlier, only the losses due to the scattering to the substrate were estimated here, and the numerical values for this case are presented in the table in Fig. 8.4. The values in the table were obtained by averaging the results from 10 profiles extracted from 10 different position in the AFM scan. The error bars represents the variation depending on the position. The formulas and other details for this calculations are presented in the Chapter 8.

The theoretical estimations presented here give the right prediction for the order of magnitude of the propagation losses measured experimentally. These calculations demonstrate that a waveguide surface with the typical MBE morphology can couple the light from the guided to the radiated modes and provoke significant propagation losses. According to the theory these losses grow very quickly with the mode order and can easily reach 10-20 dB/cm for a roughness amplitude of several nanometres. At this point it should be clear that the surface roughness is identified as one of the main sources of the propagation losses. But still there may be some doubts about the exact value of its contribution to the overall losses due to the absence of the precise calculations. The final experimental proof that indeed the surface roughness is responsible for an overwhelming part of the propagation losses for N2291 sample will be presented in the Section 5.3.

5.3.2 MOVPE surface

The surface morphologies of MOVPE and MBE layers are completely different, see Fig. 5.8. Due to the much larger lateral scale Λ of its roughness, the MOVPE surface does not provide high enough spatial frequencies to couple the guided and the radiated modes. The much lower spatial frequencies characterising this type of surface, can provide only small deviations of the modal wave vector. This result in a clearly observable light diffusion in the plane of a planar waveguide, see Figs. 5.10(e)-(h). The goal of this section is to provide a numerical estimation showing that nanometre scale roughness can induce a significant in-plane diffusion of guided modes.

The experimental results for G3416 sample will serve as an example for this section. According to these results, the light for the TM2 mode was scattered over a 4cm segment on the screen which was placed 15cm away from the sample, see Fig. 5.10(g). This means that the light was scattered over a 15° angle, or that there was a deviation angle $\theta = 7.5°$

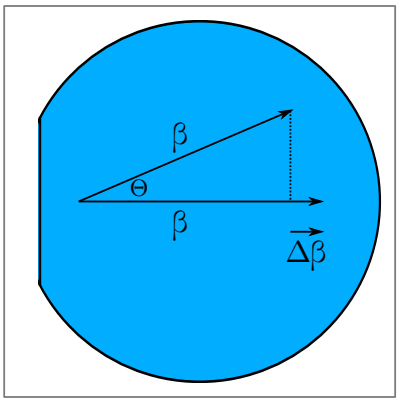

Mode	TE0	TE1	TE2
Coupling length	20mm	5mm	2mm

Figure 5.12 – (a) A scheme demonstrating coupling of the same order modes with the wave vector β which are guided in two different directions separated by the angle θ. The table attached to this figure summarizes the values of the coupling length for different TE modes.

from the initial propagation direction. From the deviation angle θ one can easily calculate the wave vector difference $\Delta\beta$ necessary to create this deviation according to the formula:

$$\Delta\beta = \beta - \beta\cos\theta = 2\beta\sin^2\frac{\theta}{2} \tag{5.2}$$

where β is the wave vector of a given mode, see Fig. 5.12. For example, for the fundamental TE0 mode $\beta_0 = 23\mu\text{m}^{-1}$ at 633nm wavelength. And the $\theta = 7.5°$ deviation angle would correspond to a $\Delta\beta = 0.2\mu\text{m}^{-1}$, difference which can be introduced by a sinusoidal perturbation of the surface with a period $\Lambda = 30\mu$m.

Unfortunately it is impossible to make reliable measurements of such a perturbations with nanometre amplitude and such a large lateral scale with the AFM technique due to numerous artefacts which appear when scanning large areas. That is why let us just suppose that there is a sinusoidal perturbation with 1nm amplitude and the necessary period. This perturbation couples two guided modes with the same order but propagating in slightly different directions. The strength of the coupling between these two modes is often characterized by the coupling length, which give the propagation distance after which 100% of power can be transferred from one mode to another. The table in Fig. 5.12 gives the coupling length for 3 TE modes in the waveguide with a sinusoidal perturbation of 1nm amplitude. This estimation shows that indeed, a significant power transfer can occur only after several millimetres of propagation, creating a significant diffusion. The formulas and other details for this calculations are presented in the Chapter 8. More realistic estimation should give longer coupling distances. One reason is that only a small fraction of the surface roughness contributes to a sinusoidal perturbation at a fixed frequency, that is why the effective amplitude of the sinusoidal perturbation should be smaller that 1nm. Another reason is that the walk-off effect should reduce the coupling strength for two mode propagating in different directions. In our experiments a typical propagation distance was 5mm, which is close to the characteristic coupling length calculated here.

Therefore the experimentally observed diffusion can probably be explained by the coupling process described above.

5.4 Improved surface quality

The numerical estimations presented in the previous section are clearly suggesting that in the case of the N2291 sample, the surface roughness is the main source of propagation losses. In order to verify this hypothesis, a very simple experiment was performed. A thin 60nm GaN layer was regrown on the top of N2291 sample by the MOVPE technique. This new sample with a thin MOVPE layer got a new number G3423 according to the laboratory classification, see Fig. 5.13. A subsequent optical characterization showed a remarkable improvement in terms of propagation losses. New results for the propagation losses are presented in Table 5.4, to compare with the results in Table 5.3.

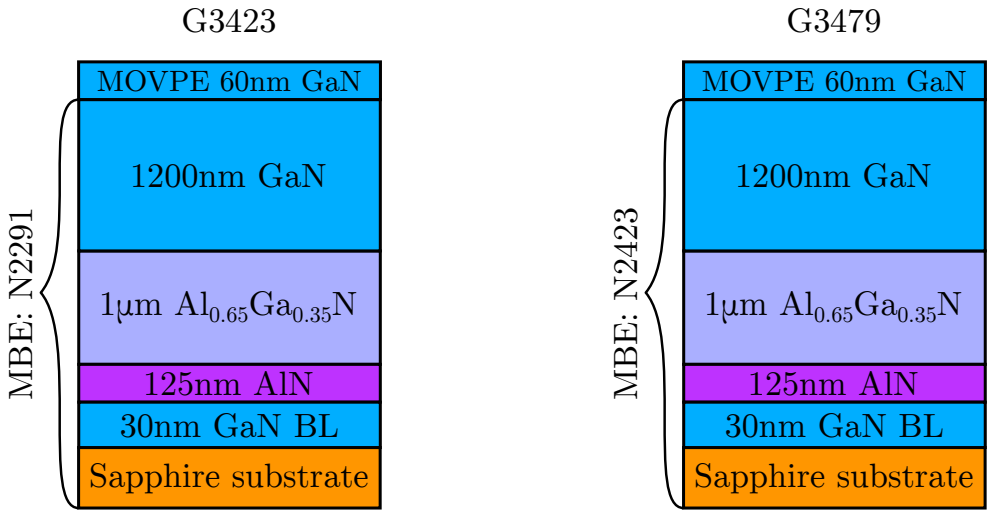

Figure 5.13 – Schemes of G3423 and G3479 waveguides. G3423 waveguide was fabricated by performing a 60nm GaN regrowth on the top of N2291 sample. G3479 is a copy of G3423 and will be discussed later

Sample	G3423: N2291(MBE)+60nm MOVPE					
Mode	TM0	TM1	TM2	TE0	TE1	TE2
Losses (dB/cm)	<1	2±1	5±1	1±1	4±1	6±2

Table 5.4 – Propagation losses in dB/cm for the TM- and TE-modes in G3423 waveguide. G3423 was fabricated by performing a 60nm GaN regrowth on N2291 sample in the MOVPE reactor. The error estimation includes losses variation depending on the position on the sample and ±1mm uncertainty in the propagation distance measurement. Adding a 60nm thick MOVPE layer leads to an important reduction of the propagation losses, (to compare with the results in Table 5.3).

After this regrowth the amplitude of the surface roughness was significantly reduced and the high spatial frequencies were eliminated, see Fig. 5.14(a). As a result, we have ob-

tained the waveguide with the smoothest surface in comparison with all previous samples.

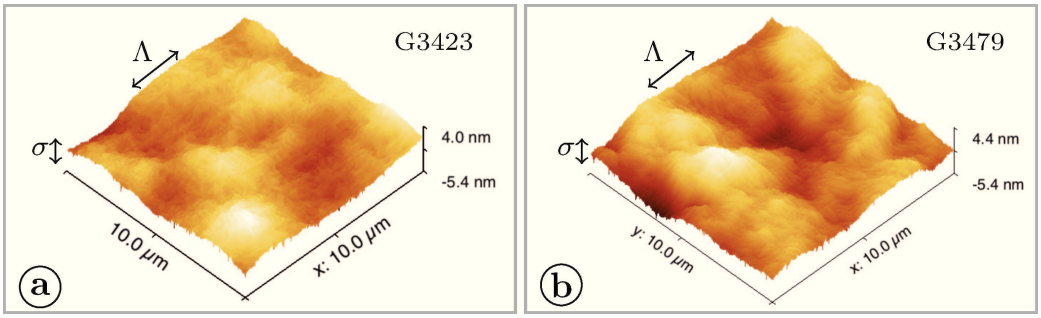

sample	epitaxy	rms, σ	Λ
G3423	MBE volume+MOVPE surface	1.3nm	2.0μm
G3479	MBE volume+MOVPE surface	1.2nm	2.1μm

Figure 5.14 – (a)-(b) AFM images of 10μm by 10μm surface areas of the G3423 and G3479 samples. The roughness amplitude σ and the characteristic lateral scale Λ are determined from the exponential fit $\sigma^2 \exp(-r/\Lambda)$ of the autocorrelation function for the surfaces. The table attached to this figure summarizes the numerical values of the σ and Λ parameters for two samples.

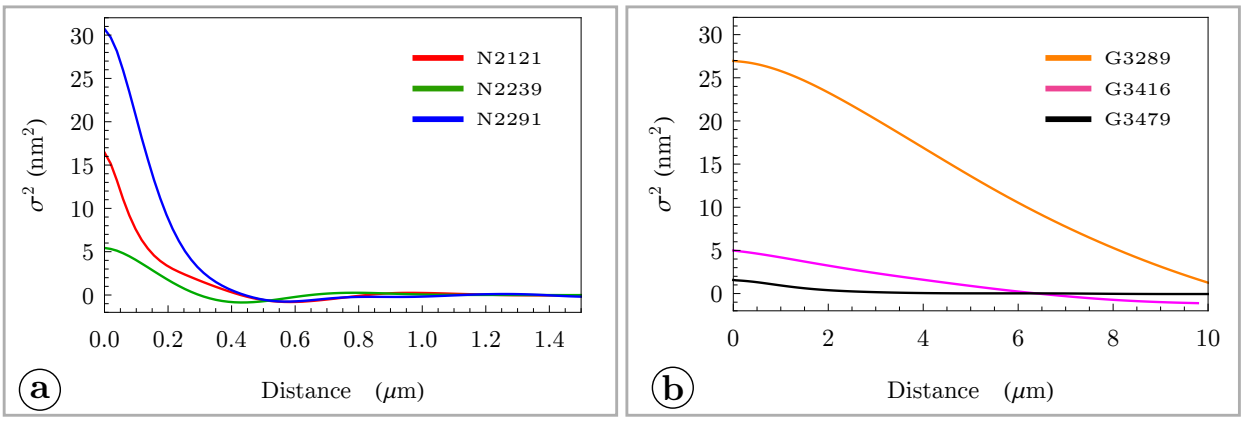

sample	N2121	G3289	N2239	G3416	N2291	G3423	G3479
rms, σ	4.1nm	5.2nm	2.3nm	2.3nm	5.5nm	1.3nm	1.2nm
Λ	170nm	6μm	210nm	3.5μm	150nm	2μm	2μm

Figure 5.15 – (a)-(b) Radial autocorrelation functions of the surface roughness for different samples. Two separate plots are used for the MBE and MOVPE surfaces due to the very different lateral scales. The table attached to this figure summarizes the numerical values of the σ and Λ parameters for different samples. The roughness amplitude σ and the characteristic lateral scale Λ are determined from the exponential fit $\sigma^2 \exp(-r/\Lambda)$ of the autocorrelation functions for the surfaces.

The summary of the surface autocorrelation functions and the evolution of the amplitude and the characteristic lateral scale for the surfaces in previously described samples

are presented in Fig. 5.15 are presented the different parameters (amplitude, lateral scale and autocorrelation function) of the roughness of the different samples we realized. As one can see from this figure, the lateral scale Λ for G3423 sample settled somewhere in between the typical lateral scales of MBE and MOVPE grown samples. But the most important factor is a very significant reduction of the amplitude σ of the surface roughness. All these improvements had a positive impact both on the propagation losses and the light diffusion addressed earlier. The drastic improvement of the propagation distance can be seen in Figs. 5.9(a)-(d) and Figs. 5.16(a)-(d). It is interesting to note that although G3423 sample had an MOVPE type surface there were no significant light diffusion observed on the photos of the m-lines, see Fig. 5.16(e)-(h).

The only drawback for the G3423 sample was the fact that the MOVPE regrowth was performed after sample N2291 went through the characterization procedure. The contamination generated significant number of point defects. In addition there was a 1cm large area on the edge of the sample, which was showing anomalous light diffusion. This area is clearly visible in Fig. 5.16(a)-(d). Nevertheless with the help of this sample we have experimentally proven that the surface roughness is responsible for most of the propagation losses.

After we discovered this important point, a new sample was fabricated : G3479. It was a copy of G3423. The only difference is that for G3479 sample the MOVPE regrowth immediately followed the MBE growth and special precautions were taken in order to eliminate any possible contaminations of the surface. This helped us to eliminate point defects and reduce by a few extra dB/cm the propagation losses. The numerical values for the propagation losses are given in Table 5.5.

Sample	G3479: N2423(MBE)+60nm MOVPE					
Mode	TM0	TM1	TM2	TE0	TE1	TE2
Losses (dB/cm)	<1	1 ± 1	4 ± 1	<1	3 ± 1	5 ± 1

Table 5.5 – Propagation losses in dB/cm for the TM- and TE-modes in G3479 waveguide. For G3479 sample MOVPE regrowth was performed immediately after MBE growth, which has allowed to reduce the sample contamination and even further reduce the propagation losses. The errors estimation includes losses variation depending on the position on the sample and $\pm$1mm uncertainty in the propagation distance measurement.

The photos of the propagation and the m-lines for the TM and TE modes are given in Fig. 5.17 and Fig. 5.18 respectively. We present this images in order to demonstrate the propagation over 2cm almost without attenuation even for higher order modes and the absence of any light diffusion in the m-lines. Another peculiar thing we would like to underline here is that the propagation trace of the TM modes became barely visible. This is something one would expect from an ideal structure due to the fact that for a TM mode, the field oscillates perpendicularly to the plane of the waveguide. These results are quite remarkable considering that the starting point of this study is shown in Fig. 5.2. Finally we have fabricated waveguides that can allow for an efficient second harmonic generation.

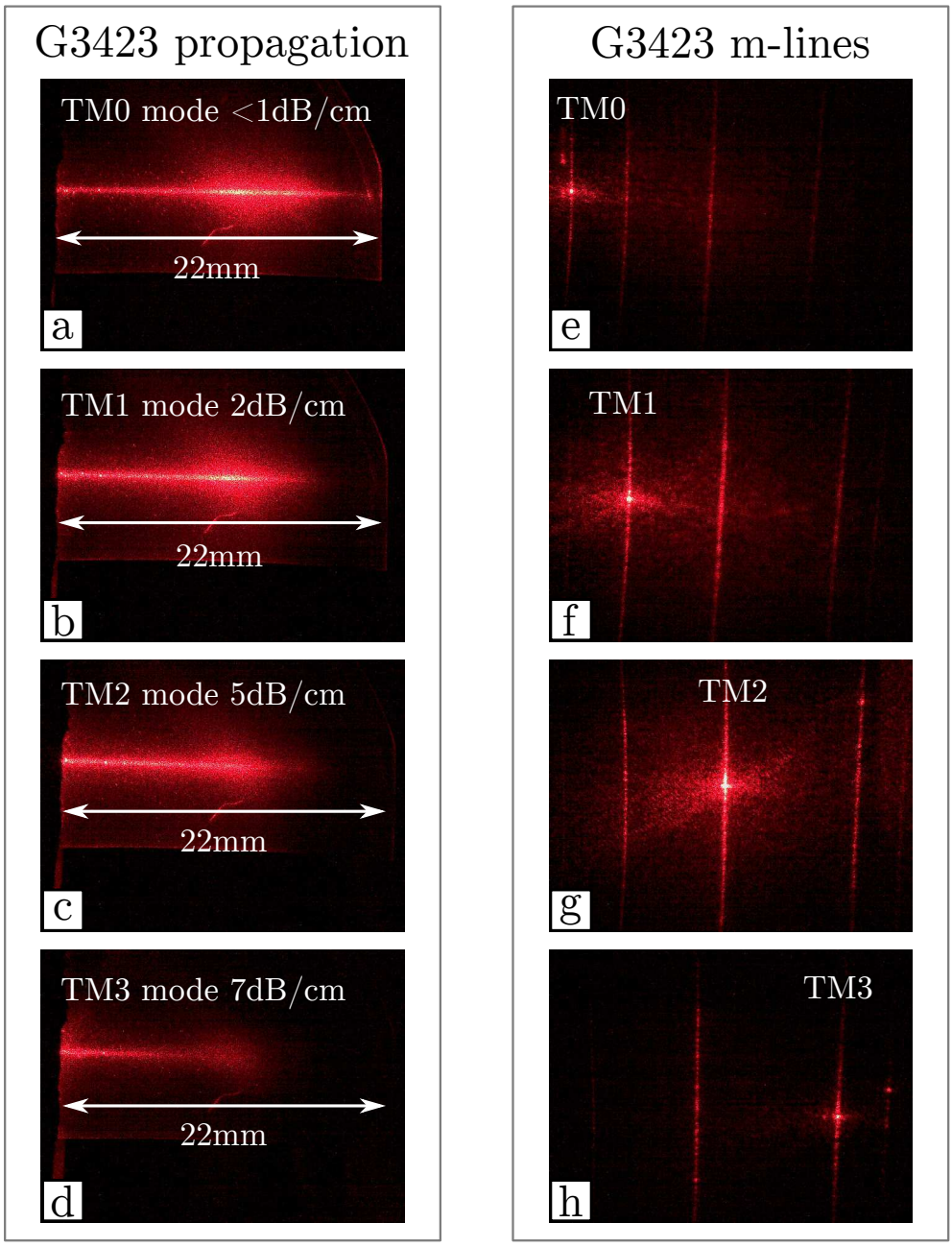

Figure 5.16 – (a)-(d) Saturated images of the light diffused along the propagation lines of TM0-TE3 modes in G3423 sample with the light injection in the modes TM0 in part (a), TM1 in part (b) and TM2 in part (c) respectively. For all three modes light propagates more than for 10mm distance. (e)-(h) Saturated images of the m-lines for the G3423 sample with the light injection in the modes TM0 in part (d), TM1 in part (e) and TM2 in part (f) respectively. Small inter-modal coupling is visible on all the images. For this sample the light intensity of the m-lines stays almost the same for all modes. In addition, the diffusion of the m-lines also significantly reduced in comparison to G3416 sample.

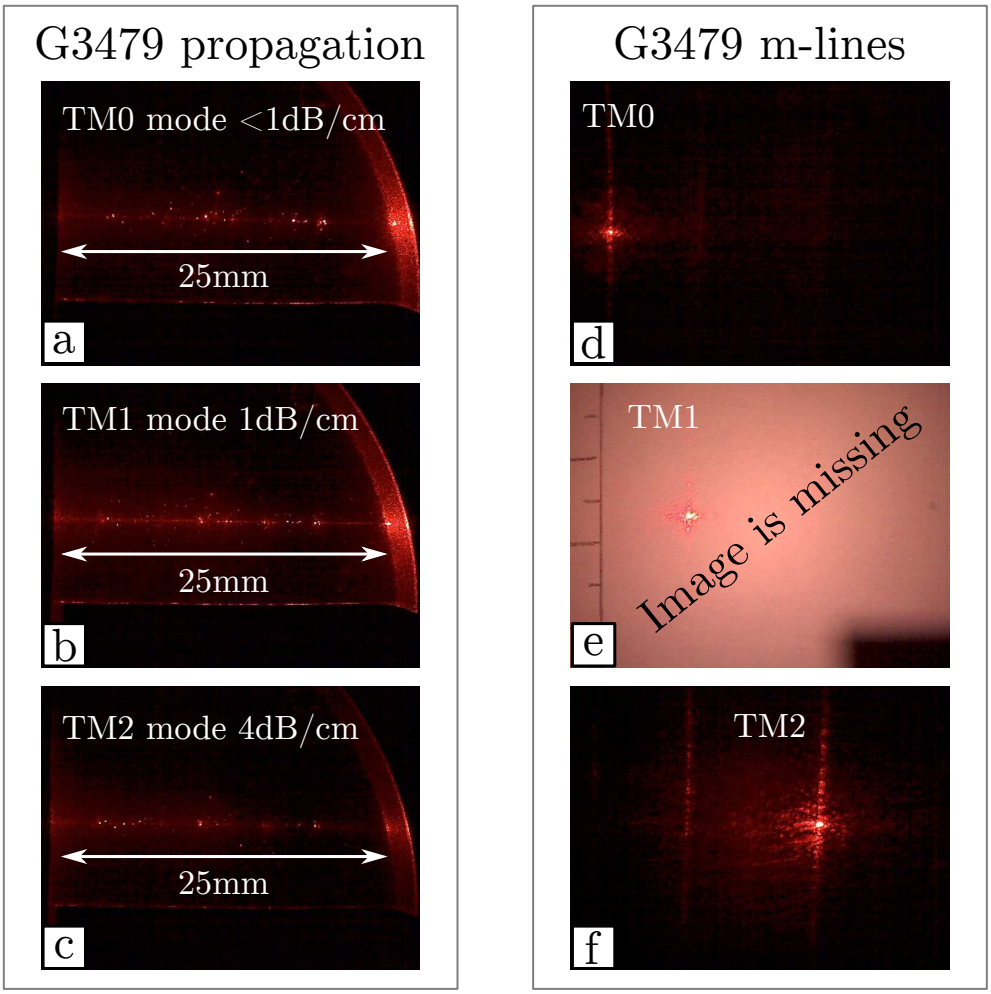

Figure 5.17 – (a)-(c) Saturated images of the light diffused along the propagation lines of TM0-TM2 modes in G3479 sample with the light injection in the modes TM0 in part (a), TM1 in part (b) and TM2 in part (c) respectively. For all three modes light propagates over the 25mm distance. In addition, much smaller light scattering in the direction perpendicular to the plane of the waveguide is observed for the TM-modes in comparison to the TE-modes in Fig. 5.18, as it should be due to the different orientations of the dipole excitations. (d)-(f) Saturated images of the m-lines for the G3479 sample with the light injection in the modes TM0 in part (d), TM1 in part (e) and TM2 in part (f) respectively. Small inter-modal coupling is visible on all the images. For this sample the light intensity of the m-lines stays almost the same for all modes.

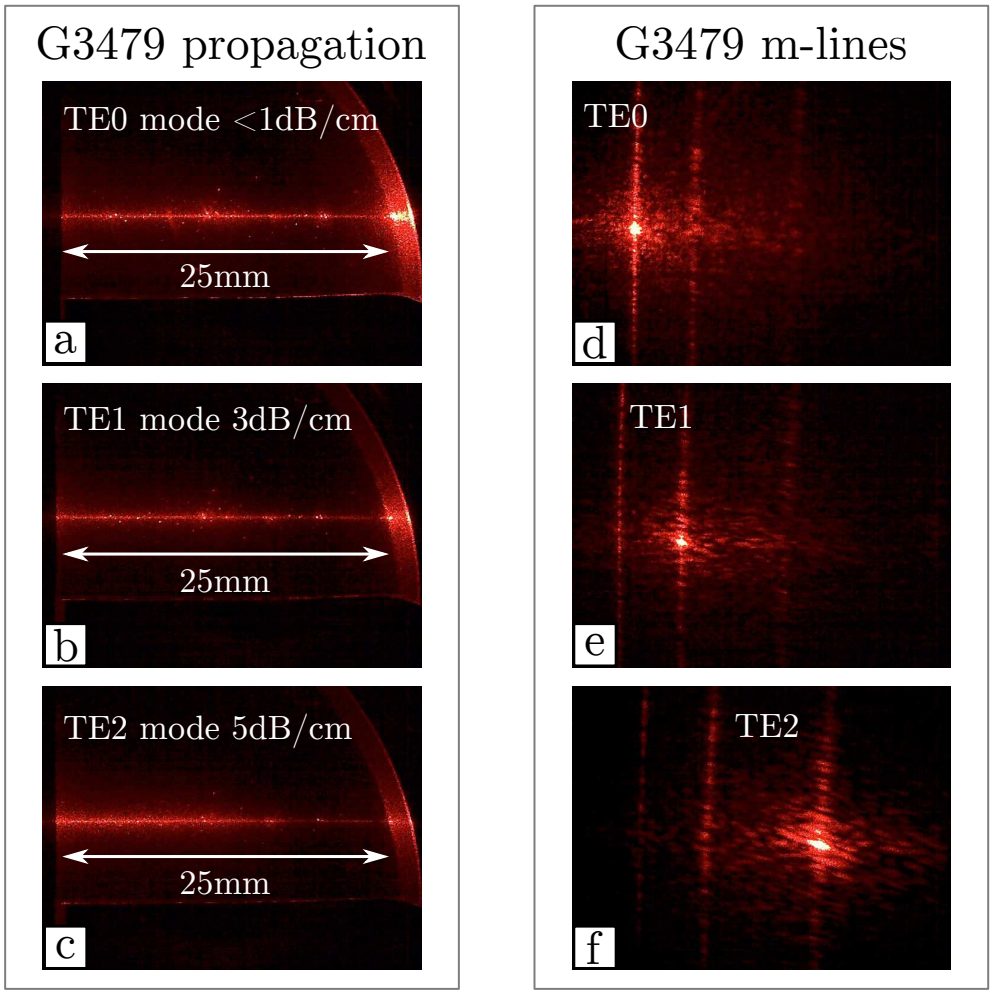

Figure 5.18 – (a)-(c) Saturated images of the light diffused along the propagation lines of TE0-TE2 modes in G3479 sample with the light injection in the modes TE0 in part (a), TE1 in part (b) and TE2 in part (c) respectively. For all three modes light propagates over the 25mm. . (d)-(f) Saturated images of the m-lines for the G3479 sample with the light injection in the modes TE0 in part (d), TE1 in part (e) and TE2 in part (f) respectively. Small inter-modal coupling is visible on all the images. For this sample the light intensity of the m-lines stays almost the same for all modes in contrast to N2291 sample. In addition, the diffusion of the m-lines also significantly reduced in comparison to G3416 sample.

5.5 SHG results on sapphire substrates

5.5.1 First observations of the second harmonic generation

The main subject of this study was the second harmonic generation (SHG) in GaN waveguides using modal phase matching between TM0 pump and TM2 second harmonic. This choice was motivated by the fact that this mode combination allows for power conversion from the near-infrared to the visible spectral region. In this case it was relatively easy to observe the SHG and also, we were well equipped with laser sources, passive optic elements and detectors adapted for these spectral regions.

Previous sections describe the drastic reduction of the propagation losses, which was obtained by developing AlN/AlGaN optical cladding layer and by reducing the surface roughness of GaN waveguides. The SHG experiments started to be feasible, when the propagation distance for the TM2 mode reached several millimetres and when it became possible to selectively couple and decouple the light in this mode with the prism coupling technique.

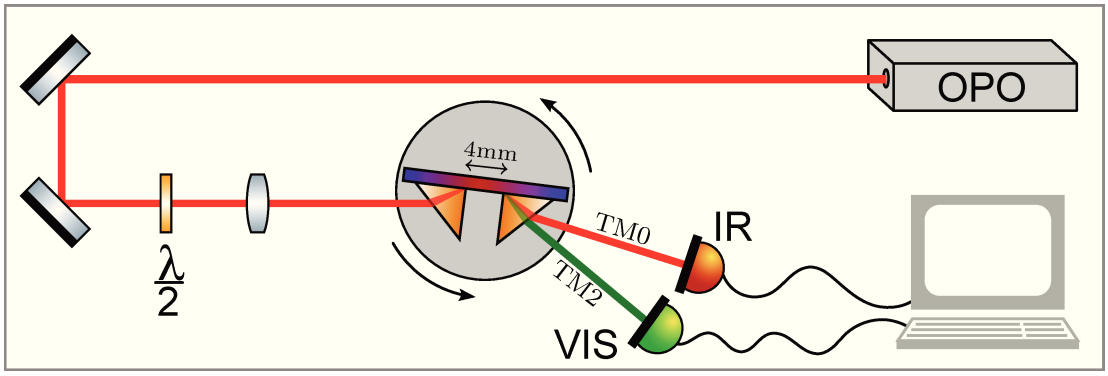

Figure 5.19 – (a) A general scheme of the second harmonic generation experiment for the planar waveguides.

The general scheme of our experiment is shown in Fig. 6.13. A pulsed EKSPLA NT242 OPO with 1kHz repetition rate and 4ns pulse duration was used as a pump source for this set-up. Before the injection the pump was focused by a convex lens of 17cm focal length. Due to the absence of lateral confinement in planar waveguides this focalization is important since it allows to benefit from a higher power density. The pump at 1260nm was selectively injected in the TM0 mode with the first prism. After the SHG process on the 4mm segment of the waveguide, the pump and the newly generated second harmonic at 630nm were decoupled with the second prism. The second harmonic and the pump, which at phase matching travel with the same effective index, were decoupled at different angles and naturally separated due to the dispersion of the prism. Photo-diodes were used for the average power measurements and pyro-electric detectors were used for the measurements of the pulse energy in the pulse-by-pulse detection. More details on this experimental set-up can be found in Chapter4.

Although the SHG is a physical process without any threshold, the detector sensitivity introduces a practical threshold in the experiment.. That is why, whith the first samples, we had to limit ourselves to an observation of the SHG without being able to measure the efficiency. The photos of the SHG for the waveguides from the previous sections are shown in Fig. 5.20. These photos clearly show the remarkable progress that was done for the second harmonic power output due to the losses reduction. While, at the beginning, we obtained only a few nano-watts of second harmonic power in Figs. 5.20(a)-(b), this value reached several thousands of nano-watts for the best G3479 waveguide in Fig. 5.20(d). Actually, for the G3479 waveguide, it became possible to perform a synchronized pulse-by-pulse detection with the pyro-electric sensors and to calculate the SHG efficiency avoiding the errors induced by the use of average values. The results of these measurements will be presented in the next section.

The average power for the pump and the second harmonic could be measured with the photo-diodes even for N2291 and G3416 waveguides. Unfortunately these photo-diodes

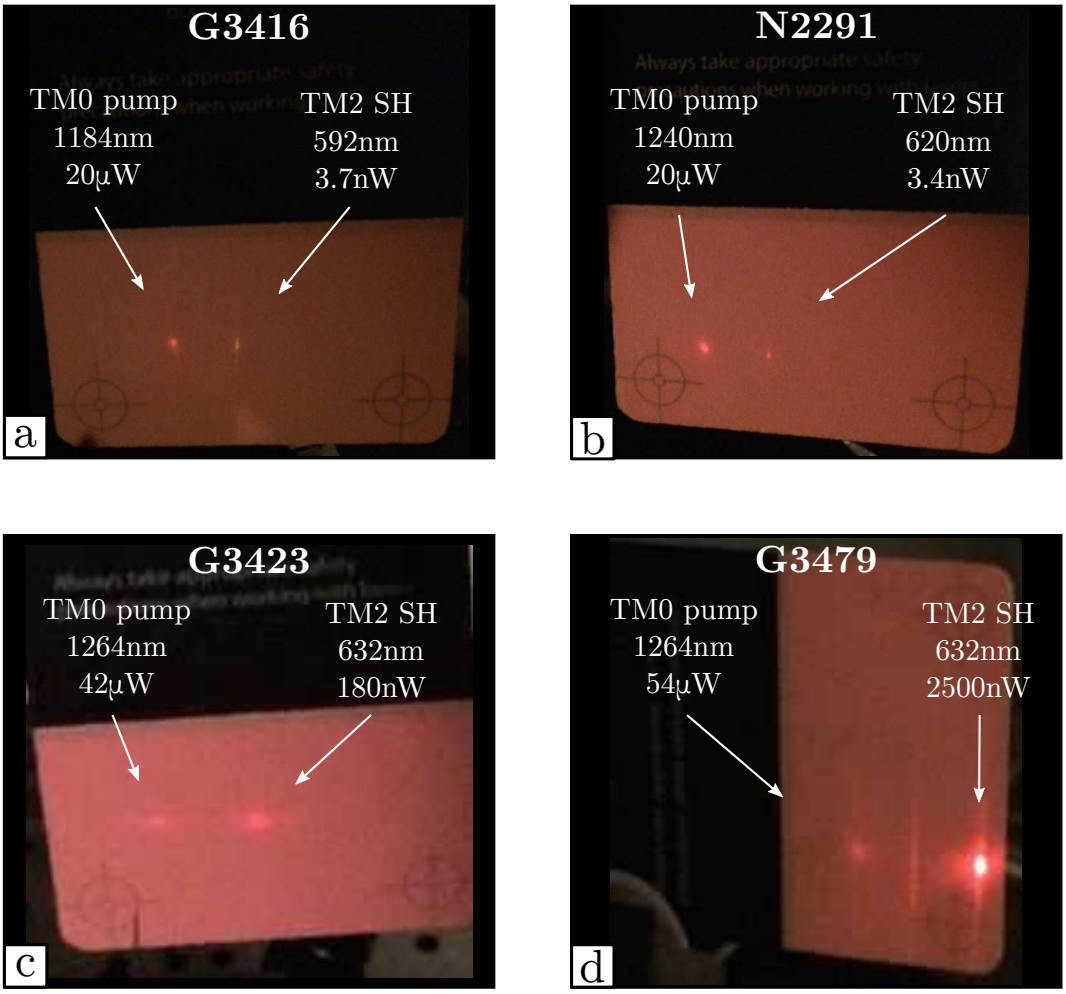

Figure 5.20 – (a)-(d) Photos of the second harmonic generation in four different waveguides.

were not adapted to the 1kHz repetitions rate and 4ns pulse duration of the OPO source, so they were not showing correct absolute values for the average power. Nevertheless these photo-diodes could be used for comparative measurements and for obtaining the acceptance curves. The acceptance curves give the average power of the second harmonic as a function of the pump wavelength. The important quantities for these curves are not the absolute values of the power but the width of the curve and the wavelength at phase matching.

The acceptance curves for the waveguides are presented in Fig. 5.21. The table in this figure summarizes the phase matching wavelengths predicted by the theory and measured in the experiments. The experiment matches the theory within 1% error showing the advantage of epitaxy in terms of control of layer thickness and composition.

5.5.2 Efficiency of the second harmonic generation

This section presents the efficiency estimations for the second harmonic generations in G3479 waveguide, which had the lowest propagation losses in comparison with all other

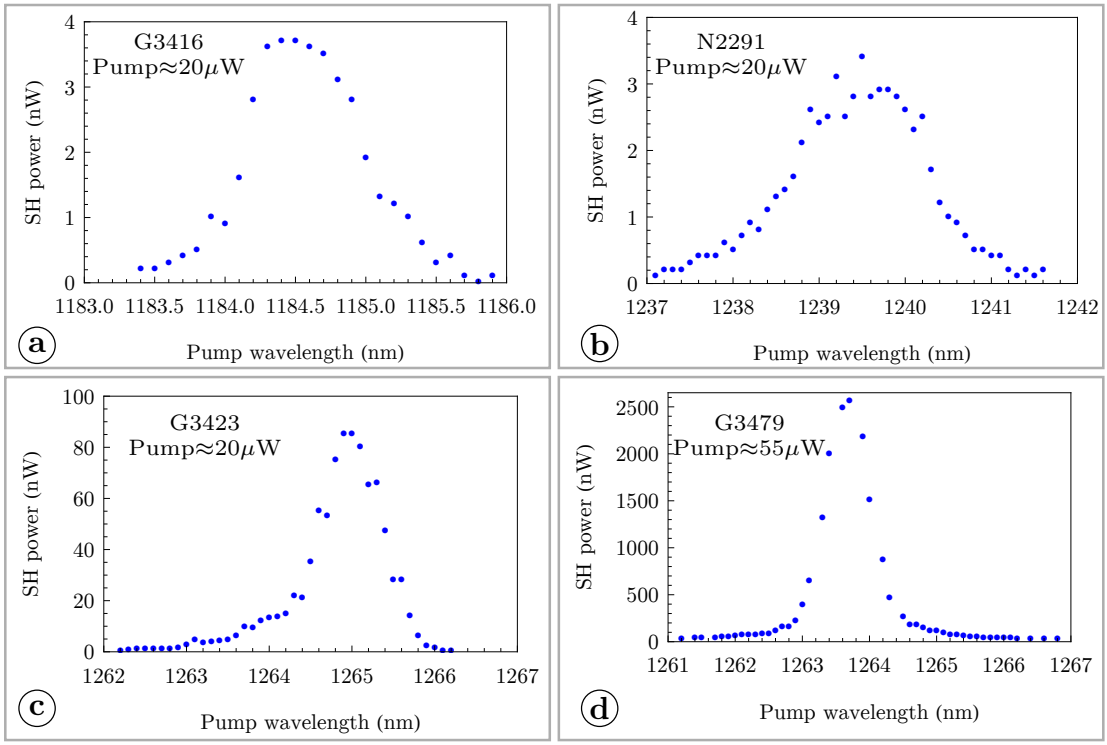

sample	G3416	N2291	G3423	G3479
theory	1197.6nm	1245.1nm	1272.9nm	1272.9nm
experiment	1184.4nm	1239.5nm	1265.0nm	1263.8nm

Figure 5.21 – (a)-(d) The average harmonic power measured as a function of the pump wavelength for four different samples. The table attached to this figure summarizes theoretical and experimental values for the phase matching wavelengths.

samples described in the previous sections. These results are compared to the best efficiencies which were reported earlier for other AlGaN based structures.

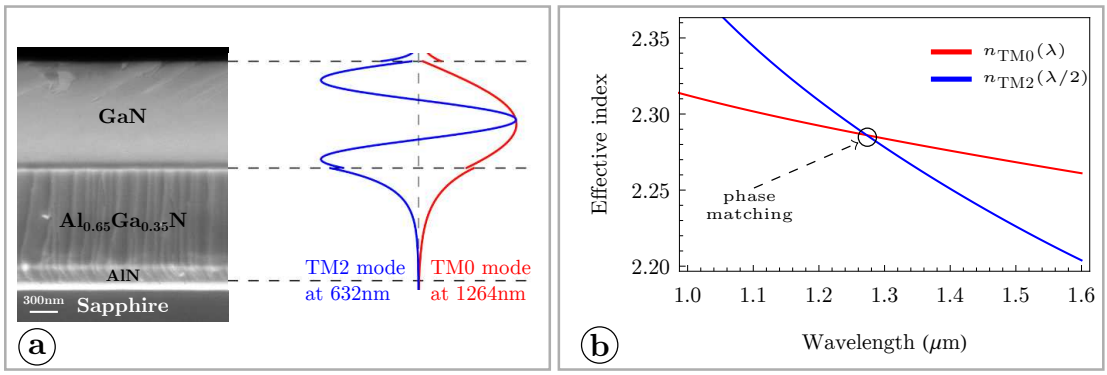

Figure 5.22 – (a) A cross-sectional SEM image of the fabricated waveguide together with the electric field distributions for the TM0 mode at 1264nm and TM2 mode at 632nm wavelengths. (b) The effective refractive indices of these modes as a function of the wavelength; the phase matching is reached at the crossing point.

A cross-sectional SEM image of G3479 waveguide is shown in Fig. 5.22(a). The

GaN layer thickness and the Al content in the AlGaN cladding of G3479 waveguide were optimized in order to reach the phase matching between TM0 and TM2 modes with the harmonic wavelength around 630nm. The electric field distributions for the TM0 and TM2 modes are superimposed with the SEM image in Fig. 5.22(a). The plot in Fig. 5.22(b) shows the effective indices for the TM0 and TM2 modes as a function of the wavelength; at the crossing point of the two curves the phase matching condition is reached.

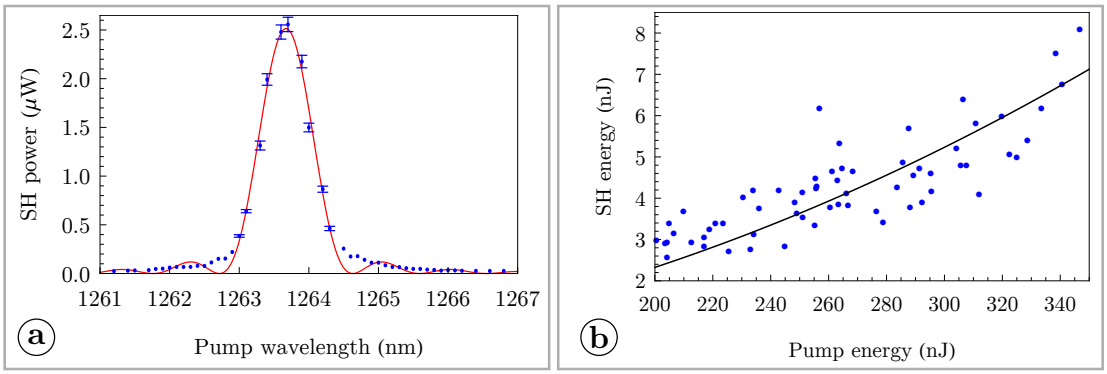

Figure 5.23 – (a) The average harmonic power measured as a function of the pump wavelength using a silicon photo-diode; the red curve represents the experimental data fit with the square of the sinc function. (b) SH pulse energies as a function of the pump pulse energies; the black curve represents the quadratic fit of the experimental data. Results in part (b) were obtained by a synchronized pulse-by-pulse detection of the second harmonic and the pump with pyro-electric sensors.

The same experimental set-up as previously was used, see Fig. 6.13. First, a silicon photo-diode was used to measure the average harmonic power as a function of the pump wavelength, see Fig. 5.23(a). A sharp phase matching curve was observed; this curve was in close agreement with the theoretical acceptance function. Then two pyro-electric detectors were used to perform a pulse by pulse synchronized detection of the harmonic and the pump at the maximum of the second harmonic signal in Fig. 5.23(a). The results of the synchronized detection are shown in Fig. 5.23(b). It should be noted that the variation of the pump energy between 200nJ and 350nJ was not obtained by an attenuator; this variation is due to the OPO energy fluctuations from pulse to pulse. These laser fluctuations may also explain the deviation of the experimental data from the quadratic fit in Fig. 5.23(b). Indeed, for a given energy of the pump pulse its duration may also fluctuate around 4ns changing the peak pump power and introducing the deviations into the harmonic signal.

For 350nJ of pump energy 7nJ of second harmonic was collected, which means that an energy conversion of 2% was reached. Using a quadratic fit for the experimental data in Fig. 5.23(b), and assuming a 4ns pulses duration and a 4mm interaction distance we estimate the average conversion efficiency to be $0.15\%\cdot W^{-1}cm^{-2}$.

In Table 5.6 we compare our results to the state of the art results obtained for different AlGaN structures, such as micro-rings, micro-disks, photonic crystals, ridge waveguides and PO-GaN planar waveguides. We believe that in our case the low propagation losses were an essential factor for the high conversion efficiency. The same conclusion can be drawn for the AlN micro-rings with a relatively low nonlinear coefficient 1 pm / V but with very high quality factors Q=230 000 corresponding to 1.5dB/cm losses at 1550nm.

Ref.	Structure	pump wavelength	pump laser	max. power conversion	efficiency
[18]	AlN μ-ring	1550nm	cont., P_{max}=27mW	12%	2.5%·mW^{-1}
this work	GaN planar waveguide	1260nm	pulsed, 4ns, 1kHz P_{peak}=90W	2%	0.15 %·W^{-1}cm^{-2}
[13]	PO-GaN	1600nm	pulsed, 130fs, 80MHz P_{peak}=670W	0.1%	$1.2 \cdot 10^{-4}$ %·W^{-1}cm^{-2}
[7]	GaN PhC	1550nm	cont., P_{max}=0.78mW	$2 \cdot 10^{-4}$%	$2.4 \cdot 10^{-4}$ %·mW^{-1}
[40]	AlN ridge	1550nm	cont., P_{max}=50mW	$0.3 \cdot 10^{-4}$%	$0.7 \cdot 10^{-5}$ %·mW^{-1}
[16]	GaN μ-disk	1500nm	cont., P_{max}=1.1mW	$2 \cdot 10^{-7}$%	$2 \cdot 10^{-7}$ %·mW^{-1}

Table 5.6 – Summary of best reported efficiencies of second harmonic generation for different AlGaN based guiding structures.

The results of the theoretical modelling presented in Chapter **??** suggest that the obtained efficiency of 0.15%·W^{-1}cm^{-2} can be further improved. The first step would be the fabrication of ridge waveguides starting from the high quality planar guiding layers. The ridge waveguides would allow to obtain a higher lateral confinement and to reach 10%·W^{-1}cm^{-2} conversion efficiencies. The main challenge in this case is to preserve the same low propagation losses that we observed for the planar waveguides. Low propagation losses of 1.5dB/cm at 1550nm have been already demonstrated for AlN micro-rings [18]. An additional advantage of our approach is that in our case the waveguide width acts as a free parameter in a few micron range. This can allow for the fabrication of few micron wide waveguides that are less sensitive to the side wall roughness and still suitable for modal phase matching. The next step in the efficiency improvement would require some kind of polarity inversion. One solution is the planar polarity inversion combined with modal phase matching; this approach could yield 100%·W^{-1}cm^{-2} conversion efficiencies. Another solution is to use periodically oriented GaN (PO-GaN) structures that may allow 1000%·W^{-1}cm^{-2} conversion efficiencies. The first tests of ridge waveguides fabrication and polarity inversion will be presented in the next two sections.

5.6 Tests of ridge waveguide fabrication

This section presents the results we obtained, testing the first batch of ridge waveguide. We speak here only about a test, because this was done already at the end of the project. During this project significant progress was achieved in the modelling, fabrication and characterization of planar waveguides. Also a fair amount of time was dedicated to the study of the SHG in micro-disks within the collaboration with C2N laboratory. The results for the micro-disks will be presented in Chapter 6. The fabrication of ridge waveguides started to make sense only when the low-loss planar waveguides were finally obtained, which happened toward the end of the project. As a result, the fabrication was done in CRHEA laboratory, with no particular optimization of the lithography nor the etching procedures. The main interest was more in the optical study. The goal was just to con-

struct and to play with another type of experimental set-up adapted to ridge waveguides, which obviously was different from the set-up for planar waveguides.

Naturally the best planar waveguide G3479 was used for the fabrication. We used a lithography mask with 2.5μm wide waveguides separated from each other by 2.5μm . The guides were etched by RIE. After the etching a simple cleavage was done in order to reveal the injection facets. SEM images of the obtained waveguides are presented in Fig. 5.24. As one can see from this image, neither the injection facets nor the waveguides walls were

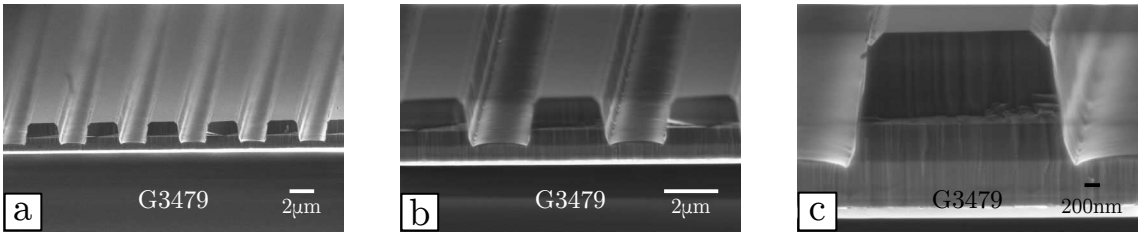

Figure 5.24 – A cross-sectional SEM image of the ridge waveguides fabricated from the G3489 sample.

perfect. The injection facets contained numerous defects due to the difficulty in cleaving the sapphire substrate. Much better cleavage results were obtained for silicon substrates, see next Chapter 6. The images show also significant roughness for the waveguide walls and a 18° deviation from the vertical. Moreover, the upper corners of the waveguides were attacked during the etching due to the fact that the resist thickness was not properly optimized. Obviously, all these defects had a negative impact both on the light coupling, decoupling and propagation in the waveguides.

The 2.5μm width was chosen for two main reasons. One reason was to reduce the impact of the wall roughness by fabricating large waveguides. Another reason was to preserve the modal phase matching between the TM00 and TM20 modes due to the fact that large waveguides present almost the same mode spectrum than the initial planar waveguides. It is true that these waveguides are multi-mode in lateral direction and one would suppose that this may induce some problems for light injection. But it turns out that for the end-fire coupling the overlap of the beam profile with the higher order modes is negligible in comparison with the overlap with the fundamental mode.

Since the ridge waveguides have a finite lateral width, a red-shift for the phase matching wavelength should be observed in comparison to the initial planar waveguide. In order to calculate the new phase matching condition the finite element simulations were performed using the commercial COMSOL software. The simulation results are presented in Fig. 5.25. According to the simulations the new phase matching wavelength should be shifted to 1320nm in comparison to 1273nm for the initial planar waveguide.

The fabricated waveguides were used for the SHG experiments. The details about the experimental set-up are presented in the Chapter 4. Once again the pulsed EKSPLA NT242 OPO with 1kHz repetition rate and 4ns pulse duration was used as a pump source for this set-up. The light was injected into the waveguide by the end-fire coupling technique using a Mitutoyo objective with x50 magnification and 0.5 numerical aperture. It is difficult to give a reliable estimation for the injection efficiency due to the fact that the waveguides facets were not perfect and the actual size of the focalization spot at the facet was not know. It was necessary to focus the light slightly before the facet in

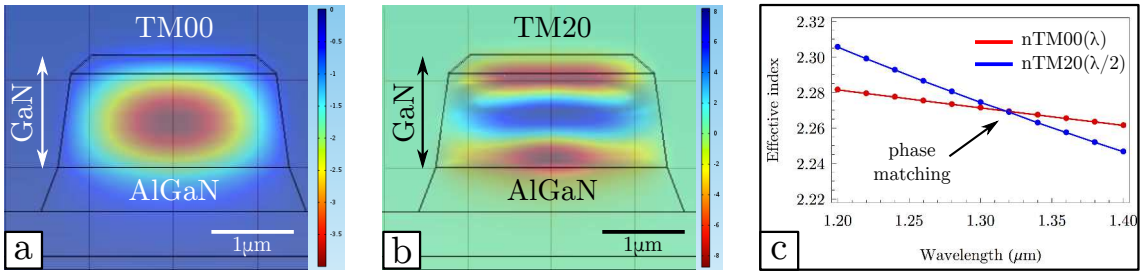

Figure 5.25 – (a)-(b) Profiles of the TM00 and TM20 modes. (c) The effective refractive indices of these modes as a function of the wavelength; the phase matching is reached at the crossing point. All the calculation presented in this figure are obtained by using COMSOL finite elements software.

order to avoid the possible focalization inside the waveguide, which normally leads to the material damage. The length of the waveguides was 4.5mm. After 4.5mm propagation the light was collected by another Mitutoyo objective with x100 magnification and 0.5 numerical aperture and sent either on a camera or an appropriate detectors depending on the objective of the measurements. It should be noted that not all of the light was collected by the second objective due to the fact that the numerical aperture for the TM00 and TM20 modes was 0.7. Also a 15% light coupling to the adjacent waveguides was observed, although according to simulations the coupling between two GaN waveguides separated by 2.5μm of air should be negligible.

The results of the SHG experiments are presented in Fig. 5.26. The part (a) show the photo of the second harmonic at 655nm wavelength. The acceptance curve measured with a silicon photo-diode in presented in part (c). The phase matching was reached for 1309nm wavelength, which is in close agreement with the COMSOL simulations. By using sCMOS and SWIR InGaAs cameras from Photonic Science the images of the pump and the second harmonics modes were taken, see Fig. 5.26. The image for the TM00 mode confirms that a selective injection in the fundamental mode is possible even for large multi-mode waveguides. A strong TM/TE coupling reaching 40% was observed for the second harmonic, possibly related to the non-rectangular shape of the guide. An attempt of the synchronous pulse by pulse detection with the pyro-electric sensors is shown in Fig. 5.26(d). The data is not showing any correlation or expected quadratic behavior. This is normal since the threshold for the second harmonic detector was 0.02J and a normal operation was guaranteed starting only from 0.3nJ according to the specifications. Therefore we can only speculate that the power conversion reached 0.5% assuming that for the 6nJ pump 0.03nJ second harmonic was generated. Assuming 4.5mm propagation distance and 4ns pulse duration this would give 1.6%$W^{-1}cm^{-2}$ conversion efficiency. It is important to note that these estimation were obtained by using the values for the pump power out-coupled from the waveguides.

To conclude we would like to underline that in this section we have shown that the concept of multi-mode ridge waveguide is working well. Such waveguides can be less sensitive to the wall roughness and still allow to satisfy the phase matching conditions. The obvious goal now is to optimize the fabrication procedure in order to reduce the walls roughness and improve their verticality.

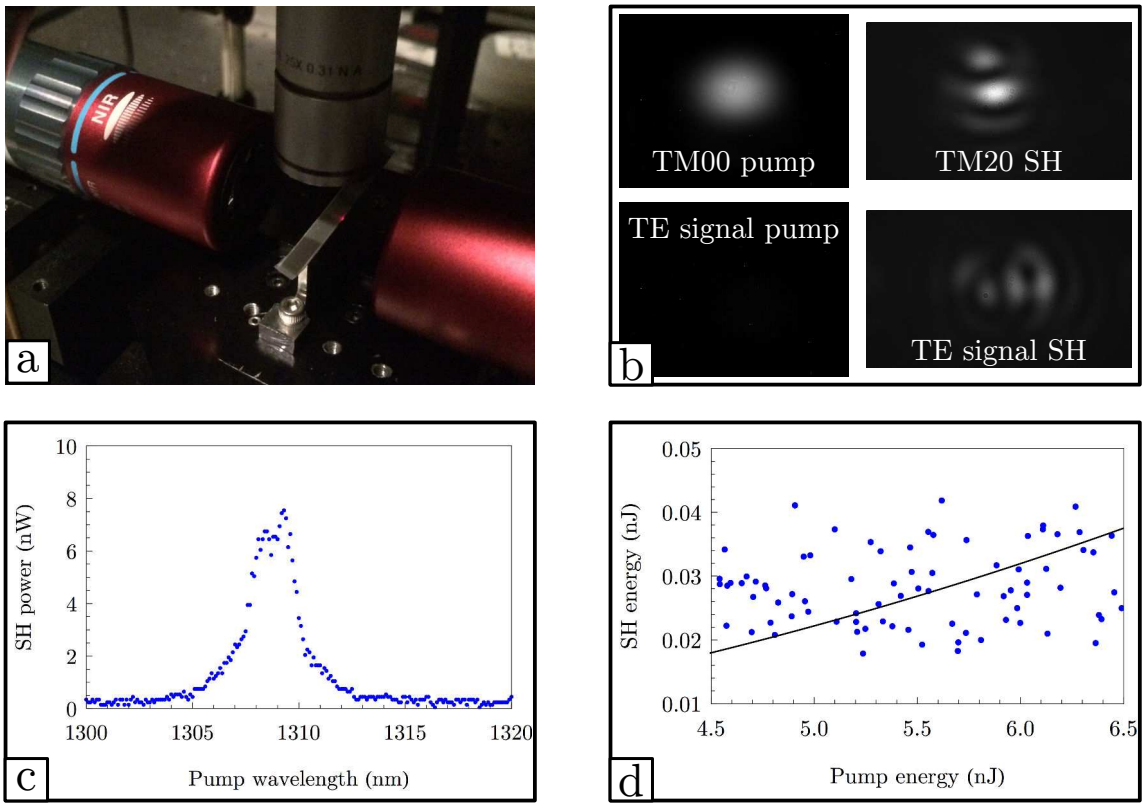

Figure 5.26 – (a) A photo of the second harmonic generation in the ridge waveguide. (b) images of the modes for the pump and the second harmonic obtained with the SWIR InGaAs and sCMOS cameras respectively. (c) The average harmonic power measured as a function of the pump wavelength using a silicon photo-diode. (d) SH pulse energies as a function of the pump pulse energies; the black curve represents the quadratic fit of the experimental data. The results in part (c) were obtained by a synchronized pulse-by-pulse detection of the second harmonic and the pump with pyro-electric sensors.

5.7 Tests of planar polarity inversion

According to the simulations presented in the Chapter 2 there is another approach based on the polarity inversion which allows to improve the SHG efficiency. One possibility is to use the planar polarity inversion in order to improve the overlap between the interacting modes. Another possibility is to use periodically oriented GaN structures which allow nonlinear interactions between the fundamental modes based on the quasi-phasematching. Here we present several tests of polarity inversion that were done in our laboratory.

A detailed study of the periodically oriented GaN waveguides was performed during the PhD thesis of S. Pezzagna (Nice, 2005). The main challenge during the growth of these structure was to find very particular conditions which allow to match the growth rates for the N-polar and Ga-polar layers. Significant progress was made during this work and as a result the OP-GaN structures with almost the same thickness for N- and Ga-polar layers were fabricated. The scheme of one of the best samples N867 is presented in Fig. 5.27. But as it is shown in Fig. 5.29(d) despite all the efforts the final surface still had macroscopic roughness mainly formed by 60nm bumps on the borders between

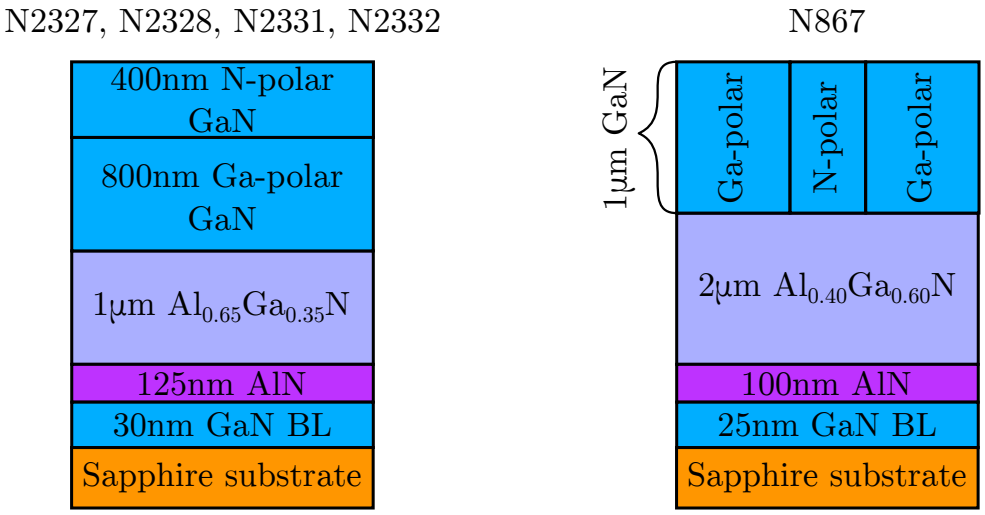

Figure 5.27 – Schemes of the samples with the planar polarity inversion (N2327, N2328, N2331, N2332) and the sample with periodically modulated polarity (N867).

two different polarities. This roughness was inducing high propagation losses going above 20dB/cm for the fundamental mode at 633nm, see Fig. 5.29(e). Moreover, the bumps were forming a diffraction grating as it proves the photo in the Fig. 5.29(f). In this case the decoupled light shows a sequence of equidistant spots, which is typical for grating diffraction. This study shows that although in theory OP-GaN structure can propose very high conversion efficiencies, in practice they fail due to the very serious technological difficulties. It seems that these structures are more adapted not for integrated optics but for bulk nonlinear optics, where there are no such high requirements regarding the surface quality.

During the current work we have performed several tests of planar polarity inversion. We were aiming at improving the overlap integral between TM0 and TM2 modes. The structures which allow this improvement are schematically shown in Fig. 5.27. Four samples N2327, N2328, N2331, N2332 for this type were fabricated. The details of the fabrication procedure are presented in Chapter 3. For all this samples the amplitude of the N-polar surface roughness was comparable to the roughness amplitude of MBE grown Ga-polar layers of the same thickness, see Fig. 5.28. Nevertheless the optical characterization for the best N2331 sample showed >20dB/cm propagation losses even for the fundamental mode. Several attempts were made in order to smooth the N-polar surface with the MOPVE regrowth, but they were not successful. These results remained a mystery and this direction was not showing much perspectives.

A decision was taken to concentrate on the fabrication of standard high quality waveguides with very smooth surfaces. And it was decided to use a collaboration with LETI in order to obtain the planar polarity inversion with the wafer bonding technique. This approach is very simple, it consists in bonding two GaN waveguides head to head on top of each other with a thin SiO_2 layer. At the end of this project the first successful wafer bonding was performed, but the sample was still going thought the process of the substrate removal, so the optical characterization for this type of structures will be performed in the future.

In spite of significant technological challenges the polarity inversion remains a very

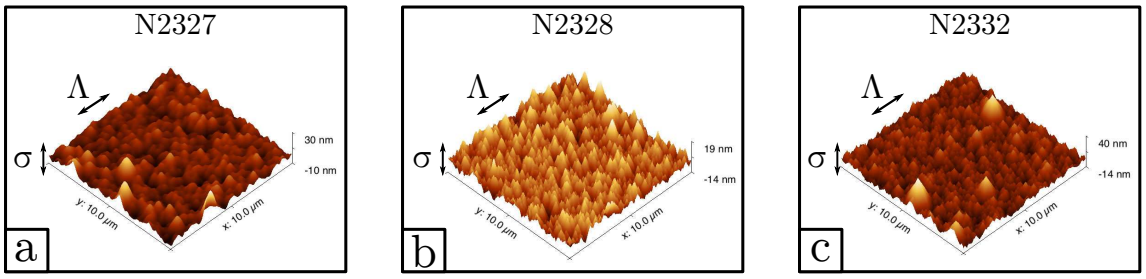

sample	N2327	N2328	N2331	N2332
rms, σ	3.8nm	4.0nm	3.9nm	5.0nm
Λ	350nm	300nm	580nm	460nm

Figure 5.28 – (a)-(c) AFM images of the N-polar suface for N2327, N2328 and N2332 samples. The roughness amplitude σ and the characteristic lateral scale Λ are determined from the exponential fit $\sigma^2 \exp(-r/\Lambda)$ of the autocorrelation function for the surfaces. The table attached to this figure summarizes the numerical values of the σ and Λ parameters for these samples.

promising approach which may lead to a significant improvement of the second harmonic generation efficiency. Probably OP-GaN structure will be developed for the application in bulk optics, while the planar polarity inversion will be used for the integrated nonlinear optics.

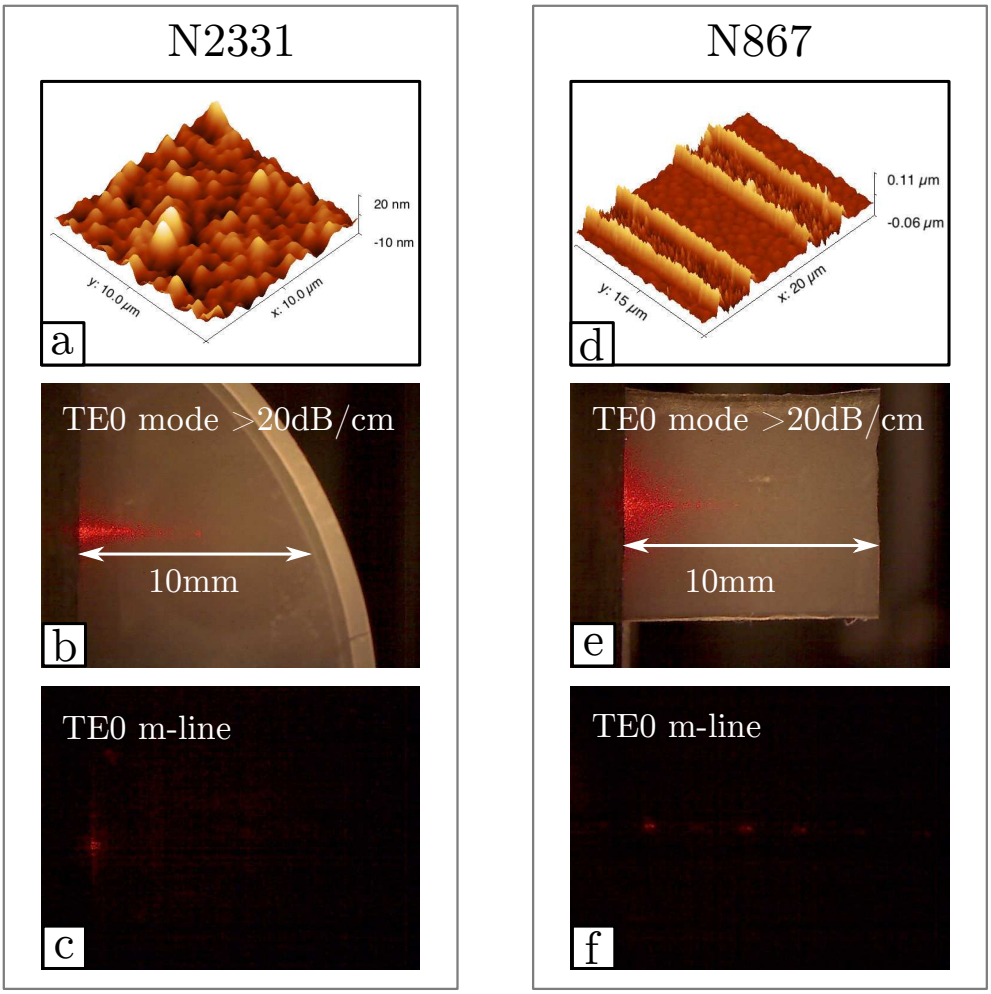

Figure 5.29 – (a) An AFM image of the N-polar surface of the N2331 sample. (b) A saturated image of the light diffused along the propagation line of the TE0 modes in N2331 sample. (c) A saturated images of the m-line for the N2331 sample with the light injection in the modes TE0. (d) An AFM image of the surface with periodically modulated polarity for the N867 sample. (e) A saturated image of the light diffused along the propagation line of the TE0 modes in N867 sample. (f) The light decoupled as a sequence of multiple spots shows that the N867 surface acts as a diffraction grating.

5.8 Conclusions

This chapter presented the results of the linear and nonlinear characterization of GaN waveguides grown on sapphire substrates. Here it is shown that by developing a proper AlGaN optical cladding and by reducing the surface roughness it is possible to reach very low propagation losses going below 1dB/cm in the visible spectral region. The low-loss waveguides described in this chapter were used for the second harmonic generation experiments based on the modal phase matching between TM0 and TM2 modes with a record high efficiency. The maximum power transfer of 2% was reached during the experiments with the $0.15\%W^{-1}cm^{-2}$ efficiency. First tests of the ridge waveguides fabrication and the planar polarity inversion show the feasibility of these two approaches for further improvements of the SHG efficiency. For the ridge waveguides the fabrication procedure

should be optimized in order to reduce the waveguide walls roughness and to improve their verticality. The technique of the planar polarity inversion based on wafer bonding should be further studied and developed. These problems will be the subject of the future studies.

Chapter 6

Waveguides on silicon substrates

Silicon is the second most used substrate for III-nitrides growth. The fabrication of AlGaN based photonic circuits on Si substrates opens new opportunities for integrated nonlinear optics. For example, one can use a selective etching between nitrides and Si for the fabrication of suspended photonic crystals and micro-disks, which allows increasing the second harmonic generation efficiency due to the cavity field enhancement. In general, due to the well-developed Si technology, it seems to be easier to perform such basic fabrication operations as cleavage, dicing, patterning, selective etching, wafer bonding and substrate removal in the case of Si in comparison to sapphire, another substrate widely used for the nitrides growth. This advantages haven't been used yet at an industrial level, but they are important at the level of research laboratories. Moreover, there is a long term interest in adding the AlGaN functionality to Si photonics based circuits. Today, Si photonic circuits are widely used for the applications in both classical and quantum optics. Despite of many advantages, Si has two main drawbacks: it is a poor light emitter due to its indirect band gap, and, because of its centrosymmetric crystalline structure, it does not have the second order nonlinearity. In contrast, III-nitrides can emit light and have quite an interesting second order nonlinearity, that opens opportunities both for high speed electro-optical modulation and efficient frequency conversion over a broad spectral range. Therefore a hybrid GaN/Si technology can significantly enlarge the quality of the photonic devices.

The obvious challenge one face to fabricate GaN waveguides appears due to the fact that Si has a large refractive index (3.57 for Si in comparison to 2.34 for GaN at the 1μm wavelength). Therefore, an optical cladding with a lower refractive index is needed to isolate the guided modes traveling in GaN from the Si substrate. Even with the optical cladding, there will always be some residual leakage into the Si substrate due to the tunnelling effect. It means, that the optical cladding has to be sufficiently thick to reduce the mode leakage to an acceptable value. In addition, the growth of thick nitride layers on Si substrates is a difficult task due to the stain, which appears during the cooling because of the large thermal coefficient mismatch between Si and nitrides, as it was explained in Chapter 3.

During this work we have studied three types of optical cladding. The first one based on AlGaN will be described in Section 6.2. AlGaN has a lower refractive index than GaN and serves both for the modes isolation and the strain reduction, as it will be explained below. The second cladding is based on SiO_2 and will be described in Section 6.3. In this section we will describe waveguides epitaxially grown on silicon on insulator (SOI) substrates. Special SOI substrates with a very thin Si layer (20nm) and a thick

oxide (500nm SiO_2) were fabricated by the LETI laboratory for this study and other ongoing projects in CRHEA laboratory. The third cladding based on air surrounding suspended AlGaN structures will be discussed in Section 6.4. In this section we will present experimental results for a micro-disk coupled to a waveguide. This set-up has allowed for the first demonstration of doubly-resonant second harmonic generation in a micro-disk using the whispering gallery modes.

In Section 6.1 of this chapter, we give a general overview of the different optical claddings in which we discuss the cladding thicknesses which are needed to achieve a good modes isolation in a broad spectral range. In the conclusion section, we compare the different approaches that were used for the waveguide fabrication and we discuss their advantages and disadvantages.

6.1 Modes leakage to Si substrates

In the previous Chapter 5 we have already shown that for waveguides grown on sapphire Substrates, different loss mechanisms exist. We have discussed the losses induced by the low quality of epitaxial layers grown at the contact of the substrate and by the surface roughness which present different morphologies depending on the growth technique. Obviously, the same losses are also present in the waveguides grown on Si substrates. In addition to these losses, one has to take into account the problem of mode leakage into the Si substrates through the tunnelling effect. There is no such problem for sapphire substrates since sapphire has a lower refractive index than AlGaN.

In general, the losses induced by the mode leakage should be calculated separately for each particular case, since they depend on a precise waveguide structure and the operation wavelength. Nevertheless, it is interesting to get a rough idea for the optical cladding which is needed for GaN waveguides.

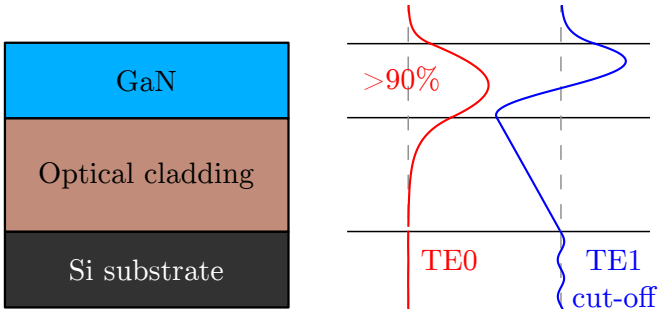

Figure 6.1 – A general scheme of a GaN waveguide on Si substrate. The TE0 mode is highly confined (>90%) in the GaN guiding layer at the cut-off of the TE1 mode.

For this purpose we will consider a simple GaN waveguide with a given optical cladding as it is shown in Fig. 6.1. The goal is to calculate the thickness of AlGaN, SiO_2 or air, which is needed to isolate the guided modes at different wavelengths which are involved in the nonlinear process that we are studying. For the pump wavelength, we adjust the GaN thickness in order to be at cut-off for the TE1 mode. In this situation the waveguide will be mono-mode for the pump and the confinement of the TE0 mode in the GaN layer will be larger than 90%, see Fig. 6.1.

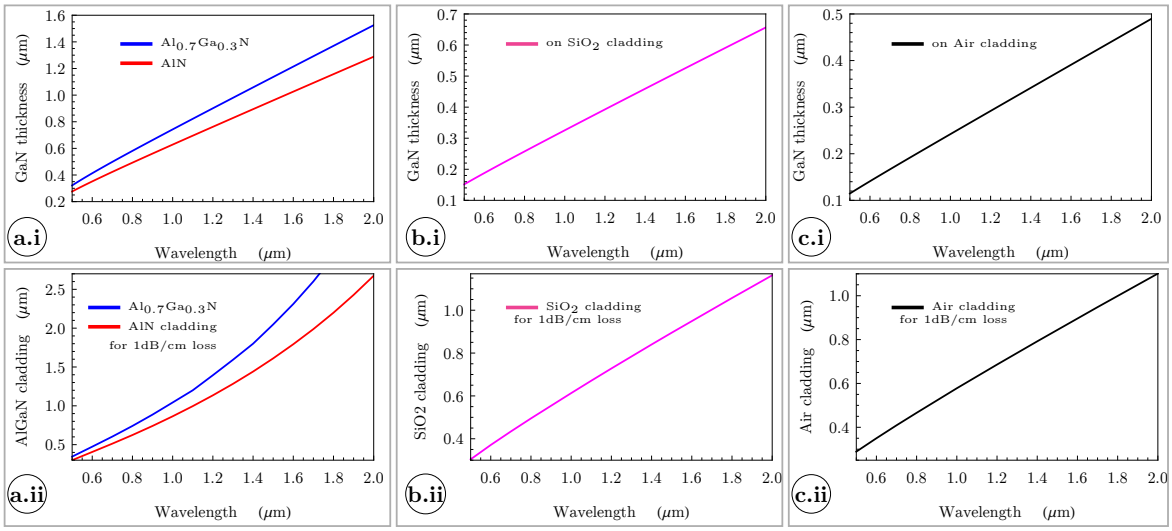

Figure 6.2 – (a.i), (b.i) and (c.i) GaN layer thicknesses that correspond to the TE1 mode cut-off for the AlGaN, SiO_2 and Air cladding respectively. (a.ii), (b.ii) and (c.ii) The thicknesses of the optical cladding necessary for <dB/cm leakage loss for the AlGaN, SiO_2 and Air layers respectively.

The adjusted GaN thickness as a function of the wavelength is presented in Fig. 6.2 for the AlN and $Al_{0.7}Ga_{0.3}N$ claddings in part (a.i), for the SiO_2 cladding in part (b.i), for the air cladding in part (c.i). Using this data we have calculated the thickness of the optical cladding needed to maintain the propagation losses due to the mode leakage below 1dB/cm. The thickness of the different claddings as a function of the wavelength is also presented in Fig. 6.2, the thickness of $Al_{0.7}Ga_{0.3}N$ and AlN in part (a.ii), the thickness of SiO_2 in part (b.ii), the thickness of air in part (c.ii).

From the Fig. 6.2(a.ii) it is clear, that in order to use a mono-mode GaN waveguides at the wavelength of 1.55μm, one needs a >1.5μm AlN cladding layer. As it will be shown in Section 6.2, it is impossible to grow such thick AlN layers without cracks. It is also costly and time consuming. Therefore it is more practical to use the AlGaN cladding for shorter wavelengths. It works fine in the visible spectral region and with some efforts its functionality can be extended up to 1.0-1.2μm wavelength.

Since SiO_2 has a lower refractive index than AlGaN, one needs much thinner SiO_2 optical cladding, see 6.2(b.ii). The only problem is that GaN cannot be epitaxially grown on SiO_2. An alternative approach based on the magnetron sputtering was previously used for the direct growth of nitrides on SiO_2, but the sputtered layers have poor crystalline quality in comparison to the epitaxially grown layers. Sputtered layers have a smaller $\chi^{(2)}$ nonlinearity, they show higher intrinsic losses due to the larger quantity of defects and they cannot be used for an efficient light emission, which significantly undermines the whole idea of the hybrid GaN/Si photonics. Therefore in this PhD project we have studied another approach based on the epitaxial growth on SOI substrates, which allows benefiting from both the SiO_2 optical cladding and the higher material quality for GaN, as it will be explained in Section 6.3.

Obviously, the thinnest isolation layer can be made in theory by an air gap between the guiding GaN layer and Si substrate, see Fig. 6.2(c.ii). It turns out, that this type of structures can also be realized in practice by using a selective etching, as it will be

explained in Section 6.4. Suspended structures seem to be the simplest solution for the isolation problems. Unfortunately, these structures cannot levitate over the substrate and some beams should be used to hold the waveguides. These beam fixation introduce losses, which can be reduced to some extent by optimizing the design, but cannot be completely eliminated. All the solutions presented above have their advantages and disadvantages. Depending on the particular application one solution can be better than the others. In the following sections we will present each particular case in more details.

6.2 AlGaN optical cladding

In Chapter 3 is was explained that GaN was always grown on Si substrates in combination with AlN to avoid the formation of cracks. Indeed, due to the thermal expansion coefficient mismatch between Si and GaN, the cooling from the growth to the room temperature causes tensile stress in the nitride layer leading to the fracturing. The trick consists in growing first an AlN layer with relaxed lattice parameters which can be obtained at high temperature. A subsequent growth of pseudomorphic GaN on top of AlN puts compressive stress on GaN. Under a particular relation between the thicknesses of the different layers the compressive strain at high temperature can compensate for the tensile stress which appears during the cooling-down to room temperature and prevents the fracturing.

As we can see AlN layer can serve both for the stress compensation and the optical isolation. Therefore, it is interesting to study what are the limits of these type of layers and whether it is possible to fabricate low-loss GaN waveguides by using AlN or AlGaN cladding. Below we present the experimental results for two cases: pure AlN optical cladding in Section 6.2.1 and combined AlN/AlGaN/AlN cladding in Section 6.2.2.

6.2.1 AlN optical cladding

In the case of Si substrates, the AlN optical cladding is the most obvious solution for the isolation of the modes guided in the GaN core. In order to test the capabilities of this type of cladding several waveguides were fabricated. We progressively increased the thickness of the GaN and AlN layers. The scheme of the best waveguide A1974 with 1μm GaN and 540nm AlN layer is shown in Fig. 6.3. These are the largest thicknesses that we were able to obtain without cracks. Indeed, the A1974 sample contained also several fractures, but they were concentrated near the border of the wafer, and there was an area of about 1cm^2 in the center free of cracks. This central part of the sample was used for the optical characterization. The samples with a smaller layer thickness are not presented here since they were severely impacted by the mode leakage into the Si substrate.

A waveguide composed of a 1μm GaN layer on top of an AlN substrate is at cut-off for the TM3 mode at a wavelength of 633nm. Therefore, at this wavelength, the waveguide supports 3 TE and 3 TM modes highly confined in the GaN layer. Waveguides supporting three guided modes in the visible region were chosen, since we were interested in studying the second harmonic generation processes based on the nonlinear interactions where the harmonic is guided in one of the first three modes, as it was explained in Chapter 2. For this particular structure the following interactions are possible: 1) between the TM0 pump at 1800nm and the TM1 second harmonic at 900nm; 2) between the TM0 pump at 1140nm and the TM2 second harmonic at 570nm.

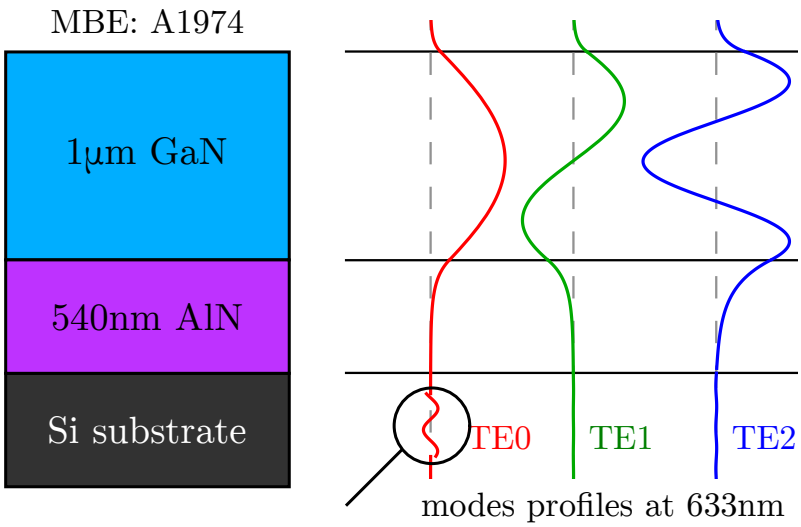

Figure 6.3 – A scheme of A1974 waveguide together with the TE-modes profiles at 633nm wavelength. The zoom indicates the radiation nature of the modes in the Si substrate.

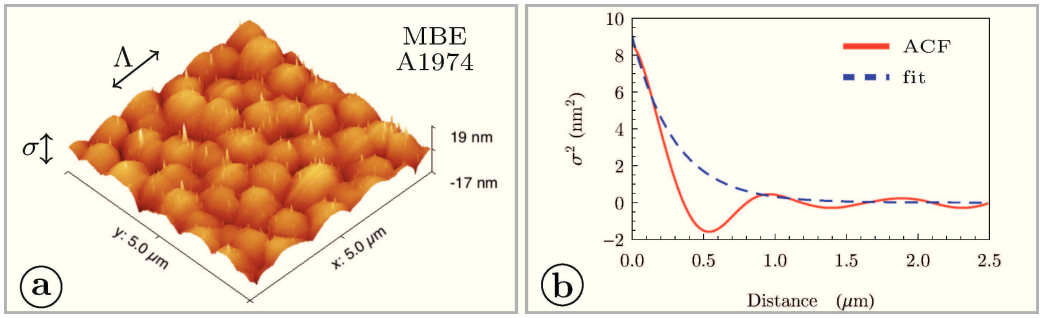

sample	epitaxy	rms, σ	Λ
A1974	MBE	3nm	0.3μm

Figure 6.4 – (a) An AFM image of 5μm by 5μm surface area for A1974 sample grown by MBE technique. (b) Radial autocorrelation function of the surface together with an exponential fit $\sigma^2 \exp(-r/\Lambda)$. The table attached to this figure gives the numerical values of σ and Λ for the sample.

The sample was grown by MBE, so it exhibits the surface roughness shown in Fig. 6.4(a), which is typical for this growth technique. The amplitude of the roughness σ is about 3nm and the characteristic lateral scale Λ is about 300nm. These parameters are obtained from the exponential fit $\sigma^2 \exp(-r/\Lambda)$ of the radial autocorrelation function of the surface show in Fig. 6.4(b). It should be noted, that the amplitude σ is equal to the standard rms roughness within a few percent accuracy. In the previous Chapter 5 it was shown both theoretically and experimentally that this type of surface roughness is responsible for the coupling between the guided and the radiated modes, which causes propagation losses. The estimation based on the same approach was also done for the TE modes in A1974 sample and they are presented in Table 6.1.

In addition to the losses caused by the surface roughness, the leakage to the Si substrate was estimated at the 633nm wavelength. As one can see from the Table 6.1 the losses combined from the surface roughness and the leakage match the losses measured ex-

Sample	MBE: N2291 at 633nm wavelength					
Mode	TE0	TE1	TE2	TM0	TM1	TM2
Losses (dB/cm) experiment	1.4±0.9	6±1	13±2	1.3±0.7	8±2	-
Losses (dB/cm) due to Si	0.03	0.3	4	0.1	1	20
Losses (dB/cm) due to roughness	1	4	10	-	-	-

Table 6.1 – Propagation losses in dB/cm for the TM- and TE-modes in A1974 waveguide. For the experimental values, the margin of error is estimated taking into account the losses variation depending on the position on the sample and a ±1mm uncertainty in the propagation distance measurement.

perimentally, which means that these are the two main sources of the propagation losses. Images of the propagation and m-lines for three TE modes are displayed in Fig. 6.5. These images are similar to those for the waveguides on sapphire substrates presented in the previous Chapter 5. The only difference is that the images for Si substrates are cleaner and clearer because Si absorbs all the light scattered towards the substrate.

As it was already indicated, these are the maximal layer thicknesses that we were able to obtain without cracks. Nevertheless, the propagation of the TM2 mode is still limited by the leakage at the wavelength of 633nm, where the linear characterization was done, see Table 6.1. It is true, that the second harmonic for this structure is meant to be generated at 570nm and there will be only 2dB/cm loss due to the leakage for the TM2 mode at this wavelength. But, unfortunately, 540nm AlN optical cladding is still not enough to isolate the TM0 pump at 1140nm, for which there is a >30dB/cm leakage. The results of this section clearly show that the pure AlN cladding may be suitable for the visible spectral region, but it does not work in the mid-infrared region due to the limitations on the layer thickness imposed by the strain. Since, the SHG requires waveguides that work well at both second harmonic and pump wavelengths, alternative solutions should be found.

6.2.2 AlN/AlGaN/AlN optical cladding

In the previous section it was demonstrated that the pure AlN cladding cannot provide a sufficient modes isolation in the near-infrared. In order to obtain the isolation, thick >600nm AlN layers have to be used, which are impossible to grow due to the tensile stress issues. This tensile stress has to be compensated for by some compressive stress imposed on the GaN layer at growth temperature. The intensity of these compressive stresses depends on the quality of the AlN layer. The better the AlN layer the more intense is the compressive stress one can introduce to the GaN layer. Therefore, it is possible to increase the AlN layer thickness only if its crystalline quality can be preserved. This can be obtained by replacing pure AlN cladding by a AlN/AlGaN/AlN optical cladding instead, as it is shown in Fig. 6.6. The thin 15-30nm AlN layer grown on top of the AlGaN layer has a much better crystalline quality than the thick 540nm AlN layer in Fig. 6.3, so it puts more compressive stress and allows to grow thicker structres.

AlN/GaN/AlN claddings were known previously for their capacity to reduce the tensile stresses. They are widely used for the epitaxial growth of several micrometres thick GaN

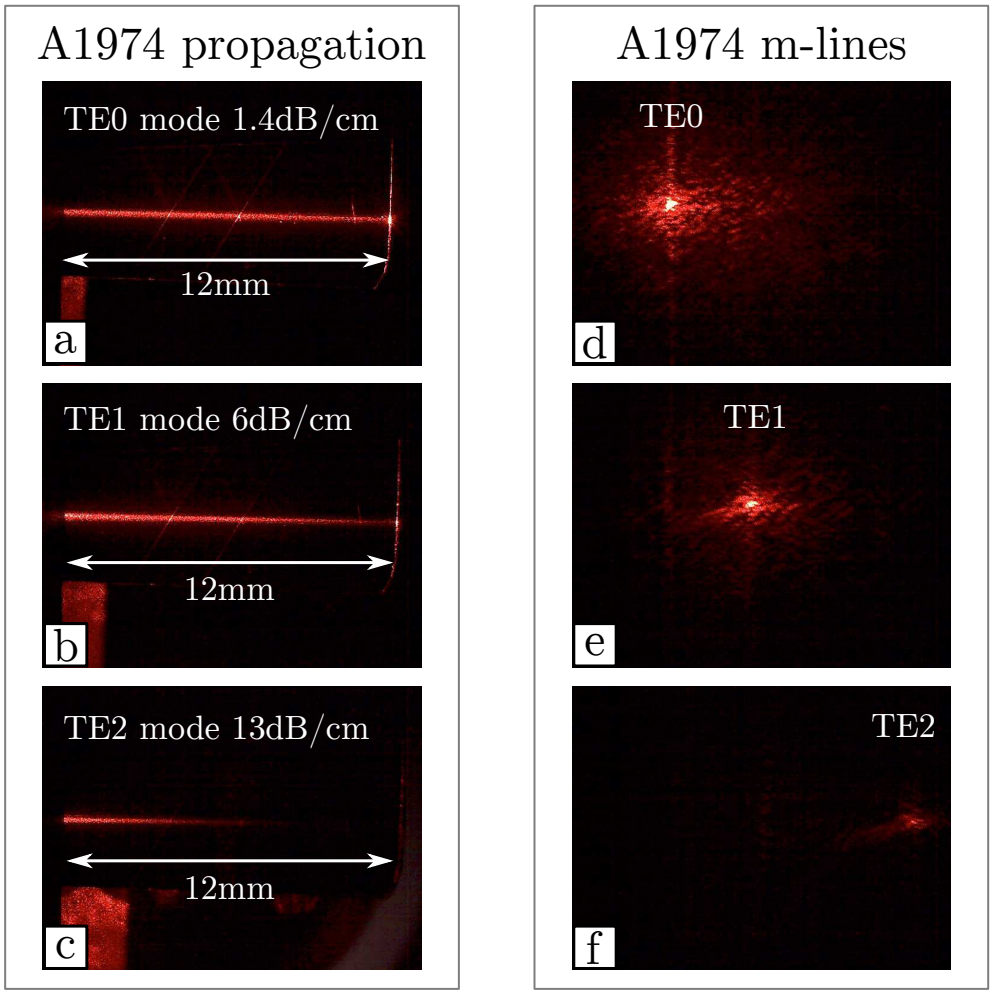

Figure 6.5 – (a)-(c) Images of the light diffused along the propagation lines of TE0-TE2 modes in A1974 sample with the light injection in the modes TE0 in part (a), TE1 in part (b) and TE2 in part (c) respectively. (d)-(f) Images of the m-lines for the A1974 sample with the light injection in the modes TE0 in part (d), TE1 in part (e) and TE2 in part (f) respectively.

layer which are crack-free. But it is also commonly known that this cladding layers contain multiple buried internal cracks and voids, which appear during the growth of AlN. AlN is in tension during growth and eventually cracks. This cracks are partially or totally refilled during epitaxy by mass transport of GaN, which leaves voids in the GaN layer. In the beginning of this PhD project it was verified that these buried cracks and voids perturb the modes propagation. Therefore these types of structures were rejected for the photonics applications, although they work quite fine for the GaN based high-electron-mobility transistors (HEMT). Closer to the end of this project it was discovered, that when GaN in the AlN/GaN/AlN cladding is replaced by the AlGaN with a high Al content, the buried cracks and voids disappear, because the smaller lattice mismatch between AlGaN and AlN tends to reduce or even eliminate the formation of cracks during the AlN epitaxy.

The AlN/AlGaN/AlN cladding opens new interesting opportunities for the GaN waveg-

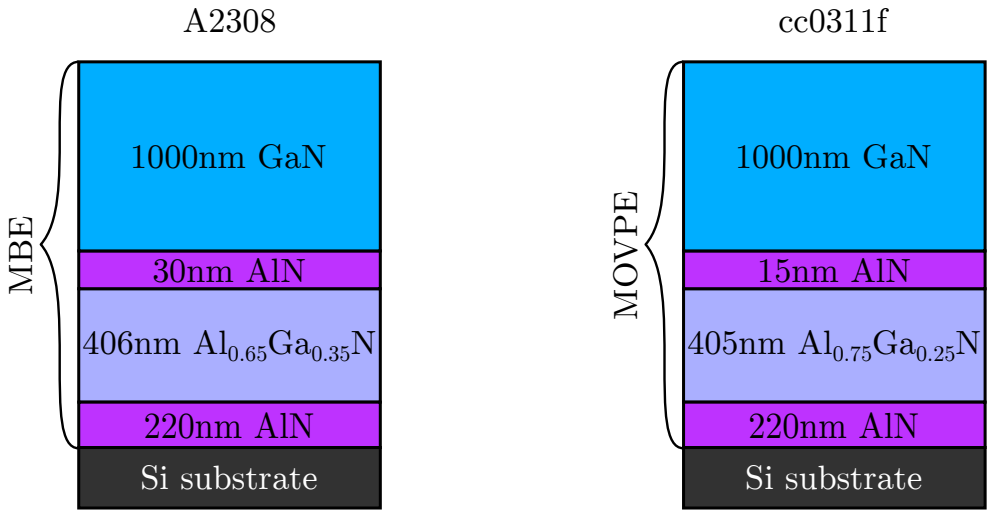

Figure 6.6 – Schemes of the two planar waveguides. A2308 waveguide was grown by MBE and cc0311f waveguide was grown by MOVPE.

uides grown on Si substrates. In the laboratory, these structures were initially developed for HEMTs and were grown by MOVPE technique. But with some additional modifications and efforts the same structures can also be grown by MBE. In order to test these structures for the photonic applications, two waveguides were fabricated A2308 grown by MBE and cc0311f grown by MOVPE, see Fig. 6.6. Since the two structures are nearly identical, the results presented below give the information not only about the performance of the optical cladding, but also allow for a direct comparison of two waveguides grown by MBE and MOVPE.

cc0311f waveguide is designed for frequency doubling between a pump at 1140nm in the TM0 mode and a second harmonic at 570nm in the TM2 mode. Moreover, using a 1μm thick GaN layer corresponds to be at cut-off for the TM3 mode at 570nm, and so the TM2 mode at this wavelength is highly confined in the GaN layer. The structure of the A2308 waveguide is similar to that of the cc0311f sample and it allows for second hamonic generation based on modal phase matching between a pump at 1150nm in the TM0 mode and a second harmonic at 575nm in the TM2 mode. The thickness of 405nm for the AlGaN layer in the cladding was chosen, since it was successfully tested many times for other applications.

The main difference between these two samples comes from their surface morphology, as it is shown in Fig. 6.7. As one can see from the table attached to this picture, the amplitude of the roughness σ is almost the same for the two cases, but there is a large difference for the in plane characteristic dimension Λ. As it was already explained in the previous Chapter 5 the high spatial frequencies present in the MBE roughness are responsible for the coupling between guided and radiated modes, which causes losses in addition to the modes leakage to the Si substrate. The experimentally measured losses for the TE modes at 633nm are summarized in Table 6.2. This table also give the estimations for the losses due to the mode leakage and due to the surface roughness. The images of the TE-modes propagation are shown in Fig. 6.8.

In contrast, the much larger in plane characteristic dimension Λ of the MOVPE surface roughness is responsible for modes diffusion in the plane of the waveguide. This diffusion

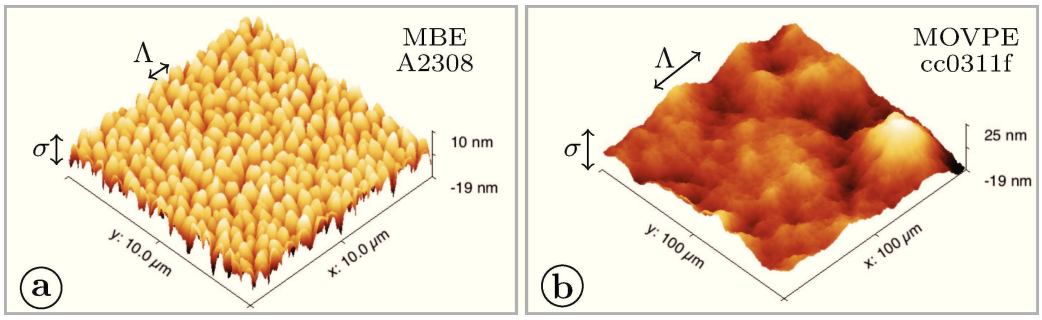

sample	epitaxy	rms, σ	Λ
A2308	MBE	4.1nm	0.5μm
cc0311f	MOVPE	5.2nm	15μm

Figure 6.7 – (a) An AFM image of 10μm by 10μm surface area for A2308 sample grown by MBE technique. (b) A similar 100μm by 100μm AFM scan for cc0311f sample grown by MOVPE. The roughness amplitude σ and the characteristic lateral scale Λ are determined from an exponential fit $\sigma^2 \exp(-r/\Lambda)$ of the autocorrelation function for the surfaces. The table attached to this figure summarizes the numerical values of σ and Λ for these two samples.

Sample	MBE: A2308		
Mode	TE0	TE1	TE2
Losses experiment (dB/cm)	3.5	9	22
Losses due to Si (dB/cm)	0.01	0.2	5
Losses due to roughness (dB/cm)	2	8	17

Table 6.2 – Propagation losses in dB/cm for the TE-modes in A2308 waveguide at the 633nm wavelength.

can already be noticed in Figs. 6.8(e) and (f). More direct confirmation of this diffusion is visible on the m-lines images in Fig. 6.9(e) and (f). We were not able to estimate the propagation losses for the cc0311f sample due to the absence of a monotonic evolution of the light intensity along the propagation lines, see Fig. 6.8. Nevertheless, from the images it is clear, that cc0311f sample shows longer propagation distances in comparison to A2308 sample, although the modes are diffusing in the plane of the cc0311f waveguide. Table 6.3 proves that this difference cannot be explained by the slight difference in the optical cladding for their waveguides, which could lead to the difference in the mode leakage. The losses due to the modes leakage to the Si substrates are nearly identical for these waveguides, as one can see from the Tables 6.2 and 6.3.

Sample	MOVPE: cc0311f		
Mode	TE0	TE1	TE2
Losses due to Si (dB/cm)	0.01	0.16	3.8

Table 6.3 – Losses due to the modes leakage for the TE-modes in cc0311f waveguide at the wavelength of 633nm.

The results presented here are very similar to the results for the waveguides grown on

sapphire substrates presented in the previous Chapter 5. In this section we get a more direct confirmation of the difference between the waveguides grown by MBE and MOVPE as we were able to grow identical structure by the two technique which was not possible on sapphire substrates.

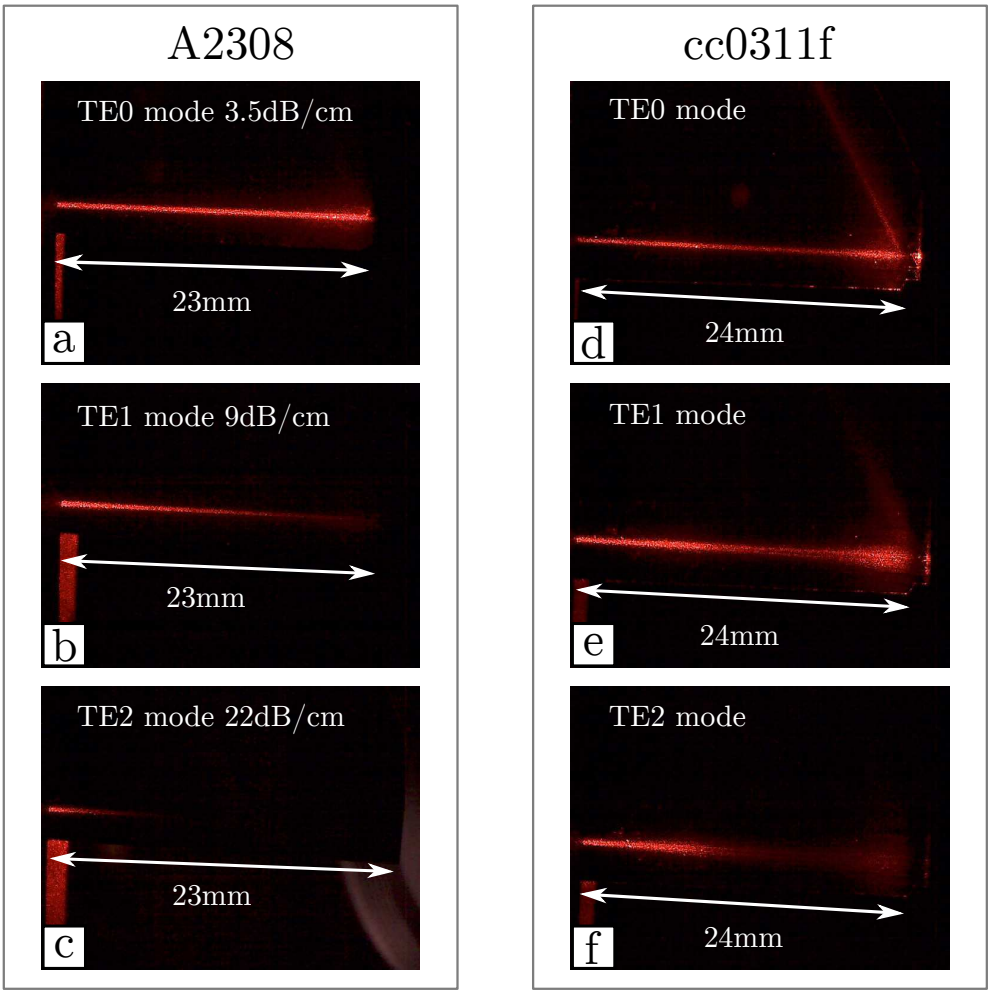

Figure 6.8 – (a)-(c) Images of the light diffused along the propagation lines of TE0-TE2 modes in A2308 sample. (d)-(f) The same images for cc0311f sample. For cc0311f sample the modes have longer propagation distance in comparison to A2308 sample, but they also show a larger diffusion in the plane of the waveguide.

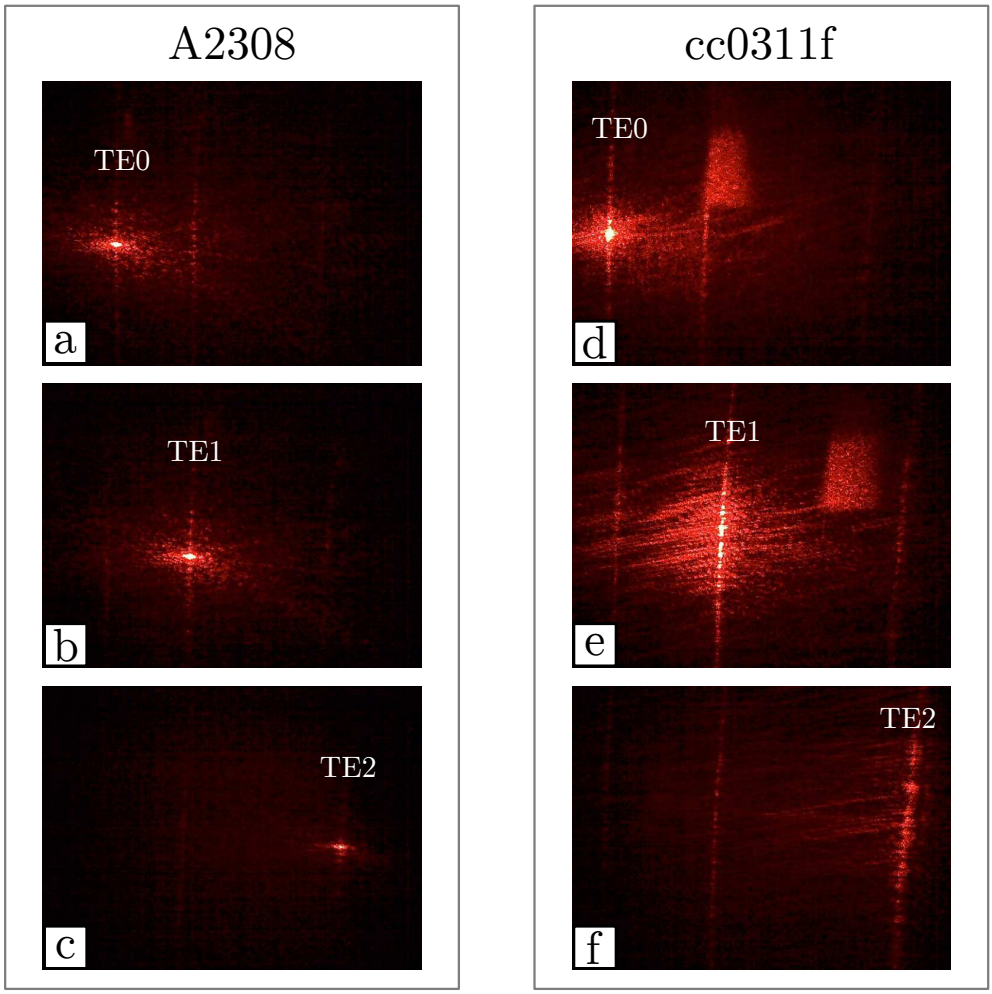

Figure 6.9 – (a)-(c) Images of the m-lines for A2308 sample with the light injection in the modes TE0 in part (a), TE1 in part (b) and TE2 in part (c) respectively. (d)-(f) The similar images for cc0311f sample. Some residual inter-modal coupling is visible on all the images. For A2308 sample, as one goes from the fundamental mode TE0 to the higher order modes, the light intensity of the m-lines decreases. In contrast, for cc0311f sample the m-lines become more diffused for the higher order modes.

Analogously to what was done on sapphire substrate, one half of the A2308 wafer was taken to benefit from the MOVPE regrowth of a thin (60nm) GaN layer. After this regrowth, the amplitude σ of the surface roughness decreased from 4 to 1 nm and the lateral scale Λ was increased from 0.5 to 5 μm, as it is shown in Fig. 6.10.

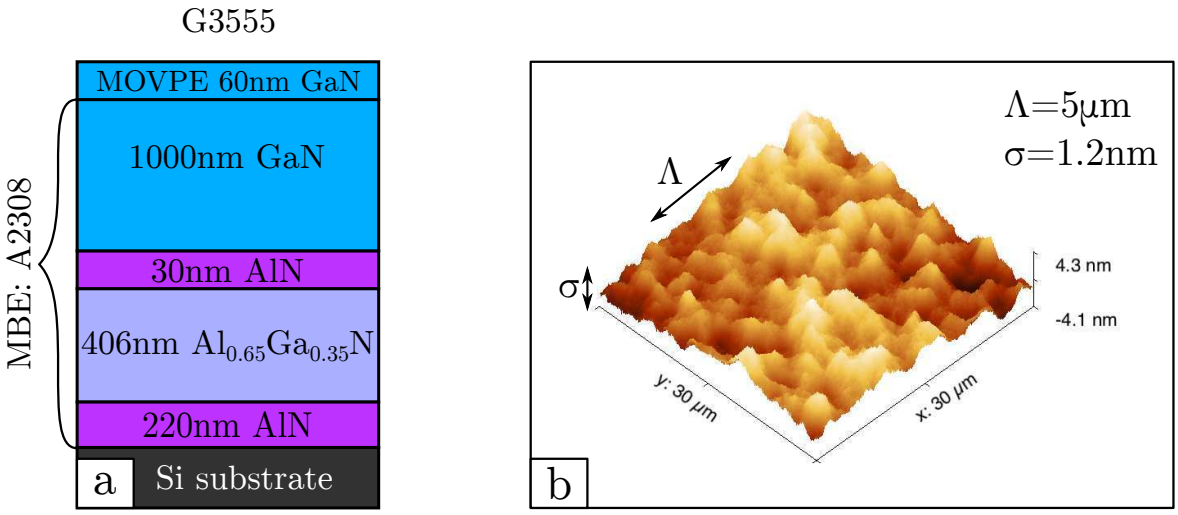

Figure 6.10 – (a) G3555 waveguide is obtained by a 60 nm GaN layer regrowth on top of A2308 sample. (b) An AFM image of 30μm by 30μm surface area for G3555 sample.

These changes had a positive impact on the propagation losses, as one can see from the Table 6.4 and Figs. 6.11(a)-(c). The modeling of the leakage provided in this table also confirms that this improvement cannot be explained just by the fact that modes leakage is reduced due to the increased GaN layer thickness. Therefore, the improvement of the propagation losses is due to the changes in the surface morphology. Moreover, the m-lines diffusion is also absent for this waveguide, as one can see in Fig. 6.11(d)-(f).

Sample	MOVPE: G3555		
Mode	TE0	TE1	TE2
Losses experiment (dB/cm)	1.5	5	8
Losses due to Si (dB/cm)	0.01	0.1	3

Table 6.4 – Propagation losses in dB/cm for the TE-modes in G3555 waveguide at the 633nm wavelength.

These results demonstrate that MBE grown waveguides covered with a thin MOVPE surface layer are better than the similar structures grown by only one of these techniques. The thin MOVPE layer drastically reduces the scattering losses, which are characteristic for the MBE grown waveguides, wihout introducing any in-plane diffusion, which is characteristic for the MOVPE grown waveguides. This happens, because the 60nm thickness of this layer is large enough for the elimination of the typical MBE roughness, but thin enough to prevent the development of the typical MOVPE roughness.

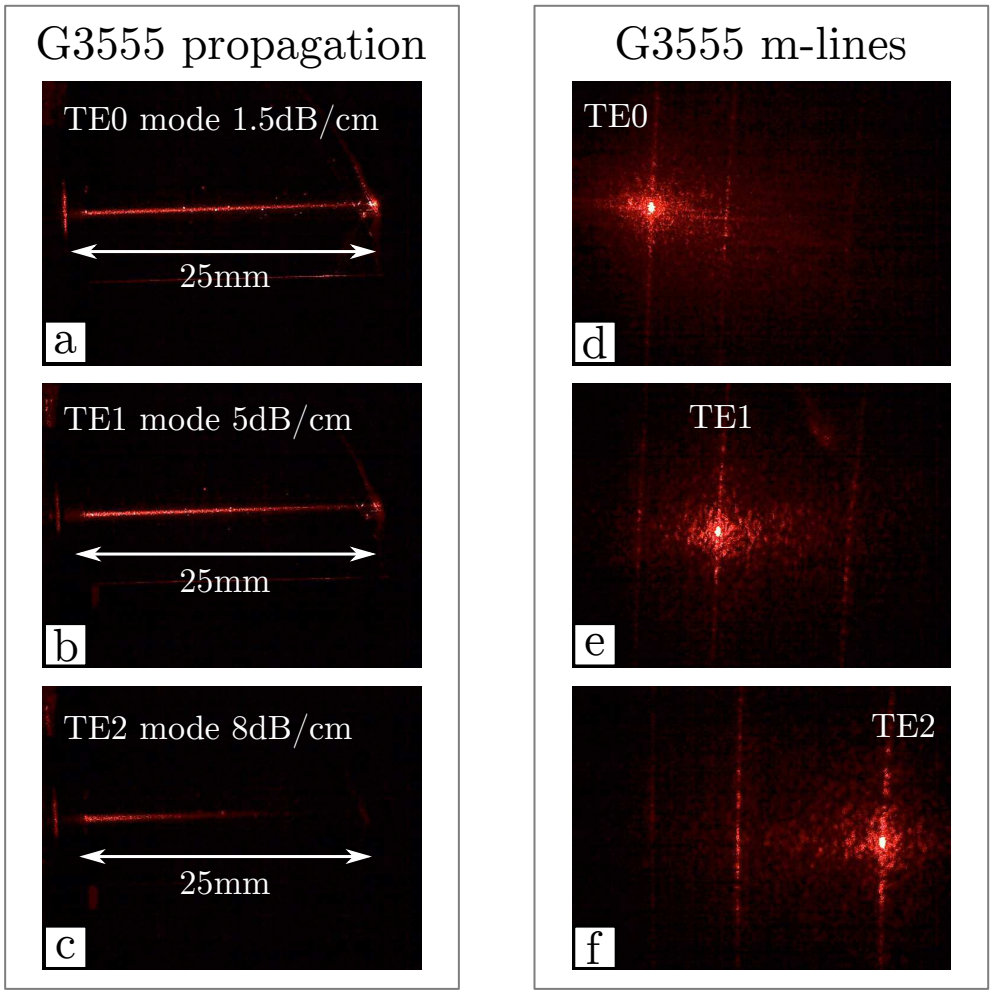

Figure 6.11 – (a)-(c) Images of the light diffused along the propagation lines of TE0-TE2 modes in G3555 sample with the light injection in the modes TE0 in part (a), TE1 in part (b) and TE2 in part (c) respectively. These images confirm the reduction of the propagation losses in comparison to A2308 sample. (d)-(f) Images of the m-lines for G3555 sample with the light injection in the modes TE0 in part (d), TE1 in part (e) and TE2 in part (f) respectively. The diffusion of the m-lines is reduced in comparison to cc0311f sample.

Throughout the manuscript we were systematically presenting the estimations of the propagation losses induced by the surface roughness. The typical amplitude of this roughness is only a few nanometers, and one could have concluded that it should not have any impact on the propagation of a wave at 633nm. The simplest direct proof, that this roughness indeed has an important impact on the propagation of visible light, was obtained during the sample observation under a microscope. Two samples A2308 and G3555, which are two parts of the same wafer, were put together for the observation, as it is shown in Fig. 6.12(a). It was a great surprise to see that only one half of the wafer had a bright spot under the microscope illumination. It shows, that the few nanometers roughness with high spatial frequencies in the case of A2308 sample can indeed scatter the light towards the observer by inducing large deviations of the wave vector. This is no longer the case when the sample is covered with the thin MOVPE layer.

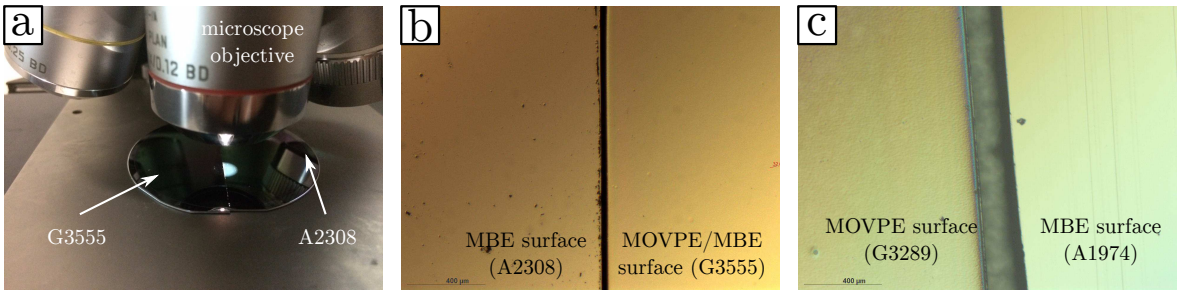

Figure 6.12 – (a) Under the illumination the A2308 surface diffuses the light towards the observer, as a bright spot (semi-disk) is visible on the surface of the sample. For G3555 sample the diffusion disappears, the surface remains dark under the illumination. (b) A comparison of the surfaces for A2308 and G3555 samples under x5 microscope magnification. (c) A comparison of the surfaces for A1974 and G3289 samples under x5 microscope magnification. A large-scale surface roughness is visible for the G3289 sample.

The low spatial frequencies of the MOVPE roughness cannot create such a large deviations of the wave vector. At the same time, the observation through the microscope with a x5 magnification gives the impression that the MOVPE surface is rough while the MBE surface seems to be completely smooth, see Fig. 6.12 (c). This is due to the fact that, with this magnification, the roughness of the MBE surface cannot be resolved, while the large-scale roughness of the MOVPE is observable.. It should be noted that the thin MOVPE layer grown on top of the MBE surface seems to be as smooth as the initial MBE surface under the microscope, see Fig. 6.12(b).

6.2.3 Observations of the second harmonic generation

The waveguides described above were designed for the generation of the second harmonic around 570nm. These waveguides still have some residual losses 2-3dB/cm for the TM2 mode at 570nm due to the leakage, but it can be tolerated. In contrast, the TM0 pump at 1140nm is highly impacted by these losses (>10dB/cm), which means that a thicker optical cladding is needed.

In order to resolve this issue, a waveguide with a thicker optical cladding was fabricated. This waveguide had the same 1μm GaN layer but a much thicker optical cladding:

77nm AlN/715nm $Al_{0.65}Ga_{0.35}N$/300nm AlN, and the grown layerwas not cracked. This cladding would be enough for the isolation both of the pump and the second harmonic from the Si substrate. Unfortunately, there was a contamination of an unknown origin during the growth and the sample surface contained numerous point defects. As a result, this sample was showing larger propagation losses at 633nm than G3555 waveguide described in the previous section. The AlN/AlGaN/AlN cladding was studied at the end of this PhD project and there was no time for the fabrication of an additional sample. Nevertheless, we are convinced that this type of cladding can give a viable solution for the modes isolation both in the visible and the near-infrared regions.

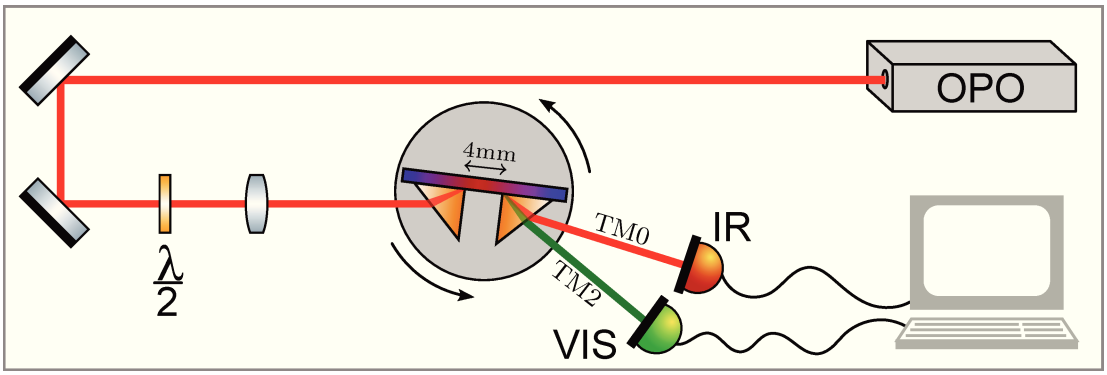

Figure 6.13 – A general scheme of the second harmonic generation experiment for the planar waveguides.

Since the desired structure with a sufficiently thick optical cladding was not obtained, A2308, cc0311f and G3555 waveguides were used for the second harmonic generation. The performance of these waveguides is limited by high propagation losses, therefore, the main goal of the experiments was a simple observation for the SHG and a comparison between the theoretical and experimental values for the phase matching wavelength.

The same experimental set-up, that was described in details in Chapter 4, was used for the SHG experiments, see Fig. 6.13. The pump from the OPO was coupled to the planar waveguides by the first prism and after about 4mm propagation distance decoupled by the second prism. A photo of the decoupled pump and second harmonic for cc0311f sample is shown in Fig. 6.14(a). The acceptance curves, which give an averaged second harmonic power as a function of the pump wavelength, were obtained for all three samples and are presented in Figs. 6.14(b)-(d). The spectral width of this curves corresponds to about 4mm propagation distance in the waveguides and it is in agreement with the theory. The phase matching wavelengths are also close to the theoretically calculated values. Although these figures indicate the average power both for the pump and the second harmonic, these values cannot be used for the correct estimation of the SHG efficiency due to high propagation losses.

The new AlN/AlGaN/AlN optical cladding has allowed an important progress towards mode isolation in the visible and near-infrared spectral regions. Thanks to the obtained improvements it became possible to realize the SHG experiments in GaN waveguides directly grown on Si substrates. The obtained results demonstrate that the thickness of this cladding can be further increased without leading to crack formation. This will allow for a complete isolation of the modes involved in the nonlinear interactions. The main advantage of this approach is its simplicity, since the structures can be grown by standard

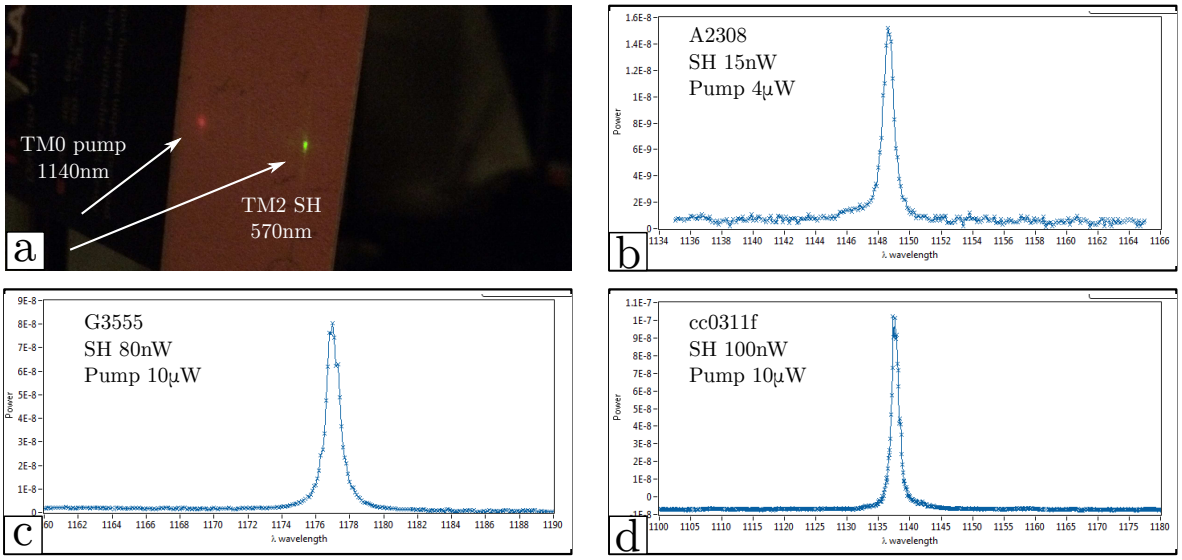

sample	A2308	G3555	cc0311f
theory	1148nm	1178nm	1144nm
experiment	1148.6nm	1177.1nm	1137.6nm

Figure 6.14 – (a) A photo of the decoupled pump and second harmonic for cc0311f sample. (b)-(c) Acceptance curves for A2308, G3555, c0311f samples respectively.

epitaxy techniques on cheap and widely available Si substrates.

In our case we have used a combination of MBE and MOVPE growth for the fabrication of the our best waveguides. It was done due to the necessity to reduce the surface roughness. In theory, the MBE surface can be smoothed by a high temperature annealing without additional MOVPE regrowth. We were testing this approach, but after several attempts we were not able to find proper conditions or the annealing, therefore a simpler approach with the additional regrowth was used. The main drawback of this approach is a possible contamination of the surface between the two epitaxy runs. It was often introducing some additional point defects to the waveguides, but overall improvement due to the loss reduction was still more important, than the negative impact of these defects. The point defects can always be eliminated by using a cleaner fabrication environment and therefore don't impose any fundamental limits on this approach.

6.2.4 Test of ridge waveguide fabrication and planar polarity inversion

Prior to the fabrication of A2308, G3556, cc0311f waveguides supporting multiple modes in the visible regions, a mono-mode at 633nm waveguide G3440 was fabricated. The structure of this waveguide is presented in the SEM image in Fig. 6.15(a). Similarly to the previous cases the sample was predominantly grown by MBE with an additional regrowth of a thin MOVPE surface layer. In this particular case the AlN layer below the GaN guiding layer was omitted, since the whole structure is relatively thin and does not suffer from excessive tensile stress. Therefore, the AlN layer putting additional compressive stress was not needed in this situation.

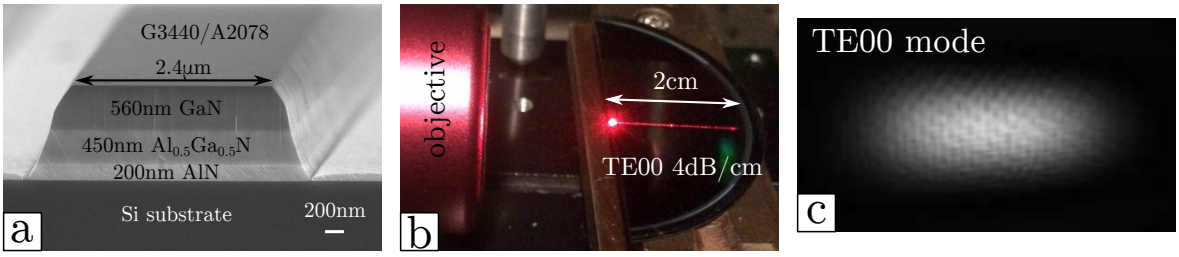

Figure 6.15 – (a) An SEM image of G3444 waveguide. (B) TE00 mode propagates over 2cm distance showing about 4dB/cm losses at 633nm. (a) An image of the TE00 mode decoupled from the waveguide.

A planar guiding layer was showing 7dB/cm for the TE0 mode at 633nm before the MOVPE regrowth and 3dB/cm after the surface was smoothed. This planar layer was used for the fabrication of the ridge waveguides shown in Fig. 6.15(a). The main goal was to test the concept of large 2.5μm ridge waveguides. The main idea behind this concept is that the fundamental TE00 mode should get less impact from the wall roughness since only a small fraction of the modal power is guided near the walls in a large waveguide. This ridge waveguide acts almost as a planar waveguide at the 633nm wavelength. It supports multiple modes with several lobes in the lateral direction (TE00, TE01, TE02,...) but it is still mono-mode in the vertical direction. The light can be predominantly injected in the fundamental mode and there is no significant inter-modal coupling, as is shown in the image of the light decoupled from the waveguide in Fig. 6.15(c). Moreover, the propagation losses, that were estimated by using the same technique as for planar waveguides, are as low as 4dB/cm, which is a quite remarkable result for the ridge waveguides. Although one can argue whether the loss measurement technique, which is based on the estimation of the scattered light attenuation along the propagation line, can be used for the ridge waveguides, the photo in Fig. 6.15(b) shows that the TE00 mode can propagate over 2cm distance, which would be impossible in the case of higher propagation losses.

These results show that large ridge waveguides give both the advantages of the 2D mode confinement and low propagation losses due to the reduced impact of the walls roughness. In the future, this type of structure with a thicker GaN layer can allow for the realization of the phase matching conditions by using the modes with lobes in vertical direction (TM00, TM10, TM20), which would have properties close to the TM0, TM1 and TM2 modes in an equivalent planar waveguide and will be less impacted by the wall roughness. It is also worth mentioning, that the nearly ideal injection facet shown in Fig. 6.15(a) was obtained by a simple cleavage of the wafer, which is much easier for Si substrates in comparison to sapphire substrates, for which we were not able to obtain good injection facets, as it was explained in the previous Chapter 5.

In addition to the simpler cleavage, Si gives other numerous fabrication advantages. They were used in order to test a new approach for the planar polarity inversion based on a wafer bonding. The whole process was tested in LETI laboratory. The idea behind the wafer bonding is schematically demonstrated in Fig. 6.16. Two thin AlN layers were grown on 2 inch Si wafers in CRHEA and were sent to LETI laboratory. In LETI the following fabrication steps were done: 1) the samples were bonded head-to-head though a thin 100nm SiO_2 layer, this gave two AlN layers with opposite polarities; 2) one Si substrate was removed by using a combination of mechanical and chemical etching; 3) the

obtained structure was bonded to a transparent in the visible and UV range substrate (sapphire in this case). The final goal was to remove the second Si substrate, but during the annealing procedure a delamination occurred and the sample was destroyed. There was only one fabrication test.

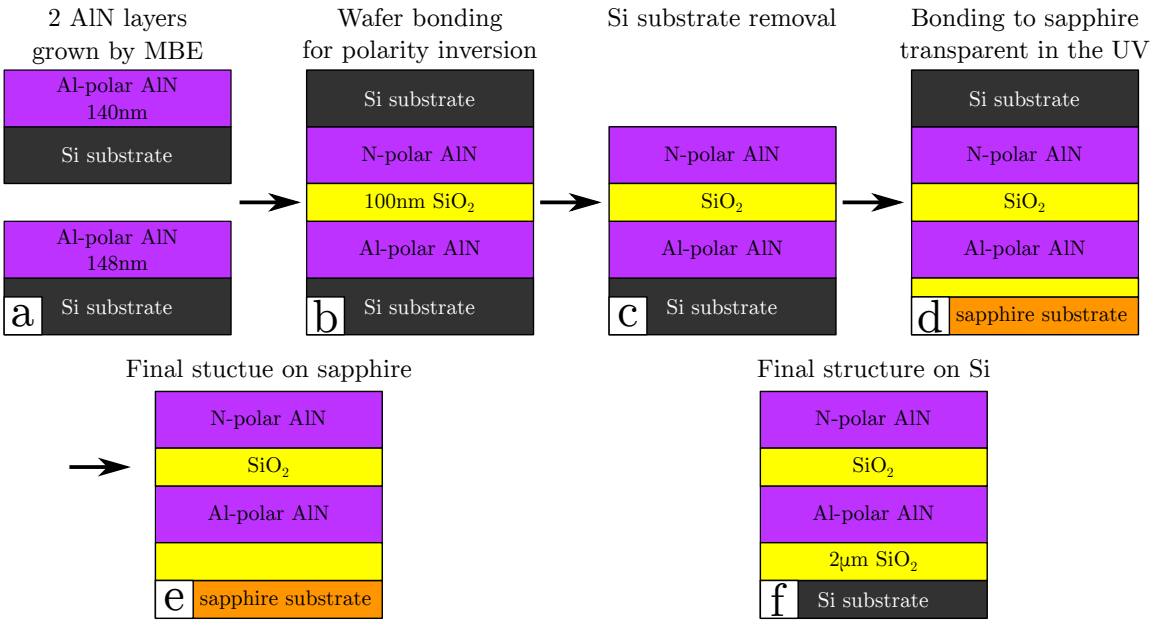

Figure 6.16 – (a) Two AlN layers grown by MBE on Si substrates. (b) The AlN layers were bonded head to head with a help of a thin 100nm SiO_2 layer. This gives a structure with a planar polarity inversion. (c) Si substrate was removed. (d) The obtained structure was bonded to a sapphire substrate. At this stage of the fabrication the delamination occurred during the annealing. (d) The final structure could be obtained with the second Si substrate removal. (e) The same structure can be realized on Si substrates with 2μm oxide layer.

The final structures that could be obtained are shown in Figs. 6.16(e) and (f). The approach based on the wafer bonding allows to obtain AlN waveguides with the planar polarity inversion, which can significantly improve the SHG efficiency, as it was demonstrated in Chapter 2. An optimization of the bonding process will be the subject of future studies.

6.3 SOI substrates

In the previous section we have discussed AlGaN-based optical claddings. We have shown, that in order to isolate the modes in the near-infrared region one needs AlGaN layers with a total thickness exceeding 1μm, which can be a difficult goal to achieve. On the other hand, the modes isolation in the visible region is a more simple task. Based on these two facts we have decided to test SOI substrates instead of pure Si substrates.

A very specific SOI substrate with a thin 20nm Si layer and a thick 500nm oxide was also kindly provided by LETI laboratory, see Fig. 6.17. The idea behind this particular structure is simple. It allows to use a combination of AlN and SiO_2 claddings for the

isolation of the modes guided in the GaN layer. At it was shown in Section 6.1, SiO_2 is a more efficient optical cladding due to its low refractive index. Unfortunately, GaN cannot be epitaxially grown directly on SiO_2, therefore a Si layer should be used in any case. The Si layer is highly absorbing in the visible region and it still has some residual absorption in the near-infrared region up to the 1.3μm wavelength. Therefore, in order to isolate the modes guided in GaN from the Si, the AlN layer is needed. In this case the isolation is needed only in the visible regions, which can be easily done, as it was shown in Section 6.2.1. Moreover, a very thin 20nm Si layer was used on top of the oxide, so it does not support any guided modes. Basically, the modes guided in GaN are interacting with the thin 20nm Si layer only though the evanescent field, which significantly reduces the impact of the Si absorption. On the other hand, above the 1.3μm wavelength the thin 20nm Si layer does not absorb and the combination of AlN and SiO_2 claddings serves for the modes isolation.

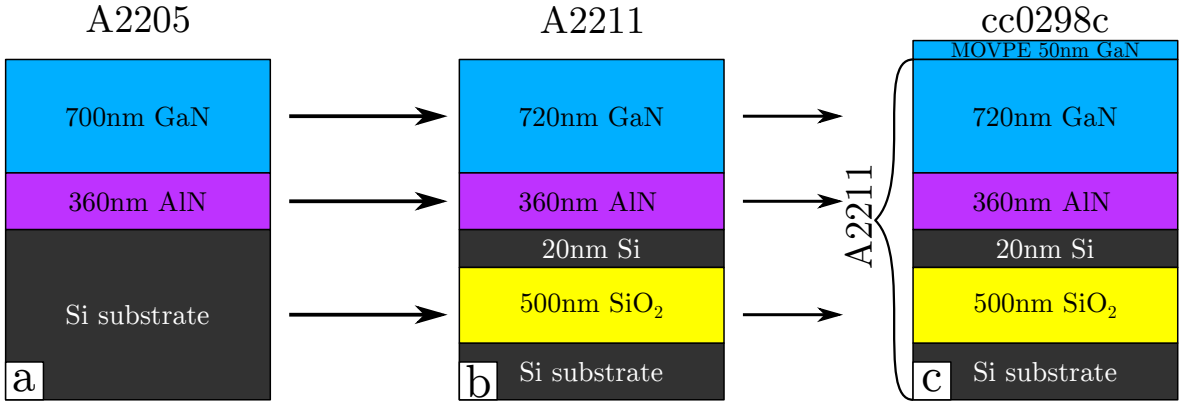

Figure 6.17 – (a) A2205 test structure grown on Si substrate. (b) The same waveguide grown on SOI substrate. (c) The surface of A2211 sample is smoothed by a thin MOVPE layer.

Prior to the growth on SOI substrates a test structure A2205 was grown on Si in order to verify the strain issues, see Fig. 6.17(a). The obtained layer contained only several cracks localized near the wafer border. Almost identical layers were regrown on SOI substrate, see Fig. 6.17(b). The layers thickness was chosen to allow for phase matching between TM0 pump at 1000nm and TM2 second harmonic at 500nm, where both of them are no longer limited by losses due to the absorption or leakage.

Unfortunately, in the case of SOI substrate numerous fractures appeared during the cooling-down process (more than 60 fractures traversing the mode propagation on 3cm distance). The conclusion was made, that the stress compensation does not work in the same way for SOI substrates. Ideally, the growth procedure on SOI substrates had to be recalibrated, but we did not have enough time nor a sufficiently large number of substrates available for multiple tests. Therefore, an alternative approach based on the growth on patterned SOI was used, as it will explained in the next Section 6.3.1.

It is interesting to notice, that the fracture follow three particular crystalline direction and have 60° angles between them. When the mode propagation is aligned with one fracturing direction, the mode does not seem to be significantly impacted by the fractures, as confirms Fig. 6.18(a). But when the sample is rotated by a few degree, the perturbation becomes very significant, see Figs. 6.18(b) and (c). This can be explained by the fact

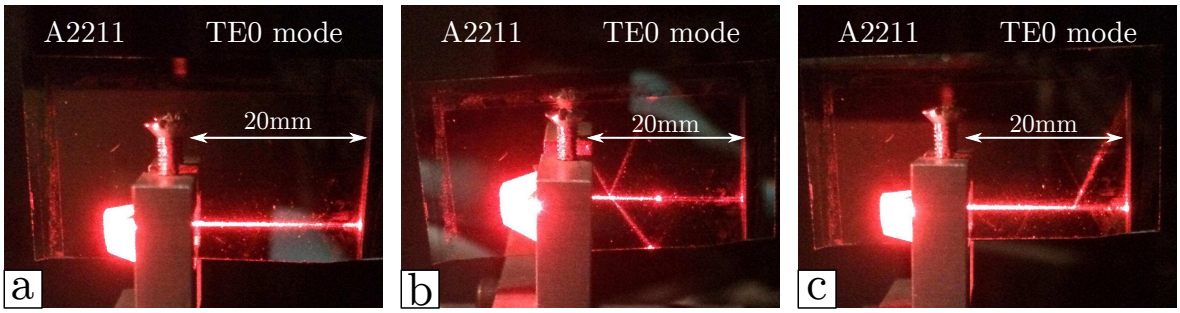

Figure 6.18 – (a)-(c) The impact of the fractures on the TE0 mode propagation in A2211 sample.

that large $>1\mu$m fractures define a set of ridge waveguides aligned in one direction in the planar layer. When the direction of the injection is precisely aligned with these ridge waveguides the perturbation is minimal. When the alignment is not precise, a significant coupling to the other principal fracturing directions can be observed.

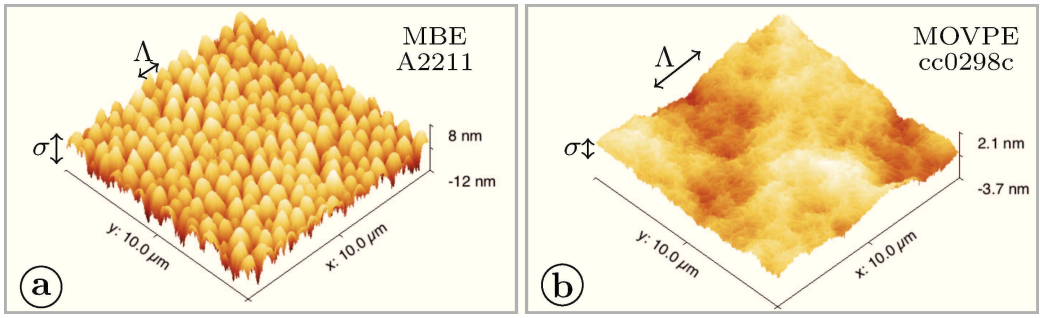

sample	epitaxy	rms, σ	Λ
A2211	MBE	2.8nm	0.4μm
cc0298c	MOVPE	0.7nm	2μm

Figure 6.19 – (a) An AFM image of 10μm by 10μm surface area for A2211 sample. (b) A similar 10μm by 10μm AFM scan for cc0298c sample. The roughness amplitude σ and the characteristic lateral scale Λ are determined from an exponential fit $\sigma^2 \exp(-r/\Lambda)$ of the autocorrelation function for the surfaces. The table attached to this figure summarizes the numerical values of σ and Λ for these two samples.

For these reasons the sample could be in principle used for the further characterization. Therefore, a standard MOVPE regrowth procedure was done. It had a positive impact on the surface roughness at the μm-scale as it can be seen from Figs. 6.19. Unfortunately, the large-scale impact of this regrowth was negative, see Figs. 6.20(a)-(c). The photos shown in part (c) of this figure demonstrate that the surface of cc0298c sample became a "dirty mirror". As a result the propagation distance of the TE0 and TM0 modes was significantly reduced. It turns out that the high temperature MOVPE regrowth does not work well on the highly fractured layers, which we do not completely understand.. To conclude, some experiments could be done with the MBE grown sample but, since the MOVPE regrowth is essential for the surface roughness reduction, an alternative approach to the waveguide fabrication was studied.

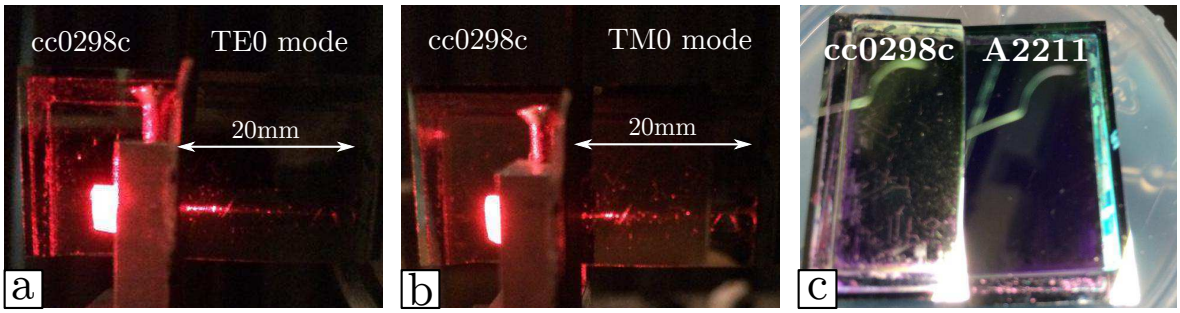

Figure 6.20 – (a)-(b) The propagation of the TE0 and TM0 modes in cc0298c is highly impacted by the defects. (c) A photo of the surfaces of A2211 and cc0298c samples.

6.3.1 Patterned SOI substrates

The alternative approach is based on a selective growth on patterned SOI substrate. The substrate patterning is widely used in the case of Si, because it allows to reduce tensile stress in the grown layers. Therefore, prior to the growth we defined 50, 100 and 200μm wide mesas by a standard RIE etching, see Fig. 6.21.

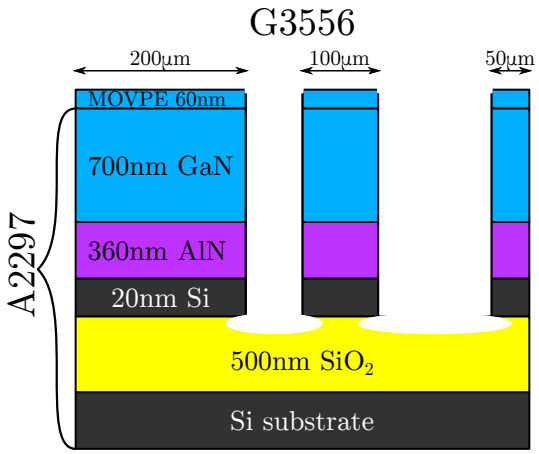

Figure 6.21 – A scheme of A2297 and G3556 waveguides grown on patterned SOI substrates.

Analogously to the previous section, A2297 structure was grown by MBE. The wafer was cleaved in two halves. One half was used for the optical experiments. Another half was used for the MOVPE regrowth and got a new number G3556. A standard 2D growth was observed on the defined Si mesas, while there were still some 3D grains formed in the regions corresponding to SiO_2, see Fig. 6.22(a). The selective growth on the patterned SOI substrate allowed to eliminate a large majority of the fractures, as one can see from Figs. 6.22(b)-(d). There were few cracks precisely aligned with the mesas, see Fig. 6.22(c). It is interesting to note, that the regions near the border of the wafer remained high fractured, see Fig. 6.22(d). This can be attributed to a different layer composition near the edge of the wafer and to the wafer contact with the support. It is well known that the grown layers were under tensile stress, but it looked like the cracks originated predominantly at the border and then propagated through the whole sample. The patterned growth allowed

both to reduce the tensile stress and to limit the propagation of the fractures formed at the border of the sample.

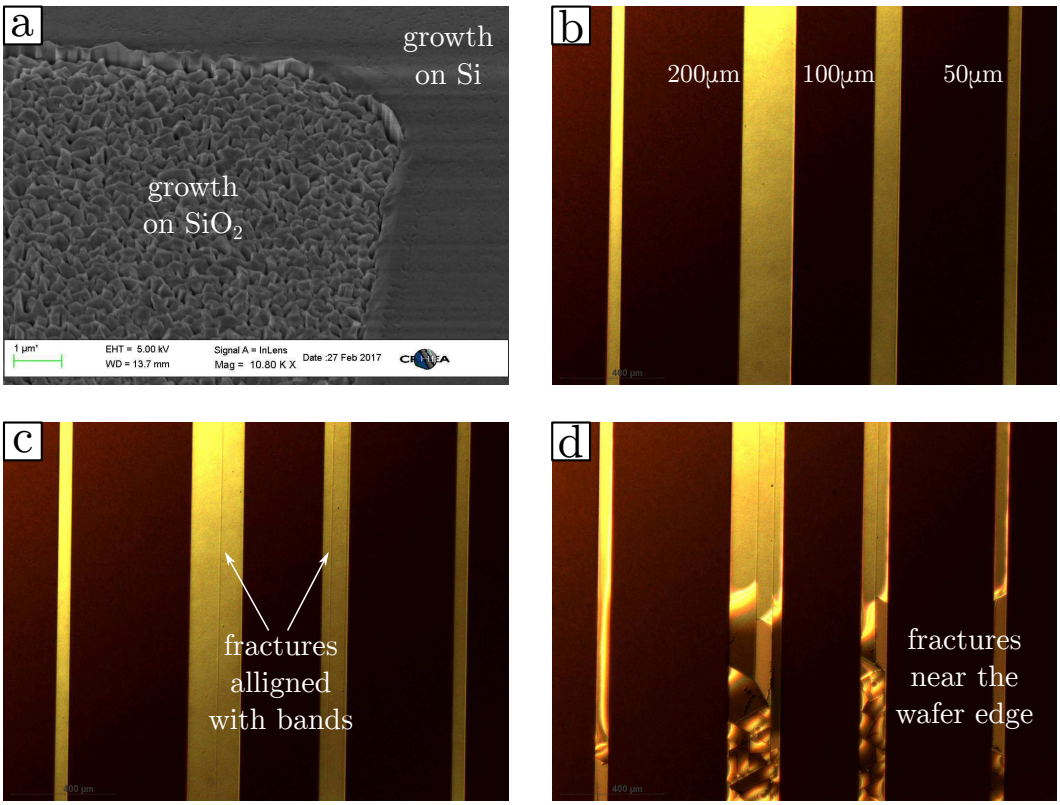

Figure 6.22 – (a) Results of the growth on the SiO_2 and Si regions. (b) 50, 100 and 200μm wide bands grown on Si (yellow bands). (c) Fractures aligned with the bands. (d) A highly fracture region near the border of the wafer.

The most important result here is that MOVPE regrowth was also successful. The amplitude of the surface roughness was reduced, as it is shown in Fig. 6.23. This had a positive impact on the propagation losses, see Fig. 6.24. In this case, it was impossible to measure the propagation losses since the light scattering was highly perturbed by the rough walls of the mesas. As a result, there were no monotonous attenuation of the scattered light along the propagation lines. Nevertheless, from these images it is clear that the modes in G3556 sample have longer propagation distanced in comparison to A2297 sample.

The 200μm mesas were used for the observation of the second harmonic generation. The acceptance curves for A2297 and G3556 samples are presented in Fig. 6.25(a) and (b). Starting from the initially grown mesas, ridge waveguides were etched for G3556 sample, see Fig. 6.25(c). The etching was not optimized and the ridge waveguides had a pyramid-type structure. Nevertheless, the ridge waveguides were used for the SHG experiments. The mode profiles of both the pump and the second harmonic were obtained by using the sensitive SWIR and sCMOS cameras, see Fig. 6.25(d). The experimental set-up is described in Chapter 4.

It was impossible to measure the acceptance curves for the ridge waveguides, since the experiments had to be done in a low-power regime under the detection limit of the

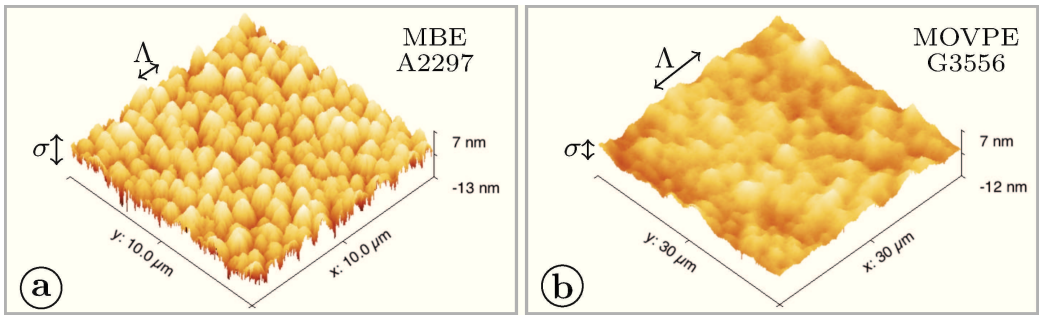

sample	epitaxy	rms, σ	Λ
A2297	MBE	2.7nm	0.4μm
G3556	MOVPE	1.4nm	5μm

Figure 6.23 – (a) An AFM image of 10μm by 10μm surface area for A2297 sample. (b) A similar 30μm by 30μm AFM scan for G3556 sample. The roughness amplitude σ and the characteristic lateral scale Λ are determined from an exponential fit $\sigma^2 \exp(-r/\Lambda)$ of the autocorrelation function for the surfaces. The table attached to this figure summarizes the numerical values of σ and Λ for these two samples.

photodiodes. Higher injection power for the pump at 1076nm was systematically burning the injection facets due to the absorption in the Si layers. This was not the case, for example, for the 1550nm pump, but this wavelength did not correspond to the phase matching. It means that the end-fire coupling with a microscope objective can pose serious problems in the absorption region of the Si-based substrates. There are two possible solutions to this problem: either to work in the spectral region where Si is transparent, or to use optical claddings with the layers thick enough, so the focalization spot aligned with the injection facet does not overlap with the Si layers. In the case of SOI the second solution is not viable, because the thin Si layer is in direct contact with the nitride layers. It means, that SOI substrates are suitable only for the nonlinear interactions with the pump above the 1.3μm wavelength.

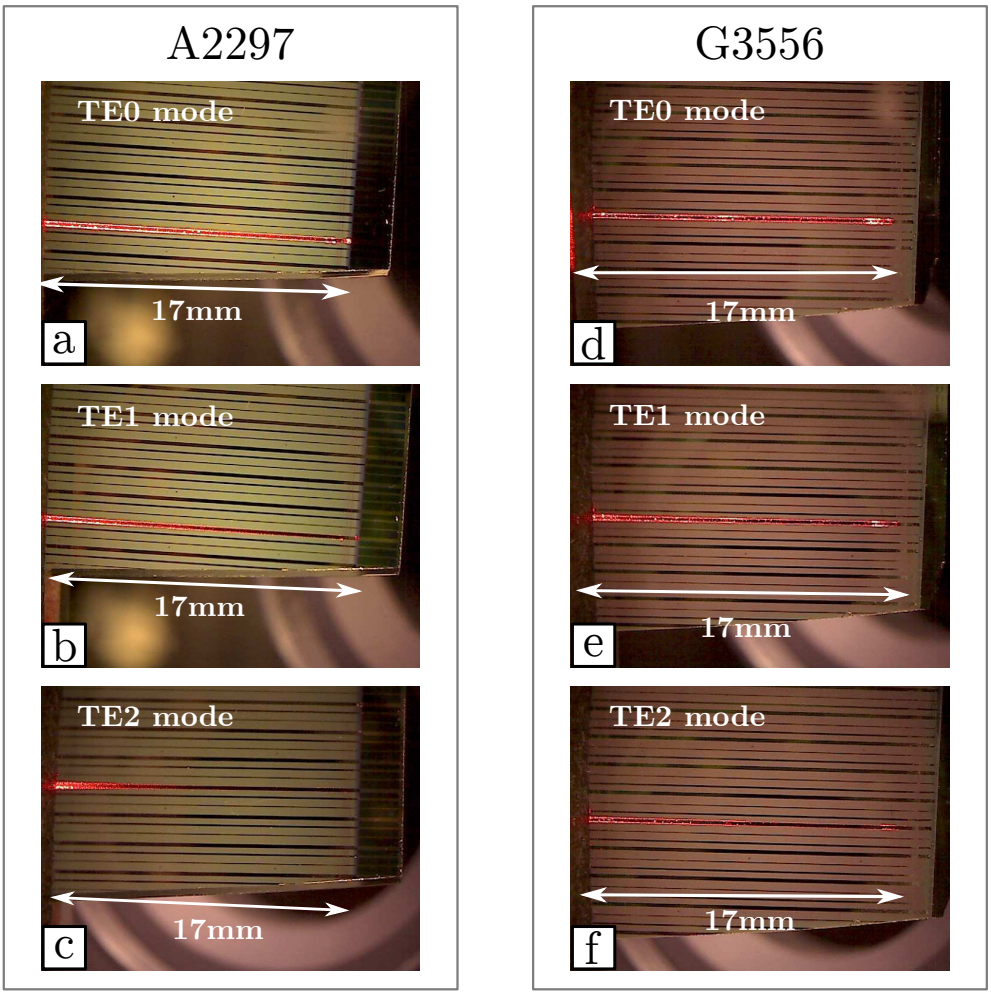

Figure 6.24 – (a)-(c) Images of the light diffused along the propagation lines of TE0-TE2 modes in A2297 sample. (d)-(f) The same images for G3556 sample. For C3556 sample the modes have longer propagation distance in comparison to A2297 sample. For both waveguides the injection is done into the 200μm mesas.

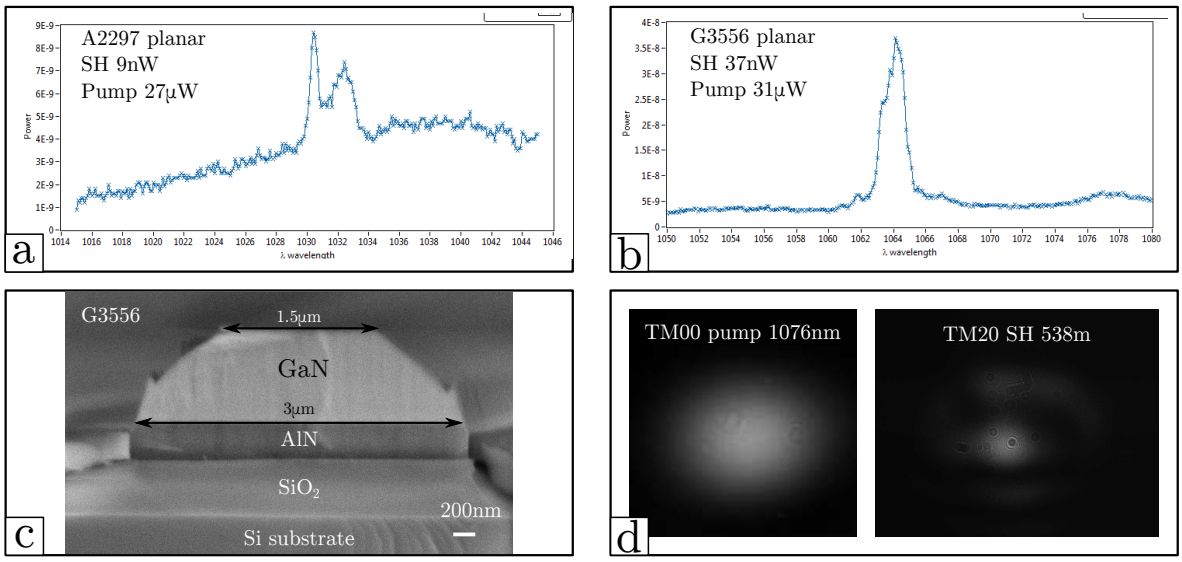

Figure 6.25 – (a)-(b) Acceptance curves for A2297 and G3556 planar waveguides. (c) An SEM image of G3556 ridge waveguide. (d) Images of the TM00 pump and TM20 second harmonic decoupled from G3556 ridge waveguide.

6.4 Micro-disks

Finally, this section presents the solution based on air optical cladding in suspended GaN structures. The structure that was chosen for the study is a micro-disk coupled to a waveguides. The experimental results presented below including both the fabrication and optical characterisation were obtained by my colleagues in C2N laboratory and were published in the following articles [4, 16]. My contribution to this work consisted in the preliminary modelling that was presented in Chapter 2. I have also participated in the discussions regarding the obtained results and their interpretation and in the articles preparation and review. For this reason, the text and the images presented below are taken from the already published articles.

6.4.1 Fabrication

The crystalline III-nitride layers were grown by molecular beam epitaxy on Si(111) substrates. An AlN buffer layer is first grown on silicon. Its thickness (245 nm) is adjusted in order to reach an optimum structural quality and to introduce enough compressive strain in the following epitaxial GaN layer (497 nm thick). This compressive strain partially compensates the tensile strain appearing during cooling due to the difference of thermal expansion coefficients between the III-nitrides and the silicon substrate. Finally, strain compensation allows one to dispose of suspended planar materials after underetching on tens of micrometers length scales. We have chosen to work with TM modes both for the pump and the second harmonic since it allows us to use the highest nonlinear coefficient $\chi^{(2)}_{zzz}$ for the second harmonic generation. The thickness of the epitaxial layer was thus adjusted so that the phase matching condition around 1550 nm could be realised for sufficiently large microdisks to avoid radiation losses and to get better mode confinement which makes modes less sensitive to the fabrication imperfections.

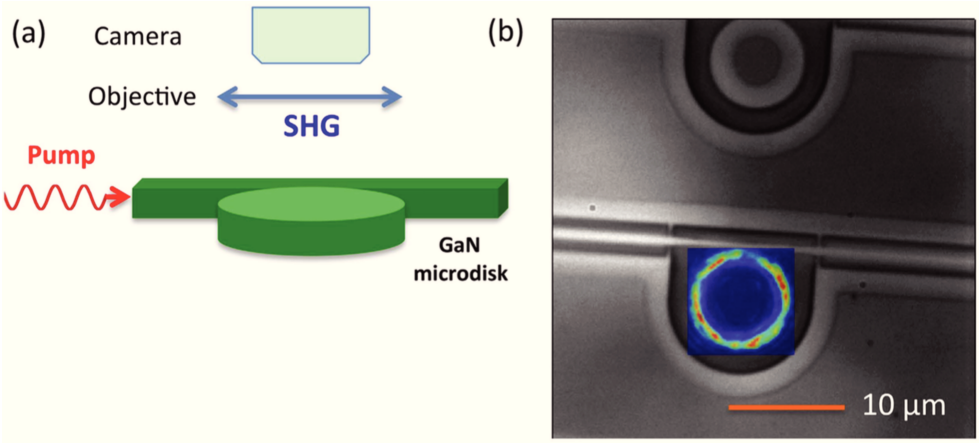

Figure 6.26 – (a) Schematics of the experiment. The second harmonic is collected perpendicularly from the layer plane. (b) Optical microscopy image of microdisks and its side-coupling bus waveguide. We have superimposed the second harmonic radiated pattern collected from the surface. The harmonic is generated by a resonant whispering gallery mode and appears as a ring at the disk periphery on the image. The harmonic is excited in continuous wave in resonance with the TM-0-0-28 mode at 1557 nm (disk diameter 7.92 μm). A filter on the collection path rejects the pump mode.

The photonic circuit consists of microdisks coupled to free-standing waveguides suspended by nanotethers. The microdisks are mushroom-type with a silicon pedestal. The coupling between microdisks and waveguides is controlled by the gap distance between both. The advantage of the coupling scheme is its mechanical stability and reproducibility as compared to coupling with an elongated fiber at the proximity of the microdisks [41, 42] or even in contact with microdisks [43]. The air gap distance was chosen in order to be at the critical coupling, i.e. for an optimum transfer of light from the waveguide to the microdisk. Light is injected by lensed fibers through inverted tapers. The global length of the structure is 500 μm. Fabrication of the structures is achieved by a combination of electron beam lithography and inductively coupled dry etching. Selective under-etching between III-nitrides and silicon is performed with XeF_2 gas. The dark contrast in the top part of Fig. 6.26(b) indicates that the structures lie on silicon while the light contrast corresponds to free-standing structures in air. One clearly sees the silicon pedestal of the microdisk. For phase matching experiments, a series of microdisks were fabricated with a variation of 8 nm in the disk diameter. This high precision on the disk diameter is obtained through dry etching and is an advantage as compared to the precision achieved with wet etching [44].

6.4.2 Set-up

In this work, we demonstrate phase matched harmonic generation mediated by the $\chi^{(2)}_{zzz}$ susceptibility element between two TM-polarized whispering gallery modes resonant at the fundamental and harmonic wavelengths. The modes confined in the microdisks can be labeled through vertical, radial and azimuthal (n, m, ℓ) indices, n and m representing the number of nodes in the vertical and radial spatial profiles and 2ℓ the number of antinodes in the azimuthal near-field profile. With the $\chi^{(2)}_{zzz}$ susceptibility, the phase matching implies the conservation of energy and orbital momentum, corresponding $\lambda_{SH} = \lambda_{pump}/2$ and $\ell_{SH} = 2\ell_{pump}$. As explained below, we will use the combination of different radial order modes TM (0, 0, 28) for the pump and TM(0, 2, 56) for the harmonic, i.e. modes differing by a factor of two in their azimuthal numbers.

The experiments were performed using a GaN-on-silicon two-dimensional photonic platform. The photonic circuit consists of microdisks coupled to free-standing waveguides suspended by nanotethers. The harmonic experiments were performed with a continuous wave laser source in the telecom band (1500-1630 nm) and the harmonic was collected perpendicularly to the layer plane with a high numerical aperture objective (0.9), as shown schematically in Fig. 6.26(a). The high numerical aperture objective allows one to collect z-polarized light emitted in directions away from the optical axis. Scattering by the microdisk sidewalls also redirects light towards the vertical direction. Figure 6.26(b) shows an optical microscope image of a microdisk and its side-coupling bus waveguide. Figure 6.26(b) also shows the superimposed spatial profile of the second harmonic signal as measured with the camera. The harmonic is observed at the periphery of the microdisk where the whispering gallery modes are located.

6.4.3 Linear characterization of microdisks

Figure 6.27(a) shows the transmission spectrum in TM polarization for a microdisk with a nominal 7.997 μm diameter and a nominal thickness of 742 nm. One observes a series

of resonant dips that correspond to the coupling to whispering gallery modes. The free spectral range is around 40 nm. The modes have been identified by comparison with the modelling presented in Chapter 2. The main resonances at 1527, 1567, 1608 nm correspond to the TM(0, 0, 29-28-27) modes. The transmission drop is close to 1, indicating that we are close to the critical coupling with an air gap distance of 400 nm. The loaded quality factors measured for TM-polarized modes vary between 6000 and 13000. These values are lower than those reported in [4] where values up to 80000 were reported for undercoupled waveguides. We attribute the lower value of quality factors to the large thickness of the present structures as compared to the $\lambda/2n$ thickness in [4]. The larger thicknesses require longer plasma-etching times that lead to a stronger mask erosion and in some cases to an increased sidewall roughness. The bending losses are not dominant for these diameters and sidewall scattering is the dominant source of loss. Let us note that as we seek a double resonance between the fundamental and harmonic resonances, a lower Q relaxes the constraint on the tuning to obtain the resonance condition. Moreover, a lower Q also enhances the bandwidth of frequency conversion. A Q around 10000 is in our case a good compromise between a large enough interaction length while keeping a moderate constraint on the double resonance condition.

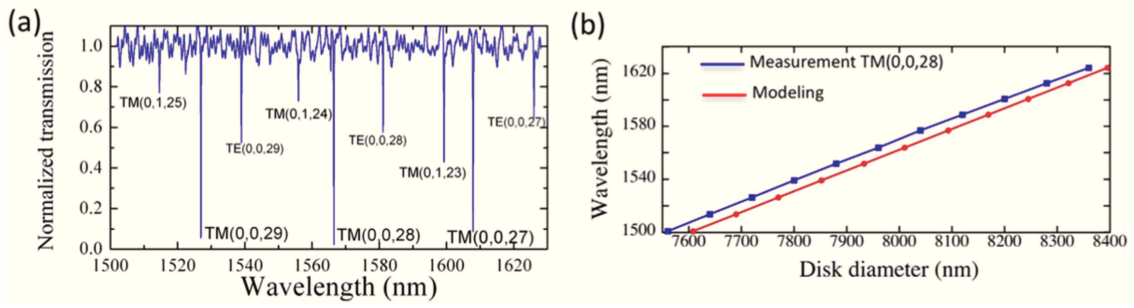

Figure 6.27 – (a) Normalized transmission of the photonic circuit for TM-polarized light injection. The modes are labeled according to their vertical, radial and azimuthal indices. The gap distance is 400 nm. (b) Spectral dependence of the TM-0-0-28 mode as a function of the disk diameter. The blue line corresponds to the measured wavelength as a function of disk diameter coded in the mask. The red line corresponds to the calculated diameter to obtain the same resonance wavelength for the TM-0-0-28 mode.

A very important feature for phase matching is the ability to shift the resonance wavelengths as a function of the disk diameter. This is illustrated in Fig. 6.27(b) that shows the resonance wavelength of the TM(0, 0, 28) mode as a function of disk diameter. The step variation in diameter for electronic lithography writing is 8 nm, i.e. one thousand times smaller than the disk diameter around 8 μm. Only a fraction of the whole measurements are shown. The measurements are obtained from a series of microdisk-waveguide structures separated by a distance of 20 μm. Figure 6.27(b) compares the spectral position of the TM(0, 0, 28) mode with the one that has been calculated with an analytical model. We observe that we can accurately track the mode from 1500 to 1630 nm by changing the disk diameter. One obtains an excellent agreement for the wavelength vs. diameter slope with a standard deviation of 5.5 nm. As compared to the modeling, there is a small offset due to the uncertainty on the refractive indices and on the exact diameter of the processed disk+waveguide. The fabricated disks can be considered smaller than the nominal ones by 48 nm, i.e. 0.6%, for the set of refractive indices considered.

6.4.4 Second harmonic generation in microdisks

Achieving double resonant harmonic conversion requires that both pump and harmonic fields are resonant with a whispering gallery mode. To assess this situation, it is possible to perform microdisk spectroscopy around the doubly-resonant signal. In the present experiments, we have investigated the dependence of the harmonic conversion efficiency as a function of the disk diameter. The resonance wavelengths of the TM(0, 0, 28) and TM(0, 2, 56) modes vary as a function of diameter, as shown in Fig. 6.27(b) for the TM(0, 0, 28) mode, but with different slopes. Consequently, one can expect to find a diameter where both pump and harmonic are resonant with the whispering gallery modes. This occurrence is shown in Chapter 2. The change in the radial index between both modes compensates for the natural dispersion of the microdisk. Note that in the following, phase matching can only occur with the TM (0, 2, 56) mode. Without conservation of the orbital momentum, the double-resonant harmonic signal would be quenched. According to the modelling, only the harmonic mode with a radial index of 2 can lead to phase matching with the TM(0, 0, 28) pump mode. As the loaded quality factors of the modes are around 10000 (full width at half maximum of 0.15 nm), it is required that $\Delta(\lambda_{\mathrm{TM}(0,0.28)} - 2\lambda_{\mathrm{TM}(0,2,56)}) < 0.15\mathrm{nm}$. We have calculated from the spectral dependence of the resonant modes vs. diameter that $\Delta(\lambda_{\mathrm{TM}(0,0.28)} - 2\lambda_{\mathrm{TM}(0,2,56)}) \approx \Delta\mathrm{Diameter}/50$

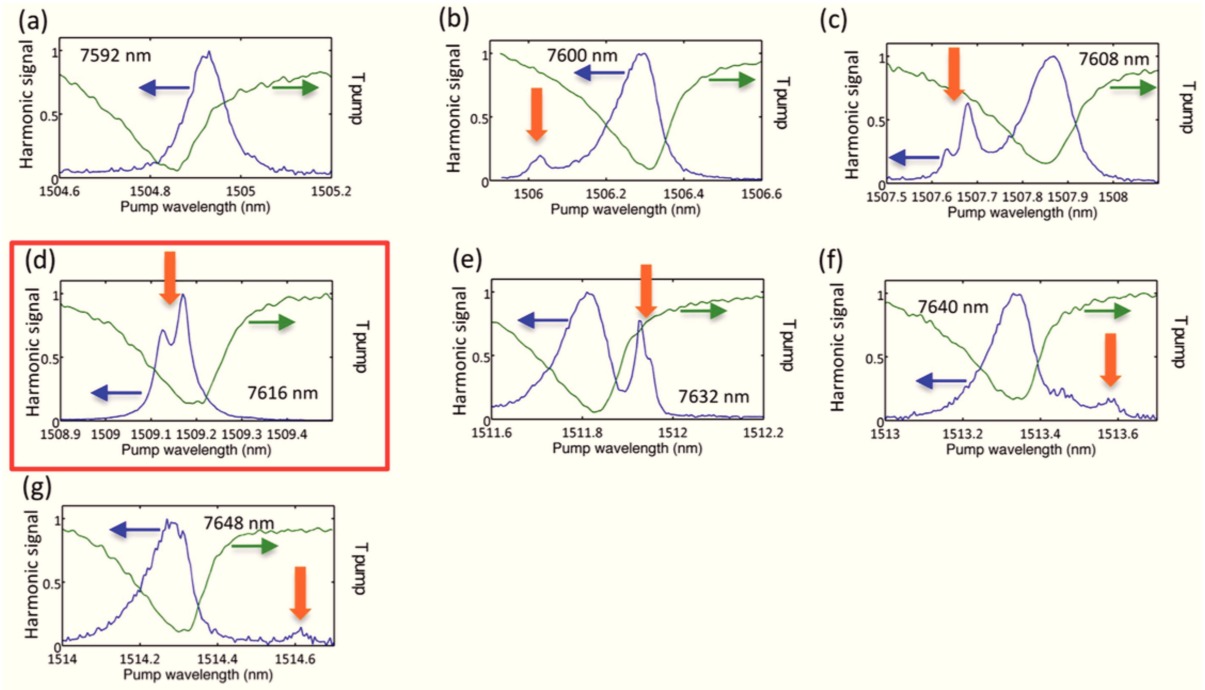

Figure 6.28 – (a)-(g) Spectral dependence of the second harmonic signal as a function of the pump wavelength for different disk diameters indicated in the graphs in nm. The green curve corresponds to the pump transmission. The blue curve corresponds to the normalized harmonic signal. The resonant enhancement at the harmonic frequency is indicated by vertical orange arrows. The red square highlights the structure where phase-matched harmonic generation is obtained.

We have thus chosen a 8 nm step of diameter variation, in order to get one resonant diameter within the resonance linewidth. Figure 6.28 shows the dependence of the

normalized second harmonic signal for different disk diameters. The images show the superposition of the transmission in green and the integrated harmonic signal (in blue). The curves have been normalized for clarity, with a different normalization factor for each curve. We will discuss below the spectral dependence of the efficiency that is maximum for the 7616 nm diameter disk (see Fig. 6.29 and the discussion below). The harmonic amplitude is obtained by spatially integrating the signal as shown in Fig. 6.26. To perform the experiments, the pump wavelength is adjusted for each diameter in order to be in resonance with the TM(0, 0, 28) mode. The curves shown in Fig. 6.28 are measured with a weak incident power (6 dBm, i.e. 440 μW in the waveguide close to the microdisk) in order to avoid the nonlinearities associated with residual absorption and the asymmetry of the transmitted signals. T he harmonic signal varies however very significantly as a function of the disk diameter. For the 7592 nm diameter, there is only one single resonance as expected when only the pump is resonant with a whispering gallery mode, i.e. no resonant whispering gallery mode at the harmonic frequency. This signal is always present for all diameters as we track the TM(0, 0, 28) mode for each microdisk diameter.

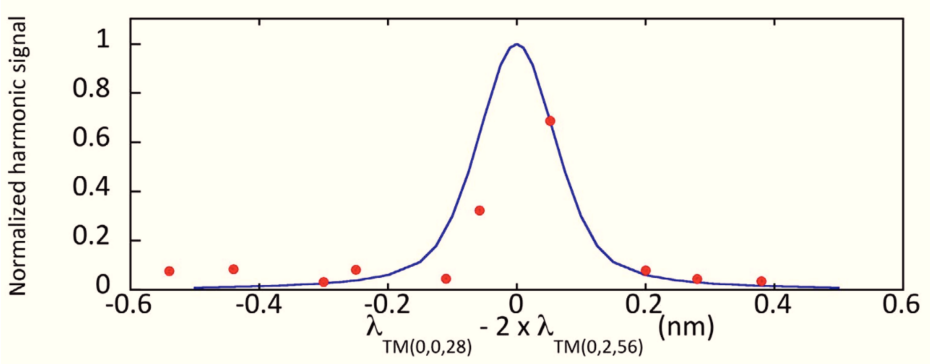

Figure 6.29 – (Experimental (dots) and calculated (full line) harmonic signal as a function of the detuning between harmonic and pump. The vertical scale for the experimental data has been adjusted so that the measurement for the 7616 nm diameter disk corresponds to the modelling. The experimental points correspond to data partially shown on Fig. 6.28.

A similar signal was also observed for the other TM(0, 0, 29-27) modes when the pump was set in resonance with them. When we increase the diameter, a novel resonance appears on the spectra as underlined by the different vertical orange arrows. We attribute this peak to the resonance of the second order harmonic with a whispering gallery mode, i.e. the wavelength of the harmonic mode is at half of this value. In order to be observed, this mode needs to fall within the spectral range where the second harmonic signal is generated, i.e. within a few linewidth of the fundamental resonant pump mode. The resonance is first observed on the short wavelength part of the spectrum, gets closer to the pump resonance and finally shifts to the long wavelength side of the spectrum. On a limited number of structures (c, d, e), one observes a splitting of the harmonic mode. This splitting could come from a sidewall roughness coupling counter-propagating modes (clockwise and counter-clockwise), thus lifting their spectral degeneracy. The linewidth of the harmonic mode is also reduced as compared to the pump mode (see modelling in the next section). The wavelength difference between the pump fundamental mode TM(0, 0, 28) and two times the wavelength of the harmonic mode TM(0, 2, 56) is minimal for the disk diameter of 7616 nm (0.05 nm as compared to 0.2 nm linewidth). For this disk, the

second harmonic signal is dominated by the enhancement due to the double resonance condition of the harmonic. Figure 6.28 thus highlights all the salient features associated with second harmonic generation: the enhancement of the second harmonic signal with a resonant pump (Fig. 6.28(a) for example), the enhancement when the harmonic is resonant with a mode (Fig. 6.28(b) for example), and the reinforced enhancement when both pump and harmonic satisfying conservation of orbital momentum are resonant and overlap, i.e. phase matching (Fig. 6.28(d)).

6.4.5 Evidence of phase-matched second harmonic generation

Following the coupled mode theory [45], the circulating second harmonic power $|B_{\mathrm{SH}}|^2$ can be written as

$$|B_{\mathrm{SH}}|^2 = \left[\frac{\alpha_{\mathrm{pump}}^2(1-|t_{\mathrm{pump}}|^2)}{1+\alpha_{\mathrm{pump}}^2|t_{\mathrm{pump}}|^2-2\alpha_{\mathrm{pump}}|t_{\mathrm{pump}}|\cos\Phi_{\mathrm{pump}}}\right]^2 \times \frac{\alpha_{\mathrm{SH}}^2}{1+\alpha_{\mathrm{SH}}^2|t_{\mathrm{SH}}|^2-2\alpha_{\mathrm{SH}}|t_{\mathrm{SH}}|\cos\Phi_{\mathrm{SH}}}|K_{\mathrm{SH}}|^2|B_{\mathrm{pump}}|^4, \tag{6.1}$$

where α_i corresponds to the resonator losses, t_i to the transmission coefficient for microdisk and waveguide coupling. Both parameters are related to the intrinsic and coupling quality factors $Q_i = \pi\frac{\sqrt{\alpha_i}}{1-\alpha_i}\frac{c}{\lambda_i\,\delta f_{i,\mathrm{FSR}}}$ and $Q_i^c = \pi\frac{\sqrt{t_i}}{1-t_i}\frac{c}{\lambda_i\,\delta f_{i,\mathrm{FSR}}}$. Φ_i corresponds to the phase shifts. $|B_{\mathrm{pump}}|^2$ corresponds to the incident pump power in the waveguide. The spectral dependence of the phase shifts is calculated by linear interpolation of the phase variation as a function of wavelength between modes of the same family differing by their azimuthal number. $\delta f_{i,\mathrm{FSR}}$ is the free spectral range in frequency units. $|K_{\mathrm{SH}}|$ accounts for the nonlinear susceptibility and mode overlap.

The first fraction of the right hand side corresponds to the square resonance enhancement with the circulating pump power while the second fraction corresponds to the resonance enhancement of the harmonic. Formula 1 can be used to calculate the spectral dependence of the harmonic response and the conversion efficiency. We deduce from this modeling an average loaded quality factor of 8000 and 15000 for the pump and harmonic respectively corresponding to $\alpha_{\mathrm{pump}} = t_{\mathrm{pump}} = 0.9926$, and $\alpha_{\mathrm{SH}} = t_{\mathrm{SH}} = 0.9921$, and a free spectral range of 40 nm for the pump. These quality factors are those that best reproduce the linewidth of the harmonic signal in the single and double resonance configuration. Figure 6.29 shows the spectral dependence of the maximum harmonic signal $P_{2\omega}$ compared to what is calculated following formula 6.1. The horizontal axis corresponds to the difference between the pump wavelength and twice the wavelength of the harmonic mode, i.e. the difference between the wavelength pointed by the orange arrow in Fig. 6.28 and the resonant wavelength of the pump mode corresponding to the dip in the transmission spectrum (right scale in Fig. 6.28). The modelled harmonic signal has been normalized to one for a zero detuning. One obtains an excellent agreement between the calculated and measured efficiency enhancement. The enhancement is, as expected, very peaked and is a signature of the achievement of phase matching in these GaN-on-Si microdisks. In this situation, within a resonance linewidth, both pump and harmonic are resonant and the orbital momentum is conserved. We note that, while we did scan disk diameters from 7550 to 8300 nm, this large efficiency enhancement was only observed in the spectral range presented in Fig. 6.29. This demonstration is to our knowledge the first

evidence of phase matching with microdisk resonators on an integrated platform obtained by systematically varying a microdisk parameter. We note that if $\Delta\ell \neq 0$, i.e. the double resonance is obtained with modes that do not satisfy the phase matching condition, there are destructive interferences and one expects to observe a dip in the spectral response as discussed in [41]. In the latter case, the conversion efficiency is quenched by orders of magnitude as there is a destructive phase matching and we would not observe the spectral dependence as reported in Fig. 6.29.

6.4.6 Discussion

The outside conversion efficiency in mW^{-1} is measured from the ratio between the collected harmonic power and the square of pump power $P_{2\omega}/P_{\omega}^2$ and is estimated as $2 \cdot 10^{-9}\mathrm{mW}^{-1}$ for an incident pump of 1.1 mW in the waveguide close to the microdisk. This value can be compared with other values reported in the literature: $7 \cdot 10^{-7}\mathrm{mW}^{-1}$ in AlGaAs microdisks [44], $4 \cdot 10^{-4}\mathrm{mW}^{-1}$ in GaP microdisks [46], $5 \cdot 10^{-5}\mathrm{mW}^{-1}$ in GaAs microdisks [43] or even $9 \cdot 10^{-2}\mathrm{mW}^{-1}$ in very high quality factor lithium niobate mm-size microdisks and 0.03 mW coupled pump power [47]. The conversion efficiency that we have measured remains limited in these experiments for several reasons. The nonlinear susceptibility of the III-nitride layer is significantly smaller than the one of GaAs (around 10 pm/V for $\chi^{(2)}_{zzz}$ as compared to 188 pm/V for $\chi^{(2)}_{xyz}$ in GaAs). The second order polarization is polarized along the z axis, i.e. no emission in the vertical direction, and we only collect a very limited fraction of the emission that is scattered toward the surface, the preferred radiation losses being in the layer plane. An integrated optimized scheme would require to engineer coupling waveguides for both pump and harmonic TM-polarized modes [48]. In forthcoming photonic circuits, we will develop architectures where the in-plane coupling of light between microdisk and waveguide is optimized as well as inverted tapers with an optimized coupling efficiency at the harmonic wavelength. The efficiency for gallium nitride microdisks is below the one of gallium arsenide microdisks but the III-nitride materials offer a much larger transparency window with the possibility of conversion between telecom wavelengths and visible spectral range. Higher efficiencies can be expected if higher quality factors are experimentally obtained.

6.5 Conclusions

This chapter summarizes the experimental results for the GaN waveguides on Si substrates. Si substrates require an optical cladding necessary for the elimination of the mode leakage. Three different approaches for the optical cladding were studied here: AlGaN based cladding on Si substrates; a combined $\mathrm{AlN}/\mathrm{SiO_2}$ cladding in the case of SOI substrates; air-based cladding for the suspended membrane-type structures.

It was demonstrated the pure AlN cladding is suitable for the modes isolation only in the visible region due to the limitations on its thickness imposed by tensile stress. A new solution based on a more complicated AlN/AlGaN/AlN allows to overcome this limitations and provide the mode isolation both in the visible and near-infrared regions. By using SOI substrates one can relax the requirements on the AlN cladding by combining both the AlN and $\mathrm{SiO_2}$ layers for the prevention of the leakage. But the utilisation of SOI substrates is limited to the Si transparency window due to the issues that occur during the

pump injection. Moreover, one needs very particular SOI substrates with a thin Si device layer and a thick oxide. The simplest solution which works over the whole transparency window of GaN is based on the suspended membrane-type structures. But this approach is also not perfect, since it suffers for the losses introduced by the supporting tapers.

This chapter presents new interesting results of the second harmonic generation in planar waveguides, ridge waveguides and micro-disks. So far, these results are limited by high propagation losses, but with some additional efforts the performance of these structures can be increased in the future. The main directions, where the efforts should be applied are: a development of a thicker AlN/AlGaN/AlN cladding, an optimization of the wafer bonding for the planar polarity inversion and an optimization of the ridge waveguide fabrication.

Chapter 7

Conclusions and perspectives

During this PhD project we have studied the second harmonic generation in GaN waveguides. The power conversion was predominantly done from the near-infrared to the visible spectral regions. Prior to this study, the performances of GaN waveguides were severely limited by high propagation losses, therefore, the main goals of this work were to understand their origin and to strongly reduce them, in order to improve the SHG efficiency.

We have made a very important progress in these directions and fabricated waveguides presenting simultaneously low propagation losses in the near infrared and in the visible. For planar GaN waveguides epitaxialy grown on sapphire, we measured propagation losses below 1dB/cm in the visible spectral region. These low-loss planar GaN waveguides were used for the demonstration of an efficient second harmonic generation process using modal phase matching and a nonlinear interaction between a TM0 pump mode in the near-infrared and a TM2 second harmonic mode in the visible region. Using a prism coupling set up, we obtained 2% of power conversion, which correspond to a normalized efficiency of 0.15% $W^{-1}cm^{-2}$. To the best of our knowledge, the obtained propagation losses and conversion efficiency were the best reported results for GaN waveguides.

Although the experiments were done in a limited spectral region, the modelling results presented in Chapter 2 show the large adaptability of the platform based on the GaN and AlN waveguides. This numerical study reveals the full potential of AlGaN waveguides by demonstrating that using different mode combinations and waveguides geometries it is possible to obtain a second harmonic signal in the ultraviolet, the visible or the near-infrared spectral regions. These results also demonstrate that further improvement of the SHG efficiency require the fabrication of ridge waveguides presenting a polarity inversion precisely positioned in the core of the waveguide to benefit from the full mode confinement and an improved overlap of the interacting modes. In this configuration, we have shown that one can obtain conversion efficiencies up to 100% $W^{-1}cm^{-2}$ which indicates that modal phase-matching is a viable alternative to quasi phase matching that requires periodically oriented GaN structures.

During this work, we fabricated ridge waveguides starting from the low-loss planar waveguides in which we obtained 2% power conversion. Unfortunately, the ridge waveguides were impacted by propagation losses higher than 10dB/cm in the visible region due to the fact that the etching procedure was not optimized yet. Nevertheless, we have been able to demonstrate second harmonic generation in these waveguides, but of course with a limited efficiency. The planar polarity inversion was also tested. We have considered two approaches to obtain it: 1) the first one was based on Mg doping during the epitaxial

growth; 2) the second one was based on cascade of wafer bounding and substrate removal performed at LETI. The layers with the polarity inverted by Mg doping presented high propagation losses >20dB/cm in the visible spectral regions, which is principally due to the surface roughness of the N polar layers. The procedure based on wafer bonding, have not been tested, as the sample was broken before the end of the fabrication.

The perspective of combining Silicon photonics circuits with nonlinear GaN waveguides is very appealing and motivated our choice to study AlGaN waveguides on Si substrates despite the fact that the fabrication of the low-loss waveguides on Si substrates is more challenging due to the problem of modes leakage. In order to prevent mode leakage, we have studied three types of optical cladding based on AlGaN, SiO_2 and air layers. The AlGaN cladding can work only in a limited spectral region ($0.5 - 1.2\mu$m), while SiO_2 and air cladding can provide the isolation over the whole transparency window of GaN. During this PhD work we did not solve completely the problem of mode leakage but made interesting progress and fabricated waveguides good enough to demonstrate SHG. The fabrication of AlGaN waveguides on Si substrates is very challenging, but it opens new interesting opportunities due to the possibility to etch selectively the nitrides or the Si. The selective chemical etching was used to develop the platform based on a micro-disk coupled to a waveguide. This platform has allowed the first demonstration of doubly-resonant second harmonic generation using the whispering gallery modes in a micro-disk.

As it was already mentioned, the main advantage of III-nitrides over other semiconductors is their large band gap. Therefore, at the end of this PhD, one can identify two directions for future studies that are high power nonlinear interactions in the near-infrared regions which will not be disturbed by two-photon absorption and second harmonic generation in the ultraviolet region.

The main progress during this project were done for GaN waveguides. Therefore a natural continuation of this project would be the development of channel GaN waveguides designed to play with nonlinear interactions between the near-infrared and the visible with the aim to handle low and high pump powers.

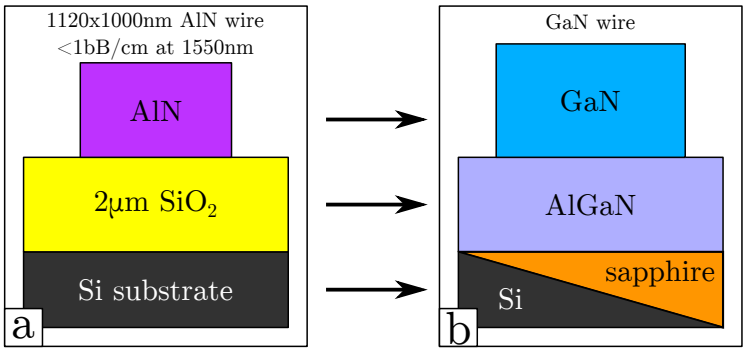

Figure 7.1 – III-nitrides channel waveguides for integrated nonlinear optics from the UV to the near-infrared spectral region.

GaN and AlGaN has both a large band gap and a relatively strong $\chi^{(2)}$ nonlinearity, which eliminate the problems of two photon absorption. So far, the only factor limiting the utilization of these materials were the high propagation losses. In this work we have showed that it is possible to fabricate epitaxially grown GaN waveguides with <1bB/cm

losses and ridge waveguides with ∼4dB/cm losses at the wavelegth of 633nm. We didn't have time to optimize the fabrication of the ridge waveguides specifically designed for second harmonic generation, but, for sure, it can be done once the initial low-loss planar layers are available, as it has been demonstrated with AlN sputtered layers by Tang team [18]. The epitaxially grown GaN waveguides has a major advantage over sputtered AlN waveguides, due to the better crystalline quality and the higher second order nonlinearity. see Fig.7.1(b).

A second perspective, is second harmonic generation in the ultraviolet region. Today the quantum efficiency of AlGaN based diodes and diode lasers remains in the order of a few percent in the ultraviolet region. Therefore it might be easier, for example, to use a GaN laser diode at 520nm and convert its radiation to the 260nm wavelength by frequency doubling in an AlN waveguide, see Fig.7.2. In Chapter 2 it was shown that this conversion is indeed possible using modal phase matching between the TM0 pump and the TM2 second harmonic. It was also demonstrated that in order to obtain a high conversion efficiency one has to use the planar polarity inversion as it is shown in Fig. 7.2(a). The final conversion efficiency depends both on the value of the $\chi^{(2)}$ coefficient and

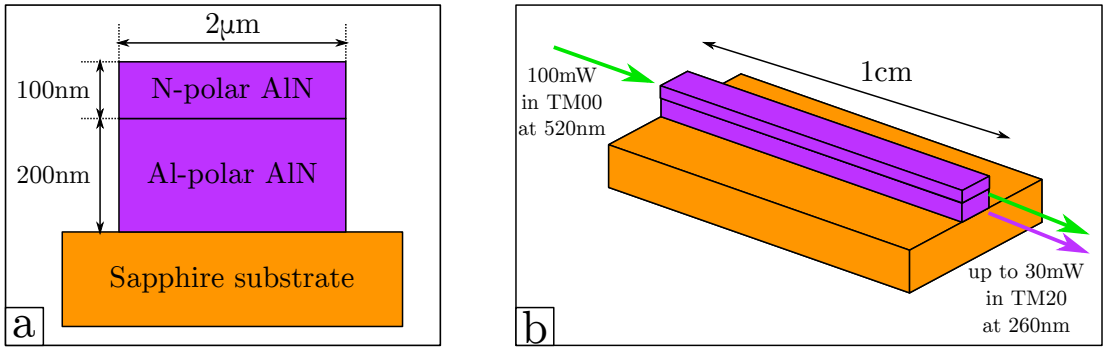

Figure 7.2 – AlN waveguides for power conversion from the visible to the ultraviolet spectral region.

the propagation losses in the ultraviolet region. The value of the $\chi^{(2)}$ increases closer to the gap, but, unfortunately, the propagation losses also increase for shorter wavelengths. If the nonlinearity is as high as 8pm/V in the ultraviolet region as it was suggested in the recent publication [24], then the power conversion can reach 30% for the 100mW pump in an ideal lossless AlN waveguide, see Fig. 7.2(b). In the case of 10dB/cm losses for the pump and 20dB/cm losses for the second harmonic, the power conversion will be only 0.3%. Without the polarity inversion the power conversion will be only 3% in the ideal lossless wavelguide. This shows that both the low propagation losses and the polarity inversion are essential for this approach to the ultraviolet light generation. We were not able to study AlN waveguides during this PhD project due to fabrication problems, by it is an interesting subject for the future studies.

On top of that, a very interesting perspective is the possibility to realize hybrid integrated systems, combining Silicon Photonics Circuits with parametric photon pair sources and electro-optically adjustable directional couplers realized in III-nitride. These circuits would be very useful for Quantum Information Processing and Quantum Sensing but they require a careful development.

Chapter 8

Formulas

8.1 Complex amplitudes, Poynting vector and nonlinear polarization

Complex amplitudes are commonly used both for formulations of the equations of the guided modes and derivations of the formulas for conversion efficiencies in different nonlinear processes. This section presents a relation between the electric polarization, the electric and magnetic field and their complex amplitudes. Here these relations are used to represent an average power flux density as a function of the complex electromagnetic amplitudes, and to give a relation between the complex amplitudes of the nonlinear polarization and the electric fields for the case of second harmonic generation. Although it may seem that the formulas given below are trivial, they often become a source of confusion as different numerical factors appear and disappear in different publications depending on a chosen normalization. The utility of this short section is to clearly define the choice that we used for all the theoretical and numerical developments we made in this manuscript.

8.1.1 Poynting vector

In this manuscript quantities rapidly varying in time are denoted by the tilde sign (˜), while quantities constant or slowly varying in time are written without the tilde. It is assumed that the fields under consideration are oscillating at single fixed frequencies. This assumption is commonly made for basic calculations of nonlinear conversion efficiencies, since the results for spectrally broad sources can be further obtained with some additional efforts by using a Fourier decomposition of a given source into a sum of monochromatic sources. Here the real rapidly varying in time quantities are defined through their complex amplitudes by the following relations:

$$\tilde{\mathbf{E}}(\mathbf{r},t) = \frac{1}{2}\left[\mathbf{E}(\omega)e^{i\omega t} + \mathbf{E}^*(\omega)e^{-i\omega t}\right], \tag{8.1}$$

$$\tilde{\mathbf{H}}(\mathbf{r},t) = \frac{1}{2}\left[\mathbf{H}(\omega)e^{i\omega t} + \mathbf{H}^*(\omega)e^{-i\omega t}\right], \tag{8.2}$$

$$\tilde{\mathbf{P}}(\mathbf{r},t) = \frac{1}{2}\left[\mathbf{P}(\omega)e^{i\omega t} + \mathbf{P}^*(\omega)e^{-i\omega t}\right], \tag{8.3}$$

where $\tilde{\mathbf{E}}$ and $\tilde{\mathbf{H}}$ are electric and magnetic fields respectively, $\tilde{\mathbf{P}}$ is the electric polarization and ω is the field's angular frequency; the bold font denotes vector quantities and the asterisk denotes complex conjugation. The same representation holds for the electric displacement field $\tilde{\mathbf{D}}$ and the magnetic field $\tilde{\mathbf{B}}$.

One of the goals during a theoretical analysis of a nonlinear process is to estimate the fraction of the pump power that could be converted to the harmonic signal. For a proper calculation of the power one needs to know the expression for the directional energy flux density given by the Poynting vector. Here it is assumed that the Poynting vector in a material is given by the formula:

$$\tilde{\mathbf{S}} = \tilde{\mathbf{E}} \times \tilde{\mathbf{H}}, \tag{8.4}$$

where $\tilde{\mathbf{E}}$ and $\tilde{\mathbf{H}}$ are electric and magnetic fields respectively and ($\times$) symbol denotes the vector product. Although there is no ambiguity for the definition of the Poynting vector in the vacuum, there has been a long discussion, on how to define the Poynting vector within a material, since one can use four different options with the fields $\tilde{\mathbf{E}}$, $\tilde{\mathbf{H}}$, $\tilde{\mathbf{D}}$ and $\tilde{\mathbf{B}}$. The review of this discussion, known as Abraham-Minkowski controversy, but it lies beyond the scope of this work. By substituting the expression (8.1) and (8.2) into the formula (8.4) one can obtain:

$$\begin{aligned} \tilde{\mathbf{S}} = \frac{1}{4}\Big[\mathbf{E}(\omega)\times\mathbf{H}^*(\omega)+\mathbf{E}^*(\omega)\times\mathbf{H}(\omega)\Big]+ \\ + \frac{1}{4}\mathbf{E}(\omega)\times\mathbf{H}(\omega)e^{2i\omega t} + \frac{1}{4}\mathbf{E}^*(\omega)\times\mathbf{H}^*(\omega)e^{-2i\omega t}. \end{aligned} \tag{8.5}$$

The part of the Poynting vector in (8.5) which oscillates at the frequency 2ω is never measured during experiments, since detectors average the signal over a time which is much larger than the period $T = 2\pi/\omega$ of optical oscillations. As a consequence the time-averaged value $\mathbf{S}$ of the Poynting vector is used for all theoretical developments in this manuscript, where $\mathbf{S}$ is given by:

$$\boxed{\mathbf{S} = \frac{1}{4}\Big[\mathbf{E}(\omega)\times\mathbf{H}^*(\omega) + \mathbf{E}^*(\omega)\times\mathbf{H}(\omega)\Big] = \frac{1}{2}\mathrm{Re}\Big[\mathbf{E}(\omega)\times\mathbf{H}^*(\omega)\Big],} \tag{8.6}$$

where the operator Re[ ] gives the real part of the expression. The vector $\mathbf{S}$ determines the rate of the energy transfer through the unit of a given area; its Si unit is the watt per square meter ($\mathrm{W/m^2}$).

8.1.2 Nonlinear polarization

Second harmonic generation (SHG) is the main nonlinear process that was studied in detail both experimentally and theoretically in this work. A very important step prior to all theoretical developments in this case is to define the nonlinear polarization, which becomes a source term in the propagation equations for the second harmonic. This step is rather technical since it involves a changing to complex amplitudes together with manipulations with the third order nonlinear tensor and some symmetry arguments. Once the components of the nonlinear polarization are defined further calculations becomes pretty straightforward.

It is well known that an external electric field induces dipole moments in a dielectric material and the material is said to be polarized in this case. The polarization of the

material is characterized by the electric dipole moment per unit volume, which is called either polarization density or just electric polarization and measured in coulombs per square meter. The polarization is represented by a vector $\tilde{\mathbf{P}}$ and in nonlinear optics this vector is often decomposed in a following sum:

$$\tilde{\mathbf{P}} = \tilde{\mathbf{P}}^{(1)} + \tilde{\mathbf{P}}^{(2)} + \tilde{\mathbf{P}}^{(3)} + ..., \tag{8.7}$$

where $\tilde{\mathbf{P}}^{(1)}$ depends linearly on the applied electric field $\tilde{\mathbf{E}}$, while the components of the $\tilde{\mathbf{P}}^{(2)}$ and $\tilde{\mathbf{P}}^{(3)}$ vectors depend respectively on the second- and the third-order products of the components of the electric field vector $\tilde{\mathbf{E}}$.

The linear polarization term $\tilde{\mathbf{P}}^{(1)}$ is responsible for the appearance of the refractive index in dielectric materials and it describes the linear-optics processes in which the optical properties of a material don't depend on the fields intensities. The third-order nonlinear polarization $\tilde{\mathbf{P}}^{(3)}$ is a source term for numerous nonlinear processes such as four-wave mixing, two-photon absorption, stimulated Raman scattering and Kerr-related effects which include optical phase conjugation, self-phase modulation, self-focusing and temporal solitons. The first- and the third-order processes can occur in any material regardless of its spatial symmetry and they are not studied in this work.

The subject of interest of this thesis is the second-order nonlinear processes which appear as all even-order processes only in noncentrosymmetric crystals. The second-order nonlinear phenomenons governed by the source term $\tilde{\mathbf{P}}^{(2)}$ include optical rectification, Pockels effect and a group of three-wave mixing processes namely second harmonic generation, sum- and difference-frequency generation, spontaneous parametric down-conversion and optical parametric amplification. In this manuscript we restrict ourselves to a detailed study of second-harmonic generation (SHG) as one of the main processes which includes all the essential features of the other second-order nonlinear phenomenons.

It should be noted that here we work with electromagnetic fields whose frequencies are much smaller than the frequency corresponding to the gap of the semiconductor. In this case the semiconductor can be considered as a simple dielectric and in addition one can assume an instantaneous response of the nonlinear polarization to the applied electric field and one can neglect the dependence of the second-order nonlinear susceptibility on the fields frequencies. For the SHG case the components of the nonlinear polarization in the time domain $\tilde{P}_i^{(2)}(t)$ are determined by the components of the pump field $\tilde{E}_j(t)$ through the relations:

$$\tilde{P}_i^{(2)}(t) = \varepsilon_0 \sum_{j,k} \chi_{ijk}^{(2)} \tilde{E}_j(t) \tilde{E}_k(t), \tag{8.8}$$

where ε_0 is the permittivity of vacuum, $\chi_{ijk}^{(2)}$ is the second-order nonlinear susceptibility tensor, the indices i, j and k are used to numerate different fields components and they run through the values x, y, z. By substituting the expression (8.1) for the fields component into the formula (8.8) one can obtain a further development:

$$\begin{aligned}
\tilde{P}_i^{(2)}(t) =& \frac{1}{4}\varepsilon_0 \sum_{j,k} \chi_{ijk}^{(2)} \left[E_j(\omega) e^{i\omega t} + E_j^*(\omega) e^{-i\omega t} \right] \left[E_k(\omega) e^{i\omega t} + E_k^*(\omega) e^{-i\omega t} \right] = \\
=& \frac{1}{4}\varepsilon_0 \sum_{j,k} \chi_{ijk}^{(2)} \left[E_j(\omega) E_k^* + E_j^*(\omega) E_k(\omega) \right] + \\
&+ \frac{1}{4}\varepsilon_0 \sum_{j,k} \chi_{ijk}^{(2)} \left[E_j(\omega) E_k(\omega) e^{i2\omega t} + E_j^* E_k^*(\omega) e^{-i2\omega t} \right],
\end{aligned} \tag{8.9}$$

where the term constant in time is responsible for the optical rectification, namely an appearance of a static electric field, an the term of the polarization $\tilde{\mathbf{P}}^{(2)}(t)$ oscillating at the frequency 2ω is a source term for the second harmonic field. By using a standard for this manuscript representation (8.3) for the SHG polarization source term:

$$\tilde{\mathbf{P}}^{\mathrm{SHG}}(t) = \frac{1}{2}\left[\mathbf{P}(2\omega)e^{i2\omega t} + \mathbf{P}^{*}(2\omega)e^{-i2\omega t}\right], \tag{8.10}$$

one can obtain the following relation between the complex amplitudes of the SHG polarization source term and the complex amplitudes of the pump field by relating the oscillating terms in the formulas (8.9) and (8.10):

$$\text{SHG:} \quad P_i(2\omega) = \frac{1}{2}\varepsilon_0 \sum_{j,k} \chi^{(2)}_{ijk}\, E_j(\omega) E_k(\omega) \tag{8.11}$$

In general a third order tensor in three dimensions has 27 components, but the specific $\chi^{(2)}_{ijk}$ tensor has much less independent components due to numerous symmetries. To represent the independent components of the second-order nonlinear susceptibility one often uses a so-called contracted notation. To introduce the contracted notation first a new tensor d_{ijk} is introduced:

$$d_{ijk} = \frac{1}{2}\chi^{(2)}_{ijk}, \tag{8.12}$$

where the factor of $\frac{1}{2}$ appears due to historical convention. In this case the formula for the complex amplitudes of the nonlinear polarization (8.11) can be rewritten in the form:

$$\text{SHG:} \quad P_i(2\omega) = \varepsilon_0 \sum_{j,k} d_{ijk}\, E_j(\omega) E_k(\omega) \tag{8.13}$$

Using the symmetry of d_{ijk} in its last two indices a contracted matrix $d_{i\ell}$ can be introduced by the following rule:

jk	xx	yy	zz	$yz,\ zy$	$xz,\ zx$	$xy,\ yx$
ℓ	1	2	3	4	5	6

Then the nonlinear susceptibility d_{ijk} can be represented by 3×6 matrix and the formula (8.13) can be written in the following form:

$$\text{SHG:} \quad \begin{bmatrix} P_x(2\omega) \\ P_y(2\omega) \\ P_z(2\omega) \end{bmatrix} = \varepsilon_0 \begin{bmatrix} d_{11} & d_{12} & d_{13} & d_{14} & d_{15} & d_{16} \\ d_{21} & d_{22} & d_{23} & d_{24} & d_{25} & d_{26} \\ d_{31} & d_{32} & d_{33} & d_{34} & d_{35} & d_{36} \end{bmatrix} \begin{bmatrix} E_x(\omega)^2 \\ E_y(\omega)^2 \\ E_z(\omega)^2 \\ 2E_y(\omega)E_z(\omega) \\ 2E_x(\omega)E_z(\omega) \\ 2E_x(\omega)E_y(\omega) \end{bmatrix} \tag{8.14}$$

Not all component of the $d_{i\ell}$ matrix in (8.14) are independent. Specifically for the $6mm$ hexagonal crystalline symmetry of AlGaN semiconductors there are only three independent components d_{15}, d_{31} and d_{33} with an additional simplification $d_{15} = d_{31} = -\frac{1}{2}d_{33}$ for

an ideal wurtzite crystal. For the specific case of second-harmonic generation in AlGaN semiconductors which is considered in great detail in this manuscript the formula for the nonlinear polarization takes the form:

$$\text{SHG:} \quad \begin{bmatrix} P_x(2\omega) \\ P_y(2\omega) \\ P_z(2\omega) \end{bmatrix} = \varepsilon_0 \begin{bmatrix} 0 & 0 & 0 & 0 & d_{15} & 0 \\ 0 & 0 & 0 & d_{15} & 0 & 0 \\ d_{31} & d_{31} & d_{33} & 0 & 0 & 0 \end{bmatrix} \begin{bmatrix} E_x(\omega)^2 \\ E_y(\omega)^2 \\ E_z(\omega)^2 \\ 2E_y(\omega)E_z(\omega) \\ 2E_x(\omega)E_z(\omega) \\ 2E_x(\omega)E_y(\omega) \end{bmatrix} \tag{8.15}$$

To conclude, this section gives a detailed derivation of the formulas for the Poynting vector (8.6) and the complex amplitudes for the nonlinear polarization (8.15); both formulas are taken into a frame to stress their importance. The formula (8.6) will be used on multiple occasions to calculate the power confined in different guiding structures. The nonlinear polarization defined by (8.15) will serve as a source term in the evolution equations for the second harmonic. In this manuscript the formulas (8.6) and (8.15) are in an agreement due to the consistent choice of the representation of the fields and polarizations through their complex amplitudes given by (8.1), (8.2) and (8.3). All the derivation here are given within the approximations of an instantaneous response of the nonlinear polarization to the applied electric field and a constant second-order susceptibility. These derivations are clear and easy to follow in contrast to general cases treated in classic reference books on nonlinear optics. These approximation are absolutely justified since, the general case is rarely considered in practice. In a final remark it should be noted that the consistency in the complex amplitudes representation is very important for the subject of integrated nonlinear optics, since different representation are often used in different books on integrated and nonlinear optics (for example, Boyd and Yariv), and a direct use of formulas for integrated and nonlinear optics coming from different books may lead to errors.

8.2 Second-harmonic generation in waveguides

In this work we have studied both planar and ridge waveguides. For the planar waveguides the equation presented below were solved predominantly by using analytical methods and Mathematica software. COMSOL finite-element software was used for the ridge waveguides and some particular cases of planar waveguides, which had more than 4 different layers.

8.2.1 Modes definition

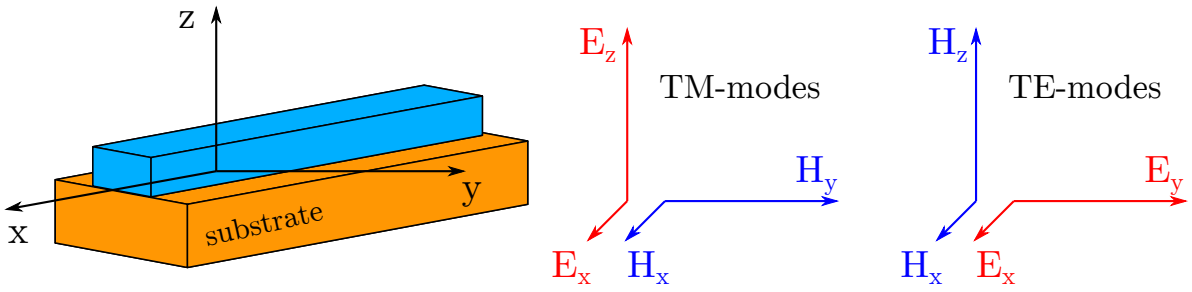

Figure 8.1 – A scheme of a ridge waveguide together with a definition of the TM- and TE-modes.

TM-modes

Equation for the TM-modes:

$$\frac{\partial^2 H_y}{\partial x^2} + \frac{\partial^2 H_y}{\partial y^2} + \frac{n_e^2}{n_o^2}\frac{\partial^2 H_y}{\partial z^2} + k^2 n_e^2 H_y = 0 \tag{8.16}$$

By the following separation of variables:

$$H_y(x, y, z) = \mathcal{A}\,\eta(z)\psi(y)e^{-i\beta x} \tag{8.17}$$

one can obtain a system of equations with boundary conditions, which can be used to determine the modes profiles and effective indices.
System of equations for the z-direction:

$$\begin{cases} \eta''(z) + \dfrac{n_o^2}{n_e^2}\left[k^2 n_e^2 - \beta_0^2\right]\eta(z) = 0, \\ \eta(z),\ \dfrac{1}{n_o^2}\eta'(z) - \text{continuous along z.} \end{cases} \tag{8.18}$$

System of equation for the y-direction:

$$\begin{cases} \psi''(y) + (\beta_0^2 - \beta^2)\psi(y) = 0, \\ \dfrac{1}{n_e^2}\psi(y),\ \dfrac{1}{n_e^2}\psi'(y) - \text{continuous along y.} \end{cases} \tag{8.19}$$

The power confined in the waveguide:

$$P = \frac{\beta}{2\omega\varepsilon_0}|\mathcal{A}|^2 \int\limits_{-\infty}^{\infty} \frac{|\eta(z)|^2}{n_e^2(z)}\,dz \int\limits_{-\infty}^{\infty} |\psi(y)|^2\,dy \tag{8.20}$$

TE-modes

Equation for the TM-modes:

$$\frac{\partial^2 E_y}{\partial x^2} + \frac{\partial^2 E_y}{\partial y^2} + \frac{\partial^2 E_y}{\partial z^2} + k^2 n_o^2 E_y = 0 \tag{8.21}$$

By the following separation of variables:

$$E_y(x,y,z) = \mathcal{A}\,\eta(z)\psi(y)e^{-i\beta x} \tag{8.22}$$

one can obtain a system of equations with boundary conditions, which can be used to determine the modes profiles and effective indices.
System of equations for the z-direction:

$$\begin{cases} \eta''(z) + (k^2 n_o^2 - \beta_0^2)\eta(z) = 0, \\ \eta(z),\ \eta'(z) - \text{continuous along z.} \end{cases} \tag{8.23}$$

System of equation for the y-direction:

$$\begin{cases} \psi''(y) + (\beta_0^2 - \beta^2)\psi(y) = 0, \\ \psi(y),\ \dfrac{1}{n_o^2}\psi'(y) - \text{continuous along y.} \end{cases} \tag{8.24}$$

The power confined in the waveguide:

$$P = \frac{\beta}{2\omega\mu_0}|\mathcal{A}|^2 \int\limits_{-\infty}^{\infty} |\eta(z)|^2\,dz \int\limits_{-\infty}^{\infty} |\psi(y)|^2\,dy \tag{8.25}$$

8.2.2 SHG efficiency

In the case of ridge and planar waveguides we have studied only the interactions between the TM-modes, since they allow to use the largest component of the nonlinear coefficient d_{33}. We have also used large ridge waveguides, which were highly multi-modal in lateral direction and were behaving almost like planar waveguides.

For the planar waveguides the SHG efficiency for the TM pump and TM second harmonic is determined by:

$$P_{SH} = \frac{2k_p^2}{\varepsilon_0 c}\left[\frac{d_{33}^2 n_P^4}{n_e^4(\omega_P) n_e^2(\omega_{SH}) n_{SH}}\right]\frac{1}{H_{eff}}\frac{1}{W}P_{pump}^2 L^2 \frac{\sin^2(\Delta\beta L/2)}{(\Delta\beta L/2)^2}, \tag{8.26}$$

where L is the propagation distance, W is the lateral confinement, $\Delta\beta = \beta_{SH} - 2\beta_P$, n_P, n_{SH} are the effective refractive indices for the pump and the second harmonic and H_{eff}

is the effective waveguide thickness which is determined in the following way:

$$\frac{1}{H_{eff}} = \frac{\left[\int_{-\infty}^{+\infty} \tilde{d}_{33}(z) \frac{\eta_P^2(z)}{n_e^4(z,\omega_P)} \frac{\eta_{SH}(z)}{n_e^2(z,\omega_{SH})}\, dz\right]^2}{\int_{-\infty}^{+\infty} \frac{|\eta_{SH}(z)|^2}{n_e^2(z,\omega_P)}\, dz \left[\int_{-\infty}^{+\infty} \frac{|\eta_P(z)|^2}{n_e^2(z,\omega_P)}\, dz\right]^2}, \tag{8.27}$$

$\tilde{d}_{33}(z)$ is the normalized profile of the nonlinear coefficient. In the case of the perfect modal overlap H_{eff} approached the actual waveguide thickness.

The solutions of the equations (8.18) together with the formula (8.26) were used in order to obtain the modelling results presented in Chapter 2.

8.3 Second harmonic generation in micro-disks

In the case of micro-disk the simulation results presented in Chapter 2 were obtained through the analytical approach based on the effective index method. It can be done due to the cylindrical symmetry, which allows to use special functions to define the solutions. Below we present some equations and formulas that were used for the modelling.

8.3.1 Modes definition

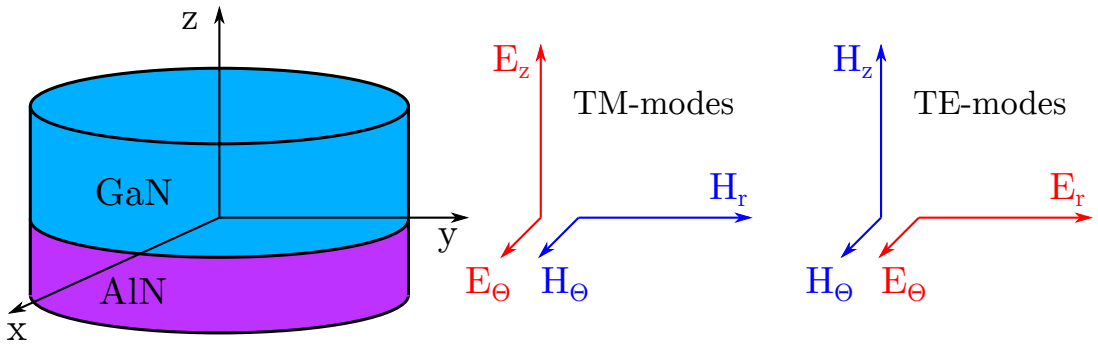

Figure 8.2 – A micro-disk scheme together with a definition of the TM- and TE-modes.

TM-modes

The TM-modes are characterised by the following field components: principal components E_z, H_r and minor components E_θ, H_θ, which means $|E_z| \gg |E_\theta|$ and $|H_r| \gg |H_\theta|$. The relations between the different field components are given by:

$$H_r = -\frac{1}{i\omega\mu_0}\frac{1}{r}\frac{\partial E_z}{\partial \theta}, \tag{8.28}$$

$$H_\theta = \frac{1}{i\omega\mu_0}\frac{\partial E_z}{\partial r}, \tag{8.29}$$

$$E_\theta = \frac{1}{i\omega\varepsilon_0 n_o^2}\frac{\partial H_r}{\partial z}. \tag{8.30}$$

By factoring out the time dependence:

$$E_z(r,\theta,z,t) = \mathcal{E}_z(r,\theta,z)e^{i\omega t} \tag{8.31}$$

we can write the propagation equation for the $\mathcal{E}_z$ amplitude:

$$\frac{\partial^2\mathcal{E}_z}{\partial r^2} + \frac{1}{r}\frac{\partial\mathcal{E}_z}{\partial r} + \frac{1}{r^2}\frac{\partial^2\mathcal{E}_z}{\partial\theta^2} + \frac{n_e^2}{n_o^2}\frac{\partial^2\mathcal{E}_z}{\partial z^2} + k^2 n_e^2\mathcal{E}_z = 0 \tag{8.32}$$

By using the separation of the variables we can find the solution of equation (8.32) in the form:

$$\mathcal{E}_z(r,\theta,z) = \mathcal{A}\,\eta(z)\psi(r)e^{-i\ell\theta} \tag{8.33}$$

$\mathcal{A}$ represents the energy stored in the microdisk.
In this case the power circulating in the microdisk is given by:

$$P_{circ} = |\mathcal{A}|^2 \delta f_{FSR}, \tag{8.34}$$

where $\delta f_{FSR} = \delta\omega_{FSR}/2\pi$ is the free spectral range. On the other hand:

$$P_{circ} = \frac{1}{2}\int E_z H_r^* \, dr \, dz = \frac{\ell}{2\omega\mu_0}|\mathcal{A}|^2 \int_{-\infty}^{+\infty} |\eta(z)|^2 \, dz \int_0^{\infty} \frac{1}{r}|\psi(r)|^2 \, dr, \tag{8.35}$$

which leads to the normalisation conditions for the TM-modes:

$$\int_{-\infty}^{+\infty} |\eta(z)|^2 \, dz = 1, \tag{8.36}$$

$$\frac{\ell}{2\omega\mu_0}\int_0^{\infty} \frac{1}{r}|\psi(r)|^2 \, dr = \delta f_{FSR}. \tag{8.37}$$

TE-modes

For the TE-modes the principal components of the field are H_z, E_r and the minor components are H_θ, E_θ, which means $|H_z| \gg |H_\theta|$ and $|E_r| \gg |E_\theta|$. The relations between the different field components are given by:

$$E_r = \frac{1}{i\omega\varepsilon_0 n_o^2}\frac{1}{r}\frac{\partial H_z}{\partial\theta}, \tag{8.38}$$

$$E_\theta = -\frac{1}{i\omega\varepsilon_0 n_o^2}\frac{\partial H_z}{\partial r}, \tag{8.39}$$

$$H_\theta = -\frac{1}{i\omega\mu_0}\frac{\partial E_r}{\partial z}. \tag{8.40}$$

By factoring out the time dependence:

$$H_z(r,\theta,z,t) = \mathcal{H}_z(r,\theta,z)e^{i\omega t} \tag{8.41}$$

we can write the equation for the $\mathcal{H}_z$ amplitude:

$$\frac{\partial^2\mathcal{H}_z}{\partial r^2} + \frac{1}{r}\frac{\partial\mathcal{H}_z}{\partial r} + \frac{1}{r^2}\frac{\partial^2\mathcal{H}_z}{\partial\theta^2} + \frac{\partial^2\mathcal{H}_z}{\partial z^2} + k^2 n_o^2 \mathcal{H}_z = 0 \tag{8.42}$$

Using the separation of the variables we can find the solution of equation (8.42) in the form:

$$\mathcal{H}_z(r,\theta,z) = \mathcal{A}\,\eta(z)\psi(r)e^{-i\ell\theta} \tag{8.43}$$

As previously, $\mathcal{A}$ represents the energy stored in the microdisk. In this case the power circulating in the microdisk is given by:

$$P_{circ} = |\mathcal{A}|^2 \delta f_{FSR}, \tag{8.44}$$

where $\delta f_{FSR} = \delta\omega_{FSR}/2\pi$ is the free spectral range. On the other hand:

$$P_{circ} = -\frac{1}{2}\int H_z^* E_r \, dr \, dz = \frac{\ell}{2\omega\varepsilon_0 n^2}|\mathcal{A}|^2 \int_{-\infty}^{+\infty} |\eta(z)|^2 \, dz \int_0^{\infty} \frac{1}{r}|\psi(r)|^2 \, dr, \tag{8.45}$$

where n is the effective index of a given mode. Combining (8.44) and (8.45) we get the following normalisation conditions for the TE-modes:

$$\int_{-\infty}^{+\infty} |\eta(z)|^2 \, dz = 1, \tag{8.46}$$

$$\frac{\ell}{2\omega\varepsilon_0 n^2} \int_0^{\infty} \frac{1}{r}|\psi(r)|^2 \, dr = \delta f_{FSR}. \tag{8.47}$$

8.3.2 SHG efficiency

For all the cases considered for III-nitride microdisks, the second harmonic is a TM-mode. The equation governing the z-component of the electric field of the second harmonic can be written as

$$E_z^{SH}(r,\theta,z,t) = \mathcal{E}_z^{SH}(r,\theta,z)e^{i\omega_{SH}t} \tag{8.48}$$

The equation for the field $\mathcal{E}_z^{SH}$ is given by:

$$\frac{\partial^2\mathcal{E}_z^{SH}}{\partial r^2} + \frac{1}{r}\frac{\partial\mathcal{E}_z^{SH}}{\partial r} + \frac{1}{r^2}\frac{\partial^2\mathcal{E}_z^{SH}}{\partial\theta^2} + \frac{n_e^2}{n_o^2}\frac{\partial^2\mathcal{E}_z^{SH}}{\partial z^2} + k_{SH}^2 n_e^2 \mathcal{E}_z^{SH} = -\omega_{SH}^2\mu_0 P_z^{NL} \tag{8.49}$$

We search the solution of the equation (8.49) in the form:

$$\mathcal{E}_z^{SH}(r,\theta,z) = \mathcal{A}_{SH}(\theta)\,\eta_{SH}(z)\psi_{SH}(r)e^{-i\ell_{SH}\theta}, \tag{8.50}$$

and in general case for the amplitude $\mathcal{A}_{SH}(\theta)$ we get:

$$\frac{dA_{SH}}{d\theta} = -\frac{i\omega_{SH}}{4\delta f_{FSR,SH}} e^{i\ell_{SH}\theta} \left\{ \int_{-\infty}^{+\infty} dz \int_0^{\infty} r\,\eta_{SH}(z)\psi_{SH}(r)P_z^{NL}\,dr \right\}. \tag{8.51}$$

TM pump and TM second harmonic

For TM pump the nonlinear polarisation P_z^{NL} is given by:

$$P_z^{NL} = \varepsilon_0 d_{33}\left(\mathcal{E}_z^P\right)^2, \tag{8.52}$$

where d_{33} =10pm/V for GaN and d_{33} =1pm/V for AlN and:

$$\mathcal{E}_z^P(r,\theta,z) = \mathcal{A}_P\,\eta_P(z)\psi_P(r)e^{-i\ell_P\theta} \tag{8.53}$$

By substituting (8.52) and (8.53) into (8.51) we get:

$$\frac{d\mathcal{A}_{SH}}{d\theta} = \mathcal{A}_P^2\mathcal{K}_{TM}e^{i\Delta\ell\theta}, \tag{8.54}$$

where $\Delta\ell = \ell_{SH} - 2\ell_P$ and

$$\mathcal{K}_{TM} = -\frac{i\varepsilon_0\omega_{SH}}{4\delta f_{FSR,SH}} \int_0^W d_{33}(z)\eta_{SH}(z)\eta_P^2(z)\,dz \int_0^R r\,\psi_{SH}(r)\psi_P^2(r)\,dr, \tag{8.55}$$

where W is the disk thickness and R is the disk radius.

Double-resonance phase matching induces two requirements: the harmonic mode should be resonant at twice the energy of the pump mode. The orbital momentum should be conserved which translates into the condition $\Delta\ell = \ell_{SH} - 2\ell_P = 0$.

TE pump and TM second harmonic

For a TE pump, the nonlinear polarisation P_z^{NL} is given by:

$$P_z^{NL} = \varepsilon_0 d_{31} \left(\mathcal{E}_r^P\right)^2, \tag{8.56}$$

where we assume $d_{31} = 0.5d_{33}$. For the $\mathcal{E}_r^P$ field from the formulas (8.38) and (8.43) we get:

$$\mathcal{E}_r^P(r,\theta,z) = -\frac{\ell_P}{\omega_P\varepsilon_0 n_o^2}\frac{1}{r}\mathcal{A}_P\,\eta_P(z)\psi_P(r)e^{-im_P\theta} \tag{8.57}$$

Substituting (8.56) and (8.57) into (8.51) we get:

$$\frac{d\mathcal{A}_{SH}}{d\theta} = \mathcal{A}_P^2\mathcal{K}_{TE}e^{i\Delta\ell\theta}, \tag{8.58}$$

where $\Delta\ell = \ell_{SH} - 2\ell_P$ and

$$\mathcal{K}_{TE} = -\frac{i\omega_{SH}\ell_P^2}{4\delta f_{FSR,SH}\varepsilon_0\omega_P^2} \int_0^W \frac{d_{31}(z)}{n_o^4(z,\omega_p)}\eta_{SH}(z)\eta_P^2(z)\,dz \int_0^R \frac{1}{r}\psi_{SH}(r)\psi_P^2(r)\,dr, \tag{8.59}$$

where W is the disk thickness and R is the disk radius.

Conversion efficiency

Double-resonance phase matching induces two requirements: the harmonic mode should be resonant at twice the energy of the pump mode. The orbital momentum should be conserved which translates into the condition $\Delta\ell = \ell_{SH} - 2\ell_P = 0$.

The conversion efficiency is calculated from the formula:

$$P_{SH}^{out} = \frac{4Q_{SH}^c}{\omega_{SH}\left(1 + Q_{SH}^c/Q_{SH}^0\right)^2}\left[\frac{4Q_P^c}{\omega_P\left(1 + Q_P^c/Q_P^0\right)^2}2\pi\delta f_{FSR,SH}|\mathcal{K}|P_P^{in}\right]^2, \tag{8.60}$$

where Q_i^c and Q_i^0 are the coupling and intrinsic quality factors for the micro-disks.

The analytical solutions of the equations (8.32) and (8.42) together with the formula (8.60) were used to obtain the modelling results for the micro-disks presented in Chapter 2.

8.4 Intermodal coupling

The formulas presented below are taken from the book "Theory of Dielectric Optical Waveguides" by Dietrich Marcuse, Academic Press, 1974. The details of rather complicated derivations for these formulas can be found in the book.

Figure 8.3 schematically shows a planar waveguide with a sinusoidal perturbation $f(x)$ on the surface:

$$f(x) = b\sin(\theta x), \tag{8.61}$$

where b is the amplitude and θ is the spatial frequency of this perturbation and x is the direction of the mode propagation.

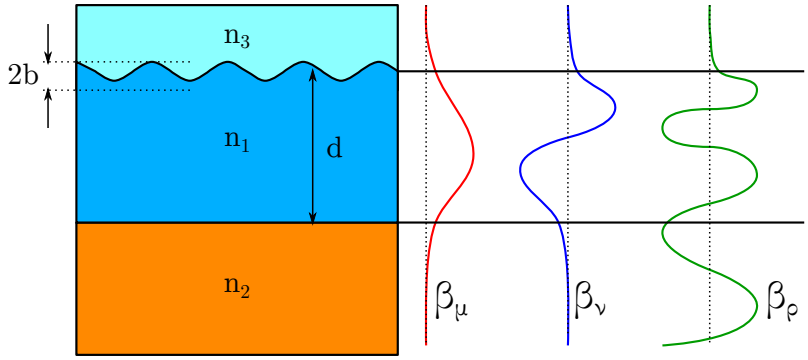

Figure 8.3 – A scheme of a planar waveguide with a sinusoidal surface perturbation. Two modes with the effective wave vectors β_μ and β_ν are confined in the guiding layer with the refractive index n_1, while the mode β_ρ is radiating to the substrate with the refractive index n_2.

It is assumed that the waveguide has a simple three-layer structure. The guiding layer has a thickness d and a refractive index n_1, while the two other layers have n_2 and n_3 refractive indices with a following relation $n_1 > n_2 > n_3$. The waveguide can support one or several guided modes depending on the values of its thickness and refractive indices. Figure 8.3 also presents an example of two guided modes with the effective wave vectors β_μ and β_ν and one radiation mode with the wave vector β_ρ.

The sinusoidal perturbation on the surface of the waveguide can efficiently couple two guided modes when the conditions $\beta_\mu - \beta_\nu = \theta$ is satisfied. A complete power transfer from one mode to another will occur after the propagation distance L_c:

$$L_c = \frac{\pi}{2R_{\mu\nu}}, \tag{8.62}$$

where $R_{\mu\nu}$ is the coupling coefficient. The coupling coefficient for two guided modes can be determined from the formula:

$$R_{\mu\nu} = \frac{\kappa_\mu \kappa_\nu b}{2\{|\beta_\mu||\beta_\nu|\,[d + 1/\gamma_\mu + 1/\delta_\mu]\,[d + 1/\gamma_\nu + 1/\delta_\nu]\}^{1/2}} \tag{8.63}$$

where b is the perturbation amplitude, d is the waveguide thickness, $\beta_i = \frac{2\pi}{\lambda} n_i^{\text{eff}}$ is the effective wave vectors for the guided modes, and the κ_i, γ_i and δ_i coefficients are defined

by the following relations:

$$\begin{aligned} \kappa_i &= (n_1^2 k^2 - \beta_i^2)^{1/2}, \\ \gamma_i &= (\beta_i^2 - n_2^2 k^2)^{1/2}, \\ \delta_i &= (\beta_i^2 - n_3^2 k^2)^{1/2}, \end{aligned}$$

where n_1, n_2 and n_3 are the refractive indices of the waveguide layers, and $k = \dfrac{2\pi}{\lambda}$ in the wave vector in free space.

Formulas (8.62) and (8.63) give a direct analytical estimation for the coupling length. In addition to these formulas one has to calculate the effective refractive indices n_i^{eff}, which can be done both analytically or by using available finite-element software. In Chapter 5 the formula (8.62) was used for the estimation of the coupling between two modes guided at a slightly different angles in a planar waveguide. Due to the small deviation angles the walk-off was neglected. The calculation were done using Mathematica software.

The sinusoidal perturbation can efficiently couple also guided and radiation modes when the conditions $\beta_\nu - \beta_\rho = \theta$ is satisfied. In this case the power transfer is irreversible, which introduces losses to the guided mode. In this case the power P_μ of the guided mode will have an exponential attenuation along the propagation direction $P_\nu = P_0 \exp(-\alpha x)$, and the loss coefficient α can be calculated according to the formula:

$$\alpha = \frac{(n_1^2 - n_3^2) k^2 \kappa_\nu^2 b^2}{2|\beta_\nu| \left[d + 1/\gamma_\nu + 1/\delta_\nu\right]} \frac{\rho\sigma^2}{2\left[\rho^2(\sigma\cos\sigma d + \Delta \sin\sigma d)^2 + \sigma^2(\sigma \sin\sigma d - \Delta\cos\sigma d)^2\right]}, \tag{8.64}$$

where b is the perturbation amplitude, d is the waveguide thickness, $\beta_\nu = \dfrac{2\pi}{\lambda} n_\nu^{\text{eff}}$ is the effective wave vector of the guided mode, $k = \dfrac{2\pi}{\lambda}$ in the wave vector in free space and the coefficient κ_i, γ_i, δ_i, σ, ρ and Δ are defined in the following way:

$$\begin{aligned} \kappa_\nu &= (n_1^2 k^2 - \beta_\nu^2)^{1/2}, \\ \gamma_\nu &= (\beta_\nu^2 - n_2^2 k^2)^{1/2}, \\ \delta_\nu &= (\beta_\nu^2 - n_3^2 k^2)^{1/2}, \\ \Delta &= (\beta_\rho^2 - n_3^2 k^2)^{1/2}, \\ \sigma &= (n_1^2 k^2 - \beta_\rho^2)^{1/2}, \\ \rho &= (n_2^2 k^2 - \beta_\rho^2)^{1/2}, \end{aligned}$$

where n_1, n_2 and n_3 are the refractive indices of the waveguide layers, and $k = \dfrac{2\pi}{\lambda}$ in the wave vector in free space, $\beta_\rho = \dfrac{2\pi}{\lambda} n_\rho^{\text{eff}}$ is the effective wave vector of the radiation mode.

The formula (8.64) was used for the estimation of the losses induced by the surface roughness for the waveguides studied in this work. In order to use Marcuse model several surface profiles were extracted from the AFM scan for a given sample. A typical example of such a profile is shown in Fig. 8.4(a) by the blue dotted curve. Further an approximation of this profile by Fourier series was developed in the following form:

$$\text{fit} = b \sum_{m=1}^{\infty} h_m \sin\left(\frac{\pi m x}{L}\right) = b \sum_{m=1}^{\infty} h_m \sin\left(k_m x\right), \tag{8.65}$$

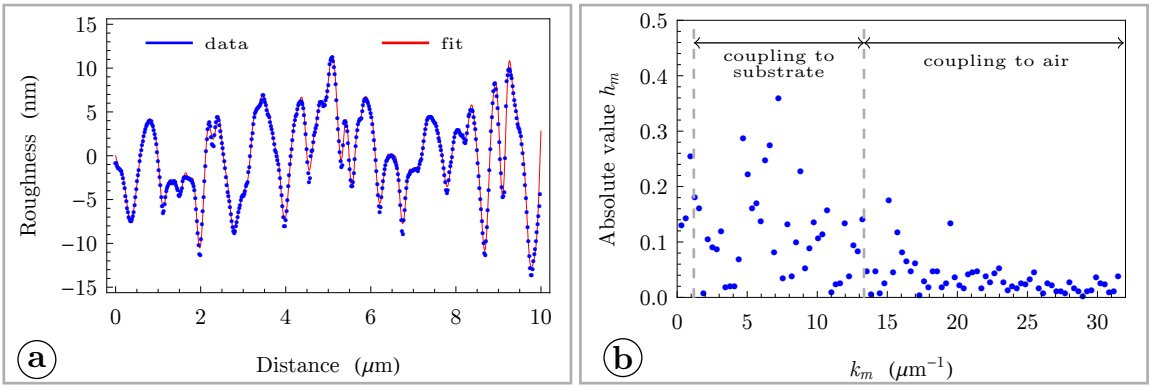

Figure 8.4 – (a) A typical surface profile for an MBE grown sample; the blue dotted curve shows the experimental data and the red solid curve shows the approximation with the Fourier series. (b) Absolute values of the decomposition coefficients h_m as a function of spatial frequencies k_m.

where L is the length of the AFM scan, b is the *rms* roughness and h_m are decomposition coefficients normalized by the condition $\sum_{m=1}^{\infty} |h_m|^2 = 1$.

The fit function traced by the red solid curve in Fig. 8.4(a) represents the Fourier series with the first 100 decomposition terms. As the result of this decomposition the surface roughness was approximated by the sum of sinusoidal perturbations with different spatial frequencies k_m. For the estimation of the propagation losses it was assumed that each spatial frequency k_m gives an independent contribution to the propagation losses with the normalized weight h_m. The absolute value for the weights h_m as a function of the spatial frequencies k_m is presented in Fig. 8.4(b).

The losses were estimated by the formula:

$$\alpha_{\text{total}} = \sum_{m=1}^{M} \alpha_m |h_m|^2, \tag{8.66}$$

where M is the number of the decomposition terms, α_m is the loss coefficient estimated by the formula (8.64) for the $m-$th sinusoidal perturbation with the spacial frequency h_m. It should be noted that the b *rms* roughness plays the role of the the amplitude b in the formula (8.64).

Bibliography

[1] J. Miragliotta, D. K. Wickenden, T. J. Kistenmacher, and W. A. Bryden, "Linear- and nonlinear-optical properties of GaN thin films," *Journal of the Optical Society of America B*, vol. 10, no. 8, p. 1447, 1993.

[2] N. A. Sanford, A. V. Davydov, D. V. Tsvetkov, A. V. Dmitriev, S. Keller, U. K. Mishra, S. P. Denbaars, S. S. Park, J. Y. Han, and R. J. Molnar, "Measurement of second order susceptibilities of GaN and AlGaN," *Journal of Applied Physics*, vol. 97, no. 5, 2005.

[3] A. W. Bruch, C. Xiong, B. Leung, M. Poot, J. Han, and H. X. Tang, "Broadband nanophotonic waveguides and resonators based on epitaxial GaN thin films," *Applied Physics Letters*, vol. 107, no. 14, 2015.

[4] I. Roland, Y. Zeng, X. Checoury, M. El Kurdi, S. Sauvage, C. Brimont, T. Guillet, B. Gayral, M. Gromovyi, J. Y. Duboz, F. Semond, M. P. de Micheli, and P. Boucaud, "Near-infrared III-nitride-on-silicon nanophotonic platform with microdisk resonators," *Optics Express*, vol. 24, no. 9, p. 9602, 2016.

[5] Y. Zeng, I. Roland, X. Checoury, Z. Han, M. El Kurdi, S. Sauvage, B. Gayral, C. Brimont, T. Guillet, M. Mexis, F. Semond, and P. Boucaud, "Resonant second harmonic generation in a gallium nitride two-dimensional photonic crystal on silicon," *Applied Physics Letters*, vol. 106, no. 8, pp. 24–28, 2015.

[6] Y. Zeng, I. Roland, X. Checoury, Z. Han, M. El Kurdi, S. Sauvage, B. Gayral, C. Brimont, T. Guillet, F. Semond, and P. Boucaud, "Imaging of Photonic Crystal Localized Modes through Third-Harmonic Generation," *ACS Photonics*, vol. 3, no. 7, pp. 1240–1247, 2016.

[7] M. S. Mohamed, A. Simbula, J.-F. Carlin, M. Minkov, D. Gerace, V. Savona, N. Grandjean, M. Galli, and R. Houdré, "Efficient continuous-wave nonlinear frequency conversion in high-q gallium nitride photonic crystal cavities on silicon," *APL Photonics*, vol. 2, no. 3, p. 031301, 2017.

[8] M. M. Fejer, G. A. Magel, D. H. Jundt, and R. Byer, "Quasi phase-matching second harmonic generation : tuning and tolerances," *IEEE Journal of quantum electronics*, vol. 28, no. 11, pp. 2631–2654, 1992.

[9] D. S. Hum and M. M. Fejer, "Quasi-phasematching," *Comptes Rendus Physique*, vol. 8, pp. 180–198, mar 2007.

[10] S. Pezzagna, P. Vennéguès, N. Grandjean, A. D. Wieck, and J. Massies, "Submicron periodic poling and chemical patterning of GaN," *Applied Physics Letters*, vol. 87, no. 6, 2005.

[11] J. Hite, M. Twigg, M. Mastro, J. Freitas, J. Meyer, I. Vurgaftman, S. O'Connor, N. Condon, F. Kub, S. Bowman, and C. Eddy, "Development of periodically oriented gallium nitride for non-linear optics," *Optical Materials Express*, vol. 2, pp. 1203 – 1208, sep 2012.

[12] D. Alden, W. Guo, R. Kirste, F. Kaess, I. Bryan, T. Troha, A. Bagal, P. Reddy, L. H. Hernandez-Balderrama, A. Franke, S. Mita, C. H. Chang, A. Hoffmann, M. Zgonik, R. Collazo, and Z. Sitar, "Fabrication and structural properties of AlN submicron periodic lateral polar structures and waveguides for UV-C applications," *Applied Physics Letters*, vol. 108, no. 26, 2016.

[13] A. Chowdhury, H. M. Ng, M. Bhardwaj, and N. G. Weimann, "Second-harmonic generation in periodically poled GaN," *Applied Physics Letters*, vol. 83, no. 6, pp. 1077–1079, 2003.

[14] D. N. Hahn, G. T. Kiehne, J. B. Ketterson, G. K. L. Wong, P. Kung, A. Saxler, and M. Razeghi, "Phase-matched optical second-harmonic generation in GaN and AlN slab waveguides," *Journal of Applied Physics*, vol. 85, no. 5, p. 2497, 1999.

[15] D. Blanc, A. M. Bouchoux, C. Plumereau, A. Cachard, and J. F. Roux, "Phase-matched frequency doubling in an aluminum nitride waveguide with a tunable laser source," *Applied Physics Letters*, p. 659, 1995.

[16] I. Roland, M. Gromovyi, Y. Zeng, M. El Kurdi, S. Sauvage, C. Brimont, T. Guillet, B. Gayral, F. Semond, J. Y. Duboz, M. de Micheli, X. Checoury, and P. Boucaud, "Phase-matched second harmonic generation with on-chip GaN-on-Si microdisks," *Scientific Reports*, vol. 6, no. July, p. 34191, 2016.

[17] C. Xiong, W. H. P. Pernice, K. K. Ryu, C. Schuck, K. Y. Fong, T. Palacios, and H. X. Tang, "Integrated GaN photonic circuits on silicon (100) for second harmonic generation," *Opt. Express*, vol. 19, no. 11, pp. 10462–10470, 2011.

[18] X. Guo, C. Zou, and H. Tang, "Second-harmonic generation in aluminum nitride microrings with 2500 %/ W conversion efficiency," *Optica*, vol. 3, no. 10, p. 1126, 2016.

[19] O. Westreich, M. Katz, Y. Paltiel, O. Ternyak, and N. Sicron, "Low propagation loss in GaN/AlGaN-based ridge waveguides," *Physica Status Solidi (A) Applications and Materials Science*, vol. 212, no. 5, pp. 1043–1048, 2015.

[20] A. Stolz, E. Cho, E. Dogheche, Y. Androussi, D. Troadec, D. Pavlidis, and D. Decoster, "Optical waveguide loss minimized into gallium nitride based structures grown by metal organic vapor phase epitaxy," *Applied Physics Letters*, vol. 98, no. 16, pp. 104–106, 2011.

[21] S. Pezzagna, J. Brault, M. Leroux, J. Massies, and M. De Micheli, "Refractive indices and elasto-optic coefficients of GaN studied by optical waveguiding," *Journal of Applied Physics*, vol. 103, no. 12, pp. 1–8, 2008.

[22] Ü. Özgür, G. Webb-Wood, H. O. Everitt, F. Yun, and H. Morkoç, "Systematic measurement of Al x Ga 1x N refractive indices," *Applied Physics Letters*, vol. 79, no. 25, pp. 4103 – 4105, 2001.

[23] N. Grandjean, A. Dussaigne, S. Pezzagna, and P. Vennéguès, "Control of the polarity of GaN films using an Mg adsorption layer," *Journal of Crystal Growth*, vol. 251, no. 1, pp. 460–464, 2003.

[24] A. Majkić, A. Franke, R. Kirste, R. Schlesser, R. Collazo, Z. Sitar, and M. Zgonik, "Optical nonlinear and electro-optical coefficients in bulk aluminium nitride single crystals," *physica status solidi (b)*, vol. 254, no. 9, 2017.

[25] A. W. Bruch, C. Xiong, B. Leung, M. Poot, J. Han, and H. X. Tang, "Broadband nanophotonic waveguides and resonators based on epitaxial gan thin films," *Applied Physics Letters*, vol. 107, no. 14, p. 141113, 2015.

[26] I. Roland, Y. Zeng, X. Checoury, M. El Kurdi, S. Sauvage, C. Brimont, T. Guillet, B. Gayral, M. Gromovyi, J. Duboz, *et al.*, "Near-infrared iii-nitride-on-silicon nanophotonic platform with microdisk resonators," *Optics express*, vol. 24, no. 9, pp. 9602–9610, 2016.

[27] N. Grandjean, J. Massies, and M. Leroux, "Nitridation of sapphire. effect on the optical properties of gan epitaxial overlayers," *Applied physics letters*, vol. 69, no. 14, pp. 2071–2073, 1996.

[28] N. Grandjean, M. Leroux, M. Laügt, and J. Massies, "Gas source molecular beam epitaxy of wurtzite gan on sapphire substrates using gan buffer layers," *Applied physics letters*, vol. 71, no. 2, pp. 240–242, 1997.

[29] J.-Y. Duboz, N. Grandjean, F. Omnès, J.-L. Reverchon, and M. Mosca, "Solar blind detectors based on algan grown on sapphire," *physica status solidi (c)*, vol. 2, no. 3, pp. 964–971, 2005.

[30] J. Massies and N. Grandjean, "Real-time control of the molecular beam epitaxy of nitrides," *Journal of crystal growth*, vol. 201, pp. 382–387, 1999.

[31] T. Huault, J. Brault, F. Natali, B. Damilano, D. Lefebvre, L. Nguyen, M. Leroux, and J. Massies, "Blue-light emission from gan/ al 0.5 ga 0.5 n quantum dots," *Applied Physics Letters*, vol. 92, no. 5, p. 051911, 2008.

[32] N. Grandjean, M. Leroux, J. Massies, M. Mesrine, and M. Laügt, "Molecular beam epitaxy of gan under n-rich conditions using nh3," *Japanese journal of applied physics*, vol. 38, no. 2R, p. 618, 1999.

[33] N. Grandjean, J. Massies, P. Vennegues, M. Leroux, F. Demangeot, M. Renucci, and J. Frandon, "Molecular-beam epitaxy of gallium nitride on (0001) sapphire substrates using ammonia," *Journal of applied physics*, vol. 83, no. 3, pp. 1379–1383, 1998.

[34] F. Semond, "Epitaxial challenges of gan on silicon," *MRS Bulletin*, vol. 40, no. 5, pp. 412–417, 2015.

[35] S. Pezzagna, P. Vennéguès, N. Grandjean, and J. Massies, "Polarity inversion of gan (0 0 0 1) by a high mg doping," *Journal of Crystal Growth*, vol. 269, no. 2-4, pp. 249–256, 2004.

[36] P. Tavernier, T. Margalith, J. Williams, D. Green, S. Keller, S. DenBaars, U. Mishra, S. Nakamura, and D. Clarke, "The growth of n-face gan by mocvd: effect of mg, si, and in," *Journal of crystal growth*, vol. 264, no. 1-3, pp. 150–158, 2004.

[37] P. Tien and R. Ulrich, "Theory of prism–film coupler and thin-film light guides," *JOSA*, vol. 60, no. 10, pp. 1325–1337, 1970.

[38] S. Vézian, F. Natali, F. Semond, and J. Massies, "From spiral growth to kinetic roughening in molecular-beam epitaxy of gan (0001)," *Physical Review B*, vol. 69, no. 12, p. 125329, 2004.

[39] D. Marcuse, "Theory of dielectric optical waveguides (academic, new york, 1974)," *Google Scholar*, pp. 181–193.

[40] W. H. Pernice, C. Xiong, and H. X. Tang, "High Q micro-ring resonators fabricated from polycrystalline aluminum nitride films for near infrared and visible photonics," *Optics Express*, vol. 20, no. 11, p. 12261, 2012.

[41] P. S. Kuo and G. S. Solomon, "On-and off-resonance second-harmonic generation in gaas microdisks," *Optics express*, vol. 19, no. 18, pp. 16898–16918, 2011.

[42] Q. Li, A. A. Eftekhar, Z. Xia, and A. Adibi, "Azimuthal-order variations of surface-roughness-induced mode splitting and scattering loss in high-q microdisk resonators," *Optics letters*, vol. 37, no. 9, pp. 1586–1588, 2012.

[43] P. S. Kuo, J. Bravo-Abad, and G. S. Solomon, "Second-harmonic generation using-quasi-phasematching in a gaas whispering-gallery-mode microcavity," *Nature communications*, vol. 5, p. 3109, 2014.

[44] S. Mariani, A. Andronico, A. Lemaître, I. Favero, S. Ducci, and G. Leo, "Second-harmonic generation in algaas microdisks in the telecom range," *Optics letters*, vol. 39, no. 10, pp. 3062–3065, 2014.

[45] A. Yariv, "Universal relations for coupling of optical power between microresonators and dielectric waveguides," *Electronics letters*, vol. 36, no. 4, pp. 321–322, 2000.

[46] D. P. Lake, M. Mitchell, H. Jayakumar, L. F. dos Santos, D. Curic, and P. E. Barclay, "Efficient telecom to visible wavelength conversion in doubly resonant gallium phosphide microdisks," *Applied Physics Letters*, vol. 108, no. 3, p. 031109, 2016.

[47] J. Fürst, D. Strekalov, D. Elser, M. Lassen, U. L. Andersen, C. Marquardt, and G. Leuchs, "Naturally phase-matched second-harmonic generation in a whispering-gallery-mode resonator," *Physical review letters*, vol. 104, no. 15, p. 153901, 2010.

[48] Z.-F. Bi, A. W. Rodriguez, H. Hashemi, D. Duchesne, M. Loncar, K.-M. Wang, and S. G. Johnson, "High-efficiency second-harmonic generation in doubly-resonant χ (2) microring resonators," *Optics express*, vol. 20, no. 7, pp. 7526–7543, 2012.